Quantitative Analysis of Stenting Effects on Cellular Response

Nii – Armah Armah

Department of Materials Science and Engineering

The University of Sheffield

A thesis submitted for the degree of

Doctor of Philosophy

2015

ABSTRACT

BACKGROUND

Generally hypothesized hemodynamic forces and procedures (surgical and stenting) leading to arteriosclerosis and in-stent restenosis still remain entirely unclear. More so, it is difficult to identify and differentiate which of the procedural injury and/or changes in the local hemodynamic forces due to stent presence influence the onset of undesired clinical events. This difficulty in identifying the main factors leading to in-stent restenosis is compounded as procedural injury and change in hemodynamic stresses usually co-exist in-vivo. To simplify the complexity in identifying the predictors of in-stent restenosis, this thesis focused on the effects of local hemodynamic forces within stented artery on endothelial cells that could lead to in-stent restenosis.

Endothelial cells (ECs) play a critical element in the maintenance of healthy artery. Experimental studies of endothelial structure and function have presented evidence that physiological hemodynamic forces promote ECs elongation and atheroprotective endothelial phenotype whilst unphysiological hemodynamic forces promote atheroprone and polygonal shaped endothelial. Based on the above stated evidence, an experimental stent-cells interaction flow bio-reactor system was developed. This system is capable of subjecting ECs cultured in vitro to similar hemodynamic forces present within stented arteries in vivo. Computational models have been developed and used as complementary tool in the quantitative analysis of the mechanical forces being applied to the cultured cells. The computational models were validated to guarantee accuracy of computational results.

METHODS AND RESULTS

Human umbilical vein endothelial cells (HUVECs) were subjected to steady and realistic physiological left anterior descending artery (LAD) flow waveforms at hydrostatic pressures of 120/80 mmHg and 100 mmHg respectively at timescales of 6, 12 and 24 hours within the stent-cell

interaction model. The morphology of cells after exposure to the flow conditions where quantified by using a commercial computational image processing programme built on a MATLAB platform. The cells were also labelled for nuclear factor – kappaB (NFkB), a key regulator of inflammatory response [375, 425] and intercellular adhesion molecule (ICAM-1) after being stimulated with 200 U/ml of tumour necrosis factor-alpha (TNF-α) or exposed to the above stipulated flow and pressure conditions.

Cultured HUVECs located anterior and proximal to the stented region of the stent-cell interaction model were observed to elongate and align more to the impinged flow direction with increasing time. These regions where marked by uniform wall shear stress (WSSs), spatial wall shear stress gradient (SWSSGs) and negligible oscillatory shear index (OSIs). This observation is consistent with investigations of the morphological changes of endothelial cells subjected to stresses in vivo and in vitro from other researchers [59, 87]. Cells within the stented region however did not show strong alignment to the fluid flow direction. These regions were marked by non-uniform WSSs, SWSSGs and very high OSIs (0.35 – 0.45). Also HUVECs within the stented region were more polygonal shaped. It was also observed that in the absence of fluid stress, hydrostatic pressure stimulated cell proliferation, elongation, random alignment and a formation of cell multi layering structure. The phenomenon of cell multi layering is however absent when there is presence of fluid shear stress. HUVECs stimulated with TNF-α for 1 hour showed very high NF-kB expression whilst those cells exposed to the stipulated combined stress and pressure conditions for the same duration did not show NF-kB expression. Increased levels of ICAM-1 were observed when cells were stimulated with TNF-α for 6, 12 and 24 hours. However cells exposed to stipulated fluid stress and pressure conditions exhibited a time-dependent selective expression of ICAM-1.

CONCLUSION

It is concluded from results of the experiments performed that different types of combined and/or individual stresses have distinctive effects on HUVECs morphological response and the genes that may be expressed by the cells.

ACKNOWLEDGMENTS

Foremost, I would like to express my most sincere gratitude to my supervisors Dr Chuh K. Chong and Dr Julian P. Gunn for their invaluable help, advice and support throughout my PhD studies.

I was also fortunate to work with excellent researchers and scientists who I benefited greatly from their support and expertise. In particular, I would like to thank Dr Frederik Claeyssens and Colin Sherborne for their help in fabricating the micro-structure semi-circular ridges using the two photon polymerisation stereolithography technique. I would also like to acknowledge Alexander White for his help in designing the flow bioreactor system and Prof John Haycock for his input in my immunolabelling work of my research.

Thank you also to Lindsey Dew, Joseph Boadi, Gifty Tetteh, Leyla Zilic, Thomas Patterson, Athasham Raza and Salman Aziz who have been a constant source of encouragement and good reasoning especially during the difficult times of my studies.

Together, my family reflect the central tenets of this thesis: thus inspiring the quest for knowledge and fostering the devotion required to complete the task. Also without their financial support this research would not have been possible. Finally, this thesis is dedicated to the Armah and Izatt Sutherland family.

STATEMENT OF ORIGINALITY

The work presented in this thesis is, to the best of my knowledge, original and that all intellectual contents presented in this thesis which are the work of other people have been duly acknowledged.

I certify that the work contained in this thesis has not been previously submitted either whole or in part for any degree at this or any other university.

TABLE OF CONTENTS

LIST OF FIGURES

LIST OF TABLES

NOMENCLATURE

Roman Symbols

A	Surface area
b	Width of test flow chamber
CV	Control volume
$\vec{F}$	Force due to presence of a field
g	Function defining flow rate vs time for a pulsatile flow waveform
g_{osc}	Oscillatory component of g
h	Height of test flow chamber
m	Gradient of best fit line
$\vec{n}$	Unit directional vector to the normal
p	Pressure
Q	Volume flow rate
r^2	Coefficient of determination
$R1$	First ridge
$R2$	Second ridge
$R3$	Third ridge
$R4$	Fourth ridge
$R5$	Fifth ridge
Re	Reynolds Number

t	time
u	Velocity
$\vec{u}$	Velocity vector

Greek Symbols

α	Womersley number
ε	Measure of error
μ	Dynamic viscosity
μ_∞	Infinite shear viscosity
μ_0	Zero shear viscosity
λ	Time constant, lambda
ω	Angular frequency
ρ	Density
σ	Variance
τ	Wall shear stress
θ	Angle

Other Symbols

k	Consistency index
n	Power Law index
D	Diameter

R	Radius

Acronyms

AMI	Acute myocardial infarction
BMS	Bare metal stent
$CABG$	Coronary artery bypass graft
CAD	Coronary artery disease
CFD	Computational fluid dynamics
DES	Drug eluting stent
EC	Endothelial cell
ECM	Extrecellular matrix
FVM	Finite volume method
$ICAM-1$	Intercellular adhesion molecule-1
ISR	In-stent restenosis
LAD	Left anterior descending
LST	Late stent thrombosis
$MAPTMS$	Methacryloxypropyltrimethoxysilane
MSE	Mean squared error
$NF-kB$	Necrosis factor - kappaB
NIH	Neointimal hyperplasia
OSS	Oscillatory shear stress

OSI	Oscillatory shear index
PCI	Percutaneous coronary intervention
$PEGda$	Poly(ethyleneglycol)diacrylate
$POBA$	Plain old balloon angioplasty
$PPFC$	Parallel plate flow chamber
$PTCA$	Percutaneous transluminal coronary angioplasty
SEM	Scanning electron microscopy
SMC	Smooth muscle cell
ST	Stent thrombosis
$SWSSG$	Spatial wall shear stress gradient
TPP	Two photon polymerisation
$Tnf-\alpha$	Tumor necrosis factor alpha
$TWSSG$	Temporal wall shear stress gradient
WSS	Wall shear stress
$HUVEC$	Human umbilical vein endothelial cell

CHAPTER 1

INTRODUCTION AND OVERVIEW

1.1 CORONARY ARTERY DISEASE: IN – STENT RESTENOSIS

Coronary artery disease (CAD) is the leading cause of death related to cardiovascular diseases worldwide [1-3]. The onset of this disease is initiated by the intimal thickening which reduces the arterial lumen size and possibly distal blood flow. This can cause tissue death downstream of the occluded artery as there is inadequate perfusion and ischemia due to reduced flow.

It has been well documented that stent implantation in occluded coronary arteries improve resting coronary blood flow [4, 5]. However, the influence of stent geometry on local fluid dynamics and hemodynamic forces within the stented artery could lead to undesirable clinical events such as restenosis and in-stent restenosis (ISR) [6, 7]. Some researchers have shed light on how these local flow dynamics characterised by low WSS, high OSI and high SWSSG could be conducive to the continuous dysfunction of the endothelium and ISR progression [8-14]. Unfortunately clinical investigations into the changes of cells signalling cascade due to unphysiological mechanical force present at the stented site has not been firmly and fully established hence the pathophysiology of ISR still remains complex. Additionally, some clinical studies have postulated differences in risk factors associated with restenosis and those of native CADs. So, although there may be many similarities in the formation of restenosis and other CADs, each disease's pathophysiology could be very distinct. Indeed, the pathophysiology of atherosclerosis involves lipid accumulation, inflammation

and smooth muscle cell proliferation that carries on for many years whilst restenosis is primarily a self-limited intimal hyperplasic process that results from damage to the integrity of the arterial wall by endovascular devices [14, 15]. Hence, some mechanical stimuli such as WSSs may not necessarily play similar a role in the progression of ISR as have been associated with plaque formation in atherosclerosis [16, 17]. Mechanisms for ISR progression should therefore be independently evaluated for its contribution to the disease state.

Computational studies have provided an alternate method in understanding and quantifying the hemodynamic forces which the cells are being predicted to experience. It has been hypothesized that WSS alters the functional properties and morphology of the cells which result in the activation of restenosis mechanisms [18, 19]. Whilst this assumption might not be totally flawed, it is difficult to make meaningful correlation between computational and experimental analyses of cells response to stresses and flow dynamics that influence the onset/progression of ISR. More so, computational analyses of the impact of local flow dynamics within stented arteries on arterial cells are built on several assumptions and fixed mathematical parameters. Computational limitations such as simplified simulation of complex stented artery geometry could also influence the ability to retrieve comprehensive data about the hemodynamic forces present in vivo. These factors therefore introduce a level of inaccuracy in the exact representation of flow dynamics and mechanical environment within a stented artery.

There is therefore a need to establish a method that could relate computational data and experimental data to understand the sequential process and independent factors of cells response that initiate restenosis.

The aim of my PhD project is therefore to address this need. To achieve this target, the project followed consecutively the below proposed plan:

1. Establishing computational model of a 2D cell-stent interaction design.
2. Fabricating an experimental model of the 2D cell-stent interaction design.
3. Analysing the effect of predicted mechanical forces on cellular response.

1.2 FORMULATION OF HYPOTHESIS AND BASIS OF PROPOSED STUDIES

1.2.1 COMPUTATIONAL MODELLING

Hemodynamic forces experienced within the cardiovascular system could be analytically modelled and/or quantified by computational fluid dynamics (CFD) modelling. This could be achieved essentially by simplifying real events and physical parameters of the cardiovascular system into physiologically relevant and simple enough simulation models whilst taking into consideration the limitations of each analysis package. Some common limitations encountered with the use of either analytical models or CFD models are computational power and tools, measurement methods and mathematical parameters which could hinder in retrieving of detailed and accurate information. Thus to ensure true results of the mechanical environment present within the cardiovascular system from either analytical or CFD modelling, each model ideally needs to be validated against experimental data [20-22]. Blood flow dynamics within the cardiovascular system is complex as flow at each cardiac cycle is unique; both between different parts of the cardiovascular system as well as during time within each specific part. It is therefore important to note that the use of analytical models which could be an adequate tool to determine some mechanical

forces such as shear stresses experienced on arterial cells with simple flows could not be that adequate to provide accurate results for complex flows. For example early studies investigating mean WSS being subjected to vascular cells were calculated analytically using the Hagen-Poiseuille equation as shown below:

$$\tau_{mean} = \frac{4\mu Q}{\pi R^3} \quad 1.1$$

where μ is the dynamic viscosity of blood, *R* is the radius of the vascular lumen and Q is the total volume flow rate. The assumptions used in this calculation are as follows:

- The vascular lumen is of exactly circular geometry
- Blood flow velocity profiles are axisymmetric and perfectly parabolic in both time and space
- Flow is laminar (Reynolds number; Re < 1000)

This method therefore obviates the need for CFD modelling especially if the physical system being analysed agrees with the assumptions made. However, healthy arterial lumen which may be considered nearly circular might necessarily not have axisymmetric blood velocity profiles due to complex geometry of the vascular vessel. Also, stenosed arteries do not have circular lumen which makes application of this method to a diseased artery not justifiable. Additionally, this analytical calculation does not capture SWSSG and TWSSG which may be experienced on the arterial cells. So, to accurately evaluate the mechanical environment of either a healthy or diseased artery and especially when considering physiologically realistic flow profiles and factors, CFD modelling may be required.

There have been several studies on the successful application of CFD simulations in evaluating the mechanical forces being subjected to arterial

endothelial cells (ECs). For example, Chaichana et al. [23] employed CFD simulations to model plaques in a left anterior descending (LAD) coronary artery generated from a patient's data and investigated the hemodynamic effect of the stimulated plaques under realistic physiological cardiac conditions. Results from the CFD analysis of this study showed low flow velocity post-plaque region and high pressure gradient at the stenotic region in the LAD as compared to the LAD without plaques. It was consequently suggested that there is a direct parallel between coronary plaques and hemodynamic changes. The study by White et al. [24] is also another example where CFD analysis was successfully applied to flow systems used to subject ECs to mechanical stimuli. In this study, the effect of TWSSG and SWSSG on ECs under sudden or ramped onset of flow in a modified parallel plate flow chamber was investigated. The modified parallel plate flow chamber had a backward facing step which would simulate spatial patterns of fluid flow separation, re-attachment and recirculation. CFD results revealed locations of the reattachment points and the highest TWSSG within the modified parallel flow chamber to the different flow conditions. Cells responses were thereby able to be mapped to the fluid dynamics and mechanical forces present.

In establishing an accurate computational model for the proposed study, it is considered imperative to determine the most appropriate rheological blood model to use especially if results are to be physiologically representative of occurrences in vivo. This is because there are some disparities in the analysis of blood flow phenomena and mechanical forces in some studies as these studies have used different blood rheological models. Hence, assessing the impact of blood flow fields and dynamics has varied. There have been many investigations, both theoretical and experimental studies which have led to the understanding of blood behaviour in stented and non-stented coronary arteries [25-30].

Many computational studies in simulating blood flow in arteries have assumed blood to be Newtonian [31-34]. However, it is known that the rheology of blood is non-Newtonian. Bearing in mind the geometrical complexity of the human coronary artery, results achieved from assuming blood to be Newtonian to determine predictors of CADs could differ greatly from that achieved from a non-Newtonian simulations. Some studies argue in favour of using non-Newtonian models in analysing blood dynamics, albeit the assumption of blood flow in coronary artery as a Newtonian fluid could be a good approximation of blood characteristic [35-37].

Soulis et al. [35] in an investigation into non-Newtonian models for molecular viscosity and WSS in the left coronary artery reported that for non-Newtonian blood behaviour, viscosity depended on the velocity gradient and varied depending on the flow conditions, the geometry of the artery and flow particulates. Hence there are many non-Newtonian viscosity models, the choice of the model of which could have noticeable quantitative and qualitative effects on the flow fields and shear stresses given the distinct geometry of the artery and parameters of each model. However, a standard non-Newtonian rheological model is not available to describe the exact behaviour of blood under all circumstances. So it is important to consider each investigation of blood flow and dynamics in the coronary artery individually. It is therefore important to choose the appropriate non-Newtonian model to achieve acceptable results in the analysis of the effect of blood dynamics in the artery. Benard et al. [29] analysed the effect various blood rheological models on changes in intra-stent flow. In the study, it was reported that steady flow simulations of Newtonian model and non-Newtonian model based on Carreau-Yasuda in a 3.5mm diameter straight coronary artery with Helistent© implantation and subjected to flow rates of 60mL/min and 140mL/min showed different WSS magnitudes. The WSSs achieved with the Newtonian model were under-estimated when compared

to the non-Newtonian model. However, a characteristic viscosity Newtonian model showed similar WSS magnitudes and distributions when compared to the non-Newtonian model. From this study, it was deduced that the use of characteristic viscosity Newtonian model could be a useful option in appropriately capturing the physics of a region of interest of which the use of a Newtonian model wouldn't be ideal.

Based on the above discussions, it is clear that the application of CFD simulations has been very useful in optimising and reproducing more realistic representation of the mechanical environment within physiological parts. It has also been useful in extending the range of quantifiable mechanical forces within cell culture fluidic flow systems; thus improving our understanding of cell mechanobiology.

1.2.2 EXPERIMENTAL MODEL

The damage to the integrity of endothelial monolayer during and after endovascular procedures has been proposed by studies as the initiator of some mechanisms that promotes restenosis and ISR [38-40]. As a result, there has been an active resurgence of studies into the technical and mechanical factors that could contribute to these adverse clinical events. For example, Briguori et al. [41] investigated the impact of stent strut thickness in relation to the rate of restenosis of nonrandomised group of patients with successful stent placement. Results achieved from the investigation led to the conclusion that thinner stent struts reduced the rate of restenosis. This result tend to agree with experimental findings which suggested that stent strut thickness could affect strut tissue coverage and therefore could lead to a delay in endothelialisation [42]. Jimenez et al. [43] and Mejia et al. [30] concluded from their studies on the effects of stent strut designs on

hemodynamic performance that stent strut designs did play a major role on influencing either a positive or negative hemodynamic performance within the stented artery. Both studies also investigated into non-streamlined and streamlined struts and suggested that streamlined stent struts prevented blood flow conditions and hemodynamic forces that were conducive to initiate mechanisms that led to restenosis. Mejia et al. [30] reported from their studies that more streamlined stent struts such as tear-drop shaped struts showed better hemodynamic performance than square or circular shaped struts. Hence, for tear-drop shaped struts, 96% of the inter-strut regions were exposed to favourable flow and hemodynamic conditions which prevented restenosis and for square shaped struts only 19.4%. The significant progresses made within this research field have led to the optimisation of stents and stent designs as well as proposals of better and efficient methods of stent implantation.

Comprehensive animal and human studies into restenosis and ISR have also helped to affirm mechanisms postulated to initiate these CADs. Karas et al. [44] and Farb et al. [45] linked arterial injury to neointimal thickness (NI) in stented coronary artery of a porcine and human respectively. Clinical investigations into the role of hemodynamic forces to the formation of NI hyperplasia in stented human coronary artery by Wentzel et al. [46] revealed the important interrelation that existed between them. It is crucial to note that these studies carried out have provided a more informed perspective into understanding the occurrence of the disease and its complexities. Nonetheless, running of these studies are expensive and so in vitro models have provided a much cheaper alternative to analyse predictors of CADs.

The design of cell culture flow systems to subject cells to predicted mechanical stimuli has facilitated the understanding of the effects of hemodynamic forces to ECs. Bio-reactor flow systems capable of producing either physiological or non-physiological flow profiles onto cultured

monolayer of ECs on a microscopic glass slide within a parallel plate flow chamber (PPFC) or modified PPFC have been used to elucidate the independent and combined effects of varied stresses on ECs [24, 47-52]. Breen et al. [52] designed a flow bio-reactor system capable of applying WSS and tensile strain of physiological proportions concomitantly to ECs monolayers. Evidence in the studies demonstrated that whilst investigation of ECs response to isolated forces in vitro could provide valuable information; the effect of combined mechanical forces on ECs in vitro could provide more accurate information of cellular response similar to in vivo conditions. Also an important revelation from this literature was that it was critical that the bio-reactor developed was biocompatible, non-cytotoxic, and appropriate for the cellular mechanical loading desired and for the duration needed in order to achieve accurate data.

Therefore, in designing an experimental model able to provide the mechanical environment realistic to that of a stented artery in vivo; it is clear that the bio-reactor flow system used be able to meet the above stipulated conditions. Also from the referenced literature on the application of bio-reactors to study ECs response to fluid dynamics [24, 47-52], it is apparent that ECs cultured on microscopic glass slide is adequate enough to represent the structural ECs lining of the artery in vivo. However, the analysis of the response of ECs cultured on microscopic glass slide substrate to simulated arterial fluid flow could be comparable to that within an artery, if arterial wall is assumed rigid. As the focus of this project is to investigate into ECs response to fluid dynamic within stented artery, the assumption that artery is rigid is justified as diseased artery is marked by calcified lesions resulting in reduced or zero arterial compliance [4, 53]. Also the presence of stent in artery may reduce flexibility of artery [54]. So, in establishing our simple cell-stent experimental model it is proposed that a microscopic glass slide be used. However, since our investigation is to mimic the fluid dynamic

within a stented artery, the glass slide would be modified to represent a 2D local geometry of a stented artery. This is achieved by using two photon polymerisation (TPP) technique to fabricate stent like polymer microstructure features on the microscopic glass slide.

TPP is a powerful microfabrication tool which has proved very useful in tissue engineering and biomedical engineering applications. Gittard et al. [55] in a review discussed how some researchers have used TPP technology to fabricate 3D microstructured medical devices, prostheses and scaffolds for tissue engineering. Koskela et al. [56] investigated into the biomedical applications of TPP by polymerising PEGda and poly(ε-caprolactone)-based oligomer (PCL-o) to create arbitrary microstructures on glass slide and studied the cell attachment, viability and migration on these structures. Human embryonic stem cells (hESCs) were static cultured on the two different polymer microstructures and results achieved showed the hESCs to have attached on the surface of both polymer microstructures. The cells were verified as viable and non-cytotoxicity of both polymers with the hESCs was also reported. However, the polymers did not promote cell migration. These two different polymer fabricated microstructures were therefore concluded to have potential for cell-based applications.

Employing the TPP technology as part of the process in designing the cell-stent interaction model is therefore thought to be suitable as bespoke biocompatible microstructures could be fabricated with micron accuracy for the cell-based application model. However microstructures fabricated using TPP may be unsuitable for direct fluid stress experimentation for numerous reasons that soft lithography method can address. For example, it is reasoned that the leaching out of uncured polymer process after the fabrication of microstructures via TPP could cause the fabricated structures to weaken. Thus the leached out structures may easily deform during the fluid flow experiment. To overcome this problem, soft lithography technique

was added to the design fabrication process. Soft lithography allows for microstructures fabricated via TPP to be replicated and also reinforces the structural strength of features fabricated. Hence, it is suggested that fabricating the stent like microstructure features on the microscopic glass slide via TPP and soft lithography would prevent significant deformation of the structures during flow experimentation which consequently could influence result analysis. The fabrication of stent like features on the glass slide is thought to simulate the local geometric change of artery as a result of stent implantation. Furthermore, flow conditions observed within the stented artery such as flow separation, flow recirculation and disturbed shear stresses are also believed to be captured when flow is simulated over the micro-fabricated stent like features. Therefore the microfabrication of the stent like features on the microscopic glass slide would create the mechanical milieu assumed to be present within stented artery.

Correlating the two studies discussed above, it is hypothesized that the presence of stent within artery creates unphysiological mechanical stimuli which may influence cells response leading to activation of ISR.

1.2.3 HYPOTHESIS

It is hypothesized that local mechanical forces such as WSS, T/SWSSG and OSI present due to stent implantation into artery could influence the morphology and molecular response of ECs which could initiate ISR.

To test this hypothesis, a computational model of a simple semi-circular helical stent was developed. This is discussed in chapter **4**. This model would serve as a foundation to establish a cell-stent interaction model to study cells response under the determined flow dynamics. Chapters **6**

discusses into details the mechanical forces present within the cell-stent interaction model. Correlating the computational model analyses to experimental cell-stent interaction studies which are discussed in Chapters **7** and **8** provide an understanding to how cells respond to the flow dynamics. This analytical study is also indicative of the local mechanical conditions within the stented artery that might/might not influence the activation of ISR.

The aim and objectives to address the proposed hypothesis are discussed below.

1.3 AIM AND OBJECTIVES

The aim is to quantitatively analyse the influence of mechanical forces on ECs within a stented artery and determine what mechanical forces, if any, correlate most strongly with the development of ISR. Particular emphasis of this study would be on the effect of the mechanical parameters at physiologically relevant levels on ECs.

To achieve the stated aim, the following main objectives are addressed:

- Use CFD to establish the most appropriate rheological blood model to use in the cell-stent experimental model.
- Develop computational simulation of a simple cell-stent experimental model to predict WSS, T/SWSSG and OSI within the model.
- Design a flow bio-reactor system to apply the predicted mechanical forces at physiologically relevant parameters on ECs.
- Quantitatively analyse the images of ECs and determine their morphological changes in response to the mechanical forces experienced.
- Label ECs for inflammatory and adhesion molecules to determine

cellular response of the cells to the predicted stimuli.

1.4 RESEARCH OUTLINE

Figure 1 shows a workflow diagram with the set objectives to achieve the given aim of project.

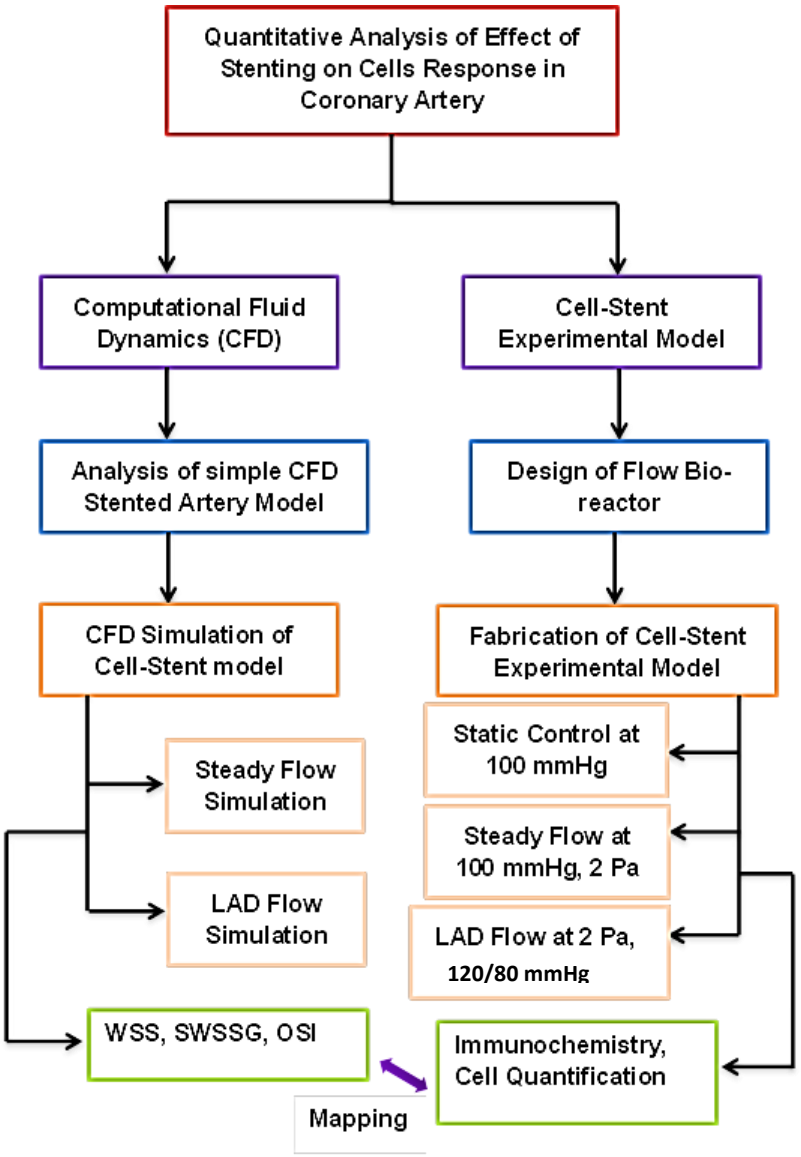

Figure 1. Diagram showing workflow of objectives to achieve aim

CHAPTER 2

BACKGROUND

2.1 CORONARY ARTERY

Coronary arteries are vessels that carry and supply oxygen rich blood to the heart muscle. As the heart is a very important organ in the body, it is necessary to ensure that the heart is always healthy. In that, blood vessels that supply nutrients to the cardiac muscles to enable the heart work must also be healthy. The heart has two main coronary arteries namely [57]:

- Right coronary artery (RCA): This artery supplies oxygenated blood to the right atrium and also to the walls of the ventricles.
- Left main artery (LM): This artery distributes oxygenated blood to the left anterior descending and the left circumflex. The LM is bigger than RCA in diameter.

Each of these main arteries also then branches into daughter arteries; thus the right coronary artery branches into the posterior descending artery and the left coronary artery also branches into the left anterior descending (LAD) and the left circumflex (LCx). Figure **2.1** shows an illustration of these arteries. The daughter arteries all supply oxygenated blood to specific parts of the heart. Blood flow at the cardiac flow phases (systole and diastole) within the different vessels of the coronary artery are however distinct [58]. For instance, the extravascular compression of the myocardial vessels in the left ventricle where intra-ventricular pressure is at its highest causes flow in the LAD to fall to zero or even sub-zero during the systolic phase. In the RCA

however, intra-ventricular pressure is low during systole phase and so blood flow in the RCA is not heavily influenced as compared to that of the LAD. During the diastolic phase, the LAD becomes patent which causes an initial heavy inflow of blood and subsequently flow under aortic pressure. The blood flow in the LAD is therefore characterised by negative and positive flow in the systole and diastole phase respectively whereas in RCA there is positive blood flow at both systole and diastole phase.

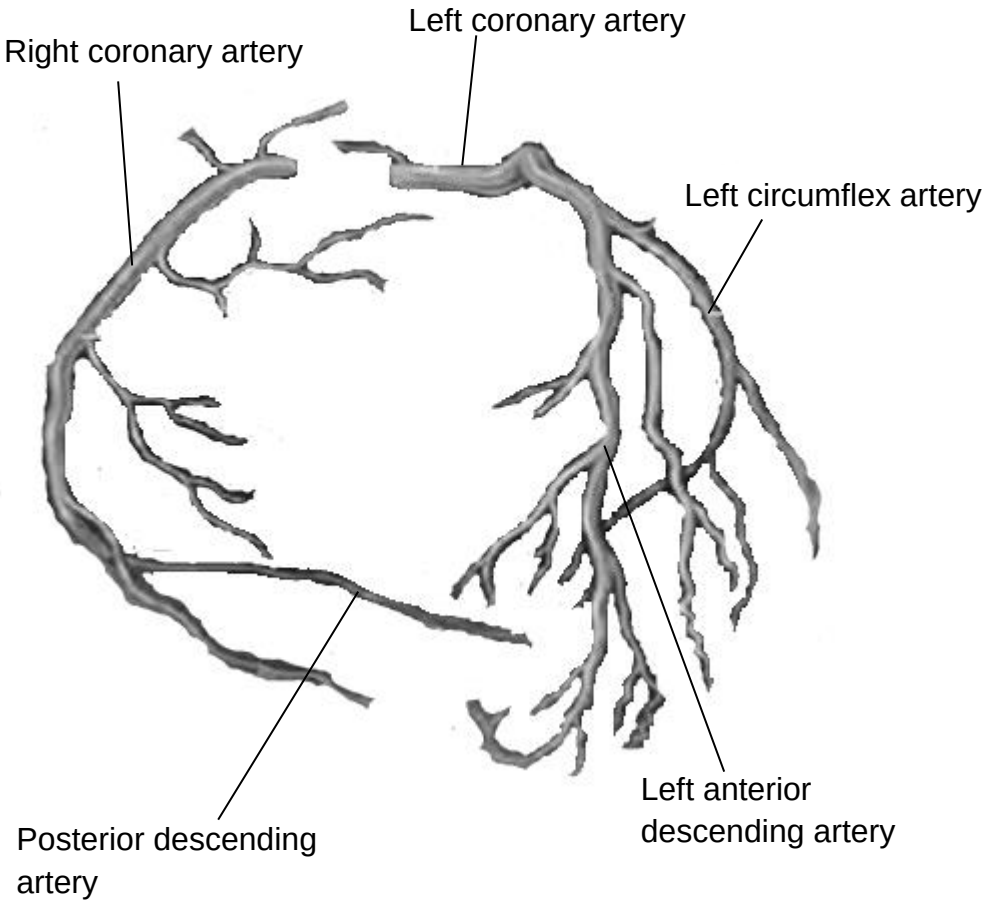

Figure 2.1 Anatomical illustration of the distribution of coronary arteries [55].

2.1.1 ARTERIAL WALL ANATOMY

Arteries are built of three distinctive wall layers:

- **Tunica Intima**: This layer is composed of three components; a simple squamous epithelium called endothelium, a basement membrane and an internal elastic lamina. The tunica intima rests on a tissue membrane rich in elastic and collagenous fibre. It also serves as an antithrombotic surface.
- **Tunica Media:** This layer consists of mostly smooth muscles fibres which encloses the tunica intima and an external elastic lamina. The elastic lamina helps the artery to expand and recoil during the expansion and contraction of the heart in circulating blood into the arterial system. The vasoconstriction and vasodilation of the smooth muscle fibres help to regulate the blood pressure.
- **Tunica Externa:** This layer is relatively thin as compared to the other two layers and has connective tissue made up of irregularly arranged elastic and collagenous fibres. The tunica externa provides tensile strength to the artery.

These distinctive arterial wall layers are illustrated in Figure **2.2**.

Arteries are constantly being subjected to mechanical stresses as a result of continuous flow of blood through them as shown in Figure **2.3**. Some of the mechanical stresses which may be experienced in arteries are the hoop stresses and compressive stresses which are as a result of the pressure of blood flow. The endothelium also experiences a direct impact of shear stresses which is caused by the friction of blood flow on the endothelial surface. These and other stresses in arteries are important stimuli that influence atherogenesis by regulating the functions of ECs, activities of the smooth muscle cells and the interaction of ECs with blood components.

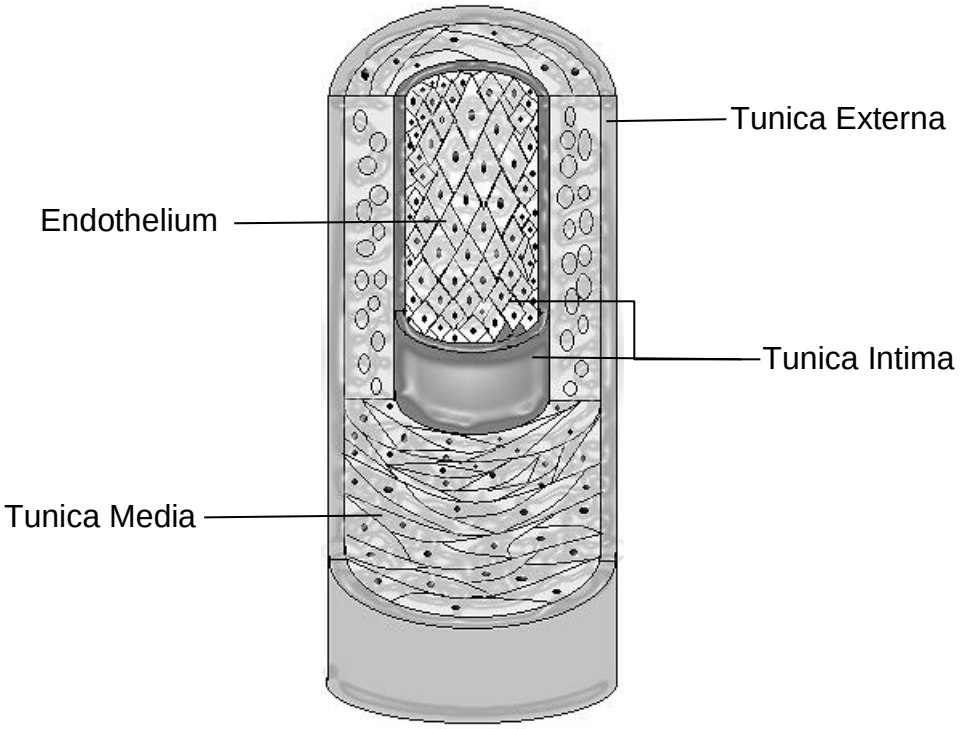

Figure 2.2 Anatomy of arterial wall layers

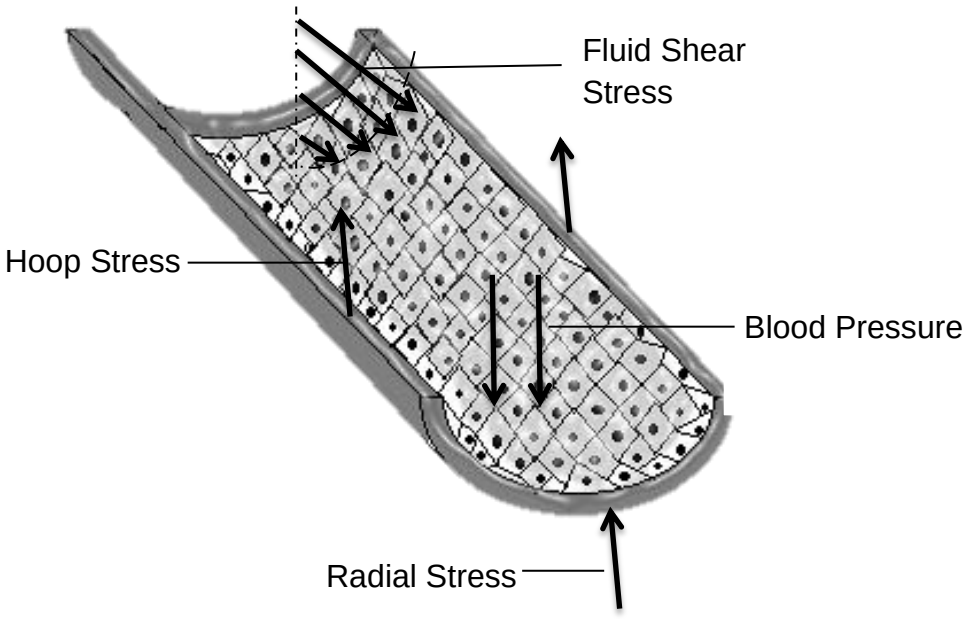

Figure 2.3 Diagram of stresses experienced on arterial wall

Additionally, there is evidence that mechanical forces associated with blood flow in the artery play a vital role in the acute control of the vascular tone and the regulation of the arterial architecture [59-61]. A review article by Epstein et al. [62] reported a direct correlation between arterial remodelling and arterial stress. For example, there is an increase in width of arterial wall to width of artery lumen ratio when there is an elevation in arterial stress. Therefore increase in local blood flow in the artery is associated with arterial lumen diameter increase, whereas decrease in flow results to a decreased lumen diameter. Kohler et al. [63] investigated the effect of increased blood flow on neointimal thickening of endothelialised polytetrafluoroethylene grafts in male baboons. Results from the studies showed a significant decrease in the cross-sectional area of neointimal thickness with increase of blood flow and stress (arterial lumen increase), whereas decrease or complete cessation of blood flow resulted in a rapid elevation of neointimal thickness (arterial lumen decrease).

Although the biological process of arterial remodelling may involve the cellular activities of many different cells in the artery, it is suggested that the endothelium plays a prominent role [62]. In that, the endothelium which ideally lines the interior surface of the artery is constantly being subjected to direct impact of mechanical forces and humoral factors. The endothelium therefore serves as sensory cells which transduces mechanical and humoral stimuli and elicit biological responses which consequently may affect the arterial structure.

In the next section of this chapter, an overview to the cause and treatment of coronary artery disease are discussed. Additionally, this section would discuss the role of endothelium dysfunction to mediate the initiation and or progression of coronary artery disease.

2.2 CORONARY ARTERY DISEASE

Coronary artery disease (CAD) is the hardening and thickening of the walls of arteries that supply blood to the myocardium; hence obstructing adequate perfusion throughout the blood vessels. This is caused by the build-up of fatty substances, calcium and cholesterol-containing deposits (plaques). Whilst the exact cause of this disease still remains unknown there are various factors which have been attributed to aid the progression of the disease such as smoking, high blood pressure, diabetes, obesity and high cholesterol.

Symptoms of coronary artery disease are not always obvious as some may go unnoticed and only become apparent after an episode of a heart attack. However, some associated symptoms of CAD are angina, palpitations and irregular heartbeat.

CAD is the most common cause of death in developed countries such as the UK and USA. Clinical review reports on CAD by the National Health Service (NHS) in the UK showed that about one in five men and one in seven women die from this disease [1]. The 2010 statistical update on CAD in the USA also showed that CAD was the main cause of death in one is six people [2]. Despite these disturbing statistics, it has been reported that there has been a recent decline in CAD mortality in developed countries whilst in the developing world both CAD mortality and the prevalence of CAD risk factors are on the sharp increase [3]. The decline of CAD mortality in developed countries is thought to be attributable to the identification of CAD risk factors which have led to better treatments for CAD patients and successful preventive efforts [64]. Over the past years, CAD mortality in the US has declined by 60% [65]. A study to show CAD mortality rates in developing countries estimated that mortality rate of CAD in developing countries would

double from 1990 to 2020 accounting for approximately 82% of death relating to CAD worldwide [3]. The increase in CAD mortality in developing countries is thought to be attributable to the urbanisation and "globalisation of dietary habits" – thus the culture of fast-food in the developing countries [66-68]. For instance in some developing countries, increased tobacco use is associated with urbanisation and hence such lifestyle is adopted by the people living in these countries. Unfortunately smoking tobacco increases the risk of developing atheromatous plaques in the coronary artery which contributes to the progression of CAD. In 2003, a survey conducted on tobacco use in India showed that 30% of the Indian population between the ages of 15 years and over either smoked or chewed tobacco [69]. A study found CAD prevalence in the urban parts of India to have risen from 1% in 1988 to 13.2% in the year 2007 [70].

2.3 CAUSES OF CAD

Dawber et al. [71] indicated that the underlying cause for CAD was atherosclerosis. Atherosclerosis could lead to myocardial infarction (MI) or acute myocardial infarction (AMI). These can cause total blockage of blood flow through the coronary artery causing the heart cells to die. As discussed in a review by Aboyans et al. [72], atherosclerosis occurs mostly in large arteries. However, it was acknowledged that there was a wide disparity in what constituted a large and/or a small artery in relation other types of arteries being compared. Hence definition of a small or a large artery was based on the site where the atherosclerosis was present; thus proximal atherosclerosis occurred in large arteries and distal atherosclerosis occurred in small arteries. Atherosclerotic lesions could also be classified based on their severity. A report by Stary et al. [73] characterised the lesions into four main types based on their morphological features. The first two (type I and

type II) found mostly in children although could occur in adults.

- The initial stage of the lesion development is known as type I. Lesions at this stage are marked by small amounts of lipids in the arterial intima.
- The type II lesions consist mainly of macrophages foam cells and more distinctively defined.

Atherosclerotic lesions could be termed type III when smooth muscle cells (SMCs) start to colocalize in the intima. At this point also, there is a significant presence of extracellular lipid droplets observed at lesion site and lesions tend to produce extracellular matrix [74]. This is the last stage of when the lesion is considered clinically silent (thus type I to type III) and before classed as an advanced lesions.

Further development of the lesion and continuous stimulation of SMCs proliferation and migration into the intima by chemoattractant factors eventually lead to fibrous cap forming on top of the lesion [75]. This stage of the lesion is classified as type IV. The advanced stage of the lesion is further categorised into sub-types with each type indicating the developmental stage of the fibrous cap, its clinical manifestations and fatal outcomes [73].

2.3.1 ASSOCIATION OF ARTERY MORPHOLOGY WITH ATHEROSCLEROSIS

Studies have shown that atherosclerosis is more prone in arterial regions which are curved and bifurcated [8, 76, 77]. It has been suggested that these geometrical complexities of the artery could lead to complex flow field which possibly changes the haemodynamic conditions of the artery and hence influence the pathogenesis of atherosclerosis [78]. Dvir et al. [79] in a study

investigating the relationship between RCA morphology with atherosclerosis reported that C-shaped RCA was associated with atherosclerosis whilst the sigma-shaped RCA was not. In the study, the coronary angiogram of 120 patients with RCA dominance was examined. Out of the 120 patients, 60 of them had no significant obstruction in the RCA whilst the other 60 patients had significant obstruction in the RCA. In the examination, it was reported that C-shaped RCA was shorter in length (115 $\pm$ 23 mm) compared to the sigma-shaped RCA (140 $\pm$ 31 mm). More so, there was significantly more atherosclerosis in the proximal region of the C-shaped RCA compared to the sigma-shaped RCA.

These findings tended to agree with Dvir's previous studies which made strong relation between short RCA and atherosclerosis [80]. In the previous studies by Dvir et al. [80] it was suggested that short RCA had a higher possibility of having fibrous plaque; hence higher susceptibility to atherosclerosis. Conversely in a long RCA, pressure decreases proportionally to the length of the RCA and therefore the longer the RCA the more the RCA is able to absorb cardiac cycle pulsations which could change the haemodynamic conditions in the artery and influence the onset of atherosclerosis.

Several autopsy and angiography studies have reported proximal atherosclerosis to be more dominant in the coronary arteries [81-85], especially in the LAD and LCx arteries [86] as compared to distal atherosclerosis. Strong et al. [87] also attested strongly to these reports that stated LAD and LCx to be more disposed to atherosclerosis as it was reported that these arteries had more proximal branches which are described as predilection sites of atherosclerosis lesion formation. Gazetopoulos et al. [88] examined the association of the length of LM artery and the degree of atherosclerosis formation in 204 dead patients. In the investigation it was found that atherosclerotic lesions in LAD and LCx arteries with short LM

occurred quicker and progressed rapidly as compared to atherosclerotic lesions in LAD and LCx arteries with long LM. It was therefore suggested that the long LM artery may employ some protective mechanism against the development of atherosclerosis in its branches.

2.3.2 ASSOCIATION OF MECHANICAL FACTORS WITH ATHEROSCLEROSIS

As briefly discussed in section **2.1.1**, ECs are known to play an important role in the homeostatic functions in response to several chemical and mechanical stimuli due to blood flow and blood pressure [89-91]. Hence normal functions of the ECs are essential and dysfunction of the cells plays a significant role in the occurrence and progression of the arterial disease. Many studies have reported that local mechanical and haemodynamic factors may be significant to the progression of atherosclerosis [92-94]. More so, WSSs in particular have been often linked to influence the development and localisation of the atherosclerotic plaque [16, 95, 96]. This principle is supported by the reasoning that WSS is proportional to the gradient of the flowing blood velocity particularly of a laminar flow in a regular sized artery. Hence WSS closely represents the local blood flow and could be considered as the most probable stimulus to cause ECs to respond to changes in blood flow rate. Experimental studies on the effect of WSSs on endothelial function revealed that WSSs above 4Pa cause the endothelium surface to be irreversibly damaged [97]. Additionally, the rapid flow change, oscillatory flow with flow reversal and low net flow could encourage endothelial dysfunction which may promote atherosclerotic plaque formation in the artery [98-100].

It has been postulated that low WSS due to low blood velocity leads to the arterial region becoming prone to atherosclerosis. In a study by Morrisett, low

WSSs were reported to influence the increase of low density lipoproteins which have been associated to atherosclerosis formation [101], whilst at the same time increase the permeability of the endothelium layer to the lipoprotein.

The progression of these phenomena over a period of time initiates the onset and formation of atherosclerotic plaque. The growing plaque tends to minimise the lumen size which therefore causes lower and disturbed flow at the post-stenotic regions of the artery. These occurrences and flow pulsation which generates oscillatory shear stress (OSS) which may further facilitate the formation of atherosclerosis lead to the progression of atherosclerotic plaque downstream of the lesion [92]. In a study by Ku et al. [102], the effects of pulsatile flow conditions on hemodynamic forces to intimal plaque deposition in human carotid bifurcations was examined. A laser Doppler velocimetry was used to calculate the WSSs in the bifurcations and comparison made between the WSS and intimal plaque thickness. Results from the study showed strong correlation between intimal plaque thickness and low WSS and oscillations in the WSS direction. This led to support the hypothesis that low WSSs and OSS could be key predictors of atherosclerotic plaque formation and localisation.

It is worth noting however that although significant correlation between low WSS and atherosclerosis development has been generally accepted and presented in most literature, recent study by Peiffer et al. [103] has concluded otherwise. In a systematic review of literature that compared hemodynamic forces with atherosclerotic plaques, Peiffer et al. reported that the evidence of the aforementioned hypothesis was less robust. It was also stated that interpretations of data from the different studies to support the current consensus were subjective; hence diverse techniques have been used to characterise the lesion distribution and the hemodynamic factors that might have caused them. To attest to this statement, Peiffer took five studies

that made a quantitative point-by-point comparison between lesion location and low WSS and OSS into account. The use of a point-by-point analysis was considered as a rigorous method for quantifying this relationship. Results achieved from the studies did reveal no significant connection between the low and oscillatory stresses and intimal thickening [104-108]. It should be made clear that although these findings are interesting revelations and heterodox to the established theory of low and oscillatory stresses, the level of significance is very much dependent on the statistical method used. Wentzel et al. [109] reached a conclusion that the significance level of the correlation between WSS and atherosclerotic lesion predilection sites in coronary arteries were affected depending on whether or not stresses data were averaged in the axial artery direction.

2.4 TREATMENT OF CAD

Treatments of CAD have involved coronary-artery bypass grafting (CABG), percutaneous coronary intervention (PCI) and/or medical treatments.

- **Medical Treatments:** Over the past years, medical treatments of CAD have improved because of the availability of new and more potent drugs that lower the risks factors and development of CAD. The availability and use of cholesterol-lowering drugs such as statins, blood pressure lowering drugs, calcium blockers and anti-platelet agents have helped lower the risk of CAD development in high risk patients [110].

- **Percutaneous Coronary Intervention:** PCI treatments of CAD have improved in the past decades and thus revolutionised the management of CAD. The use of stents, - bare metal stents (BMS)

and drug eluting stents (DES) together with dual anti-platelet therapy has reduced CAD morbidity and mortality associated with PCI and made PCI safer [111].

- **Coronary Artery Bypass Graft:** Studies of CABG treatment in high risk CAD patients- patients with diabetes and patients with multi-vessel disease revealed that CABG significantly reduced the rate of mortality and increased the rate of complete revascularisation in these groups [112-114].

PCI and CABG are both established treatment modalities of invasive revascularisation for CAD patients; however the debate on which treatment modality is best is still on-going [115-117]. Most of the conclusions reached on this debate have hugely been based on some factors such as the morphology and location of the lesion in the artery in addition to the medical conditions of the patient. Other factors such as complications and risk factors associated with each treatment have also been taken into account. Nonetheless, these factors used in comparing the efficacy and safety of CABG and PCI have sometimes led to conflicting data. Optimal treatment of CAD has therefore not been achieved and hence more needs to be done.

The use of PCI has increased over the years becoming, one of the most common medical interventions being performed [118, 119]. Further studies by Mack et al. [120], Ulrich et al. [121] and Gerber et al. [122] have all shown data which revealed increase in PCI treatment and decrease in CABG treatment for CAD between the years 1987 to 2004. In a recent national audit of PCI procedures published in 2014 by the British Cardiovascular Intervention Society it is reported that about 4 in 5 CAD patients are treated with PCI whilst 1 in 5 CAD patients are treated with CABG [123]. On the account of CAD treatment modalities presented, it is clear that PCI has been and still is very relevant in the management of CAD.

Although PCI has been suggested as the most preferred treatment choice for CAD, it is necessary to clarify that optimal treatment with PCI has not been achieved. However, there have been great improvements over the years to make PCI treatment more efficient. These improvements, successes and limitations in the use of PCI for CAD treatment is discussed in the next chapter.

2.5 THE NEED FOR CORONARY ARTERY STENTS

The initial method of performing PCI involved “plain old balloon angioplasty” (POBA) where an inflatable balloon with the aid of a catheter is inserted into the clogged artery to open it. However, its success was hampered by many problems such as restenosis, acute vessel closure and coronary artery dissection [124-126]. To reduce these complications the coronary stent was invented. The stent was to serve as a scaffold to hold open the occluded lumen and prevent vessel closure after PCI. The “Wall” stent was the first coronary stent to be implanted in a human and this was done by Sigwart et al. [127] in 1986.

In 1993, the use of coronary stents during PCI became widely accepted after the publication of two benchmark trials; the Belgium Netherlands Stent Arterial Revascularisation Therapies Study (BENESTENT) and the North American Stent Restenosis Study (STRESS) which provided evidence of the safety of stenting and also significant improvements in angiographic outcomes [128, 129]. These studies established the use of coronary stent implants during PCI as the standard of care and also drove the Food and Drug Administration to approve bare metal stents (BMSs) to treat occluded blood vessels [130].

2.5.1 THE SUCCESS AND COMPLICATIONS OF BMS

By 1999, 84.2% of PCI procedures involved the use of BMS [131] due to the positive results published in the above mentioned benchmark trials. In the STRESS trial, it was reported that restenosis decreased from 42% to 32% and in the case of BENESTENT trial, restenosis decreased from 32% to 22% [130]. Also, in a further study on POBA and coronary stents, it was reported that the restenosis rate with the use of BMS was about 20% - 30% which was better compared to POBA which had restenosis rate of about 30% - 60% [126].

Despite the reported advantages of BMS implantation during PCI, for instance the decreased rate of restenosis; the BMS restenosis rate is still considered clinically unsatisfactorily high due to the exponential increase in the use of BMS during PCI. In addition, BMS restenosis is very prominent in high risk patients. Subsequent trials on BMSs also showed that there were some risk factors and concerns related with this procedure. These trials reported that BMS implants resulted in acute and sub-acute stent thrombosis (ST) rates of 16%-24% and also in-stent neointimal hyperplasia (NIH) [44, 132-135]. The rise of some of these problems as a result of BMS implantation were directly related to the abnormal proliferation and migration of vascular smooth muscle cells (VSMCs) at the stented site of the artery [136]. Additionally, injury to the endothelial layer of the artery due to stenting initiated inflammatory responses which also contributed to the event of restenosis [137, 138]. The initial use of BMS during PCI has led to more problems compared to the use of POBA alone as more incidents of ST, myocardial infarction (MI) and death were reported [128, 129]. Ultimately, the advent of BMS implantation during PCI which was thought to be the breakthrough in reducing restenosis and thrombosis now seemed elusive. However, subsequent practices and management during and after BMS

implantation such as optimising the collocation of the stent struts to the vessel wall and using dual-antiplatelet therapy after the stent implantation have led to significant reduction of ST [139-142]. These improvements in the management of BMS implants nonetheless did not reduce the occurrence of restenosis. BMS were still associated with a 20% to 30% rate of restenosis within 6 months of implantation [136] and an increased rate of target lesion revascularisation (TLR). Some literatures reported that repeat revascularisation occurred in about 60% - 80% of restenotic lesions [143-145].

Reports on the advent of BMS ISR had been previously perceived as a benign event since clinical presentation of ISR had been silent [146]. However, Chen et al. [147] concluded from their study on the benignity of BMS ISR that clinical ISR was more severe than assumed. The study showed cases of unstable angina (36%) and myocardial infarction (MI) were the manifestation of ISR and that patient with unstable angina required hospitalisation. Nonetheless, depending on the classification applied to what clinical cases were considered as the acute coronary syndrome of BMS ISR, the statistics of the benignity of ISR could differ. Walters et al. [148] classified acute coronary syndrome as a combination of rest angina and acute MI and hence in the report stated 68% of acute coronary syndrome accounted for BMS ISRs.

POBA, atherectomy, brachytherapy and repeat stenting have been some of the re-intervention mechanisms employed to prevent ISR [149-151]. However as reported by Yokoi et al. [150] and Lemos et al. [151] some of these treatments such as POBA increased the rate of restenosis to 85% and also treatment failure occurred in about 30% of cases after brachytherapy. It is thus concluded that restenosis is the bane of PCI treatment with BMS.

2.6 UNDERSTANDING THE ONSET/PROGRESSION OF ISR

Since ISR remains the main complication associated with the use of BMS during PCI, many studies have tended to focus on understanding factors that initiate the onset and/or progression of ISR. These studies could be grouped into two main sections namely experimental studies and computational studies.

2.6.1 EXPERIMENTAL STUDIES

The mechanisms of restenosis have been under investigation since this disease was realised to limit the efficacy of POBA in treating CAD patients. Pathological studies by Nobuyoshi et al. [152] on the causes of restenosis after POBA treatment in 20 CAD patients proposed three major mechanisms of restenosis. These mechanisms were; thrombus formation due to endothelial denudation, intimal proliferation of VSMCs as a result of plaque splitting and elastic recoil due to the expansion of the vessel wall. Out of the three mechanisms, intimal proliferation of VSMCs was considered to be the main mechanism of restenosis. The conclusion reached by Nobuyoshi et al. tend to agree with earlier studies by Garth et al. [153] which also examined the pathological changes in the coronary arteries of three CAD patients who died after POBA intervention. The report demonstrated that these patients had prominent proliferation of SMCs on the neo-intimal and intimal surfaces of the coronary arteries. These intimal proliferations of SMCs were attributed to cause restenosis in the patients after POBA. However, Clowes et al. [154] investigation into a rat ballooned carotid artery to demonstrate the contribution of SMCs migration to injury induced intimal thickening (IT) showed that SMCs migration alone without proliferation accounted partly for

the accumulation of intimal SMCs. The study therefore suggested that SMCs migration could play an important role in cells response to injury. Nonetheless, this dogma of SMCs proliferation and migration being the main mechanism responsible for the onset/progression of restenosis after POBA have been suggested as false in later studies.

Clinical and animal studies have questioned the dogma which suggested SMCs proliferation and migration to be the predominant mechanism of restenosis after POBA [155-157]. This was because arterial remodelling rather than SMCs proliferation and migration was found to be the dominant factor responsible for restenosis after POBA. This may explain the reason for the failure in strategies that were employed to prevent restenosis which were based on limiting SMCs proliferation after POBA treatment. An intravascular ultrasound (IVUS) study by Mintz et al. [158] pointed out that restenosis after POBA was determined predominantly by the direction and magnitude of arterial wall remodelling.

2.6.1.1 ISR IN BMS

Meta-analysis of ISR after stent placement with various coronary artery stent types by Kastrati et al. [159] highlighted that main predictors of restenosis be explored among lesion and procedural parameters. The knowledge of these factors would aid in predicting the risks of the disease. Indeed whereas restenosis in POBA has been shown to be mainly due to arterial remodelling, ISR after BMS implantation have been attributed primarily to neointimal (NI) tissue proliferation/migration and extracellular matrix (ECM) accumulation [160, 161]. Arterial remodelling involves the expansion of the media and external expansion membrane during plaque development [162]. The plaque is located within the media and does not develop into the lumen. However,

the lumen area tends to diminish when the plaque growth reaches above 40% area stenosis. On the other hand, NI tissue proliferation/ migration involves smooth muscle cells within the medial layer of the artery migrating into the intima where they continue to proliferate [163]. Continuous migration and proliferation of these smooth muscle cells consequently cause intimal thickening which also results to luminal size reduction. Hoffmann et al. [160] in a study predicting the pattern and mechanisms of ISR using IVUS confirmed that intimal hyperplasia was the main mechanism of late lumen loss after BMS implantation. Results from the study also demonstrated that stents were able to resist remodelling forces that otherwise may have contributed to restenosis and hence arterial remodelling was not the major mechanism of ISR. Subsequent studies from Hoffmann et al. [164] on chronic arterial responses to stent implantation showed that BMS induced tissue proliferation both within the endo-luminal surface of the stent and in the tissue layers surrounding the stent struts. It has been postulated that there could be no parallels drawn between NI proliferations with injury period despite evidence that NI development is closely linked with medial dissection during stent placement [15]. It is therefore suggested that NI formation is a product of complex mechanisms which might also involve the axial displacement of the primary stenotic lesion to neighbouring arterial segments during stenting.

In other studies, arterial injury and inflammation have been linked to ISR [45, 165]. Animal studies by Karas et al. [44] and Schwartz et al. [166] into the relationship between arterial injury and NI thickness in stented porcine coronary artery released data which established proportional relation between artery injury and intimal SMCs proliferation. This relation of intimal SMCs proliferation due to arterial injury was similar to that seen in human restenosis. Farb et al. [45] performed an experimental investigation into the relationship between arterial injury, inflammation and NI tissue growth after

stenting in human coronary artery. In the study it was concluded that the use of coronary stents during PCI may result in medial damage or the stent struts may penetrate into a lipid core which induces arterial inflammation which is linked with increased NI tissue growth. Figure **2.4** shows the association of arterial injury with increased NI tissue growth. In a related study by Komatsu et al. [167] it was observed that there were extensive accumulations of macrophages which are known to be types of inflammatory cells at site of stent restenosis.

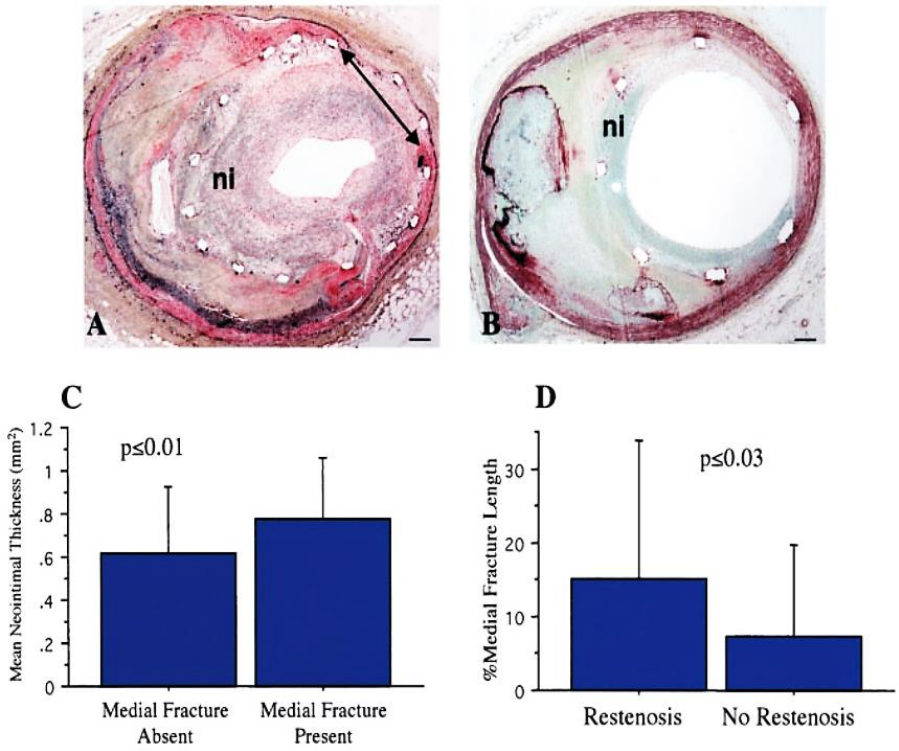

Figure 2.4 Photomicrographs (A and B) and bar graph (C) showing the link between arterial injury (medial fracture, arrow in A) with increased NI thickness against stents in which the arterial media was undamaged (B). Medial fracture length as a percentage of the circumference of the internal elastic lamina was more in restenotic stents compared with stents without restenosis (D). A and B, Movat pentachrome stain. Scale bars = 0.23mm in A and 0.30mm in B. [45]

Continuous advancements in the study of ISR have led to the understanding that the mechanisms leading to ISR is complex and not as simple to be related to one event. In a study by Mitra et al. [168] the complex mechanisms of ISR was divided into two phases namely the early phase and the late phase. Figure **2.5** shows the sequential order of mechanisms leading to ISR at the early and the late phase.

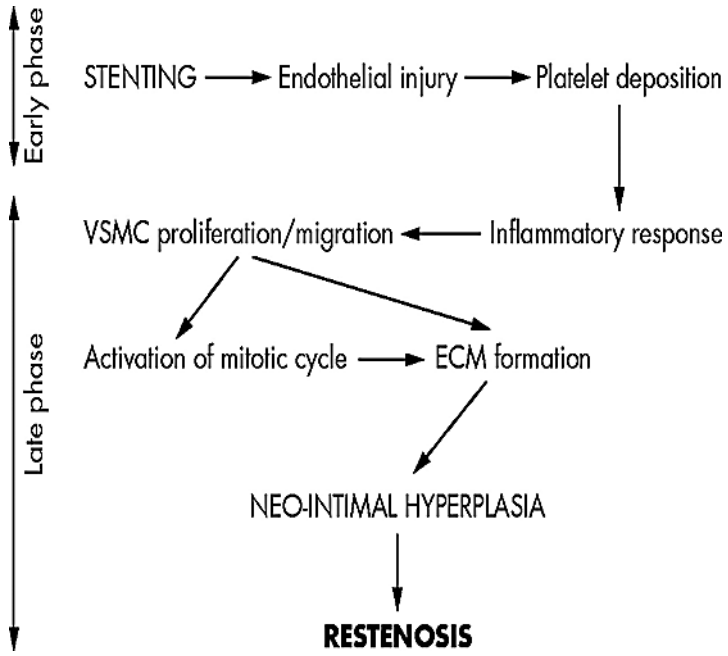

Figure 2.5 Sequential order of mechanisms of ISR at early phase and late phase [168].

As shown in figure **2.5**, endothelial injury during stenting leads to a cascade of cellular events which finally causes the onset of restenosis.

2.6.1.2 LIMITATIONS IN EXPERIMENTAL STUDIES

Many comprehensive experimental studies on the mechanisms of restenosis and ISR have been carried out in order to provide an integrated view of the pathophysiology of restenosis that explains the central role of SMCs proliferation/migration, arterial remodelling and/or inflammation. Needless to say, these studies have provided better understanding and evaluation techniques of each disease which has led to the development of more efficient treatments/prevention methods of ISR and restenosis [169-171]. Nonetheless, there is an uncertainty that exits over the exact cause of ISR and restenosis. One of the reasons why the exact cause of ISR has still not been known is due to the fact that cellular and molecular pathways involved in each of the mechanisms leading to ISR have not been fully identified [168].

Many animal models of restenosis have also provided great insights into human restenosis and allowed the development of better treatments. For instance, profound platelet inhibition with GP I1B/IIIa antagonist has been revealed to minimise NI proliferation in both animals and clinical restenosis in humans [172]. Unfortunately however, this is one of the few breakthroughs made in relation to using a specific treatment application which has proved successful in reducing mechanisms leading to restenosis in animals to also reduce clinical restenosis in humans. Reason for the lack of breakthroughs may be due to the fact that the pathophysiology of restenosis in animals is not exactly similar to that of humans and hence application of treatments to restenosis in humans may be to some extent limited.

2.6.2 COMPUTATIONAL STUDIES

Absolute comprehension of the mechanisms of restenosis and ISR is very important for the future development of therapies to prevent and/or treat these clinical diseases. The fact that restenosis and ISR are prominent in arteries which are tortuous, bifurcated and angulated makes it more difficult to achieve experimental data to quantify processes involved in the onset/progression of disease [18, 173-175]. However, the use of computational models to simulate stenotic arteries has provided alternate method to investigate the factors which causes restenosis and ISR in arteries.

Many computational studies into restenosis in blood vessels have been driven by the hypothesis that pathological changes are in part associated to WSS changes that result to activation of mechanisms of the disease [18, 19]. Hence CFD models have been elicited to investigate the blood flow dynamics within stented arteries [27, 176, 177] and also the interactions between stents and the arterial wall that leads to ISR [178, 179]. Experimental studies by Ku et al. [8], Zarins et al. [9], and Friedman et al. [10] into factors that contribute to the increased rate of restenosis have suggested strong correlations between intimal thickening increase and WSSs. It has also been reported that WSS could alter the orientation and morphology of the endothelial cells which may increase the susceptibility of the arterial walls to restenosis and atherosclerosis [180, 181].

Due to the substantial evidence linking WSSs to NI hyperplasia in arteries which have been reported in many literatures, early numerical and experimental studies into ISR and/or restenosis in stented arteries have tend to focus primarily on the influence of WSSs to the onset of ISR [7, 182, 183]. Needless to say other mechanical forces within the stented artery which may

equally be major predictors of restenosis might have been overlooked. Furthermore, on a macro-scale, the presence of the stent struts results in local geometric changes of the artery with flow conditions within the stented regions being characterised by flow separation, flow recirculation and disturbed shear stresses [184]. Thus the hemodynamic milieu within the stented artery is marked by complex and co-existing mechanical factors which might also contribute to the development of restenosis. A study by Rouleau et al. [11] used CFD analysis to quantify ECs response to both WSS and SWSSG. In the study it was reported that ECs subjected to only WSSs elongated and aligned in the direction of flow whilst ECs subjected to combined SWSSG and WSSs did not exhibit preferred alignment and elongation. Sakamoto et al. [185] also reported similar observations from their studies on the effect of SWSSG on the morphological changes of ECs and suggested that SWSSG may act as a suppressor to ECs morphological response to flow. These results are indicative of ECs responses at stented arterial regions where flow is highly disturbed both in vivo and in vitro [186, 187]. Also, in an investigation into the effect of WSSs on intima hyperplasia in a rabbit carotid artery, Wang et al. [188] used CFD to provide quantitative data of the flow field distribution and WSS in the artery. Results from their studies showed that blood flow was severely disturbed at the stenosed region of the artery. Additionally increased intima hyperplasia was observed at regions with high SWSSG and thus led to a proposal that SWSSG may play significant role in endothelial dysfunction.

The use of CFD modelling has not only elucidated the effects of combined mechanical forces on ECs functioning but also helped to optimise stent designs and to determine stent's mechanical parameters which could influence disease progression. Blouza et al. [176] and Dehlaghi et al. [27] in a study to analyse WSS in stented artery used CFD simulations to obtain optimal parameters of stent that could lead to reduced rate of restenosis. In

both studies, it was concluded that the blood flow pattern and WSS magnitude were significantly influenced by the stent thickness, strut shape and strut spacing. Hence, to minimise the risk of restenosis due to changes in fluid dynamics and associated mechanical factors created by the presence of stent; these stent parameters are needed to be taken into consideration.

2.6.2.2 LIMITATIONS IN COMPUTATIONAL STUDIES

The surge of technological advancements has led to the increase of computational studies in analysing CADs and the treatment options to determine how to optimise the safety and efficacy of these treatments. However, it is important to note that these computational simulations are built on some assumptions and fixed parameters. The assumption that blood could be considered as a Newtonian fluid when simulating blood flow in coronary arteries is very common in many literatures. Although this assumption might not be totally flawed, it nonetheless does not give very accurate account of blood behaviour. This is because the rheology of blood is non-Newtonian and considering the fact that the human coronary artery is of a complex shape, results achieved from assuming blood to be Newtonian to determine predictors of CADs could differ greatly from that achieved from a non-Newtonian simulation and/or experiment. Rodkiewicz et al. [189] investigated Newtonian and non-Newtonian flow through a curved tube and highlighted differences between the Newtonian and non-Newtonian flow patterns.

On the other hand, non-Newtonian blood models used in CFD are obtained by parameter fitting to experimental viscosity data attained under steady state conditions and at a certain shear rate [190-192]. However, it is mostly assumed that the steady flow conditions are analogous to pulsatile flow

conditions and hence results achieved should show exact representation of blood behaviour. This assumption is however implausible since the reformation of red blood cell rouleaux is different under each of the flow conditions [193]. It is therefore worth stating that physiological blood flow phenomena have not been fully understood. Hence computational simulation of blood flow to understand the onset of ISR is still an on-going process.

Finally, most CFD studies have restricted to using simple computational geometries such as straight tubes for the analysis of fluid dynamics in stented coronary artery as modelling the exact shape of the artery could involve very complex procedures [176, 178, 179, 194]. However, a study showed that the effect of hemodynamic forces and stresses acting on a blood vessel may differ depending on the shape of the blood vessel [195]. This means that using simple CFD models could limit our knowledge on factors that influence ISR.

2.7 DRUG ELUTING STENTS (DES)

The effort to minimise and/or prevent in-stent NIH ultimately led to the development of DES [196]. Inhibiting leukocyte infiltration and SMCs proliferation by coating BMS with anti-proliferative agents such as sirolimus and paclitaxel, cardiologists hoped this would solve the problem of restenosis [196, 197]. The DES consisted mainly of three elements:

- a stent platform
- a polymer that served as a drug carrier
- an anti-proliferative drug.

The initial stent platform of DES was made of 316L stainless steel; same metal alloy used for BMS. This was because 316L stainless steel was radio-

opaque and provided enough radial strength with minimal recoil [111]. Drug eluting stents were first approved in Europe in 2002 whilst in the USA, the FDA for the use of sirolimus-eluting stent (SES) (Cypher®, Cordis Corporation) was granted in April 2003. Paclitaxel-eluting stent (PES) (Taxus®, Boston Scientific) was later granted FDA approval in March 2004. Randomised controlled trials on the implant of both SES and PES in patients with de novo coronary lesions showed that both DESs were very potent in reducing restenosis and NIH at 6-12 months when compared to BMS [198-205]. Furthermore, studies on clinical safety and efficacy of the use of SES and PES revealed that both the DESs minimised late lumen loss [206, 207]. A meta-analysis of 16 randomised clinical trials of SES versus PES which included 8,695 patients with CAD showed major reduction in TLR with the use of SES [208]. Due to the positive results achieved from the use of DES, in 2005 it was reported that 85% of all stents implanted in the USA and Europe were DES [209].

2.7.1 STENT OPTIMISATION

Continuous experimental studies into ISR have led to the revelation that maintaining endothelial cell integrity (coverage and quality) is important in reducing the adverse clinical events after stent implantation [210, 211]. This is because damaging the endothelial cell layer could initiate blood coagulation which may consequently lead to thrombosis [212]. So to minimise damage to the endothelial monolayer, research has tend to focus on optimising the stent parameters. More so, the research on stent optimisation has mostly been focused on DES since many of the stent implantations during PCI has now involved the use of DESs. Furthermore, advances in CFD modelling and finite element analysis of fluid-structure

interaction has led to more robust and efficient way of analysing mechanical interactions between stents and the arterial wall. These have therefore led to better stent optimisation techniques. Some criteria used in determining DES performance are: acute recoil, tissue stresses, hemodynamic disturbance, drug delivery, uniformity of drug distribution and flexibility of the stent [213]. Hence stent design optimisation has been concentrated in these areas.

Briguori et al. [41] investigated the impact of stent strut thickness in relation to the rate of restenosis. Results achieved from the investigation led to the conclusion that thinner stent struts reduced the rate of restenosis. This result tend to agree with experimental findings which suggested that stent strut thickness could affect strut tissue coverage and therefore could lead to a delay in endothelialisation [42]. Figure **2.6** shows the rate of restenosis in lesions treated with two different stents: one stent having a strut thickness of <0.10mm and the other stent having a strut thickness of >0.10mm.

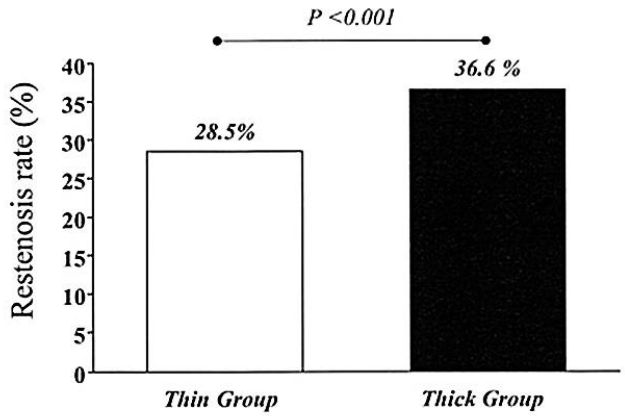

Figure 2.6 Restenosis rate in lesions treated with stent strut thickness >0.10mm (Thin Group) and stent strut thickness of <0.10mm (Thick Group) [41].

Many studies have numerically demonstrated that the geometry of the stent struts could influence the perturbation of the flow fields [28, 30, 43, 183, 214].

This as a result creates recirculation and flow separation characterised by unphysiological mechanical forces at the peri-strut regions which have been postulated to serve as nidus for procoagulant molecules entrapment and precipitate thrombus formation [215-217]. It has therefore been predicted that strut-induced flow disruption could be further attenuated if cross-sectional strut shape is streamlined (semi-circular arc shape) than non-streamlined (rectangular shape) [43]. Mejia et al. [30] quantified the effect of both streamlined struts and non-streamlined struts on WSSs within the peri-strut regions and affirmed that 4% of the regions around streamlined struts were exposed to low WSS whilst that of non-streamlined struts was 81%.

As we appreciate the synergistic beneficial effects of stent strut streamlining and thinning as critical determinants for favourable post stent implantation hemodynamic milieu, it is also important to note that these factors are limited by the need to maintain adequate stent radial strength to prevent recoil.

2.7.2 SECOND GENERATION DES

Progress in stent optimisation led to development of second-generation drug eluting stents which has been suggested to be better than first-generation DES. Second-generation DESs were composed of cobalt chromium (CoCr) as this alloy possessed more radial strength and better radio-opacity which allowed for thinner stent struts as opposed to 316L stainless steel [218, 219]. Radial strength is the measure of the stent's strength and ability to maintain the shape of the vessel lumen [220]. Hence adequate radial strength of the stent is very important in order to minimise stent recoil. Additional advantage of using CoCr as a stent platform is that due to its mechanical strength properties, unique stent designs that could facilitate precise drug delivery to target lesions could be built [221]. Furthermore, a variety of biocompatible

polymers could be built on to these unique stent to serve as drug carriers. The use of CoCr led to the creation of different DESs such as Endeavor Zotorolimus-eluting stent (ZES) and Xience V everolimus-eluting stent (EES) which have been claimed to have better efficacy compared to the first-generation DES. This claim has been supported by several clinical studies which have compared the superiority of ZES (second-generation DES) to SES (first-generation DES) and have revealed that ZES had greater endothelial coverage of struts, significantly lower in-stent restenosis and TLR [222-225].

Clinical outcome data has shown that second-generation DESs are better than BMS in promoting arterial wall healing [226]. However, this evidence has been questioned lately with the emergence of studies which have showed varied results in the efficacy of stents. In a study by Joner et al. [227], first-generation DESs (PES and SES), second-generation DESs (ZES and EES) and BMS were implanted into the iliac arteries of a rabbit to investigate the trends in endothelial coverage and recovery; thus an indicator of arterial healing between the stents. The result of the study affirmed that at day 14 there was significantly greater endothelial coverage in EES, followed by ZES then PES and lastly SES. However on day 28 there wasn't any statistically significant difference of endothelial coverage amongst the different type of stents. It was also postulated that stent struts lacking endothelial coverage served as nidus for focal aggregates of platelets and inflammatory cells. Results of this study are illustrated in figure **2.7**.

Animal models of stenting may maintain predictive value to some significant extent to humans as arterial healing stages are remarkably similar [228]. Nonetheless, it is imperative to note that interpretation of animal data is highly contingent on factors which might or might not significantly influence results as compared to that of humans. In a review study comparing vascular healing after DES placement in both humans and animals it was reported

that there was characteristic difference in the healing timeline between humans and animals [228]. Thus long term follow up of patients with DES placement for restenosis is necessary.

In 2011 and 2012, Boston Scientific unveiled their new stents called OMEGA™ and PROMUS Element™ respectively which were both built on a platinum chromium platform. Using platinum chromium alloy, stent designs could be further optimised to improve conformability, minimise recoil and enable precise drug delivery across complex lesions due to the increased radio-opacity of the stents [220, 229].

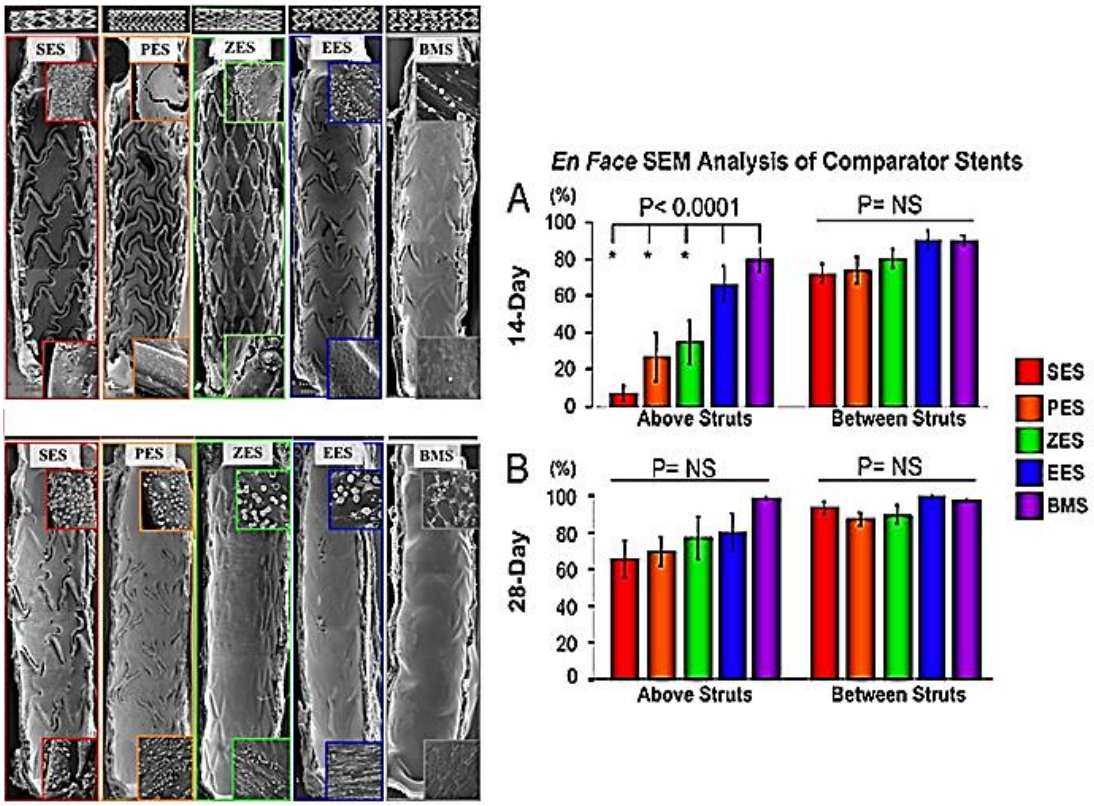

Figure 2.7 Radiographic images of endothelial coverage of stents at day 14 **(top left)**, Radiographic images of endothelial coverage of stent at day 28 **(bottom left)**, Scanning morphmetric analysis bar graphs showing quantitative analysis of endothelial coverage between stents at day 14 **(A)** and day 28 **(B)** respectively [227].

2.8 COMPLICATIONS WITH DES USE

Clinical enthusiasm owing to the advantages of DES over BMS was lessened due to concerns over ST after DES implantation [230].

One of the main criticisms of the first-generation DES was that initial clinical investigations into ISR with the use of first-generation DESs during PCI were only concentrated on patients who had stable de novo lesions. As a result of the biased patient selection, data achieved from the clinical trials about the efficacy of DES were positive. Early studies on DES by Spaulding et al. [231], Kastrati et al. [232], and Stone et al. [233] all involved patients who had simple lesions and conclusions from their results were that there were no significant mortality and morbidity rates in DES use. These results however do not reflect the real world as patients may present with complex lesions. Hence clinical outcomes from DES treatment on complex lesions could be devastating. Comparative studies of DES use between simple and complex lesions have shown higher rates of deaths, MI and repeat revascularisation in the latter [234, 235].

Additionally, patients may present different medical conditions which mean a clinical intervention using DES may not be the appropriate form of treatment for a specific patient. Also, although the use of DES reduced restenosis compared to BMS, concerns were raised about ST which seemed to be the “Achilles heel” of this device. Luckily, ST is rare; however it is an unpredictable event that causes high rate of deaths (45% to 75%) and MI (25% to 65%) [236-240]. The first cases of late stent thrombosis (LST) were reported by McFadden et al. [241] when four patients implanted with DES over a year (two with SES and two with PES) developed LST and MI after stopping their anti-platelet treatment. Reported treatments after a diagnosed case of LST and MI have involved balloon angioplasty, re-continuation of the

anti-platelet treatment and intra-aortic counter-pulsation [242, 243]. Although these treatments have proved successful in managing ST and MI, complications associated with these treatments however could lead to death. Waters et al. [242] investigated a case study of 4 CAD patients who developed LST following treatment of ISR with DES after cessation of anti-platelet treatment. In the investigation it was affirmed that one case patient died after being treated with vasopressor therapy and intra-aortic counter-pulsation following a diagnosis of MI. The death of the patient was attributed to complications associated with cardiogenic shock which was due to acute MI. Finn et. al [39] concluded from a study on pathological correlates of late DES thrombosis that the lack of re-endothelialisation was the most powerful predictor of ST. It was stated the reason for the lack of re-endothelialisation was as a result of non-uniform incomplete healing of the arterial wall. The causes for the non-uniformity and incompleteness of arterial wall healing however remain unknown. It is postulated that the lesions characteristics, drug dose and distribution and the biocompatibility of the polymer may have important roles to play in the incomplete healing of the artery. Nevertheless the influence of each of these factors to cause this problem has not been fully understood hence increasing the complexity and difficulty in the study of LST with DES. Hwang et al. [244] study on how physiological transport forces govern drug distribution for stent-based delivery provided a possible explanation for the non-uniform healing with DES. From the study it was understood that the nearness of the lesion to the drug coated stent did not guarantee adequate drug distribution. More so, the local concentrations of the drug are extremely dependent on the stent strut spacing and therefore inconsistencies in the distances between the struts will increase the difference in concentrations, leading to non-uniformity of arterial healing and subsequently result to LST. Researchers are now looking into the physiochemical properties of the drug and geometric stent characteristics to help explain the onset of LST in DES implantations.

2.8.1 CONCERNS ABOUT DURATION OF DUAL ANTI-PLATELET THERAPY

Meta-analysis of randomised and observational clinical outcome data has demonstrated that patients with DES implantation have reduced rates of death and MI with the extended use of aspirin and clopidogrel [245-248]. Nonetheless, the optimal duration of continuous dual anti-platelet therapy after DES implantation remains a central issue. This is because the administering of aspirin and clopidogrel to DES patients has been associated with some side effects. In the CURE trial, CAD patients who were on both clopidogrel and aspirin medication were observed to have major bleeding [249]. Previous studies into the side effects of clopidogrel and aspirin therapy demonstrated that the bleeding was not life-threatening and that the clinical benefits of dual anti-platelet therapy outweighed the side effect [249-251]. However, in the Global Registry of Acute Coronary Events (GRACE) registry by Moscucci et al. [252] major bleeding was reported as life-threatening as patients who had severe bleeding were reported to be at a higher mortality risk.

Lastly, there exist some discrepancies in data showing the potential adverse effects of prolonged dual anti-platelet therapy in CAD patients. In an observational cohort study on the influence of extended use of clopidogrel after DES implantation by Park et al. [253], it was reported that continued clopidogrel use beyond 1 year did not reduce ST and adverse clinical events. In the TYCOON (Two-Year ClOpidOgrel Need) registry however, investigation into the effectiveness of dual anti-platelet therapy use in preventing ST showed positive results [254]. In the study, 447 CAD patients were treated with DES and out of the 447 patients, 173 of the patients were put on dual anti-platelet therapy for 12 months and the rest of the patients were put on dual anti-platelet therapy for 24 months. Follow-ups on the two

patient groups revealed no difference in adverse clinical events; however, there were reported 5 cases of ST in the 12 month group and in the 24 months group 1 case of ST. The conclusion therefore reached on the study was that prolonged anti-platelet therapy does not affect clinical events but significantly reduces the rate of ST. From these conflicting data, it could therefore be concluded that it remains still unclear if prolonged dual anti-platelet carry better prognosis after PCI.

The unexpected discoveries of the complications associated with the DES use have ultimately generated an uncertainty about its efficacy and safety.

2.9 PROGNOSIS OF ST

Prognosis of ST still remains very poor as there are no known exact causes of this disease. However, many studies and registries have identified implicating factors that may increase the risk of ST.

2.9.1 PATIENT FACTORS

One of the independent predictors of ST is the patient factor. ST is more likely to occur in high risk patients; thus patients with renal failure and diabetes. Spaulding et al. [231] and Karvouni et al. [255] reported incidents of very LST in diabetic patients after SES implantation. Also, though studies on the relation between renal insufficiency and ST is limited, initial studies have suggested that chronic kidney disease is associated with stent thrombosis in patients who have undergone PCI with DES [256].

The management and treatments to prevent and/or minimise the risk of LST

in patients could sometimes lead to the opposite effect. For instance brachytherapy or PCI for acute coronary syndrome, left ventricular ejection fraction and ST segment elevation myocardial infarction can lead to episodes of LST [257, 258]. The strongest independent predictors of ST are the early discontinuation of dual antiplatelet therapy. A rate of 7.8% in ST was recorded in patients who had prematurely discontinued taking clopidogrel, aspirin or both in a report study by Park et al [259]. Kuchulakanti et al. [260] reported an increase in LST in patients who discontinued taking clopidogrel compared to those who kept up with the clopidogrel therapy; thus suggested that clopidogrel compliance was vital in high-risk patients.

2.9.1.1 CLOPIDOGREL RESISTANCE

The benefits of clopidogrel in the prevention of ST are well established but it emerged that some patients treated with clopidogrel show signs of resistance [261, 262]. Clinical trials have led to the suggestion that patients who are non-responsive to clopidogrel may be at a greater risk of thrombotic outcomes [263, 264]. The principal mechanisms leading to clopidogrel resistance are not completely elucidated, but are thought to probably occur through clinical, cellular factors and/or pharmacokinetics of clopidogrel in the patient's system [261, 265]. Further studies are therefore needed to provide better understanding on the impact of individual response variability to clopidogrel that could lead to better treatment management.

2.9.2 LESION CHARACTERISTICS

Examples of lesion characteristics that could influence the onset of ST and adverse clinical events include lesion length, calcified and complex lesion in the artery [141, 266].

Hougaard et al. [267] in a randomised study assessed the influence of lesion length on clinical outcomes amongst patients treated with EES and SES. In the study, 383 patients with short lesions and 890 patients with long lesions were treated with EES. Also, 417 patients with short lesions and 900 patients with long lesions were treated with SES. Results obtained from this study revealed significant adverse cardiac events in the patient group who long lesions (8.8%) compared to patients who had short lesions (6.2%). Conversely, there was not any significant difference in adverse cardiac events between patients with long lesions treated with either EES (8.6%) or SES (9.1%). These results therefore attest to the fact that lesion characteristic as suggested by many studies is a predictor of adverse clinical outcomes and ST.

2.9.3 BIOLOGICAL FACTORS

In addition to the above predictors mentioned, biological factors such as hypersensitivity reaction and drug resistance have been reported to contribute to the development of early/late ST [238, 268, 269]**.**

In a clinical investigation study by Virmani et al. [238] it was shown that localised hypersensitivity reactions after DES implantation plays a probable role in the pathogenesis of LST. The study involved a 58 year old man who died of LST 18 months after having two SESs implantation for unstable

angina. Findings presented after angiographic and ultrasound showed no incidence of NI formation, however, an autopsy showed the stented arterial regions with severe localised hypersensitivity reaction consisting mainly of T lymphocytes and eosinophils. Conclusion therefore reached on this study tended to suggest that pharmacokinetic elution profile of SES might have caused an adverse reaction in the artery which might have led to the development of LST.

2.9.4 MECHANICAL AND TECHNICAL FACTORS

Inadequate stent expansion and stent malapposition are predisposing factors for ST. A study by Kenichi et al. [38] to investigate factors that contributed to ST after SES implantation concluded that stent under-expansion was one of the associated factors. Additionally, malappositioning of stents in arteries especially ones with significant tortuosity have been suggested to play a role in the pathogenesis of LST [40]. Stent design parameters could also be critical to influence ST and restenosis; hence studies have also been focused on stent optimisation. In a report by Gurbel et al. [270] stent designs were affirmed to influence the degree of platelet activation which contributed to the pathophysiology of ST.

2.10 THE DEBATE: BMS VERSUS DES

2.10.1 MORTALITY/ MI

The controversy over either BMS or DES being the better stent intensified as publication of 4 studies raised concerns about the increased mortality rate associated to DES use.

- Nordmann et al. [271], performed an evaluation on the effect of DES and BMS treatment on patients with CAD on cardiac and non-cardiac death. In the randomised trials, sirolimus-DES and paclitaxel-DES treatment for CAD did not reduce the mortality rates when compared to BMSs. Interestingly however; preliminary results suggested that sirolimus-DES use led to significant increase in non-cardiac mortality.

- In the BASKET (Basel Stent Kosten Effektivitats Trial) study by Pfisterer et al. [272] which assigned randomly 746 patients to either DES or BMS and treated them with clopidogrel reported that there was no difference in the rate of 18 months cardiac mortality/MI between DES and BMS patients. Nonetheless, a discontinuation of clopidogrel resulted to 4.9% of cardiac death/MI for DES patients as compared to 1.3% which occurred in BMS patients. Figure **2.8** shows the statistical data of clinical outcomes with the use of BMS and DES.

- Camenzind et al. [230] analysed a pooled data of mortality rates from the Cypher and Taxus randomised trials and compared with that of BMS to come to a conclusion that mortality rates were higher with first-generation DES compared to BMS.

- Comparative study on mortality/MI rate between two study groups; one group being patients treated with BMS and the other group being

patients treated with DES using data from SCAAR (Swedish Coronary Angiography and Angioplasty Registry); Lagerqvist et al. [273] presented results which associated increased mortality rate with the use of DES.

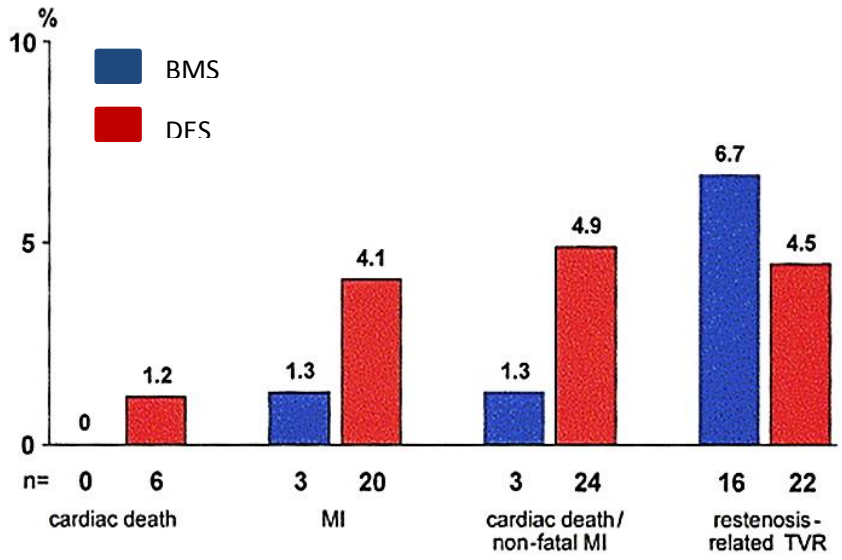

Figure 2.8 Statistics of late clinical outcomes (7 – 18 months) after BMS (blue colour bar) and DES (red colour bar) implantation [272]

These studies have triggered research into investigating the general comparison between DES and BMS in terms of mortality and morbidity at short- and long-term follow-up. A meta-analysis comparing the safety and effectiveness of DES and BMS in patients conducted by Stettler et al. [274] reported that sirolimus-eluting stents were clinically better than BMS and paclitaxel-DES. Additionally, the rates of mortality for patients treated with paclitaxel-DES, sirolimus-DES and BMS were similar. Kirtane et al. [275] and Kastrati et al. [232] concluded on the safety and efficacy of DES and BMS; that is, there were no substantial differences observed in the rates of mortality/MI after DES or BMS use.

2.10.2 ENDOTHELIALISATION

Delay in endothelialisation because of the anti-proliferative agents of DES could cause stent struts to remain thrombogenic which consequently increases the risk of ST which is associated to 45% of mortality [39, 241]. Conversely BMSs have been demonstrated to facilitate complete endothelialisation after implant thus minimising the onset of stent thrombosis [39].

2.10.3 SUMMARY

It is clear that coronary stents are an indispensable component of modern PCI, although associated with some adverse clinical events such as restenosis and ISR. The understanding of mechanisms that lead to these diseases after stent implantation is however unclear as pathophysiology of each disease is complex and influenced by many cellular and molecular events. Therefore identification of good therapeutic targets is complicated.

Researchers have performed a lot of studies to disclose mechanisms leading to restenosis and ISR both experimentally and computationally. Nonetheless substantial evidence to suggest the main predictors of ISR and restenosis has still remained elusive.

The use of computational modelling tool such as CFD has helped to quantify the mechanical milieu predicted to be experienced by cells within artery. Cellular responses that lead to initiate ISR within stented artery can therefore be mapped onto these quantified local mechanical stimuli. Hence possible mechanisms that may initiate ISR can be identified. In the next chapter, CFD is used to quantify the mechanical forces within a stented artery.

CHAPTER 3

COMPUTATIONAL FLUID DYNAMICS (I)

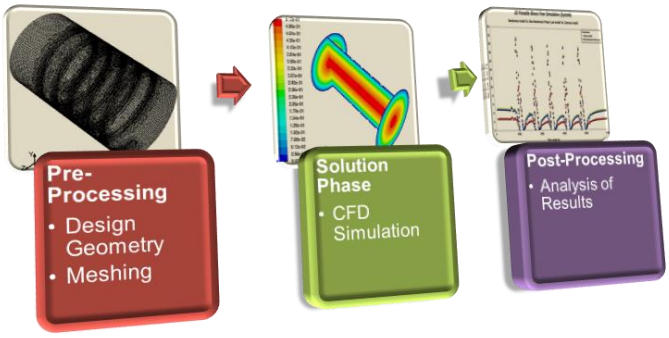

Figure 3. Graphical chart showing the processes involved in CFD simulation

There are three main processing phases involved in CFD simulation namely; the pre-processing, solution and post-processing phase as shown in figure **3**. It is essential that caution is taken when performing each processing phase involved in the CFD simulation. This is because CFD results obtained have been shown to be operator specific and thus each phase that is poorly simulated can lead to final results being highly misleading [276].

In this chapter, CFD simulation of blood flow dynamics within a stented artery is analysed. However, before this analysis was performed, the appropriate blood rheological model to use for the flow simulation was established.

3.1 ESTABLISHING APPROPRIATE BLOOD RHEOLOGICAL MODEL

3.1.1 INTRODUCTION

Vascular endothelial cells are known to play an important role in the homeostatic functions in response to several chemical and mechanical

stimuli due to blood flow. To investigate these mechanical stimuli and its potential effects on cell function, researchers have employed both experimental and numerical methods. Numerical methods however have been the preferred choice by researchers especially when analysing a wide range of hemodynamic parameters.

Evidence relating shear stresses to NIH has led to investigating the influence of stents on the local blood flow dynamics and associated stresses that lead to stenosis within stented arteries [8-10]. Blood plays an imperative role transporting oxygen and nutrients throughout the body. Its circulation is dictated by its rheological properties and the characteristics of the blood vessel it flows through [277]. It is commonly known that blood is thixotropic and exhibits non-Newtonian characteristics. However above shear rate of $100s^{-1}$ blood is considered to exhibit Newtonian characteristic in large arteries [31-34]. Ignoring the non-Newtonian effect of blood based on the aforementioned argument is plausible especially if artery is healthy and of regular size [278]. Nonetheless, this argument weakens when complex arterial geometry and transient blood flow which may involve reverse flow directions or stops are considered. Thus the non-Newtonian effects could become significant in this case.

Current consensus suggests WSS as the dominating mechanical stimulus in stent performance as stated by Mejia et al. [279]. So, the constitutive blood model chosen must take into account the local shear rate dynamics at the stented arterial region. In predicting the effects of different constitutive blood models on resulting transient WSSs in a stented coronary artery; Mejia et al. [279] compared Newtonian blood model against non-Newtonian blood model under normalised cardiac waveform. Two Newtonian blood models were simulated; the first using a Newtonian viscosity of 3.5 cP which is the lower viscosity limit of blood. The second Newtonian model used a calculated characteristic viscosity of 4.7 cP. For the non-Newtonian blood model, a

Carreau-Yasuda viscosity model was employed. Three different time points of the cardiac cycle were selected for analysis; two of the time points corresponded to ascending and descending flow with instantaneous Reynolds number of 190 respectively and the third corresponded to the peak flow rate. Results obtained at these time points all showed the two Newtonian viscosity blood models to have under-estimated the WSSs within the stented artery when compared to the non-Newtonian model. Thus prediction of the risk of restenosis in stented arteries could be over-estimated when Newtonian models are used. The use of characteristic Newtonian viscosity here to compensate for the under-estimation of viscosity observed with the Newtonian model and to produce quantitatively similar WSSs when compared to Carreau-Yasuda model just as reported by Benard et al. [29] did not produce expected results. The WSS levels of the characteristic Newtonian model although higher than the Newtonian model still were substantially lower than the non-Newtonian model. The authors of this study argued that the discrepancies between results achieved and that reported by Benard et al. was likely to be due to the different flow models used. Whilst Benard et al. simulated the flow dynamics in the stented artery under steady-state conditions; Mejia et al. simulated a transient flow condition. Additionally, this discrepancy observed is supported by the investigations of rheological blood models by Soulis et al. [35] which suggested that blood viscosity model is dependent on flow conditions amongst many other factors. Careful interpretation of CFD simulations is therefore required as results obtained are operator specific and also poorly executed simulations could potentially produce highly misleading data.

It is suggested that validating CFD simulations against experimental data will prevent misleading interpretations of CFD analysis. Hence in this section, different constitutive blood viscosity models is compared against experimental blood rheology to determine the blood model that best fits the

experimental blood data. Using the best fit blood viscosity model as a bench mark, quantitative assessment of the WSSs difference between the best fit model and other blood viscosity models in a helical stented artery under LAD physiological flow would be determined.

3.2 ANALYTICAL METHOD

3.2.1 VALIDATION OF CFD VISCOSITY BLOOD MODEL

In the LAD, ECs are predicted to experience a mean WSS of 1.38±0.1 Pa to maintain normal homeostatic functions [280]. So in determining the most suitable rheological blood model to mimic blood dynamics in the artery, it was important to also determine the nature of blood viscosity under these stresses as viscosity influences greatly the blood flow phenomena. Haematocrit levels also play important role in determining the behaviour of blood. Haematocrit is the percentage volume of red blood cells (RBCs) in blood. Blood fluidity at a specific shear rate and temperature is determined by haematocrit; hence alterations of haematocrit could influence greatly haemorheological variations in disease [281]. Also paucity of blood fluidity may affect vascular tissue perfusion and subsequently result in vascular tissue dysfunction [281].

Newtonian model and non-Newtonian models based on Carreau and non-Newtonian Power Law were therefore validated against experimental blood rheology data of normal haematocrit level of 45% [282, 283]. The three different rheological blood model under investigation thus; Newtonian model, non-Newtonian Power Law and Carreau models were analysed using the analytical formulation presented in table **3.1**.

Table 3.1 Formulations of rheological blood models

Blood model	Viscosity Parameter
Newtonian model [278]	$\tau = \mu\dot{\gamma}$ $\mu = 0.0035\ Pa.s$
Carreau model [282]	$\mu = \mu_\infty + (\mu_0 - \mu_\infty)[1 + (\lambda\dot{\gamma})^2]^{(n-1)/2}$ $\lambda = 3.313s, \quad n = 0.03568, \quad \mu_\infty = 0.00345\ Pa.s,$ $\mu_0 = 0.056\ Pa.s$
Non-Newtonian Power Law model [284]	$\tau = k\dot{\gamma}^{(n-1)}$ $n = 0.7,\ k = 0.017kg\ s^{n-2/m},\ \mu_0 = 0.0001\ Pa.s,$ $\mu_\infty = 0.1\ Pa.s$

3.2.2 ANALYTICAL MODELLING

Given the analytical equation for WSS in a pipe, assuming the shape of the artery is analogous to a pipe:

$$\tau = \mu\dot{\gamma} \tag{3.1}$$

where τ is the WSS, μ is the dynamic viscosity and $\dot{\gamma}$ is the shear rate.

and flow is laminar, spatially and temporally fully developed throughout the artery, then the use of computational modelling is obviated. Thus the use of analytical modelling to assess the relationship between the shear rate and viscosity of each constitutive blood model is appropriate.

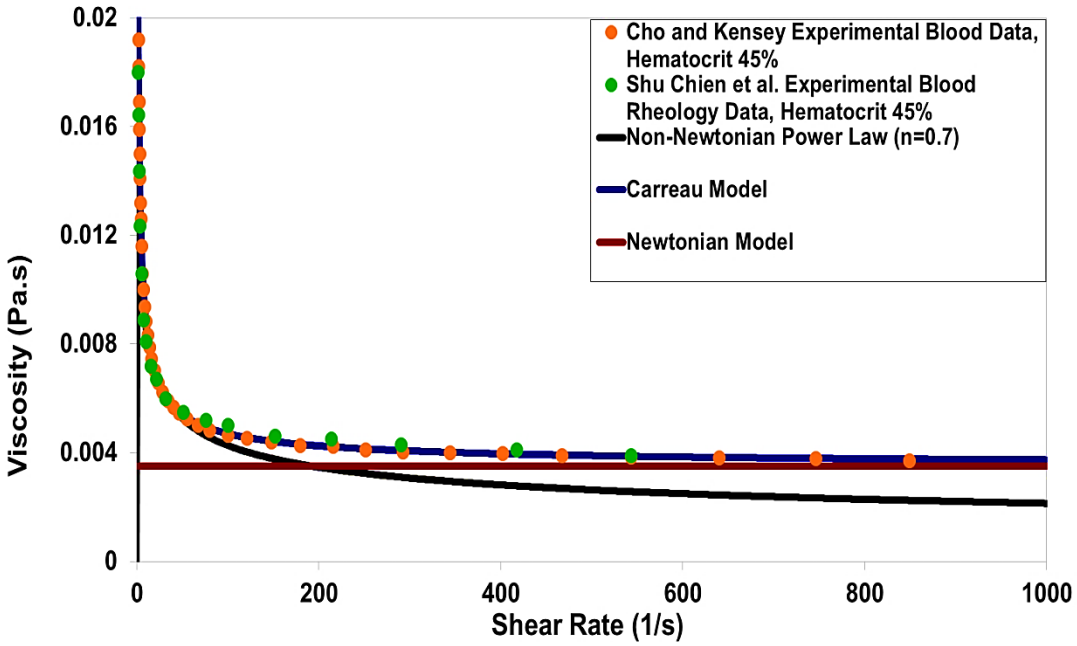

Figure 3.1 Comparative analysis of blood viscosity between experimental data and computational rheology blood data.

It is observed in figure **3.1** that the Carreau viscosity model fits best the experimental rheological blood data of Cho et al. and Chien et al. respectively. Hence it is proposed that Carreau model is the best amongst the other analysed constitutive blood model in capturing the non-Newtonian viscosity of blood and consequently the effects of flow hemodynamic in the LAD. Nonetheless as discussed earlier in this section, many studies have suggested Newtonian model to mimic the non-Newtonian characteristics of blood above shear rate of $100s^{-1}$. Taking the mean WSS in LAD is 1.38 ± 0.1 Pa, then using equation **3.1** and viscosity of 0.0035 Pa.s, the calculated mean shear rate respective to the physiological mean WSS is $394.3s^{-1}\pm28.6s^{-1}$. Thus in the LAD, the mean shear rate is above $100s^{-1}$ and so based on the above deductions, Newtonian viscosity model is an appropriate alternative model to use in simulating flow hemodynamic in the LAD.

Additionally, the data produced in figure **3.1** tends to support this consensus and more so if the dynamic Newtonian viscosity is modified to 0.004 Pa.s instead of 0.0035 Pa.s as suggested by [285] then a much better agreement could have been observed between the Newtonian and Carreau model.

3.3 COMPUTATIONAL METHOD

3.3.1 STENTED LAD ARTERY (PRE-PROCESSING PHASE)

In section **3.2** the use of analytical method to determine the relationship between viscosity and shear rate of different constitutive blood models is sufficient as the geometry of artery and flow is considered simple. In the case of a stented artery however, the presence of the stents results in local arterial geometric changes and complex flow with subsequent changes in local shear rates as previously discussed. Thus the effect of non-Newtonian blood viscosity on hemodynamics in the stented artery could be more complicated than in a simple artery. Additionally, although blood viscosity is considered virtually constant at high shear rate condition [282], the instantaneous shear rate for example in the LAD varies significantly over a cardiac cycle. So the artery is predicted to experience an immensely different viscosity over a cardiac cycle which consequently could affect its mechanical milieu; more especially in that of a stented artery.

Taking into consideration the above stipulations, it is clear that CFD is required to accurately analyse the mechanical environment of the stented LAD artery and also investigate if the Newtonian viscosity model still remains an acceptable alternative able to capture correctly the hemodynamics in the stented artery.

3.3.2 GEOMETRICAL CONDITIONS

A 3D straight stented LAD was designed with an arterial diameter of 3mm after a fully deployed helical stent implantation. The LAD artery was assumed to be straight with a rigid wall. This assumption was supported by evidence in literatures which emphasised that artery curvature decreased after stent implantation. In a comparative study by Zhu et al. [54] on coronary artery dynamics pre- and post-stenting, a stent length of $18mm$ was implanted in a LAD artery. Results attained from the stented artery affirmed that regions of the LAD at which pre-stent mean curvature was at the greatest were evidently straightened by the stent. The stent dimensions were modelled similar to typical coronary stents; thus stent strut diameter of $0.15mm$ and struts pitch-to-pitch distance of $0.7mm$ [30].

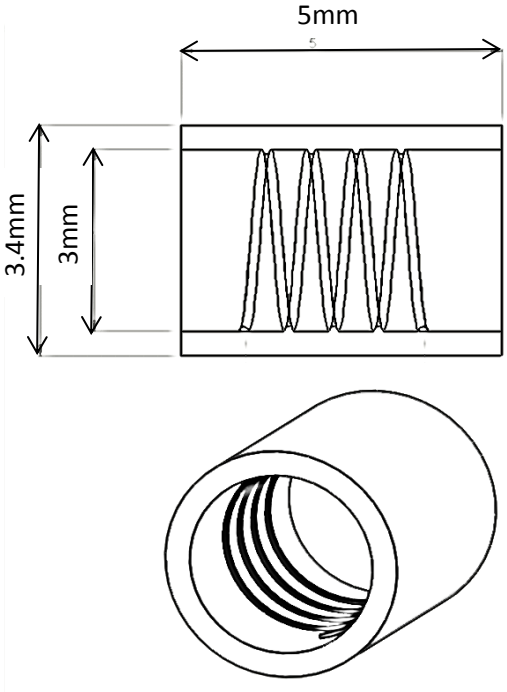

Figure 3.2 Geometry of helical stented LAD

3.3.3 GOVERNING EQUATIONS

Based on predicted complexity of blood flow dynamics in the stented LAD artery and the assumption that blood is incompressible, a finite volume method (FVM) is implemented to analyse the flow. FVM is a well-established and robust CFD technique which enables the numerically solving of the Navier-Stokes (N-S) equation that governs fluid flow [286]. The fluid flow is governed by the following equations:

- The N-S equation which describes the momentum conservation of the fluid;

$$\frac{\partial \vec{u}}{\partial t} + (\vec{u} \cdot \nabla)\vec{u} = -\frac{\nabla p}{\rho} + \mu \nabla^2 \vec{u} + \vec{F} \quad 3.2$$

Writing the Navier-Stokes equations in this form allows for the various uses of non-Newtonian blood models.

- The continuity equation which describes the mass conservation of the fluid;

$$\frac{\partial \rho}{\partial t} + \nabla \cdot \rho \vec{u} = 0 \quad 3.3$$

where $\vec{u}$ is the velocity vector, t the time, p the static pressure, ρ the blood density, $\vec{F}$ is other forces, and μ the kinetic viscosity.

A no-slip condition was applied to the artery wall and a fully developed LAD pulsatile velocity profile was applied at the inlet boundary of the artery. At the outlet boundary, normal diffusive flux for all flow variables was assumed to be zero. This outlet boundary condition is used in cases where velocity and pressure details of the flow exit are not known prior to solving the flow problem. The equation describing this condition is given below:

$$-p\vec{n} + \frac{1}{Re}\frac{\partial \vec{u}}{\partial \vec{n}} = 0 \qquad 3.4$$

where $\vec{n}$ is a unit directional vector normal to the outlet boundary.

3.3.3.1 SOLUTION PROCEDURE FOR GOVERNING EQUATIONS

The governing equations for the fluid motion are highly nonlinear, hence are solved using a segregated iterative algorithm built in ANSYS Fluent 13 software (Ansys inc., Canonsburg, PA, USA). The segregated iterative algorithm used to solve the flow problem is the FVM. The use of FVM has achieved widespread acceptance because of its accuracy and also as it is a thoroughly validated CFD technique. So, in solving a given flow problem using this computational numerical algorithm, the following steps are involved:

- **Discretisation of flow domain:** Based on the reasoning that fluid dynamics in the flow domain are governed by N-S equations which are a set of partial differential equations and thus couldn't be solved analytically, the entire flow domain is discretised into control volumes CV also known as cells [286]. Discretising the flow domain as shown in figure **3.3** converts the partial differential equations into several algebraic equations; one for each CV which

is then solved generally using iterative method. Discretising the governing equations is mostly demonstrated by considering a steady-state conservation equation for transport of a mass.

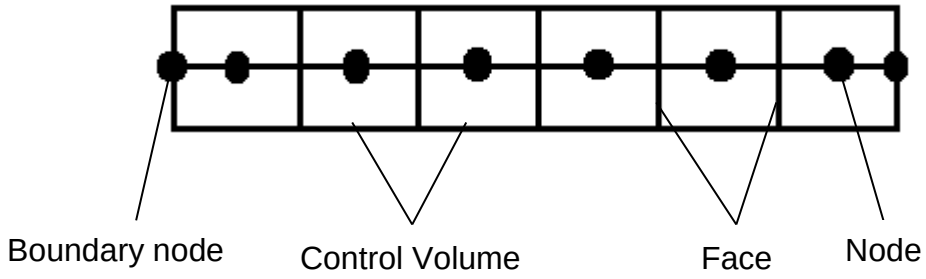

Figure 3.3 Discretised flow domain

- **Integration of governing equation:** After discretisation of the flow domain, the momentum and continuity equations shown in equations (3.2) and (3.3) respectively are integrated over a constant volume V and enclosed surface A; the CV. This is shown in the given formulation below [286]:

$$\int_{CV} \frac{\partial(\rho\vec{u})}{\partial t} dV + \int_A \vec{n} \cdot (\rho\vec{u}\vec{u}) dA = \int_A \vec{n} \cdot (\mu \nabla \vec{u}) dA + \int_{CV} \vec{F}\, dV \qquad 3.5$$

$$\int_{CV} \frac{\partial \rho}{\partial t} dV + \int_A \vec{n} \cdot (\rho\vec{u}) dA = 0 \qquad 3.6$$

where $\vec{u}$ is velocity vector, p the pressure, t the time, ρ the fluid density, μ the kinetic viscosity, and $\vec{n}$ a directional vector normal to surface A. Discretisation of equations 3.5 and 3.6 over time and space produces

algebraic equations describing transport of mass and momentum through the CV at each time step [287]. In the case of a transient simulation, it becomes necessary for the governing equations to be discretised in both time and space. Spatially discretising time-dependent equations are similar to that of a steady-state case. On the other hand, temporal discretisation involves integration of every term in the partial differential equation which yields a set of algebraic equations at each CV describing the transport of mass and momentum over a time step Δt [287].

- **Iteration of algebraic equations:** The algebraic equations from the flow discretisation are then finally solved by iteration with a selection of a convergence criterion which ensures that there are no significant changes in results when further iterations are performed [287]. Solutions were therefore judged to have met convergence criterion when scaled residuals for continuity and all three velocity components; (x-, y-, and z-velocity) have fallen to below 10^{-5}.

3.3.4 MESH GENERATION AND MESH INDEPENDENCE

Achieving mesh independence of a model although not a sufficient condition to ensure complete accuracy of results is nonetheless an essential requirement in validating CFD results [288]. Solutions are termed to be mesh independent when to they are independent of grid density, simulation time and further computational iterations performed.

The flow domain of the stented LAD was discretised using a CutCell algorithm in Ansys Workbench 13. This algorithm is a mesh generator which results in meshes having a high proportion of hexahedral cells as illustrated in figure **3.4**. Mesh refinements studies where then performed by using the

WSS results attained from the simulation of stented LAD model after each successive refinement as a measure for determining the convergence behaviour of results. Thus increasing the cell number over the entire flow domain generates finer meshes: (coarse mesh: 61159, 244651; medium mesh: 460271, 621698; and finest mesh: 936716, 1070554, hexahedral cells respectively). For each successive mesh generated, an increased cell density was imposed at immediate regions around the stent strut where most complex flow dynamics is anticipated. Mesh independence is considered to be achieved when relative WSS error percentage between two successive meshes is $\leq 5\%$.

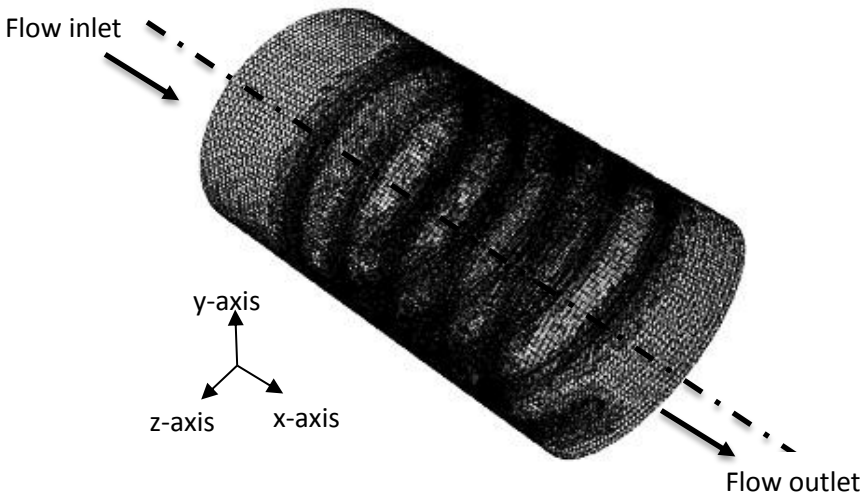

Figure 3.4 Hexagonal Meshing of stented LAD. The dashed line is a center line showing axisymmetric stented artery and the arrows show flow direction

Figure **3.5a** shows the WSS distributions and magnitude across a selected section of the stented LAD for each mesh. A general agreement exists in the WSS distributions for all the meshes; however a detailed examination of the WSS magnitudes reveals that there is an appreciable difference between the different meshes at the peri-strut regions as shown in figure **3.5b**. Thus to quantify these WSS magnitude differences, the mean WSS magnitude of the

region where flow at the peri-strut region was deemed to have recovered was taken. Table **3.2** shows result of the mean WSS from the coarsest to the finest mesh simulations.

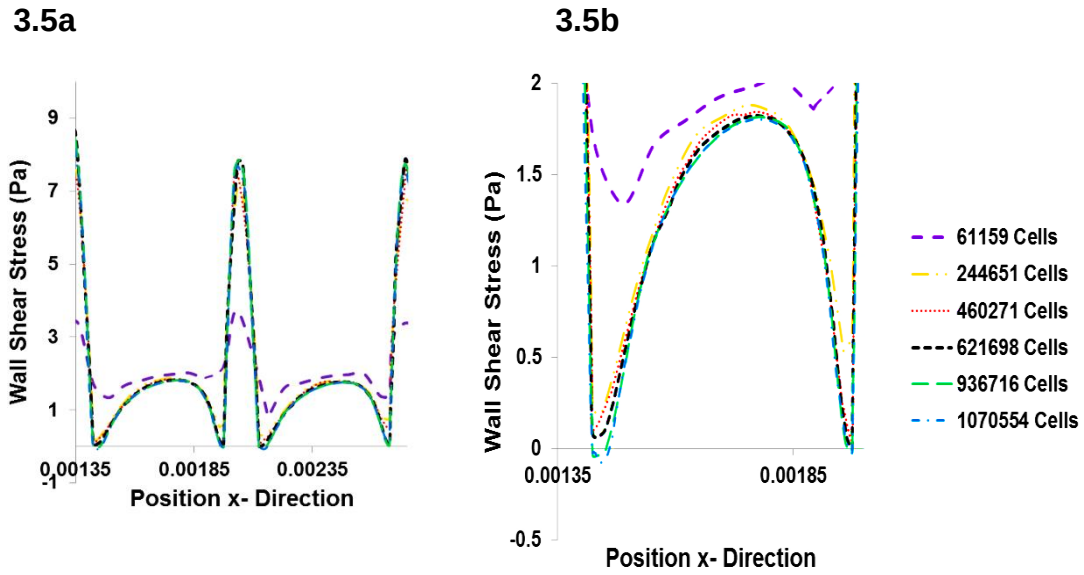

Figure 3.5 Comparison of WSSs in stented LAD between all meshes. (Figure 3.5a) shows a general WSS distribution within the stented model and (Figure 3.5b) is the WSS at a zoomed in section of the peri-strut region.

Table 3.2 Mean WSS of recovered flow at peri-strut region

Mesh Refinement	Number of Cells	Mean WSS (Pa)
Coarsest	61159	1.92
↓	244651	1.82
	460271	1.76
	621698	1.73
	936716	1.64
Finest	1070554	1.62

The results here tend to suggest that mesh with insufficient spatial resolution could yield over-estimated WSS levels. Considering the finest mesh obtained as a "gold standard", the relative percentage WSS error [289] between successive meshes, where i is the order of mesh number and τ_6 is the WSS of the finest mesh is calculated to be 18.5%, 12.3%, 8.6%, 6.7%, 1.2% respectively. It is therefore demonstrated that mesh independence is established at 936716 cells and that this density was sufficient enough to provide acceptable accurate CFD results as further mesh refinement (1070554 cells) yielded an insignificant change to the WSS magnitude. The mesh of 936716 hexahedral cells represents a compromise between result accuracy and computational costs, and so this mesh density is used in the simulation of the flow dynamics with error < 5% expected in results. The computational cost in running simulations for the different mesh densities is shown in table **3.3**. A Viglen Omnino all-in-one desktop pc with a random-access memory of 4.00 GB was used for the CFD simulation.

Table 3.3 Computational costs for different mesh densities

Mesh Density	Computational Cost		
	Hours	Minutes	Seconds
61159	0	4	49
244651	0	24	20
460271	0	33	48
621698	1	26	23
936716	2	23	3
1070554	2	52	54

3.3.5 SIMULATION (SOLUTION PHASE)

With the convergence criterion established to ensure that results are insensitive to mesh density, integrations of the fluid flow governing equations thus equations **3.5** and **3.6** are then solved by iterations. Since the pressure term of the discretised Navier-Stokes equation is unknown and fluid flow cannot be determined if flow pressure field is neglected, a method to couple pressure and velocity is needed. Thus Semi-Implicit Method for Pressure-Linked Equations (SIMPLE) algorithm was used for velocity-pressure coupling [290]. Simulations were therefore executed using a pressure based Navier-Stokes solver on a double precision solver FVM platform. Pressure and momentum were discretised using a second order scheme as this provided for a second order accurate numerical solution in space.

Flow boundary conditions controlling the model included no slip at the tube walls and velocity inlet and outlet boundary conditions. A user defined function (UDF) was written to apply a physiological pulsatile LAD inlet velocity flow waveform derived by Marcus et al. [58] at the inlet boundary of the model. This flow waveform is shown in figure **3.6**. Also, the flow velocity waveform imposed at the inlet boundary was assumed to be parabolic. At the outlet boundary, a constant pressure value was specified and a zero normal derivative was also specified for the velocity. To eliminate start up effects, three cycles of the LAD flow waveform was performed with only the results from the third cycle taken for analysis.

Since the present study is based on transient LAD physiological flow, it becomes imperative to perform a time step convergence in addition to the mesh convergence done in order to ensure better accuracy of results. Thus temporal discretisation should be sufficient enough to produce accurate time evolution of velocity component of a transient flow. This is necessary

especially as there are significant time dependent flow dynamics within the LAD flow cycle. So simulation of each LAD pulse cycle was discretised into 300 time steps of size 0.005s which was used for final CFD analysis as further discretisation of time step produced negligible results but only increased computational cost. Solutions for each time step were deemed to have converged when the normalised scaled continuity residuals and x-, y-, and z- velocity components had fallen to below 10^{-5} or after 200 iterations.

Blood was assumed incompressible with a density, ρ of $1057 kg/m^3$and an average inlet velocity, V of $0.265 m/s$ [291]. Considering blood flow to be Newtonian with dynamic viscosity μ of $0.35\, mPa.s$ through the LAD of internal diameter, D of $3mm$ the mean Reynolds number, Re is calculated to be 240. Blood flow is therefore considered laminar as Re calculated is less than 1000 [292]. Re is defined as [43]:

$$Re = \frac{\rho V D}{\mu} \qquad 3.7$$

Taking a normal resting heart rate of an adult to be 70 beats/min (i.e $\omega = 7.3$), Womersley number, α that defines the unsteady nature of the LAD flow is calculated to be 2.4. Wormersley number is defined as [293]:

$$\alpha = \frac{D}{2}\sqrt{\frac{\omega \rho}{\mu}} \qquad 3.8$$

Thus flow is laminar and satisfies physiological LAD flow dynamics [294].

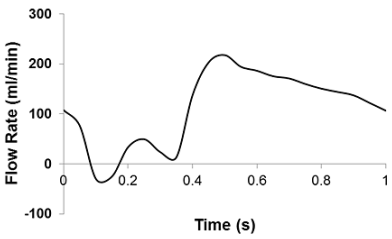

Figure 3.6 LAD flow waveform

3.3.6 QUANTIFICATION OF BLOOD MODEL DIFFERENCES

A quantitative measure of WSSs within the stented model with the use different constitutive blood models was introduced to determine the WSS differences between each model in the analysis of blood flow dynamics. So for the quantitative analysis different time points of the LAD cardiac cycle; thus $t1 = 0.1s, t2 = 0.2s, t3 = 0.3s, t4 = 0.4s, t5 = 0.5s, t6 = 0.6s, t7 = 0.7s, t8 = 0.8s, t9 = 0.9s \; and \; t10 = 1s$ were taken. Data produced from using Carreau model in the flow simulation was considered as the target data as this model was shown to best fit the experimental rheological blood data. The Newtonian and non-Newtonian Power Law models were compared to the Carreau model to find the agreement between each set of data. Quantitative analysis of the disagreement between Carreau model and the Newtonian and non-Newtonian Power Law models were performed by the formulation given below:

$$\varepsilon = 100 \times \frac{(|A_{(s;t)} - B_{(s;t)}|)}{0.5 \times (A_{(s;t)} + B_{(s;t)})} \qquad 3.8$$

where ε is the measure of error between two different constitutive blood models. A and B are the acquired and target averaged WSS data respectively produced from the flow simulation at instantaneous time point t and at specific region s within the stented artery. The specific region s, is a 0.2mm square area taken at the inlet, outlet and peri-strut regions where flow is assumed to be most stable. In the case of the peri-strut region, the most stable flow region is where flow is deemed to have recovered; thus have similar WSS magnitudes as that of the inlet and outlet regions. The fit of the agreement WSS data produced by the two rheological models was considered good if ε was less than 0.1 and excellent if less than 0.05.

3.4 RESULTS

3.4.1 DATA ANALYSIS (POST-PROCESSING PHASE)

Pulsatile LAD flow computation of three different constitutive blood models (Newtonian, non-Newtonian Power Law, Carreau) within a stented artery was performed and the WSS data in the stented model from each blood model was analysed. Figure **3.7** shows the WSS distributions within the stented artery at specific instantaneous time points of the LAD flow waveform.

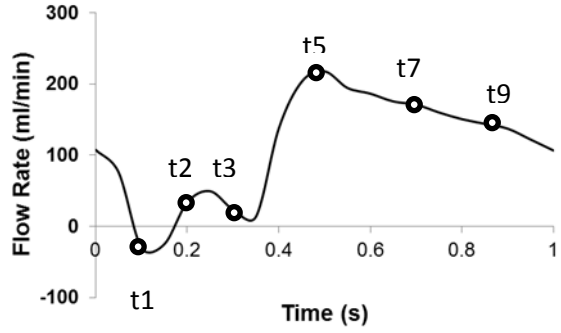

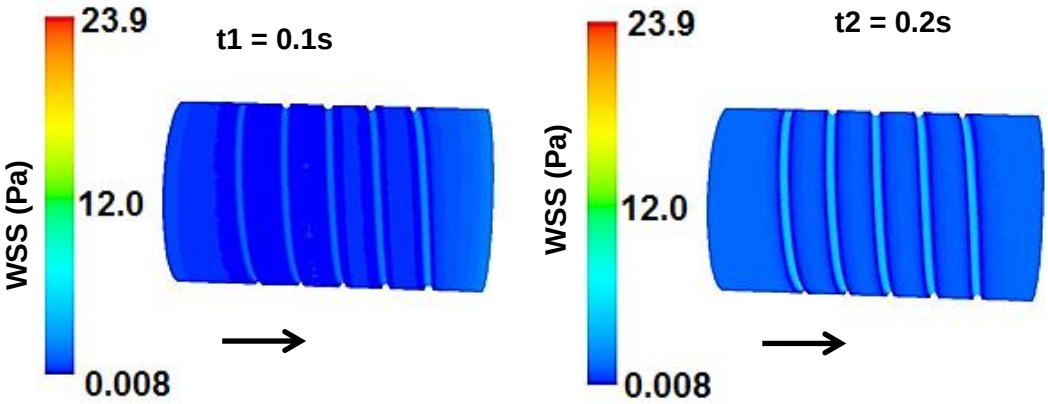

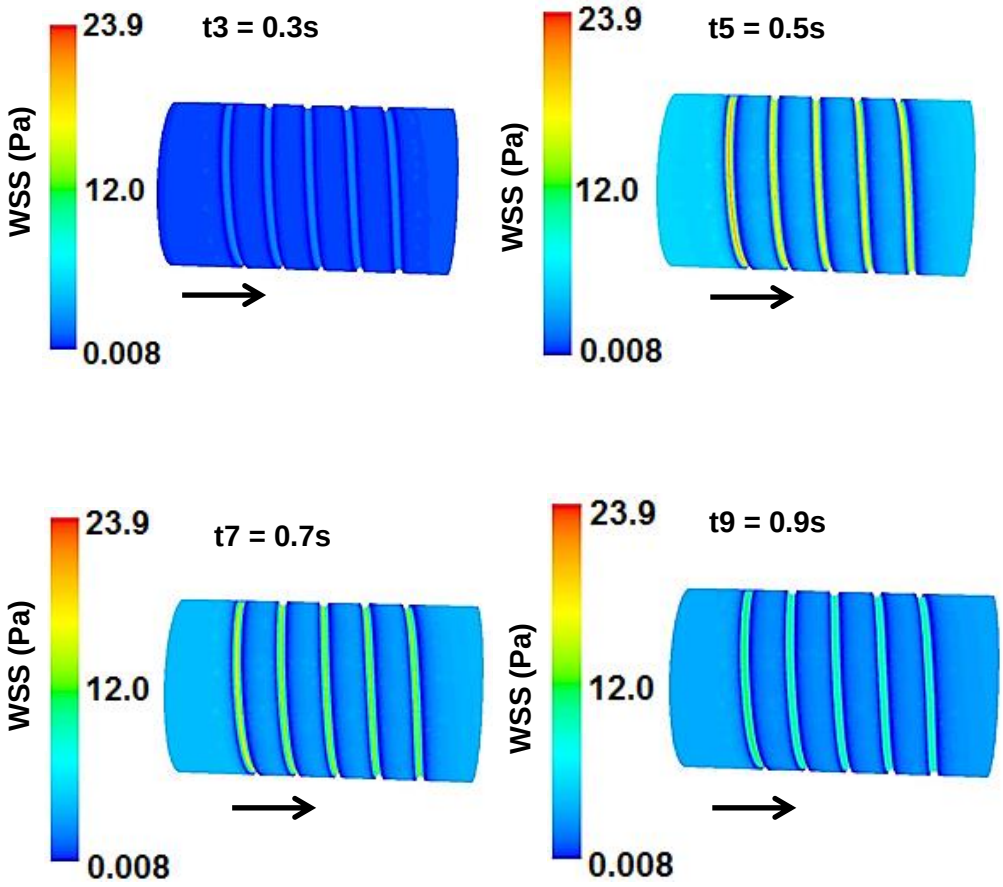

Figure 3.7 shows an xy-plane of WSS distribution (Pa) contour plots within stented LAD artery at time points of 0.1s, 0.2s, 0.3s, 0.5s, 0.7s and 0.9s. Flow direction is indicated by arrow (left to right). WSS magnitude shown on the colour bar legend ranges from 0.008 Pa (indicated by the colour dark blue) to 23.9 Pa (indicated by the colour red).

The grooves shown in figure **3.7** represent the stent position within the artery. It is noticed that at time; t5 = 0.5s, the WSS magnitudes recorded at these grooves are the highest (~19 Pa) comparatively to the WSS magnitudes recorded at other time points. Additionally, lower WSS magnitude across the LAD stented artery were recorded at time t1 = 0.1s, t2 = 0.2s and t3 = 0.3s

Figure **3.8** shows the WSSs generated along the centre plane of the stented artery by the different constitutive blood models at instantaneous time points of a complete LAD cardiac cycle.

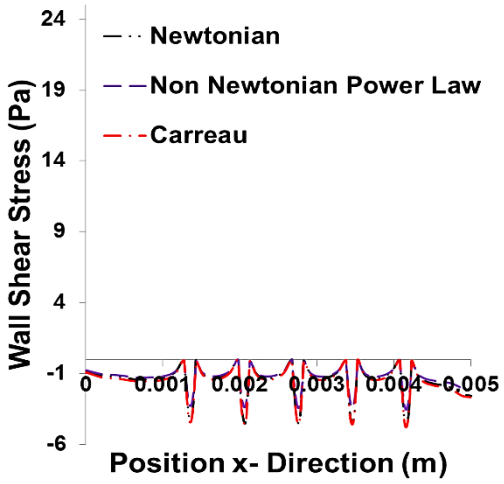

t1 = 0.1s

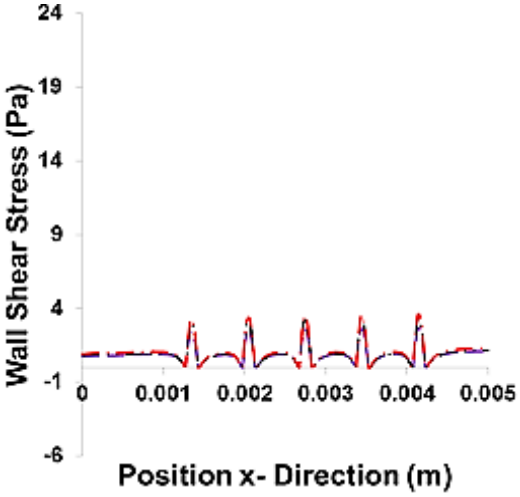

t1 = 0.2s

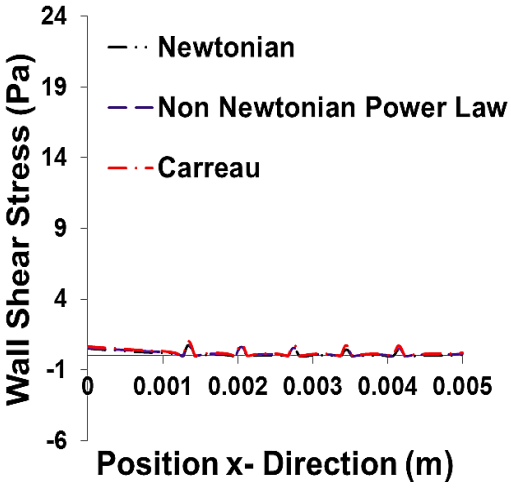

t3 = 0.3s

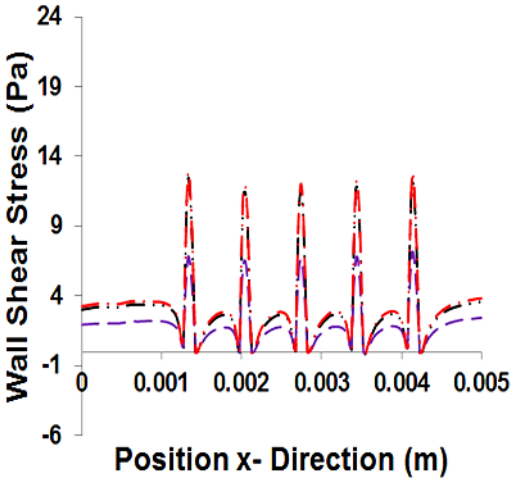

t4 = 0.4s

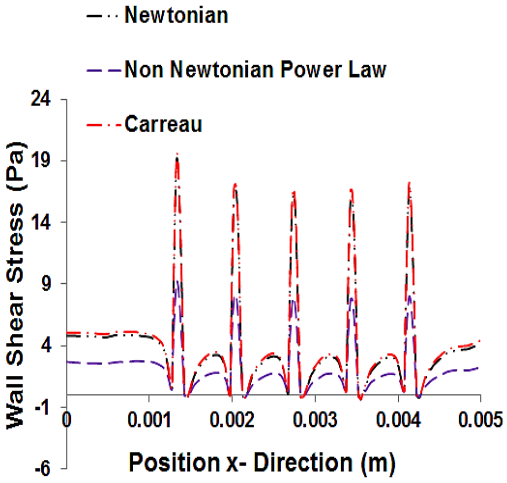

t5 = 0.5s

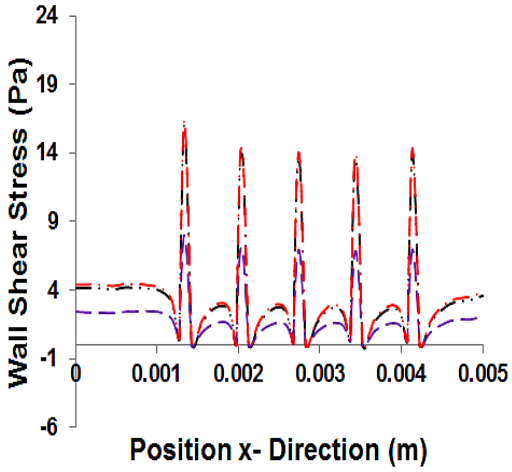

t6 = 0.6s

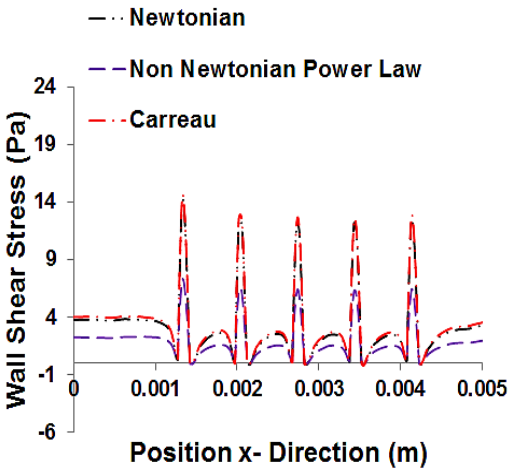

t7 = 0.7s

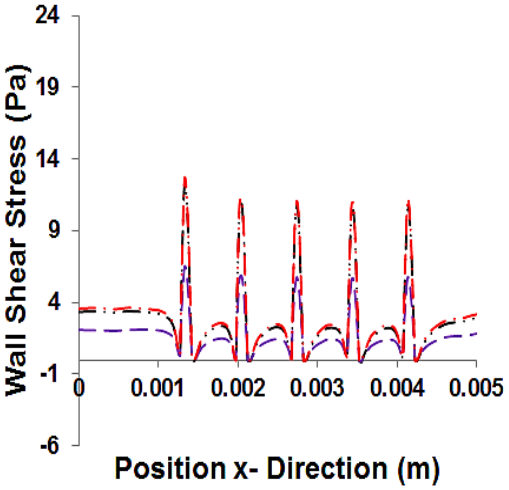

t8 = 0.8s

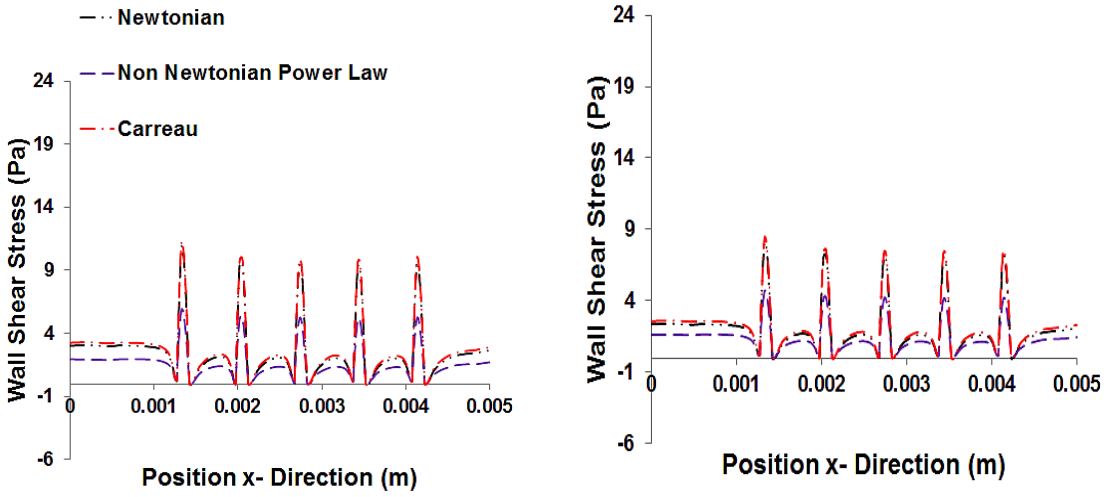

Figure 3.8 Line Graph of WSSs (Pa) in stented LAD artery using different constitutive blood models and at different time points.

As seen from figures presented in figure **3.8**, WSS magnitudes experienced on the stents are higher compared to the WSS magnitudes at regions around the stent. This phenomenon is similar to that shown in figure **3.7**. It is also noted that at t4 = 0.4s to t10 = 1s, the first stent strut in relation to the flow direction (thus from left to right) experiences high WSS compared to that of the consecutive stent struts. Plausible reason for this occurrence is that flow over the first ridge is faster than the subsequent struts and from Bernoulli's equation the pressure at the first strut would be lower than the subsequent struts. As pressure is high at the immediate regions of the strut due to low fluid velocity, this creates a pressure difference across the strut. This pressure difference leads to increase WSS magnitudes.

Newtonian, non-Newtonian Power Law and Carreau models are seen to produce similar WSS pattern along the centre plane of the stented LAD as shown in results figure **3.8**. Nonetheless, WSS magnitudes at selected time points of the LAD waveform amongst the three models are different. This result was expected and consistent with similar studies of Benard et al. [29]. From this study we could appreciate that non-linear and linear flow models

generate differences in near wall viscosity behaviour which results in the alteration of WSSs recorded. It is also observed that increased flow rate led to an emphasis of fluid perturbation within the stented region of the artery and yielded a WSS rise. Minimal WSS levels are experienced at immediate peri-strut regions and with peak WSS levels experienced on top of stent struts. WSS levels are also observed to increase with increase in flow recovery within inter-strut regions. Quantitative analysis of WSS error between the different blood rheological models at different time points within the stented artery is shown in Table **3.4**.

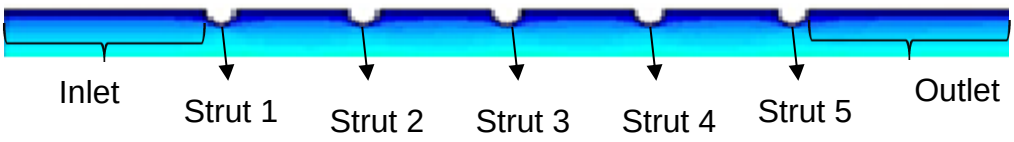

Table 3.4 Quantitative measurements of WSSs (Pa) error between different constitutive blood models and at varied regions and time points.

	Measure of Error between WSS data	
Time: t1 = 0.1s		
	Newtonian Vs. Carreau	Carreau Vs. non-Newtonian Power Law
Inlet	0.0595	0.1744
Inter-strut 1 and 2	0.0248	0.0753
Inter-strut 2 and 3	0.0242	0.0858
Inter-strut 3 and 4	0.0258	0.0977
Inter-strut 4 and 5	0.0201	0.0768
Outlet	0.0190	0.194
Time: t2 = 0.2s		
	Newtonian Vs. Carreau	Carreau Vs. non-Newtonian Power Law
Inlet	0.1724	0.2514
Inter-strut 1 and 2	0.0642	0.0655
Inter-strut 2 and 3	0.0642	0.0719
Inter-strut 3 and 4	0.0766	0.0837
Inter-strut 4 and 5	0.0631	0.0648
Outlet	0.0881	0.1182

	Measure of Error between WSS data	
Time: t3 = 0.3s		
	Newtonian Vs. Carreau	Carreau Vs. non-Newtonian Power Law
Inlet	0.4099	0.1086
Inter-strut 1 and 2	1.0557	0.1745
Inter-strut 2 and 3	1.6118	0.2771
Inter-strut 3 and 4	2.1068	0.3624
Inter-strut 4 and 5	2.0252	0.3527
Outlet	2.7880	0.4632
Time: t4 = 0.4s		
	Newtonian Vs. Carreau	Carreau Vs. non-Newtonian Power Law
Inlet	0.0390	1.3473
Inter-strut 1 and 2	0.0209	0.4165
Inter-strut 2 and 3	0.0221	0.4321
Inter-strut 3 and 4	0.0253	0.4736
Inter-strut 4 and 5	0.0194	0.3582
Outlet	0.0202	0.4812
Time: t5 = 0.5s		
	Newtonian Vs. Carreau	Carreau Vs. non-Newtonian Power Law
Inlet	0.0229	1.9033
Inter-strut 1 and 2	0.0148	0.6036
Inter-strut 2 and 3	0.0166	0.6287
Inter-strut 3 and 4	0.0194	0.6735
Inter-strut 4 and 5	0.0158	0.5311
Outlet	0.0178	0.74
Time: t6 = 0.6s		
	Newtonian Vs. Carreau	Carreau Vs. non-Newtonian Power Law
Inlet	0.0280	1.6904
Inter-strut 1 and 2	0.0169	0.5461
Inter-strut 2 and 3	0.0187	0.5703
Inter-strut 3 and 4	0.0215	0.6167
Inter-strut 4 and 5	0.0172	0.4810
Outlet	0.0194	0.6853

	Measure of Error between WSS data	
Time: t7 = 0.7s		
	Newtonian Vs. Carreau	Carreau Vs. non-Newtonian Power Law
Inlet	0.0316	1.5635
Inter-strut 1 and 2	0.0190	0.5123
Inter-strut 2 and 3	0.0211	0.5367
Inter-strut 3 and 4	0.0244	0.5841
Inter-strut 4 and 5	0.0195	0.4538
Outlet	0.0224	0.6516
Time: t8 = 0.8s		
	Newtonian Vs. Carreau	Carreau Vs. non-Newtonian Power Law
Inlet	0.0367	1.4095
Inter-strut 1 and 2	0.0217	0.4687
Inter-strut 2 and 3	0.0243	0.4942
Inter-strut 3 and 4	0.0283	0.5409
Inter-strut 4 and 5	0.0226	0.4188
Outlet	0.0267	0.6097
Time: t9 = 0.9s		
	Newtonian Vs. Carreau	Carreau Vs. non-Newtonian Power Law
Inlet	0.0416	1.2851
Inter-strut 1 and 2	0.0247	0.4350
Inter-strut 2 and 3	0.0279	0.4612
Inter-strut 3 and 4	0.0327	0.5072
Inter-strut 4 and 5	0.0263	0.3922
Outlet	0.0319	0.5768

	Measure of Error between WSS data	
Time: t10 = 1s		
	Newtonian Vs. Carreau	Carreau Vs. non-Newtonian Power Law
Inlet	0.0563	1.0140
Inter-strut 1 and 2	0.0327	0.3504
Inter-strut 2 and 3	0.0370	0.3752
Inter-strut 3 and 4	0.0437	0.4162
Inter-strut 4 and 5	0.0353	0.3209
Outlet	0.0447	0.4874

From the WSS error data presented in Table 3.4, Newtonian is noticed to compare more closely to Carreau model than non-Newtonian Power Law compared to Carreau model.

3.5 DISCUSSION

Numerical transient simulations were applied to a straight helical stented artery under LAD pulsatile flow conditions for Newtonian and two non-Newtonian viscosity blood models. The WSS distribution trends within the stented artery are observed to be same for all the blood viscosity models investigated at the selected cardiac time points; however the WSS magnitudes differed from one viscosity model to another.

Based on the CFD results presented, the WSS distributions within the stented LAD artery can be seen as highly non-uniform. During the flow deceleration phase (t_1) characterised by a negative flow rate, the WSS magnitudes produced by Carreau model and Newtonian model are seen to be very similar throughout the entire stented arterial region. The agreement between these two constitutive blood models at this phase was considered excellent within the areas of interest thus; inlet and outlet regions of the stented artery and inter-strut regions, $\varepsilon < 0.05$. The agreement between the

non-Newtonian Power Law and the Carreau model within the inter-strut regions was considered good as $\varepsilon < 0.1$. Conversely, the agreement between these two latter constitutive blood models at the inlet and outlet regions was considered poor as $\varepsilon > 0.1$. On the top of the stent struts, WSS magnitudes produced by the non-Newtonian Power Law model was observed to be lower compared to the Newtonian and Carreau models which recorded very similar WSS magnitudes.

At the acceleration phase (t_2) characterised with a forward flow rate, the WSS magnitudes produced by the Newtonian and the non-Newtonian Power within the inter-strut regions are shown to have good agreement with that of the WSS magnitude produced by Carreau model within the same regions; thus $\varepsilon < 0.1$. At the inlet and outlet regions, there was a poor agreement between the non-Newtonian Power Law and Carreau model ($\varepsilon > 0.1$). Also, the agreement between Newtonian and Carreau model at the inlet region was poor, however at the outlet region the agreement between the two models was good. It is suggested that the difference of WSS error seen between these two regions may be as a result of the local dynamic nature of flow at the respective regions which could influence the impact of both constitutive blood models.

At deceleration phase (t_3), flow rate is predicted to be very minimal and this is marked by the very low WSS magnitudes as shown in figure **3.8**. However, the WSS magnitudes produced by all the blood models being investigated were seen to be incongruent to each other at the regions of interest. The measures of error difference between the three rheological models were very poor ($\varepsilon > 0.1$) and thus the error difference considered very significant. It is noted however that Newtonian model at this phase compared worse to Carreau model as opposed to non-Newtonian Power Law compared to Carreau model.

During the continuous acceleration phases (t_4, t_5) and deceleration phases (t_6, t_7, t_8, t_9 and t_{10}) with each phase having a forward flow rate and considerable high flow rate magnitude, the WSS magnitudes produced by the Newtonian model and Carreau model are seen to be more comparable throughout the entire region of the stented artery. The agreement between the Carreau and Newtonian models were also considered to be excellent as $\varepsilon < 0.05$. Conversely the agreements between the non-Newtonian Power Law and Carreau models at these different phases were observed to be very poor $\varepsilon > 0.1$. Additionally, non-Newtonian Power Law model was observed to under-estimate the WSS magnitudes produced within the stented artery during these phases.

From the results analyses it is noted that Newtonian model is able to capture very closely most of the non-Newtonian blood viscosity's (Carreau model) effect on WSS magnitudes within the stented LAD model. For instance at cardiac time points of (t_1, t_2, t_4, - t_{10}) the agreement between WSS data produced by Newtonian model and the Carreau model at regions of interest were considered excellent and thus the error difference in WSS data between these two rheological models used for the LAD flow simulation considered insignificant. Therefore the assumption that Newtonian model could serve as an acceptable rheological model to analyse the non-Newtonian blood characteristics within straight stented LAD is justifiable.

At time point (t_3) of the cardiac cycle however, the Newtonian model is noted not able to mimic the behaviour of the non-Newtonian rheological blood model. Whilst this result is indicative of the fact that Newtonian model is not able to fully capture the behaviour of the non-Newtonian rheological blood model over a complete cardiac waveform of the LAD, general results nonetheless show that Newtonian model agrees very well with the non-Newtonian rheological blood model over 80% of the LAD cardiac cycle. Thus the Newtonian model and Carreau model is observed to show a good

agreement quantitatively in the WSSs during the LAD cardiac cycle. On the contrary, non-Newtonian Power Law model is found to produce much lower WSS values. This observation is consistent with other observations made by Soulis et al. [35], Liu et al. [295] and Johnston et al. [296] in the investigation of non-Newtonian blood flow in the human coronary artery. It should be noted however that although observations made on the effect of non-Newtonian Power Law model on WSS correlated to that reported by Soulis et al., Liu et al., and Johnston et al; each study reported was carried out under different flow condition. Liu et al., investigated into the influence of non-Newtonian model on WSS in right coronary artery under non-physiological unsteady flow conditions whilst Soulis et al., and Johnston et al., performed their investigation simulating steady flow conditions. On the other hand, investigation on the impact of non-Newtonian blood models on WSS reported in this thesis was conducted using physiologically realistic LAD pulsatile flow conditions. Also, in the investigation by Soulis at el. [35] it was reported that at mid- to high strain rates Carreau model tends to behave like Newtonian model. The centre-line velocity used in the simulation of the constitutive blood models in this thesis is $0.53\ m/s$ and at mid- to large velocity centre-lines (around $0.1\ m/s \leq$) it has been reported by Liu et al. [295] and Johnston et al. [296] that WSS magnitude for Carreau and Newtonian models are similar whilst Power Law model produces very low WSSs. This therefore tends to explain further the reason why the WSS magnitudes of the Carreau and Newtonian models observed are similar and that of non-Newtonian Power Law model are much lower.

A CFD analysis by Razavi et al. [297] into stenotic flow dynamics using six non-Newtonian viscosity models; (i.e. Power Law, Carreau Yasuda, Carreau, Generalised Power Law, modified Casson, Walburn-Schneck) and a Newtonian model suggested Carreau model as a suitable model for the analysis of stenotic fluid flow dynamics in a carotid artery under pulsatile flow

conditions. In the study it was suggested that the cut-off value for global non-Newtonian importance factor; IG = 1 for which blood flow could be assumed to exhibit non-Newtonian behaviour. IG defines the relative difference between Newtonian viscosity value and non-Newtonian viscosity value over an entire fluid model [192]. So in the analysis of IGs of the non-Newtonian models it was observed that Carreau and Carreau Yasuda models predicted moderate IG values whilst the other models predicted either high or low IGs. Using either high or low IG models could lead to overestimation or underestimation of non-Newtonian behaviour respectively. This consequently could dominate the effect of the mechanical parameters such as WSS magnitudes being recorded and therefore could produce a false representation of the mechanical milieu present in the artery. The use of Carreau model on the other hand produced a moderate non-Newtonian behaviour which therefore showed better representation of the mechanical environment in the artery. This conclusion from Razavi et al. [297] thus tend to further support the reason why Carreau model was considered as the benchmark for comparing the Newtonian and non-Newtonian Power Law effects on WSSs within the stented LAD artery in addition to having shown in figure **3.1** that Carreau model best fitted experimental blood rheological models.

3.5.1 LIMITATIONS

One limitation of this study was that a straight stented tube was used as a model for the stented LAD artery. This simplified geometry of the artery constitutes another assumption because the anatomical shape of the artery is tortuous and curved. Additionally, stenosis is more prone to arterial regions which are curved and bifurcated because of the strong relation existing

between recirculation regions induced by the effect of curvature and atherogenesis process. Seo et al. [214] investigated into the flow fields within straight and curved vessels and revealed that the extent of flow disturbance and flow separation is dependent on angle of arterial curvature.

Also, a simplified helical stent design was modelled to investigate the effect of stent on flow characteristics. Whilst the hemodynamic data achieved helps us appreciate the effects of stent on fluid flow dynamics it is however known that not all stent designs alter hemodynamic parameters in the same manner and probably analysis of different constitutive blood models on complex stents may not be comparable. Comparative studies of different stent designs but of identical stent parameters within arteries have shown disparities in local hemodynamic milieu which have been likely attributed to the difference in stent design [298, 299]. It is also reasoned that most standard commercial stents have stent connectors which links two struts together. These connectors increase the complexity of the stent designs and depending on their length and the alignment to fluid flow could affect the hemodynamic environment [300]. Therefore analysis from our simplified stent geometry may not be sufficient enough to capture different flow dynamics that may be present in a real case.

It is therefore not clear how Newtonian and Carreau models would compare when more complex arterial and stent geometries are examined.

3.6 CONCLUSION

In summary, the choice of rheological viscosity model used for analysing blood flow behaviour and in assessing its impact on WSS in stented LAD artery as afore discussed can significantly affect WSS magnitudes. This subsequently influences our judgment in predicting accurately stented

arterial sites more prone to restenosis. Endothelial transport properties have been reported to alter as a result of endothelial structural and functional changes mediated by WSS [301]. Hence it is important to quantify accurately the WSS that may induce ECs functional and structural changes.

As discussed in section **3.5** of this chapter, the use of non-Newtonian Power Law in simulating blood flow in a stented coronary artery led to under-estimation of WSS magnitudes. Conversely, the use of Carreau model and Newtonian model showed similar WSS magnitudes under realistic pulsatile LAD flow condition simulation. So, the choice of rheological blood model used to simulate blood flow could under-estimate or over-estimate WSS predicted in arterial models. From the WSS data presented in this chapter, the use of Newtonian model other than Carreau model in the analysis of WSSs in a straight stented LAD, is a better alternative option. This proposition is made based on the reasons that:

- 75% of total coronary blood flow occurs during the diastolic period [302] and at this period Newtonian model is seen to be able to mimic the non-Newtonian rheological blood model based on Carreau model.

- Additionally, the 10% which constitutes the total percentage of which Newtonian model is not able to mimic the non-Newtonian rheological blood models behaviour occurs during systolic where flowrate is very low. It is postulated that taking into account a complete cardiac cycle (1s), the failure of the Newtonian model to capture the non-Newtonian blood behaviour for a tenth of a second may result in an insignificant effect in the general analysis of blood flow dynamics on EC response.

Finally, as illustrated in figure **3.8**, the use of different rheological blood models in blood flow simulation within stented artery resulted in comparatively different WSS magnitudes; however WSS distributions were

similar. Interestingly, WSS magnitude recorded on the first stent strut respective to the flow direction was the highest compared to the subsequent stent struts which showed relatively lower WSS magnitudes. Explanation to this observation was that fluid flow tends to reduce in speed as it flows across successive struts. So, employing Bernoulli's equation, it is deduced that pressure on the first stent strut would be the lowest compared to the subsequent struts. Additionally, flow speed at the very immediate regions of stent strut is very low and thus pressures at these regions are high. The pressure difference gives rise to the WSS magnitudes which therefore implies that the lower the pressure on top of the strut, the higher the WSS magnitude.

CHAPTER 4

FLOW BIOREACTOR

4.1 EFFECTS OF STRESSES ON ECs RESPONSE

Numerous studies have established relationships between ECs structure, transport properties and gene activity changes to mechanical stresses [51, 303-308]. The mostly reported ECs alteration when subjected to fluidic WSS has been in its morphological change. When ECs are not stimulated thus by stress they are shown to be cobblestone-like and disposed to a random cell alignment nature. However when they are exposed to appropriate physiological fluidic WSS levels, they have been shown to elongate and align in the direction of flow in a time dependent manner [308]. It should be made clear however that ECs in vivo are not only subjected to fluidic WSS but also tensile hoop strain as a result of cyclic stretching and contraction of arterial walls [309]. These shear stress and tensile strain coexist and may impact the function of ECs to the onset of arterial disease [310]. In the case of a diseased artery, the arteries are said to be stiffer [311]. Thus the cyclic stretching and contraction action of arteria walls are reduced or become negligible. From the above discussion it could therefore be assumed that WSS play dominant role influencing ECs response within diseased arteries. So, the effect of tensile hoop strain on ECs could be ignored based on arterial stiffness.

It is agreed that CFD analysis of local hemodynamics within stented artery based on the assumptions of rigid arterial wall and fixed stent may affect

WSS and fluid flow dynamics results. So performing fluid-structure interaction analysis of the local hemodynamics within the stented artery which takes into account arterial wall compliance may produce further hemodynamic data that CFD simulations may fail to capture. Nonetheless, a study by Chiastra et al. [312] on the necessity of modelling fluid-structure interaction for stented coronary arteries revealed that CFD analysis based on the assumption of rigid arterial wall for fluid-structure interaction simulations are adequate when analysing WSSs.

When ECs are stimulated under hydrostatic pressure in the absence of fluidic stresses, the cells are shown to elongate with time but have a random cell alignment disposure [313]. Further investigations into the independent effects of hydrostatic pressure and fluidic stress on EC response have shown increase in cell proliferation and a formation of a multi-layered cell structure when the cells are exposed to only hydrostatic pressure [313]. When cells are exposed to a physiological laminar WSS however, proliferation is inhibited and cells form a monolayer structure [314]. Interestingly, White et al. [24] have suggested that temporal gradient but not spatial gradient shear stress stimulates EC proliferation. Also disturbed WSS is predicted to influence EC proliferation [315]. Investigations into the response of ECs to combined hydrostatic pressure and shear stress have shown ECs to elongate and align to the flow direction and also exhibit a monolayer structure [316]. It is therefore postulated that shear stress has an over-riding effect on ECs morphology when the cells are subjected to combined shear stress and hydrostatic pressure. Studies by Bond et al. [317, 318] into the morphological changes of EC nuclei indicated that nuclei elongated and aligned with applied shear stress. This implied that there is a parallel behaviour between morphological changes of EC and its nucleus. However one needs to be very careful when making assumptions of nuclei behaviour based on that of EC behaviour as there is quiet a weak correlation

between nucleus elongation and stress. Thus other factors such as pulsatility of flow or arterial wall stiffness may influence nucleus elongation [317]. Understanding ECs morphology can be beneficial in predicting arterial sites which are healthy and those prone to diseases. It is suggested that arterial sites having ECs of cobblestone morphology are more atheroma prone whereas sites with elongated ECs are athero-protected [92, 181, 319].

Endothelial morphological changes and functions mediated by mechanical stresses are regulated by very complex molecular signalling cascades [320]. A study by Warboys et al. [305] into the effect of chronic and acute stresses on ECs function demonstrated that chronic shear stress reduced ECs permeability to macromolecules. It was suggested that this ECs response was achieved as constant shear stress induced nitric oxide (NO) synthesis through production of phosphatidylinositol 3-OH (P13K) and soluble guanylyl cyclase. Increase permeability of endothelium layer to macromolecules such as lipoprotein over a period of time has been suggested to trigger atherosclerosis [92], thus this stress-NO phenomenon could help explain the athero-protective nature of ECs subjected to shear stress.

4.2 TYPES OF STRESSES ON ECs

Several studies have produced compelling evidences to suggest a link between WSSs and the disposure to an arterial site being prone to disease [12, 109, 321-323]. Whilst these evidences are acceptable, they are still not sufficient and therefore it is not prudent to exclude other factors that may influence the anatomic state of an artery. Hence, other additional theories have been postulated based on either temporal (TWSSG) or spatial (SWSSG) rate of change of the WSS or oscillatory shear index (OSI) [11, 324-326]. These additional theories allow for the consideration of the

physiological pulsatile blood flow behaviour in the arteries and also the complex geometrical structure of the artery.

4.2.1 TEMPORAL WALL SHEAR STRESS GRADIENT (TWSSG)

The dynamic nature of blood flow with respect to the cardiac cycle gives rise to TWSSG. White et al. [50] postulated that TWSSG induced increased endothelial turnover by stimulating ERK 1/2 activation. This effect has been implicated to contribute in the development of atherosclerotic lesions [327]. TWSSG is calculated by the mathematical formulation given below:

$$TWSSG = \frac{\partial \tau_w}{\partial t} \quad 4.1$$

where $\partial \tau_w$ is the change in WSS and ∂t is the change in time.

4.2.2 SPATIAL WALL SHEAR STRESS GRADIENT (SWSSG)

The complex geometric shape of the artery could cause local spatial variation of the stresses acting on ECs. It has been implied that these local changes of stresses acting on the EC could induce intercellular junction gaps which consequently would lead to uncontrolled permeability of macromolecules [328, 329]. SWSSG is calculated by the mathematical equation given below:

$$SWSSG = \frac{\partial \tau_w}{\partial s} \quad 4.2$$

where ∂s is the change in distance.

4.2.3 OSCILLATORY SHEAR INDEX (OSI)

OSI is the measure of deflection of the WSS vector from the main directional blood flow; thus an indication of flow disruption during the flow cycle in the artery as suggested by Ku et al. [102]. A study by Zhang et al. [330] into the flow patterns and WSS in the human carotid artery made a correlation between elevated OSI with increased risk of stenosis in the artery. This OSI formulated as:

$$OSI = 0.5 \times \left(1 - \frac{\left|\int_0^T \overrightarrow{\tau_w} dt\right|}{\int_0^T |\overrightarrow{\tau_w}| dt}\right) \quad 4.3$$

where $\overrightarrow{\tau_w}$ is the instantaneous WSS vector at a cardiac time point, dt is the change in the time point over a complete cardiac period T.

Substantive evidence to explain the onset and progression of atherosclerotic lesions still remains elusive. Hence it begs the questions if current popular flow metric; i.e. WSS, SWSSG, TWSSG and OSI are enough to capture physiological blood flow physics? And do these metrics accurately quantify the essence of ECs response to dynamic flow so commonly suggested in many literature? Chakraborty et al. [331] demonstrated that directionality of shear significantly affected ECs response when the effects of biaxial oscillatory shear stress on ECs were investigated. Thus it was implied that directional oscillatory shear index could play a critical role in atherogenesis.

4.3 FLOW BIOREACTOR SYSTEMS FOR SUBJECTING ECs TO FLUIDIC STRESSES

As discussed in sections **4.1** and **4.2**, ECs undergo morphological and

functional changes under mechanical stress and there have been numerous experimental evidences to demonstrate these phenomena. The use of flow bioreactors to simulate measured mechanical stimuli on cells has proved critical in quantifying of cells response to different dynamic stresses [24, 49, 51, 304]. Some of these studies are summarised in table **4.1**.

Table 4.1 Flow bioreactor subjecting ECs to mechanical stimuli

	Mechanical Stresses						
Ref.	WSS	SWSSG	TWSSG	OSI	Pressure	Flow	ECs
Ohashi [332]	Yes	No	No	No	Yes	Steady	BAEC
Galbraith [308]	Yes	No	No	No	No	Steady	BAEC
Vara [333]	Yes	No	Yes	No	Yes	Physio -logical	HUVEC
Conklin [334]	Yes	No	Yes	Yes	Yes	Physio -logical	PCCA (*ex vivo*)
Estrada [48]	Yes	No	Yes	Yes	Yes	Physio -logical	HAEC
Dolan [335]	Yes	Yes	No	No	Yes	Steady	BAEC
Punchard [336]	Yes	No	Yes	No	Yes	Physio -logical	HUVEC
Dardik [337]	Yes	Yes	Yes	No	No	Orbital	BAEC
Lane [338]	Yes	No	No	No	No	Steady	HUEPC

White [24]	Yes	Yes	Yes	Yes	Yes	Steady	HUVEC
Frangos [47]	Yes	No	No	No	Yes	Steady	HUVEC

HUVEC = Human Umbilical Vein Endothelial Cell, BAEC = Bovine Aortic Endothelial Cell, HAEC = Human Aortic Endothelial Cell, PCCA = Porcine Common Carotid Artery segment, HUEPC = Human Umbilical Endothelial Progenitor Cell.

4.3.1 INTEGRAL PARTS OF FLOW BIOREACTOR SYSTEM

4.3.1.1 FLOW CHAMBER

In flow bioreactor systems, the design of the flow chamber is one of the most integral part of the bioreactor system [339]. The flow chamber houses the ECs and also influences the mechanical environment being experienced by the cells. One of the most widely used and well characterised flow chambers is the parallel plate flow chamber (CytoDyne, La Jolla, CA) [47]. This flow chamber is a simple and re-usable device which houses ECs seeded on a substrate; mostly on glass microscope slides to be subjected to predicted flow dynamics. The parallel plate flow chamber (PPFC) allows for a uniform distribution of WSSs on cells. In other studies, the PPFC has been modified to allow for a wide range of mechanical stimuli which the conventional PPFC is not able to achieve. One such example was illustrated by DeVerse et al. [340] who housed ECs in a cone-and-plate shearing device; thus subjecting the cells to both steady WSS and oscillatory shear stress to investigate and characterise the inflammatory state of the ECs. Other flow chambers used by

researchers are the compliant cylindrical grafts which facilitate cells to be subjected to shear stress and hoop stretch [336, 341] and the converging flow chambers which cause spatial variation of shear stress to be experienced on the cells [335, 339].

4.3.1.2 FLOW CIRCUIT PUMP

A simple flow circuit pump is normally used to apply steady flow of culture media to subject cells to measured steady stress. However, the physiological nature of blood flow in arteries is transient and so there is temporal variation of stress suspected to be experienced by ECs in vivo. To capture this temporal stress dynamics, researchers developed programmable syringe pump which would vary the flow rate produced with respect to time and thus produced pulsatile flow instead of a steady flow waveform [24, 342, 343]. This application led to cultured ECs experiencing temporal variation of shear stress. Whilst data achieved from the afore-mentioned references helps us appreciate the independent effects of temporal shear stress variation on cells, conclusions made from the results may highly not be applicable to the physiological response of ECs in vivo. This is because the syringe pump was programmed to apply non-physiological flow parameter on the cells. More so, there was no constant recirculation of culture media to the cells thus experimentation period was short. This as a result could influence our ability to accurately predict ECs response in vivo as short-term and long-term exposure to either independent or combined mechanical stimuli could cause ECs to respond differently [305]. To overcome these limitations, other investigators have developed new pulsatile perfusion systems which could produce physiological flow parameters over a continuous long period of time [336, 344, 345]. As noted in sections **4.3.1.1** and **4.3.1.2** the flow chamber

and flow circuit pump are important parts of the flow bioreactor system that aid in achieving desirable flow metrics and creating predicted mechanical environment for cells. Furthermore, it is also of equal importance when conducting cell experimental studies with the bioreactor system that the system is able to be kept under good sterile conditions and provide the ECs with the appropriate temperature, CO_2, pH and oxygen. Additionally, the flow tubing used for the system should be non-compliant to yield accurate and repeatable mechanical stresses on the cells over the desired period of time.

4.4 DESIGNING FLOW BIOREACTOR SYSTEM

In designing the flow bioreactor system, one of the main objectives set out to achieve was for the system to be able to produce a LAD physiological waveform with its associated WSS waveform as illustrated in figure **4.2**. Also the system was to be simple, cheap and able to produce similar flow dynamics in a stented LAD artery as discussed in section **3.4**.

4.4.1 DESIGNING FLOW CIRCUIT

The design of the flow circuit system was based on that of Conklin et al. [334]. Conklin et al. developed a pulsatile perfusion system which consisted of a peristaltic pump that yielded a steady flow and a custom designed cam-driven physiologic flow simulator to superimpose physiologically relevant pulsatile flow waveform on top of the steady flow. An advantage of this system was that the cam-driven physiologic flow simulator could be easily detached from the system when only steady flow is desired. Additionally the system allowed independent control of flow rate and pressure subjected to

the cells. The disadvantage to this system however was that accuracy of the pulsatile flow waveform reproduced to that targeted was poor. El-Kurdi et al. [346] designed a similar flow perfusion system to that of Conklin et al. but with an added advantage of the system being able to produce a pulsatile flow waveform that was more comparable to the targeted waveform. Whilst it would appear to be of a better judgement to therefore base the design of the flow bioreactor system to that of El-Kurdi et al., it is noted that El-Kurdi's flow system is highly complicated compared to that of Conklin et al. and also likely to be relatively more costly to establish. Hence it was deemed appropriate to base the flow design on that of Conklin et al. as the design was simple and relatively cheap to build. It is proposed that the limitation of the flow system by Conklin et al. could be overcome by including a feedback control system to the flow simulator to keep a constant angular velocity of the camshaft and thus improve the accuracy of the flow waveform produced throughout the flow cycle. Additionally, it is noted that Conklin's flow system was designed to study intact vascular segments however it is anticipated that this system could be easily modified to incorporate any type of flow chamber to investigate ECs response to various mechanical stimuli.

Illustrated below is a schematic diagram of the flow bioreactor system. The bioreactor system works by drawing culture media from a reservoir (A) by the use of a peristaltic pump (B) through a non-compliant tube. A compliance chamber (C) is connected to the tube to dampen oscillations that may arise from the use of the peristaltic pump. The desired pulsatile flow waveform is then superimposed onto the flow through the action of the cam-driven pulsatile flow simulator (E) and to ensure that this pulsation effect is not dampened by the compliance chamber, a one-way flow check valve (D) is connected to the tube. The pulsatile flow now passes through a test flow chamber (H) were cells cultured on a substrate are housed. To build pressure in the system, a flow resistance valve (J) is used to lower the

outward flow rate thereby causing a build-up of media in the compliance chamber which consequently leads to an increase change in pressure. The flow waveform and pressure are quantified using the flow sensors (F) and pressure sensors (G) connected to analogue to digital converters. A sterile filter (K) is connected to the media reservoir which allows for gaseous exchange.

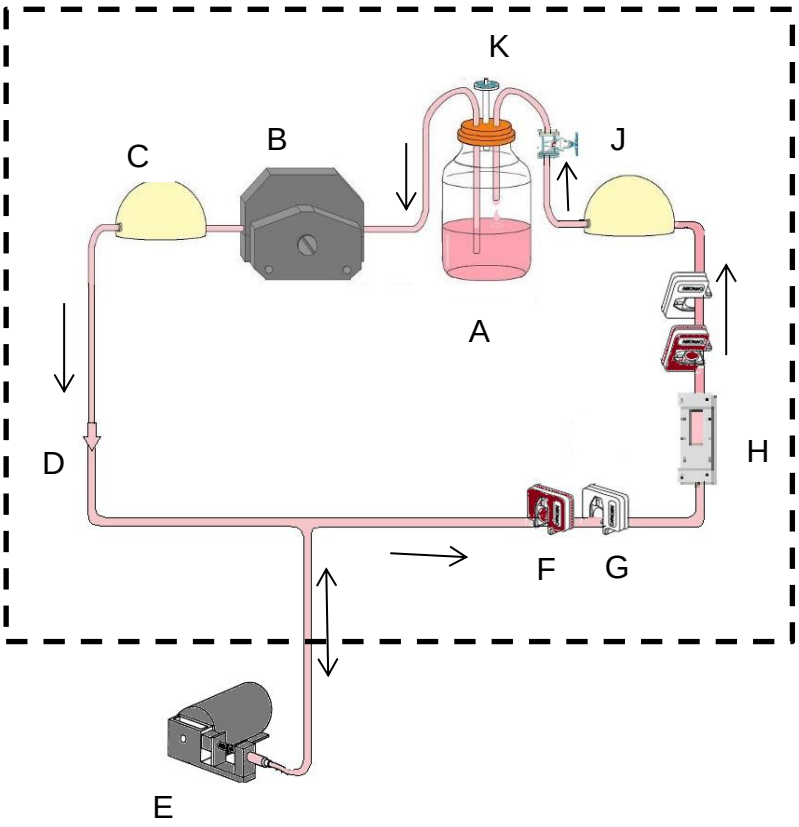

Figure 4.1 Shows a schematic diagram of flow bioreactor system setup. Components housed in the incubator are shown within the dashed line square. The arrows show culture media pathway during flow experiment. A = media reservoir, B =peristaltic pump, C = compliance chamber, D = one-way flow check valve, E = cam-driven pulsatile flow simulator, F = flow sensor, G = pressure sensor, H = test flow chamber, J = flow resistance valve, K = filter.

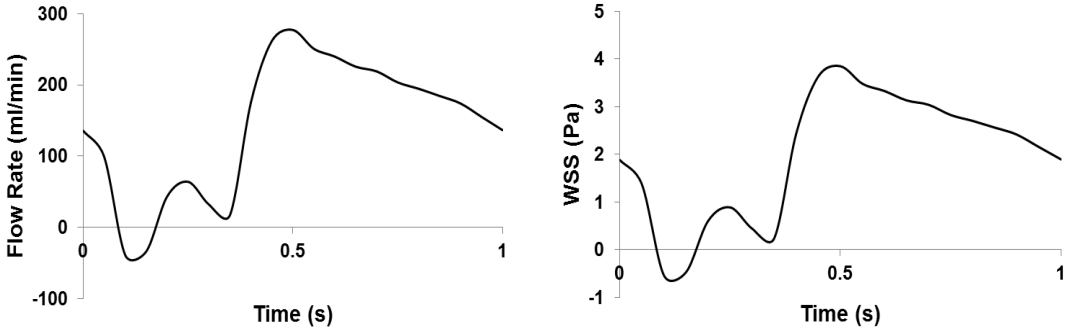

Figure 4.2 LAD waveform; Flow rate (L), WSS (R) [58].

4.4.1.1 FLOW AND PRESSURE SENSORS

To ensure accurate recordings of the flow and pressure data in the system, it was crucial that the sensors used to take the measurements were able to:

- Record sufficient data points to ensure reproducibility of predicted flow and pressure waveforms.
- Sensitive enough to detect any slight changes that may occur in the flow and/or pressure at low and high levels. Thus higher accuracy in the measurements is obtained.
- Maintain sterility of flow experiment.

To achieve the above stipulated requirements, it was suggested that ultrasonic flow sensors be used. This is because these sensors have no contact to the flow media as they are clamped onto the flow tubing and measurements are taken via the acoustic nature of the fluid flow. Hence the sterility of the fluid flow experiment is maintained. The flow sensor selected for the flow measurement was the Em-Tec SonoTT Clamp-On transducer (www.em-tec.com/index.php?topic=produkte&subtopic=emtecProducts). The

flow data were then taken on a flow computer (BioProTT) that controlled the sensor. To calibrate the flow sensor for our system, a peristaltic pump was used to produce a referenced steady flow rates through a $3.2mm$ internal diameter tubing. The flow sensor was used to measure the flow rate produced by the peristaltic pump using the BioProTT flow computer. To also verify that the peristaltic pump was producing the required flow rate, analytical measurements were made by timed collection of the steady flow volume exiting the tube over at least 60 seconds. Figure **4.3** and table **4.2** shows the agreement of flow rates between that measured with the flow sensor and also from the analytical measurements to that produced by the peristaltic pump. All measurements were repeated at least three times and performed under similar conditions that the cell experiments would be conducted such as keeping the fluid flow at a temperature of $37℃$.

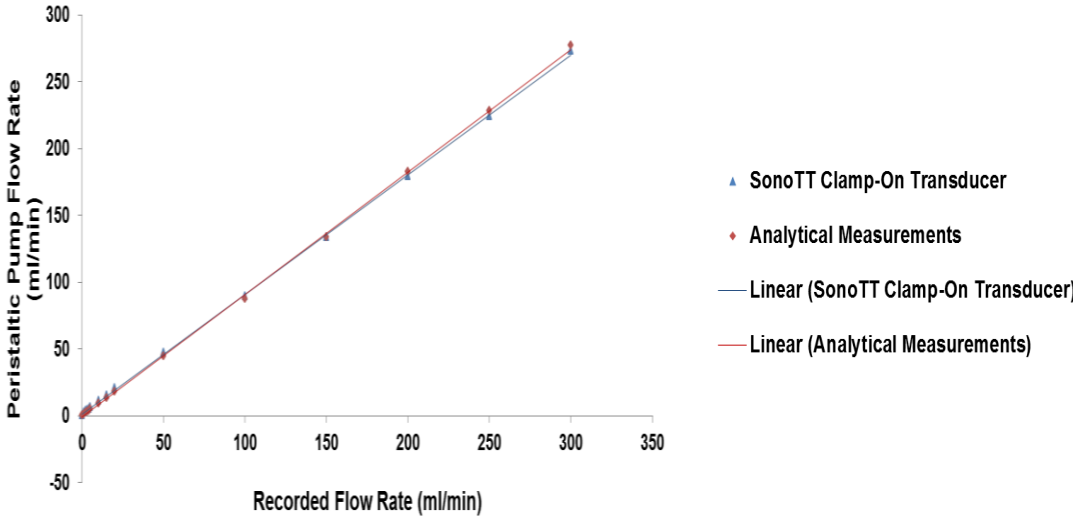

Figure 4.3 Calibration of flow sensor and peristaltic pump

Table 4.2 r^2 values and gradient of best fit line (m) for correlation between flow rates measured analytically or from a SonoTT clamp-on flow sensor to flow rate from a peristaltic pump.

Flow Measurement Device	**m**	**r^2**
SonoTT Clamp-On Flow Sensor	0.9011	0.9997
Analytical Measurements	0.9115	0.9996

To also measure the physiological pressure in the system whilst still keeping the flow experiment under sterile conditions, a piezoelectric pressure sensor (Physiological Pressure Transducer, AD Instruments; MLT844) was used. This pressure sensor is used in combination with appropriate signal amplifier equipment (Bridge Amp, AD Instruments; ML221) and a PowerLab 4/25T, AD Instruments; ML845 which serves as an analogue to digital converter. The pressure signals from the pressure transducer are read on a PowerLab LabChart software (LabChart 6, AD Instruments) installed on a computer. The LabChart is set to convert the signals which are in voltages to pressure unit mmHg. It is important that the pressure transducer is able to measure accurately a wide range of pressure; for example of relevant physiological pressure levels and at a sampling rate at least as high as for the fluid flow. To calibrate the pressure transducer, different referenced amount of distilled water at temperature of 37℃ is put into a centimetre calibrated column and the pressure transducer used to record the pressure in unit voltage exerted by each referenced amount of distilled water. Figure **4.4** shows the calibration graph of the pressure transducer. Table **4.3** shows the correlation between pressure (mmHg) and the voltage measured.

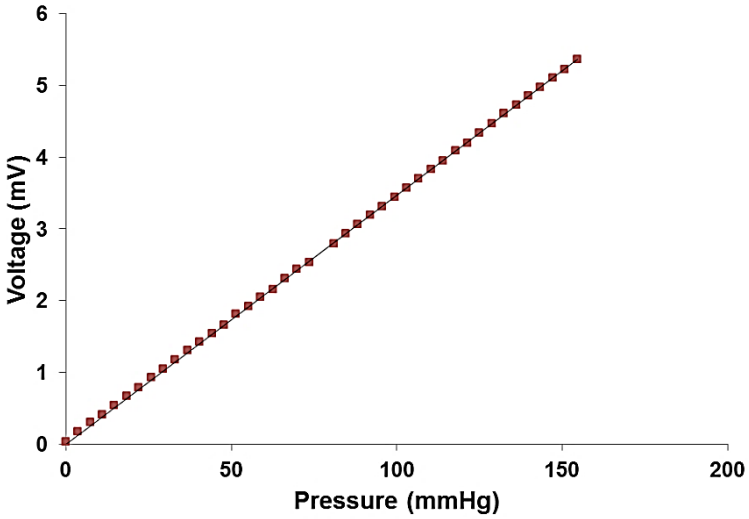

Figure 4.4 Calibration of pressure transducer

Table 4.3 r^2 values and gradient of best fit line (m) for correlation between pressure and measured voltage of pressure sensor.

Pressure Sensor Device	**m**	**r^2**
Pressure Transducer	0.0347	0.9999

4.4.1.2 CAM DRIVEN PULSATILE FLOW SIMULATOR

The cam driven pulsatile flow simulator shown in figure **4.5** was built in-house and can power different cams independently to simultaneously produce different flow waveforms. However since the interest of this project was to investigate the LAD flow, only the LAD cam was used. The LAD cam is attached to a shaft which is connected to a power motor (V5253, Rotalink, UK) at one end and at the other end a bearing which constrained its rotation.

A proportional-integrated-differential (PID) control system (RedDrive 10A, Rotalink, UK) was also connected to the motor to ensure that constant angular speed throughout the flow cycle was maintained. A push rod with one end attached to a carbon filled polytetrafluoroethylene (PTFE) cap was kept constantly in contact with the cam by the use of a stainless steel spring. The other end of the push rod which had a no head screw was connected to a plunger of a syringe whose barrel is held fixed. When the motor is powered on, the shaft tends to rotate which causes the cam to consequently rotate and also cause a forth and backward motion of the plunger in the syringe barrel. The shape of the cam and angular speed with which the shaft rotates determines the velocity of the plunger and also the flow rate at which fluid exits out the syringe barrel. In the case of producing a physiological waveform, the shaft is caused to rotate at $60rpm$ (revolution per minute) to give a pulse frequency of physiological level.

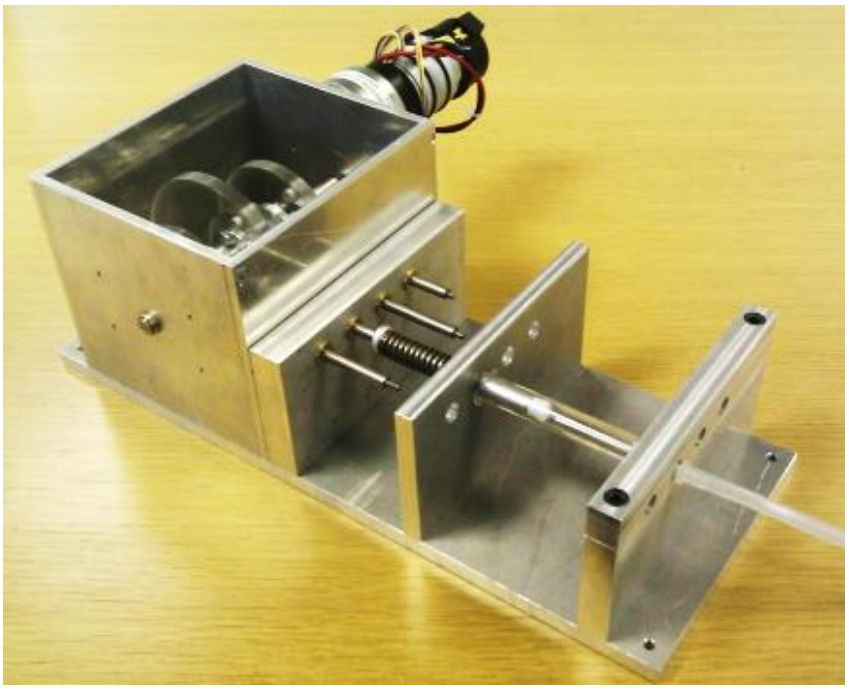

Figure 4.5 Cam driven pulsatile flow simulator

The design of a cam to produce a particular pulsatile waveform can be achieved by having define the flow rate in the periodic waveform over a complete time period, T. Thus given a function $g(t)$ that defines the flow rate, the pulsatile component of the waveform could be calculated as follows:

1. Firstly, subtract the mean flow rate from the function $g(t)$ to get the oscillatory component:

$$g_{osci}(t) = g(t) - \frac{\int_0^T g dt}{T} \quad 4.4$$

2. Based on the cross sectional area of the syringe barrel (a) and the oscillatory component of the flow rate $g_{osci}(t)$, the velocity of the plunger $u(t)$ is determined:

$$u(t) = \frac{g_{osci}(t)}{a} \quad 4.5$$

3. Integrate $u(t)$ with respect to time to get the particular position of the plunger (x) as a function of time with respect to an arbitrary datum:

$$x(t) = \int u(t) dt \quad 4.6$$

4. Add a constant, c to the above calculated step:

$$x'(t) = x(t) + c \quad 4.7$$

5. Define the angle at which the cam turns on a cycle:

$$\theta(t) = 2\pi t \qquad 4.8$$

6. To finally produce the shape of the cam, plot x' against θ in polar coordinates:

The plotted coordinates from the above calculations are then exported for CNC machining. Figure 4.6 shows a cam profile of a LAD flow waveform.

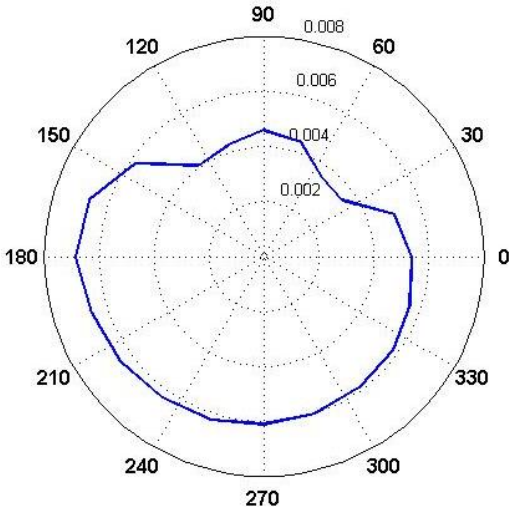

Figure 4.6 Cam profile of LAD waveform

4.4.1.3 PERISTALTIC PUMP AND TUBING

It was important to use a peristaltic pump which could provide a given flow rate required to produce a predicted WSS especially in the case where

physiological WSS levels are being considered. Hence the peristaltic pump selected to use for the flow system was a Masterflex LS 115/230 drive from Cole-Parmer, UK which could deliver very high flow rates (~348 ml/min).

Also the tubing used for the flow system was required to have acoustic properties suitable for use with the flow sensor, ability to withstand the fluid flow forces and made of materials suitable for cell culture applications. Hence PharMed tubing of internal diameter $3.2mm$ and of thickness $1.6mm$ from Fisher Scientific, UK which satisfies the above stated characteristics was used.

4.4.2 DESIGNING FLOW CHAMBER

A parallel plate flow chamber was developed to house the ECs cultured on a custom designed glass substrate. In designing the parallel plate flow chamber, notice was taken of the fact that the dimensions of the flow chamber and the flow media viscosity do affect the magnitude of WSSs associated with the LAD flow waveform produced on the cells. Hence to relate the predicted WSS applied to the ECs to the flow rate of the media and the flow chamber, a constant K is defined. This constant, K is given by the mathematical formula:

$$K = \frac{6\mu}{bh^2} \qquad 4.4$$

$$\tau_w = KQ \qquad 4.5$$

where μ is the media viscosity, b and h is the width and height respectively of the flow chamber, Q is the flow rate and τ_w is the

predicted WSS. The constant K, from the above equation **4.4** signifies that fluid viscosity is considered Newtonian.

As flow in the coronary artery is laminar, it is expected that the Re of flow in the flow chamber is sufficiently low to ensure that fluid flow is laminar. Thus particular consideration must be taken when choosing the constant K. To verify the condition that flow is laminar and Re is satisfied, the below mathematical equation is employed.

$$Re = \frac{\rho Q D_h}{\mu b h} \quad 4.6$$

$$D_h = \frac{4bh}{2(b+h)} \quad 4.7$$

where D_h is the hydraulic diameter. The Reynolds number of the designed flow chamber with height of $0.48mm$ and fluid density of $1000kg/m^3$ is 366.2 at a flow rate calculated to obtain a mean WSS of $2\ Pa$. Flow with Re < 1000 is considered laminar. Thus our flow condition is laminar as Re is 366.2.

4.4.2.1 DESIGNING ECs SUBSTRATE

As the aim of this project is to investigate cells response to mechanical stimuli in a stented artery, it was imperative that the mechanical environment experienced on cultured cells is similar to that of a real case. It was therefore one of the main objectives in this project to design a flow system capable of subjecting a wide range of mechanical stresses such as WSS, SWSSG, TWSSG and OSI which are predicted to be present within a stented artery on

the cells. To achieve this objective it was necessary to establish a flow chamber which could create such desired combined mechanical stimuli to be experienced on the cells. A simple generic stented LAD artery model which was to be investigated would have five independent semi-circular rings as shown in figure **4.7**. The generic stented artery had dimensions of $3mm$ internal artery diameter, stent strut diameter of $0.15mm$ and inter-strut spacing of $0.625mm$. Thus the flow and WSS dynamics applied to the cultured cells is similar to WSS dynamics in a helical stented LAD artery as described in section **3.4.1**. So, the choice to use a parallel plate flow chamber to create the mechanical stimuli needed only subjected cultured cells to spatially uniform WSS [47] and not to both spatial and temporal gradients in stress which have been suggested to be present within stented arteries [4]. However, this parallel plate flow chamber is of a very simple design and applies uniform WSS proportional to the flow rate onto cells which is one of the main stresses to be investigated in this project. It is therefore proposed that in order to use the parallel plate flow chamber, the substrate for the cultured cells should be modified so as to create the other mechanical stresses of interest i.e. SWSSG and OSI.

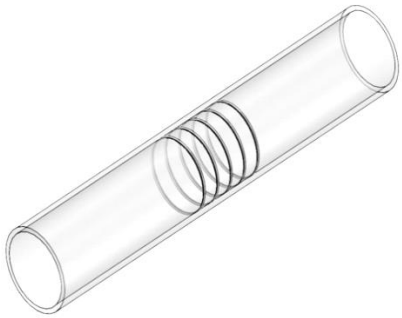

Figure 4.7 Generic stented artery model

A glass microscope glass slide which served as the substrate for the cultured cells was therefore suggested to be modified into a shape that represented a 2D shape of the generic stented LAD artery model as shown in figure **4.8**.

This was expected to create the desired mechanical milieu predicted to be subjected to ECs in the stented artery. The dimensions of the semi-circular ridges on the glass microscope slide are of the exact dimensions of the stent struts and stent spacing of the generic stented artery model. The combination of the parallel plate flow chamber and the modified glass microscope glass slide is termed as a cell-structure interaction experimental model. Detailed development and CFD analysis of the mechanical environment within the cell-structure interaction experimental model will be discussed in chapter **5**.

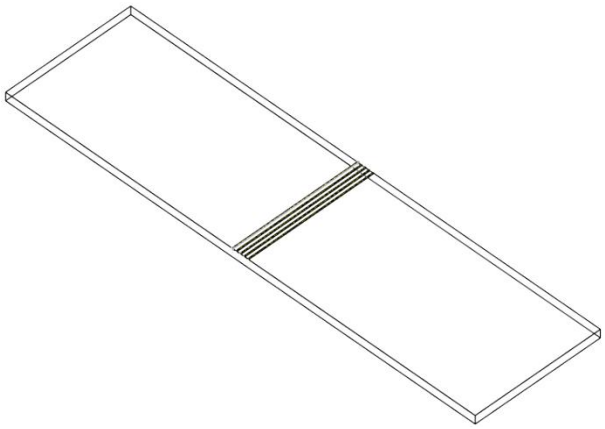

Figure 4.8 2D shape of the generic stented artery model

4.5 CHARACTERISING CELL CULTURE MEDIUM PROPERTIES

As discussed in chapter **3**, viscosity affects the shear rate of a fluid especially if it is of non-Newtonian characteristics. More so, viscosities of fluids are temperature dependent, hence it was important that the viscosity of culture medium at a temperature required for the medium to sustain cell viability be quantified. Additionally, the WSS being experienced in the flow chamber could be accurately determined if the viscosity and density of the culture

medium flowing through the flow bioreactor system are quantified.

The cell culture medium used for the flow experiment is made of the following compositions; M199 culture media (Sigma-Aldrich) containing 20% foetal calf serum (BioSera, UK), $30ug/ml$ endothelial cell growth factor (Sigma-Aldrich, UK), $30ug/ml$ heparin (Sigma-Aldrich, UK), $2mM$L-Glutamine (Sigma-Aldrich), $100ug/ml$ Penicillin Streptomycin (Sigma-Aldrich). Since the flow chamber is placed in an incubator at a temperature of $37℃$, the viscosity of the culture medium was determined at that temperature using a vibro viscometer (A&D Vibro Viscometer SV-1A).

To determine the density of the culture medium, a known volume of the medium in a graduated cylinder was weighed on a high precision balance. To ensure that measurement of the cell culture medium density recorded was accurate, the density of distilled water at $20℃$ was also determined and compared to that reported by Calvert et al. [347].

Table 4.4 Measurements of viscosity and density of cell culture medium at $37℃$ and distilled water at $20℃$.

Fluid	**Viscosity (mPa.s)**	**Density (kg/m^3)**
Culture Medium	0.64	1005
Distilled Water	1	998
Referenced Distilled Water [347]	1.002	1000

4.6 CHARACTERISING THE FLOW CIRCUIT

The flow circuit was set up as shown in figure **4.1** with the appropriate flow parameters set on the peristaltic pump and the cam driven pulsatile flow simulator to produce the desired LAD flow waveform as shown in figure **4.2** and at a physiological pressure of 120/80mmHg. The flow waveform recorded was then compared with the target flow waveform to analyse the deviation between them. Analytical measurement of this deviation was performed by calculating the mean squared error (MSE) between the two waveforms i.e. the measured and the target waveforms, normalised against the variance of the of the target waveform as shown in the equation given below.

$$MSE = \frac{\sum_{i=1}^{N}(Q_i - \bar{Q}_i)^2}{N\sigma_Q^2} \qquad 4.8$$

where Q_i and $\bar{Q}_i$ are the measured and target flow rate respectively at sampling point i on the flow waveform, N is the number of sampling point and σ_Q^2 is the variance of the target flow waveform.

Chetwynd et al. [348] used this equation to quantify the difference between a neural network predicted output and the true target output. How the two outputs compared was considered good if MSE was less than 0.1 and excellent if MSE was less than 0.05. Figure **4.9** shows the measured flow waveform compared with the target waveform and figure **4.10** shows the pressure at which the flow data was obtained. The inclusion of a feedback control system to the cam-driven pulsatile flow simulator ensured angular velocity of camshaft was kept constant throughout the flow cycle. This therefore helped improve the accuracy of the target flow waveform reproduction. Table **4.5** shows the quantitative data of the deviation between

the measured and target flow waveform.

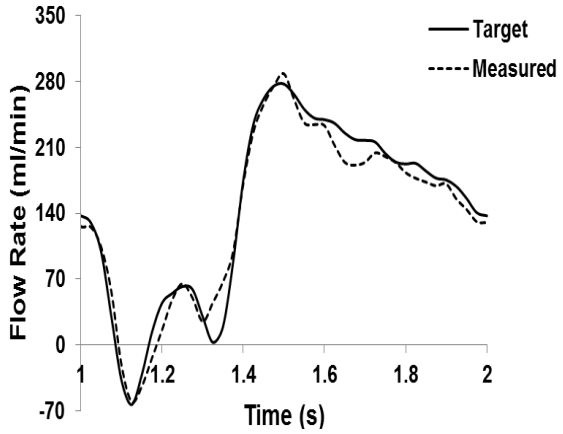

Figure 4.9 Measured vs target LAD flow waveform.

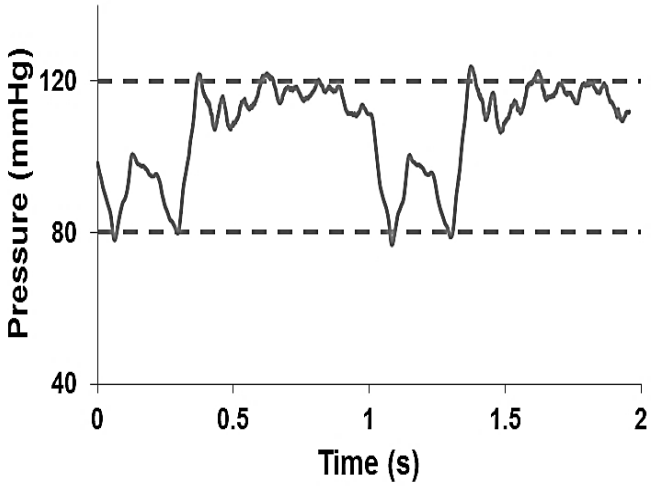

Figure 4.10 Physiological pressure at 120/80mmHg

Table 4.5 Measure of deviation between measured and target flow data

Waveform	MSE
LAD	0.031

It is observed that the flow bioreactor system designed is capable of producing the desired physiological LAD flow waveform at a physiological pressure of 120/80mmHg. Additionally quantitative analysis performed to determine how well the flow waveform produced from the system agreed with that of the target showed a very good agreement ($MSE = 0.031$). It is however acknowledged that for the system to produce a different type of waveform, a new cam is needed to be designed. Nonetheless it is reasoned that the designed flow system can allow for possible modification of flow waveform achieved if desired without requirement for new apparatus.

4.7 CONCLUSION

A modular flow bioreactor system has been designed which allows for easy addition of new features. This flow system is thus highly versatile and permits for a wide range of experiments to be performed with it. As discussed in this chapter, the flow bioreactor system is capable of running a parallel steady flow and LAD pulsatile flow experiment simultaneously. Also with the addition of the feedback control system to the in-house built cam-driven pulsatile flow simulator, higher accuracy of target flow waveform is constantly reproduced. The flow circuit, culture medium and features used in recording flow and pressure parameters have been characterised and calibrated accordingly to ensure accuracy of results. The main requirement set out in this chapter was that the bioreactor system is capable of producing LAD flow waveforms and hydrostatic pressure at physiologically relevant levels and this requirement was able to be met. Thus WSSs, OSIs, SWSSGs and TWSSGs experienced by the cells when subjected to this flow condition in the designed flow bioreactor would be of physiologically realistic levels.

CHAPTER 5

CELL-STRUCTURE INTERACTION MODEL

5.1 INTRODUCTION TO STEREO-LITHOGRAPHY

As briefly discussed in section **4.4.2.1** a glass microscope slide which was considered as a cell substrate was to be modified to represent a 2D artery with five independent semi-circular rings which served as stent as shown in figure **4.8**. So, to fabricate these stent-like structures on the glass microscope slide, a two photon stereo-lithography technique was employed.

5.1.1 STEREO-LITHOGRAPHY

Stereo-lithography is an additive manufacturing technique that involves fabricating 3D structures by selectively curing photo-curable polymer based resins in a layer-by-layer form [349]. These photo-curable polymer resins which are initially of a liquid state are sensitive to specific range of laser wavelengths and thus upon exposure to these wavelengths the resins change to a solid state. Typically the chemistry involved in this process is that the initiator component in the resin gets excited to an unstable state when a laser of a specific wavelength is beamed onto the resin. At this unstable state, the initiator tends to cleave into its radical components which as a result cause a chain of crosslinking reaction with the monomer units. Thus a solid polymer network is formed. Limitation to this technique however

is that resolution achieved is dependent on the wavelength used and diffraction of light within the polymer based resin which is dictated by Beer Lambert Law [350] .

An advanced technique to the standard stereo-lithography technique is the two-photon polymerisation (TPP) [55]. TPP technique can be used to fabricate complex bespoke structures with improved resolution and accuracy since as it involves curing a pin-point position of the resin at a time as opposed to curing the resin in bulk [351]. The main procedure involved when using TPP technique to fabricate structures is the absorption of two photons simultaneously which enables direct laser writing within photo-curable polymer resins. This direct laser writing is based on the quadratic relationship between laser excitation wavelength and the two photon absorption cross section [352]. Conditions to this relationship are only satisfied at a focal point of a laser objective where there is sufficient amount of photon flux. This pin-point location at the focal spot of the objective in an area known as a voxel [353] is of an elliptical volumetric space and acts like a single building block for creating complex structures. The laser beam outside this region has negligible effect on the photo-curable resin. Thus by translating this focal point relative to a curable resin, complex structures could be fabricated in a direct laser write approach within a bulk resin [354]. A self-smoothing effect of the 3D structure fabricated can be achieved when the voxel overlap is sufficiently close [355]. This fabricating technique has been found useful in multiple tissue engineering applications and in the preparation of medical devices with micro-scale properties [356-358]. TPP technique has also been employed to fabricate microfluidic channels as well as structures within microfluidic channels [359, 360].

5.2 FABRICATING SEMI-CIRCULAR RIDGES ON GLASS SLIDE

5.2.1 GLASS MICROSCOPE SLIDE FUNCTIONALISATION

The surface of a glass microscope slide with dimensions of $70mm\ x\ 25mm$ (Corning, USA) was initially functionalised before fabricating the semi-circular ridges on them. Piranha solution using a 3:1 mixture of sulphuric acid (H_2SO_4) and hydrogen peroxide (H_2O_2) respectively was prepared and the glass microscope slide submerged into the mixture for at least 1 hour. This solution is a powerful oxidizing agent which exposes the hydroxyl groups ($-OH$) on the surfaces of the glass microscope slide and also removes any dirt or organic residue from the slide. After an hour, the glass slide is washed in deionised water and dried prior to it being submerged into $10wt\%$ methacryloxypropyltrimethoxysilane ($MAPTMS$) solution in toluene for a minimum of 24 hours. Submerging the glass slide into $MAPTMS$ solution in toluene causes methacrylate groups from the $MAPTMS$ solution to bind to the $-OH$ groups exposed on the glass slide. This step allowed for better adhesion of polymer-resin during the polymerisation process of fabrication of the semi-circular ridges [361].

5.2.2 FABRICATION OF SEMI-CIRCULAR RIDGES

The fabrication process of the semi-circular ridges firstly involved preparing a photo-curable polymer based resin by mixing poly(ethylene glycol) diacrylate (PEGda) of molecular weight $700g/mol$ with a $4wt\%$ of photo-initiator 2-Hydroxy-2-methylpropiophenone (Sigma Aldrich, UK). This polymer resin is

then able to be cured in a $266nm$ region from the absorption of two photons produced by the TPP using a Nd:YAG microchip laser emitting at $532nm$.

To start fabricating the semi-circular ridges, a well of the prepared photo-curable polymer resin was created at a region on the functionalised glass slide where the structures were desired as shown in figure **5.1**. This sample glass slide was then affixed to a glass slide holder attached to a motorised xyz- stage. The motorised stage was controlled by computer-based software which translated the sample glass slide relative to the focal point of a stationary $20x$ laser objective lens. The focal point was positioned just below the polymer/glass slide boundary prior to fabrication and for reproducibility all glass microscope slides used were needed to be of $1mm$ thickness. The fabrication setup for patterning the desired structures is illustrated in figure **5.2**.

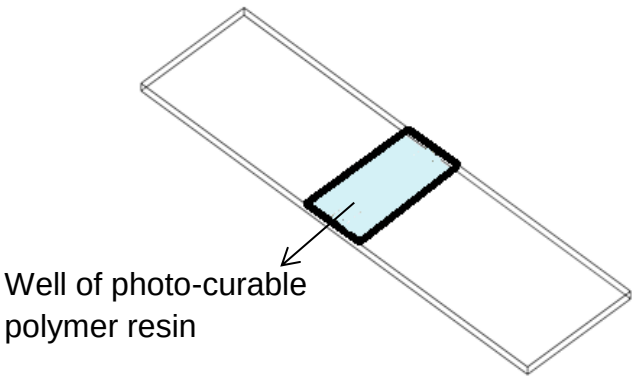

Figure 5.1 shows a well of photo-curable resin on microscope glass slide

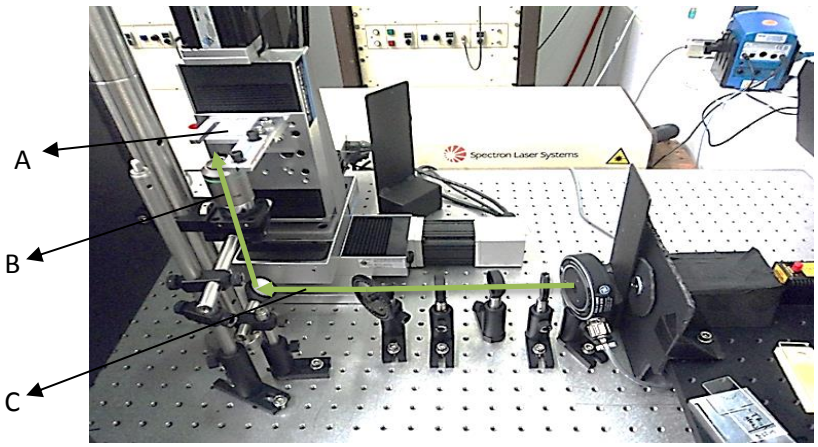

Figure 5.2 shows the fabrication setup for TPP. The glass slide is mounted on the motorised stage (A). The objective lens (B) focuses the laser beam (C) onto the mounted glass slide for fabrication process to begin.

The structural dimensions and positions of the semi-circular ridges are entered into a computer-controlled proprietary software called $N\,View$. This software converted the entered data into the xyz- stage movements and concurrently controlled the polymerising focal spot. In an initial attempt to fabricate the semi-circular ridges, the xyz- stage was programmed to trace a semi-circle oscillatory waveform with reference to the dimensions of the semi-circular ridges along the width of the glass slide (z- position) relative to the fixed objective lens. Thus a semi-circular arc is created at the end of a traced oscillatory waveform at a region along the z- position. The spacing between each created semi-circular arc was set at $1um$ to ensure sufficient attachment to the previously cured arc. This process was repeated along the width of the glass slide to produce a ridge of length $25mm$. After the specified length of the semi-circular ridge had been produced, the above processes were repeated again to create subsequent ridges at specified positions on the glass slide. Fabricating a ridge of a length of $25mm$ however took 7 hours and so fabricating 5 ridges on a glass slide took over a day. This method of fabricating the semi-circular ridges was therefore

deemed not time efficient. To overcome the problem of time spent to fabricate the desired structures, a quicker method was employed. In this new method, the ridge structure was produced by translating straight polymerised lines in a back and forth motions over the $25mm$ distance and with each line offsetted in the x- and y- position by $1um$ to create a semi-circular shape. The high confinement of polymerising region with TPP although advantageous for micro-structuring over a few mm, over long distances such as $25mm,$ any micron tilt of sample; in this case the glass slide, could be detrimental. This is because there could be significant variation of height of the ridges produced as the tilted glass slide moved relative to the fixed position of the polymerising focal spot. Upon finding out that the sample holder attached to the stage was at a slight angle to the objective lens, it was reasoned that the problem forecasted could occur. To overcome this limitation, the glass slide had to travel at an angle to offset the angle at which the glass slide was being held. To do this, the polymerising focal spot at both ends of the width of the glass slide was first determined. The glass slide was then repeatedly scanned over a localised region while gradually changing the height of the stage. At a point region on the glass slide where polymerisation occurred, a ripple light effect was observed. These ripple light effects helped determined the exact polymerising height at different regions of the glass slide. It was therefore calculated that the height difference with reference to the start and end position of the polymerising region along the $25mm$ length was $24um$.

So to fabricate a uniform straight line, the stage was set to translate the glass slide along the objective lens with an increase angle of $0.055°$ which compensated for the tilt of the glass slide with a laser scan speed of$0.6mm/s$. After polymerisation, the glass slide was gently submerged into a 50:50 solution mixture of $4-methyl-2-pentanone$ and $2-$

$propanol$ to wash away the uncured polymer resins. The advantage to this method was that the total time taken to fabricate 5 ridges, each of length $25mm$ was 8 hours. Figure **5.3** shows the fabricated semi-circular ridges on the glass microscope slide.

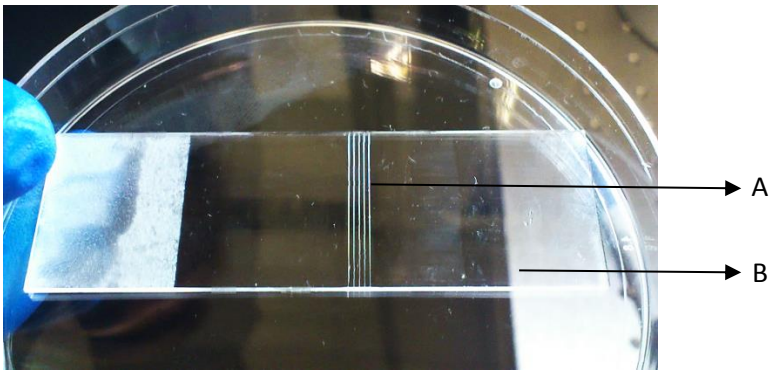

Figure 5.3 Microstructure semi-circular ridges (A) fabricated on microscopic glass slide (B)

5.2.3 CALLIBRATION OF FABRICATED SEMI-CIRCULAR RIDGES

To determine the optimal starting height position to fabricate the micro-structure ridges via TPP, different starting positions of the polymerising focal spot was calibrated. Thus for each consecutive single ridge structure fabricated, the initial focal spot height position was gradually increased by$10\,um$ through lowering the glass slide towards the objective lens by $10\,um$. This process also allowed for testing the stability of the ridge fabricated against collapse within the design parameters and during the post-polymerisation washing stage. Scanning electron microscopy (SEM) images were taken of the ridges fabricated at different starting focal spot height as shown in figure **5.4** and it is observed that the last ridge on the right has started to detach from the glass slide surface. Explanation for the

detachment of the ridge is reasoned to be as a result of there being only a small part of the ridge base attached to the glass slide due to very high starting focal spot position. The starting height of the polymerising focal spot therefore chosen for the ultimate fabrication of the semi-circular ridges was $33.1\ um$ to ensure ridge fabricated was very stable.

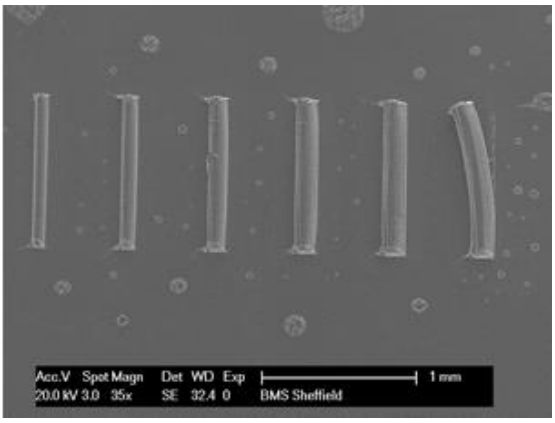

Figure 5.4 SEM images of fabricated semi-circular ridges of 1mm length, from left to right; starting height is increased by 10um.

5.3 PDMS PREPARATION AND STAMPING

5.3.1 PDMS PREPARATION

Patterning the semi-circular ridges design via TPP enables us to control the design dimensions with micron accuracy. However the directly structured ridges were unsuitable for direct experimentation for numerous reasons that polydimethylsiloxane (PDMS) replication addresses. The fragile hollow nature and the glass/polymer boundary of the fabricated structures made it unsuitable for direct use in the fluid flow experiment as they were easily washed off. Therefore a soft lithography approach for replication of the

surface ridges was adopted. A negative PDMS elastomer mould was created of the patterned surface of the microscope glass slide, and was subsequently used to reproduce the fabricated structure features via PDMS stamping for experimentation. To make the negative PDMS elastomer mould, Sylgard 184 silicone elastomer was mixed in a 1:10 weight ratio with the base silicone elastomer curing agent (Dow Corning, UK). The mixture was then degassed under vacuum in a desiccator to release trapped air caused by the mixing process, thus resulting in a clear viscous liquid. The glass microscope slide with the fabricated micro-semi-circular ridges (master slide) was placed in an aluminium rectangular-shaped box and the degassed silicone elastomer mixture was then poured over the master slide gently without introducing any air bubbles. In the case where air bubbles were introduced into the mixture whilst pouring the mixture onto the master slide, further degassing was done to remove the trapped air. The now aluminium box containing the master slide and the silicone elastomer mixture was heated to $60℃$ in an oven for at least 3 hours to cure and become solid. Figure **5.5** shows the silicone elastomer mould with in the negative imprint of the fabricated micro-structure semi-circular ridges on the master slide.

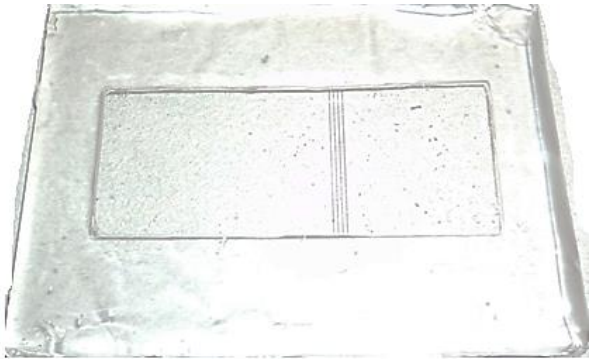

Figure 5.5 A negative imprint of master slide silicone mould used for the reproduction of test slides through PDMS stamping.

5.3.2 PDMS STAMPING

After curing of the silicone elastomer mixture into a mould, the mould was then carefully removed from the master slide to get an exact negative of the micro-structure features of the master slide onto the silicone mould. This silicone mould was used to re-create replicas of the master slide patterns via PDMS stamping. The simple technology and ease of use behind PDMS stamping makes it both a low cost and effective tool for reproducing the desired surface pattern. Also, PDMS stamping has been shown to reproduce surface features with high accuracy [362]. To create a PDMS stamp, a pre-polymer PEGda with molecular weight $250g/mol$ (Sigma Aldrich, UK) was mixed with a $2\,wt\%$ of photo-initiator 2-Hydroxy-2-methylpropiophenone (Sigma Aldrich, UK). The choice of PEGda $(250g/mol)$ use for the PDMS stamping process was because this polymer had low swelling rate which ensured firm attachment of the polymer when cured onto the glass substrate. Figure **5.6** shows the poor attachment of PDMS stamped PEGda $(700g/mol)$ as compared to that of PEGda $(250g/mol)$ after been submerged into a phosphate buffered saline (PBS) solution for 24 hours. Also, for cell culture experimentation purposes, it has been reported that PEGda with lower molecular weight helped promote better cell adhesion as compared to PEGda with higher molecular weight [363]. So, few drops of the PEGda $(250g/mol)$ mixture with the photo-initiator were placed on the silicone mould and then a functionalised glass slide was placed into the negative imprint of the mould. During this process, it was ensured that there was no air interface between the polymer mixture and the glass slide and that there was a uniform coverage of the PEGda mixture over the entire surface of the glass slide. The silicone mould with the glass slide was then placed under an ultra-violet light with the intensity of the light gradually increased from 1% to 100% to cure the PEGda polymer mixture. To facilitate easy removal of the

PDMS stamped glass slide and also ensure that the silicone elastomer mould was hydrophobic to the polymer mixture, the mould was pre-treated with $\mathrm{tridecafluoro-1H,1H,2H,2H-tetrahydooctyl\ trichlorosilane,97\%}$ (Sigma Aldrich, UK) which is a silanizing agent before being used for PDMS stamping. Replication of the fabricated micro-structure semi-circular ridges via this technique improved the structural strength of the micro-structures due to the bulk curing process during PDMS stamping. Thus the PDMS stamped glass slides were more suitable to use for fluidic flow experimentations. Figure **5.7** shows the PDMS stamped microscope glass slide with the micro-structure semi-circular ridge features.

a)  b) 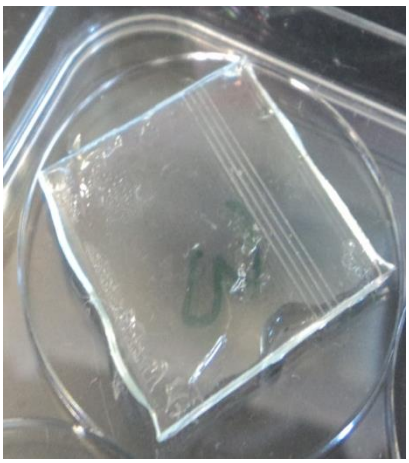

Figure 5.6 PDMS stamped glass slides with different molecular weight PEGda: 700 g/mol (A) and 250 g/mol (B) respectively after 24 hours submersion in PBS

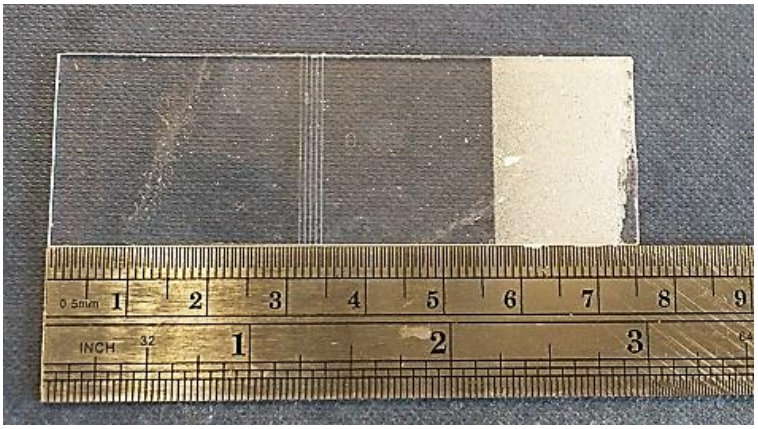

Figure 5.7 PDMS stamped microscope glass slide for flow experiment

5.4 CALIBRATION OF THE SEMI-CIRCULAR RIDGES FABRICATED VIA TPP AND PDMS STAMPING

To confirm that the micro-structure semi-circular ridges fabricated via the TPP technique met the design parameter requirements, SEM images were taken of the micro-structures as shown in figure **5.8**. To prepare the sample for SEM imaging, the sample was first mounted on a stud using a carbon adhesive and gold coated using a gold sputter coater (Edwards S150b, Crawley, UK). Gold coating of the sample helped to prevent charge build-up at areas of the sample which were non-conductive. SEM images of the sample were then generated using Philips XL-20 SEM (Philips, Eindhoven, Netherlands). The surface profile of the ridge was also determined using a profilometer (Dektak Profilometer, Veeco, USA) with a stylus force of $3\,mg$, a scan resolution of $0.056\,um/sample$ and a scan speed of $10\,um/s$. Figure **5.9** shows the surface profile of a fabricated ridge compared that of a semi-circle shape calculated analytically. Using equation **4.8**, the deviation between the target shape of the ridge and that produced via TPP was measured and this measure of error is shown in table **5.1**.

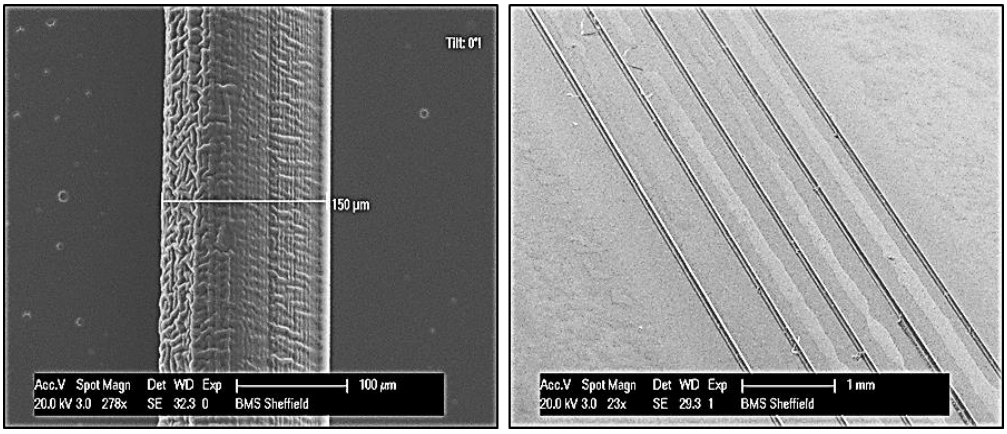

Figure 5.8 SEM images of fabricated ridges via TPP. Left: A close-up of one of the ridges. Right: All 5 semi-circular ridges on the glass slide.

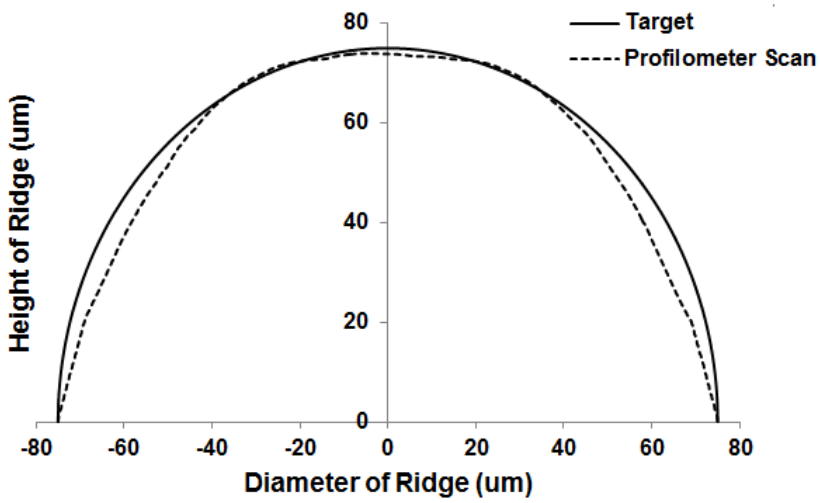

Figure 5.9 Profilometer scan of the surface of the semi-circular ridge fabricated via TPP compared to target semi-circle perimeter.

Table 5.1 Error between measured and target surface perimeter

Surface Perimeter	MSE
Semi-Circular Ridge	0.085

The agreement between the target shape of the ridge to that fabricated via TPP is shown to be relatively good as $MSE < 0.1$. However, it is presumed that the initial method employed to fabricate the ridges as discussed in section **5.2.2** could have produced better semi-circular ridge shape but this method was not very time efficient. A probable solution to this problem could be in the use of synchronised multiple focal points to fabricate many structures at a time; thus cut down the time spent on fabricating the structures but this method has not been established.

A surface scan across the entire length of the PDMS stamped semi-circular ridges was also performed using the profilometer to determine how each ridge height varied from the other. As shown in figure **5.10**, each ridge height was in between $\pm 1.5um$ of the desired height which is $75um$. It therefore could be concluded that the above discussed processes used to develop the desired structure of five independent semi-circular ridges on a microscope glass slide has been achievable with relatively minor deviations from the target structural design.

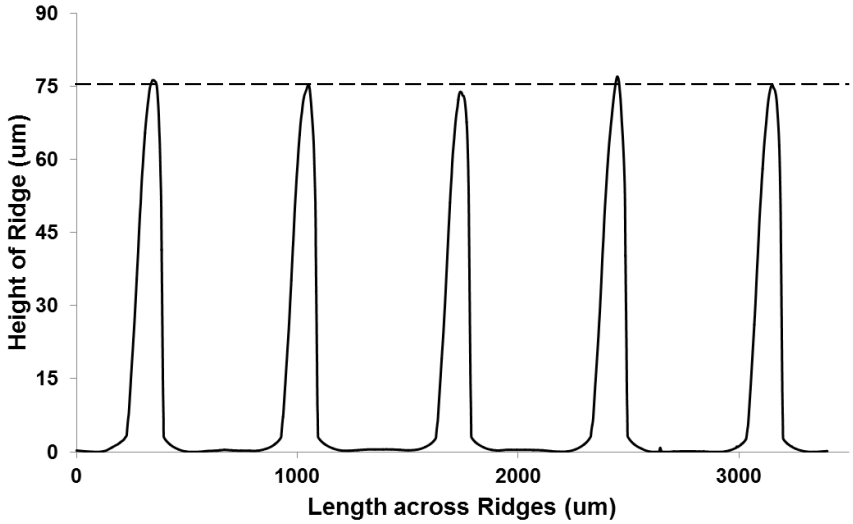

Figure 5.10 Profilometer scan of the surface of five semi-circular ridges spaced 550um apart.

5.5 RIDGE SHEATH FABRICATION

As stated in the introduction section, ECs may become denuded during the process of stent implantation. Hence at the immediate regions of the stent strut and on the stent strut, there might not be the presence of healthy ECs. To mimic this in vivo condition in the cell-structure interaction experimental model, a thin ridge sheath was fabricated. This thin sheath is used to cover the ridges before cell seeding and thus prevented cells from being seeded onto the ridges before subjecting the cells to the flow experiment.

The ridge sheath was fabricated using photo-stereo lithography in a direct laser write method. The fabrication process involved a passively Q-switched DPSS microchip laser (Pulselas P-355-300, Alphalas, Gottingen, Germany) with a wavelength $532nm$ to emit a laser beam. An ultra-violet light was then isolated from the laser beam emitted using a Pellin Broca Prism (ADB-10, Thorlabs, Germany). This ultra-violet light was expanded using a Galilean beam expander to around $8nm$ before being reflected via a silver coated mirror into a x10 objective lens (Carl Zeiss, EC Plan-Neofluar 10x, Numerical Aperture 0.3) to initiate polymerisation of a liquid polymer resin. The exposure of the laser beam emitted was controlled automatically by a mechanical shutter (LS6ZM Uniblitz Electronics). The polymer resin sample was held to a motorised xyz- stage which was controlled by two types of computer-based software which worked concurrently; thus Aerotech ANT130XY and PRO115 software that controlled the xy- translation and z-translation of the stage respectively.

The polymer resin used for the sheath fabrication process was PEGda $(700\ g/mol)$ mixed with a $4wt\%$ 2-Hydroxy-2-methylpropiophenone photo-initiator. A well of this polymer-based resin was created on a non-functionalised microscope glass slide to allow easy detachment of the

fabricated sheath from the glass slide. The glass slide sample was then affixed to the stage and was translated relative to the focal point of the objective lens via the xyz- stage to begin the fabrication of the ridge sheath process. Figure **5.11** shows the fabricated ridge sheath of $1mm$ thickness.

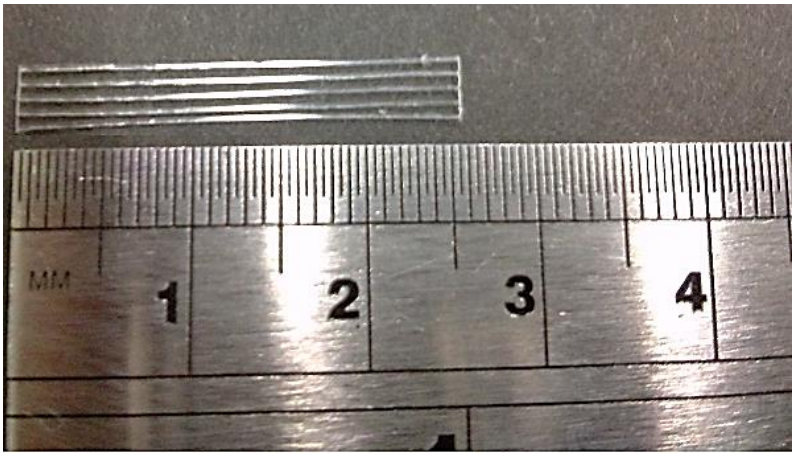

Figure 5.11 A 1mm thick ridge sheath

5.6 ASSEMBLY OF CELL-STRUCTURE INTERACTION MODEL

Assembling the cell-structure interaction model involved mounting the test glass slide with fabricated microstructure semi-circular ridges into a parallel plate flow chamber. The parallel flow chamber is formed of three main parts; namely, a top plate, bottom plate and a silicon gasket as illustrated in figure **5.12**. The plates were machined in-house. The model was assembled by first carefully placing the PDMS stamped microscope glass slide with seeded ECs into the groove on the bottom plate. The silicone gasket was then placed to fit the perimeter of the groove and finally the top plate was placed on top of the bottom plate. The two plates were held tightly together by machine screws. One end of a 2 way, 1/8 NPT – barbed connectors (Cole-Parmer, UK) was screwed into both ports of the top plate and the other end

connected to the rest of the flow circuit system. Figure **5.13** shows the complete experimental set-up of parallel plate flow chamber connected to the flow circuit system and placed inside an incubator.

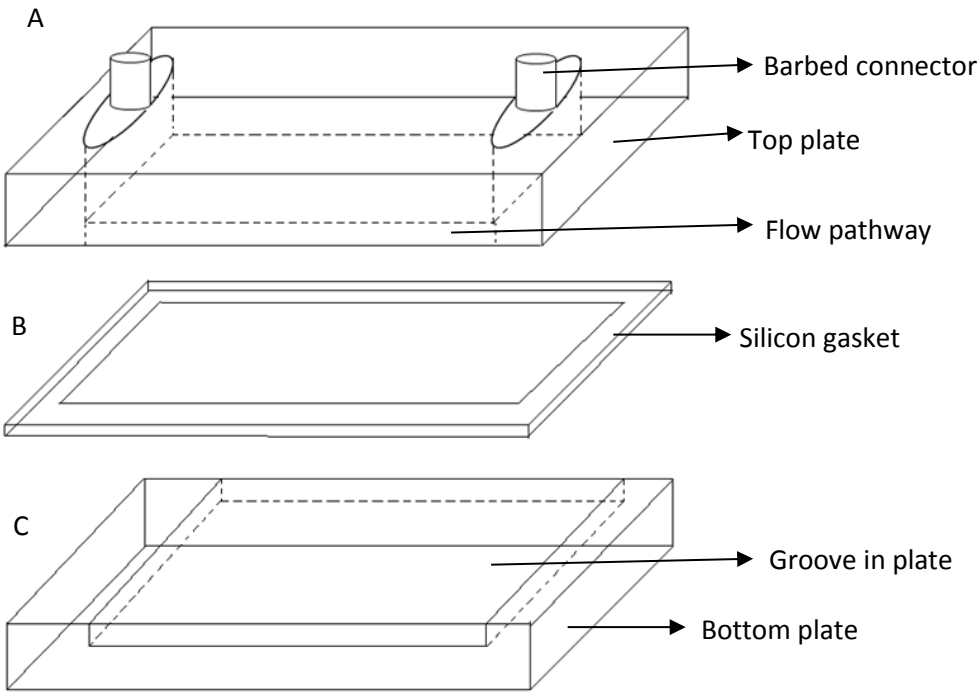

Figure 5.12. A schematic diagram of a parallel plate flow chamber for housing the PDMS stamped test glass slide.

Barbed connectors are attached to the top plate (A) to allow fluid flow to and out of the flow chamber. The dashed lines displayed on the top plate show the flow domain of the parallel plate flow chamber. The test glass slide sits within the groove of the bottom plate (B). The silicon gasket is sandwiched between the two plates to prevent fluid from leaking out of the flow domain.

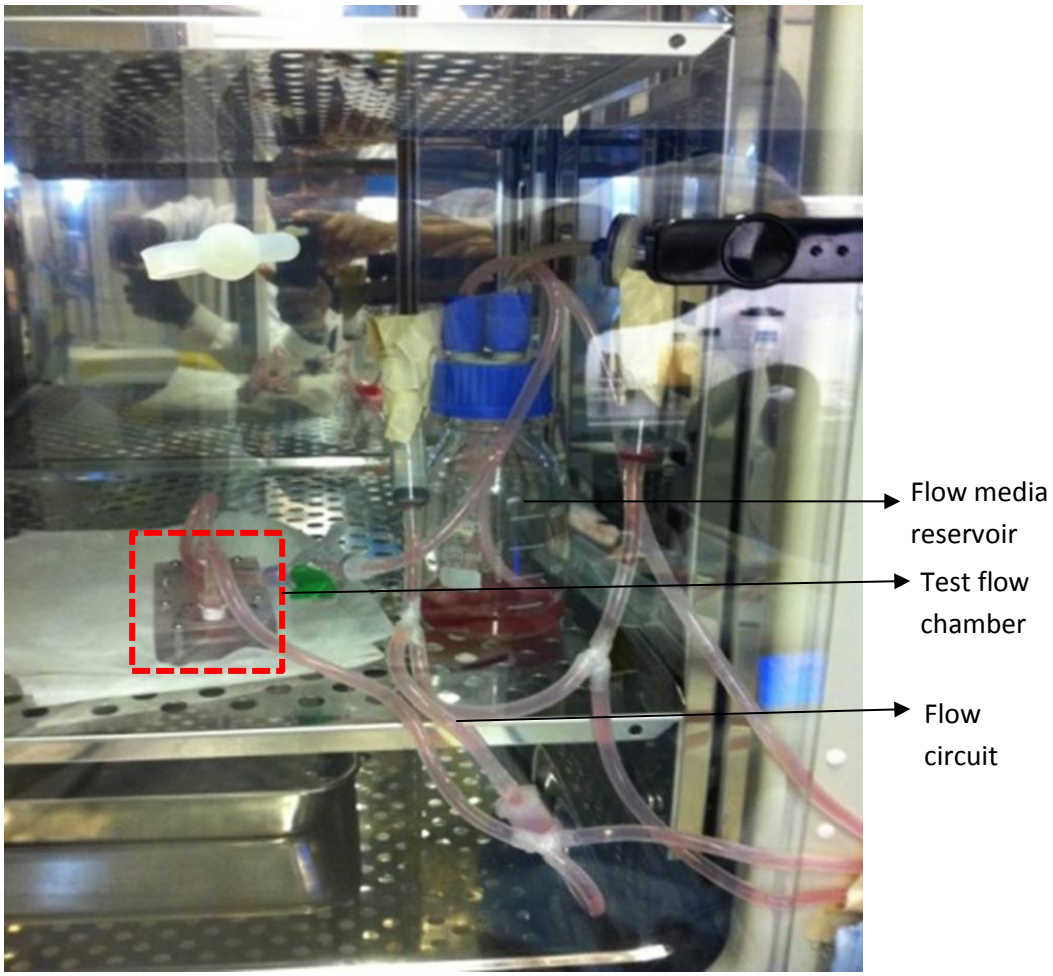

Figure 5.13 A complete set-up of test flow chamber and flow circuit system.

The assembled parallel plate flow chamber encasing the test glass slide (test flow chamber) is represented within the red dashed line square. The test chamber is placed within an incubator of $37℃, 5\% \, CO_2$ and also connected to the flow circuit system.

5.7 SUMMARY

In summary, a cell-structure interaction model was designed so that in combination to the flow circuit discussed in Chapter **4**, cultured ECs on the

modified microscope glass slide could in respect to cell position on the modified glass slide experience different magnitude of WSSs, SWSSGs and OSIs concomitantly. The model consisted of three main parts:

- A parallel plate flow chamber. This flow chamber is made of two plates; thus a bottom flat plate with a groove which houses the ECs cultured on the modified microscope glass slide and a top flat plate with inlet and outlet ports. The top and bottom plate produces a gap of a known height when put together and thereby allows fluid flow through the flow chamber
- A modified microscope glass slide. This is a PDMS stamped microscope glass slide with semi-circular micro-structure ridges. ECs are seeded on this glass slide.
- A silicone gasket. The gasket is fitted in between the two plates to ensure fluid does not leak out of the parallel plat flow chamber.

Application of TPP technique enabled for the fabrication of desired micro-structures on the glass slide and PDMS stamping enabled for a quick and easy replication of the fabricated structures on the master microscope glass slide onto other glass slides. Calibrations of the semi-circular ridge structures fabricated were observed to have deviated slightly from the desired structure dimensions but were within an acceptable range of error margin. Thus CFD analysis of the ideal cell-structure interaction model could be applicable to the cell-structure interaction model fabricated within accepted error margin.

CHAPTER 6

COMPUTATIONAL FLUID DYNAMICS (II)

In this chapter, the mechanical forces present within the cell-structure experimental model described in chapter **5** is investigated and quantified. To investigate these mechanical forces, the fluid flow domain of the cell-structure model is simulated using CFD.

6.1 CFD ANALYSIS

As discussed in chapter **3**, CFD analysis based on FVM method has been proved to enable numerical solving of complex fluid flow dynamics with high accuracy. So, flow simulations within the cell-structure interaction model were performed using FVM built in ANSYS Fluent 13 software (Ansys inc., Canonsburg, PA, USA). The fluid domain of the cell-structure interaction model in which simulations were performed is illustrated in figure **6**.

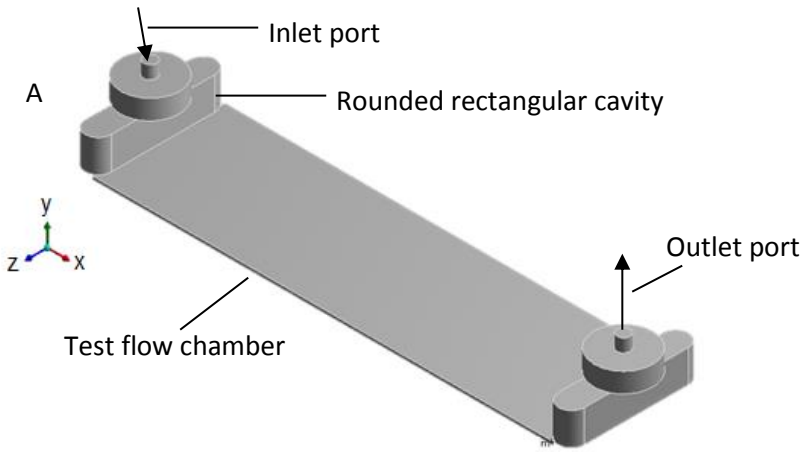

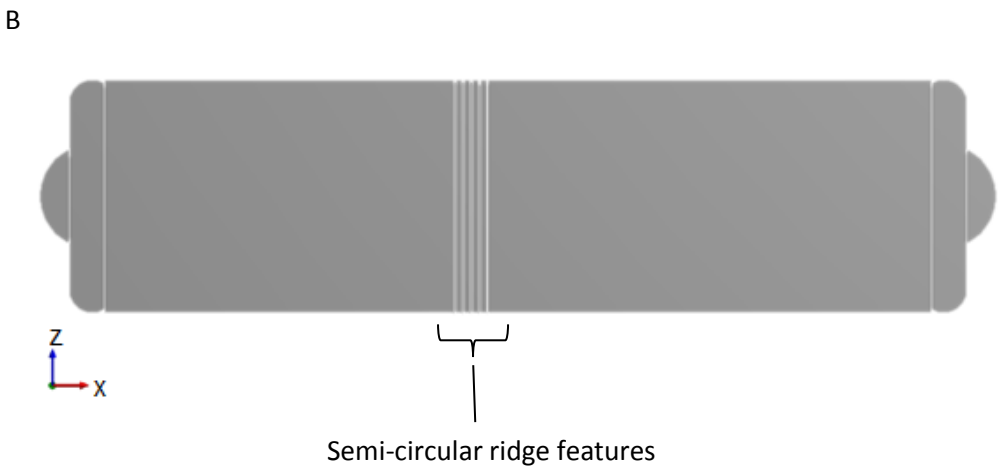

Figure 6. Geometry in which simulations were performed (Not to scale). The isometric view (A) of the modelled geometry shows the inlet and outlet flow positions and the test flow chamber where flow dynamics are subjected onto cells. The bottom view (B) shows the position of the fabricated semi-circular ridges within the test flow chamber. The semi-circular ridges are placed sufficiently far away from the inlet so that flow is developed before influenced by the presence of the ridges.

Fluid flow is simulated to pass through the inlet port of diameter 3 mm, then through a rounded rectangular cavity of length 17 mm, semi-circular width of 4mm diameter and height of 6 mm. The fluid then passes through the test flow chamber of length 71 mm, width of 20 mm and height of 0.48 mm then finally through the outlet port of same inlet port dimensions. The height of the test flow chamber was chosen to be 0.48 mm so as to achieve instantaneous WSS of 2 Pa within the flow chamber at a flow rate of 144 ml/min. This calculation is based on equation 4.5.

The fluid properties used for the CFD simulations were based of on the cell culture media which would be used during the experimental stage of investigation ECs response to complex flow dynamics. Thus the density of the flow used is $1005\ kg/m^3$ at a viscosity of $0.64\ mPa.s$. As cell culture media is suggested to be Newtonian [364], the flow was simulated to

behave as a Newtonian fluid. Using Newtonian fluid as a representation of blood flow characteristics for this model is deemed adequate. Reason for this suggestion was highlighted in chapter **3** as Newtonian fluid was showed to capture the non-Newtonian blood characteristic based on Carreau model within a straight stented artery.

Flow boundary conditions were imposed at the inlet and outlet boundary and a no slip condition set at the walls of the model. A UDF script was written to apply pulsatile LAD inlet velocity flow waveform at the inlet boundary. This flow waveform used is derived by Marcus et al. [58]. This written UDF defines the time evolution of the velocity distribution at the inlet boundary, assuming velocity profile to be parabolic and matching the volume flow rate to that described of the target LAD flow waveform shown in figure **4.9**. At the outlet boundary, a zero normal velocity derivative was specified.

Meshing of the model was done using the same CutCell algorithm used in section **3** to discretise the spatial flow domain of the cell-structure interaction model into many hexahedral cells as illustrated in figure **6.1**. To ensure CFD results were independent of the mesh density, mesh refinement studies of the model were carried by performing steady flow simulations on different mesh densities as shown in figures **6.2a** and **6.2b**. Although steady flow was simulated, it was expected that there may be some time dependent features due to the flow dynamics across the semi-circular ridge structures in the model. Therefore the flow was modelled as an unsteady flow with time steps lasting 0.005s. To ensure that a steady state solution had been reached, sufficient time steps were calculated. The WSSs recorded at the inlet of the model with the spatial flow domain discretised into 612,097 and 865,281 hexahedral cells were $1.97\,Pa$ and $1.98\,Pa$ respectively. The percentage WSS error calculated between these two mesh densities was found to be $< 1\%$ with insignificant changes to the WSS upon further mesh refinements.

This therefore demonstrated that mesh independence of CFD result was established at mesh density of 612,097 cells. Finer meshes at regions nearer to the semi-circular ridges were also ensured to enable detailed flow dynamics and WSS to be captured. Simulation settings of the flow were similar to those used in section **3**, with SIMPLE algorithm used for pressure-velocity coupling. A second order scheme was used to discretise both the pressure and momentum which ensured a numerically second order higher accuracy. The computational cost in performing flow simulation with different mesh densities is tabulated in table **6.1**.

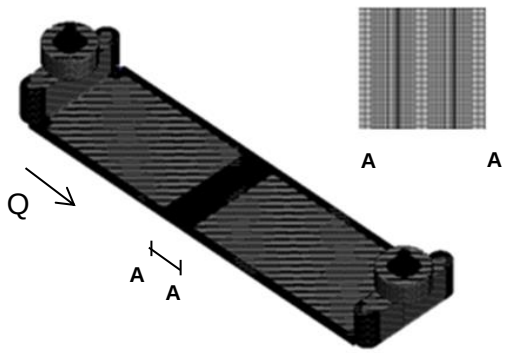

Figure 6.1 Meshed flow domain of cell-structure experimental model. A – A shows the meshed region of the semi-circular ridges

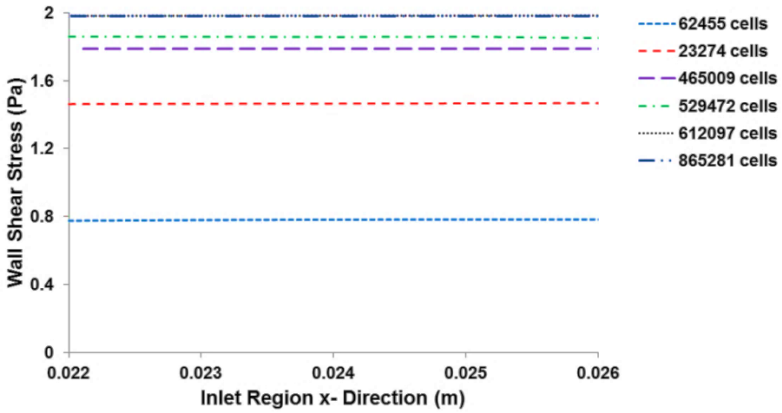

Figure 6.2a WSSs at inlet region of cell-structure model for different mesh densities. Mesh convergence is assumed at mesh density of 612097 cells.

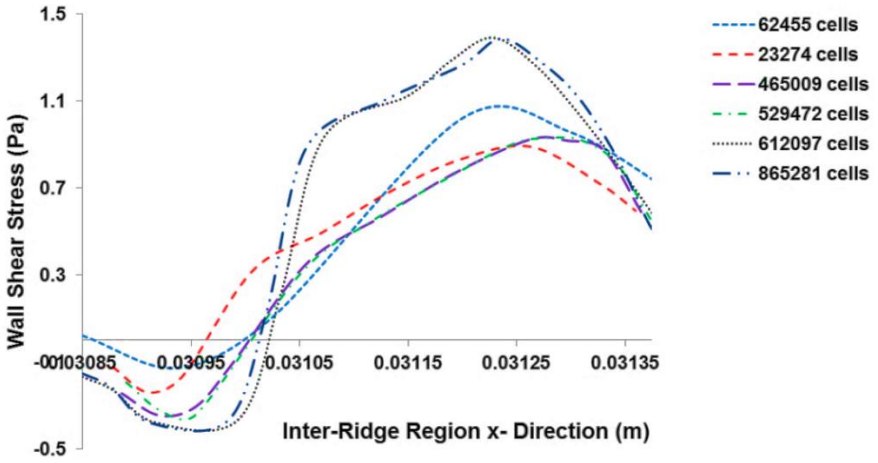

Figure 6.2b WSSs at inter-ridge region of cell-structure interaction experimental model for different mesh densities. Mesh convergence is assumed at mesh density of 612097 hexagonal cells.

The correlation between increase in mesh density and increase WSS magnitude is evident from the mesh refinement studies study although further mesh refinements resulted in insignificant WSS changes. Based on this evidence it is reasoned that the true WSS subjected on ECs is slightly higher than that of CFD analysis predictions.

Table 6.1 Computational costs for different mesh densities

Mesh Density	Computational Cost		
	Hours	Minutes	Seconds
62455	0	10	0
23274	3	5	30
465009	5	25	27
529472	9	53	42
612097	13	59	22
865281	15	9	40

Simulations of each LAD pulse cycle was discretised into 300 time steps of 0.005s time step size. Three LAD pulsatile waveform cycles were performed with results from at least the second cycle used for analysis. This was done so as to eliminate analysing data which might have been influenced by simulation start-up effects. The simulation at each time step was deemed to have reached convergence when the normalised scaled continuity residuals and the velocity components had all fallen to below 10^{-5} or after 200 iterations. This reasoning was ascertained through the examination of the WSS convergence history at different regions of the flow model which showed that this condition was adequate enough to produce data which had insignificant WSS changes upon further iterations.

6.2 RESULTS

The cell-structure interaction model was designed to apply combined mechanical stimuli such as WSS, SWSSG and OSI to seeded cells. Analysis of these mechanical stresses distributions within the model are discussed below.

6.2.1 WALL SHEAR STRESS DISTRIBUTION ANALYSIS

Figure **6.3a** shows a contour plot of the WSS distribution on the entire cultured cell surface area of the model and figure **6.3b** shows the WSS distribution specifically at the region with the semi-circular ridges under steady flow simulations to produce a steady shear stress of $2\,Pa$. The contour plot of the entire cell culture surface area shows relative spatially uniform WSS distribution at regions away from that where the semi-circular

ridges are present. Regions with the semi-circular ridges are however observed to have a wide varied range of WSS distribution. WSSs at this region tend to follow a complex pattern of alternating peaks and troughs with the top of the ridges experiencing very high WSSs and the very immediate end base of the ridges experiencing very low WSSs. This WSS distribution phenomenon is similar to that observed within the helical stented artery discussed in section **3** and also from literature [30].

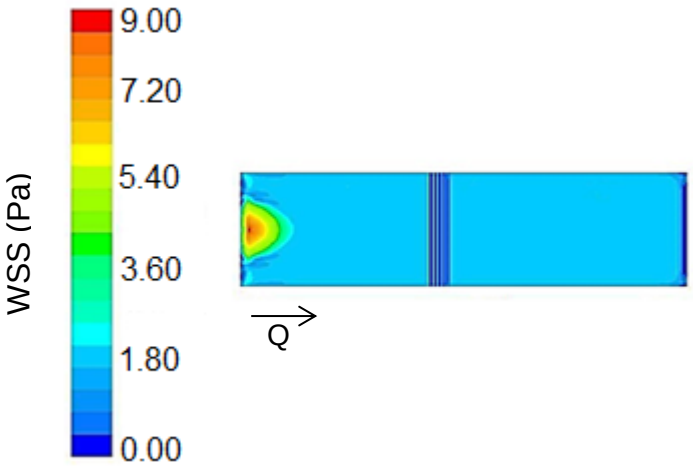

Figure 6.3a Contour plot of WSS distribution (Pa) on cell culture surface area under steady flow simulations. Flow is from left to right. Uniform WSS of magnitude ~ 2 Pa is observed at regions far away from the inlet and also at the outlet.

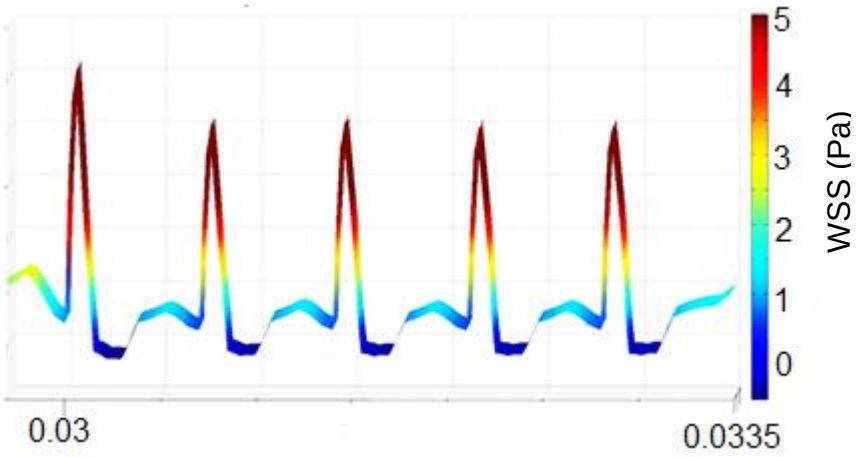

Figure 6.3b Contour plot of WSS distribution (Pa) at region with semi-circular ridges under steady flow simulations. Flow is from left to right. The plot shows WSS is highest (~ 5 Pa) at the top of the ridges and at the immediate peri-ridges the lowest WSSs (~ 0 Pa) were recorded.

A 2mm distance from the immediate side walls of the inlet, outlet and length sides of the cell culture surface area were negated in the WSS distribution analysis. Data at these regions where considered to have been strongly influenced by the entrance, exit and side wall effects of the flow chamber.

Pulsatile flow simulation of the LAD waveform at mean WSS of $2\,Pa$ over the cell cultured surface was also computed. Figures **6.4a** – **6.4f** show the WSS distributions of the entire cell culture surface area and regions with the semi-circular ridges at different time points of the LAD waveform. It was noted that WSS distributions on the entire cell culture surface area at different time points of the LAD waveform where similar to that observed under steady flow simulations although WSS magnitudes recorded were different for each time point.

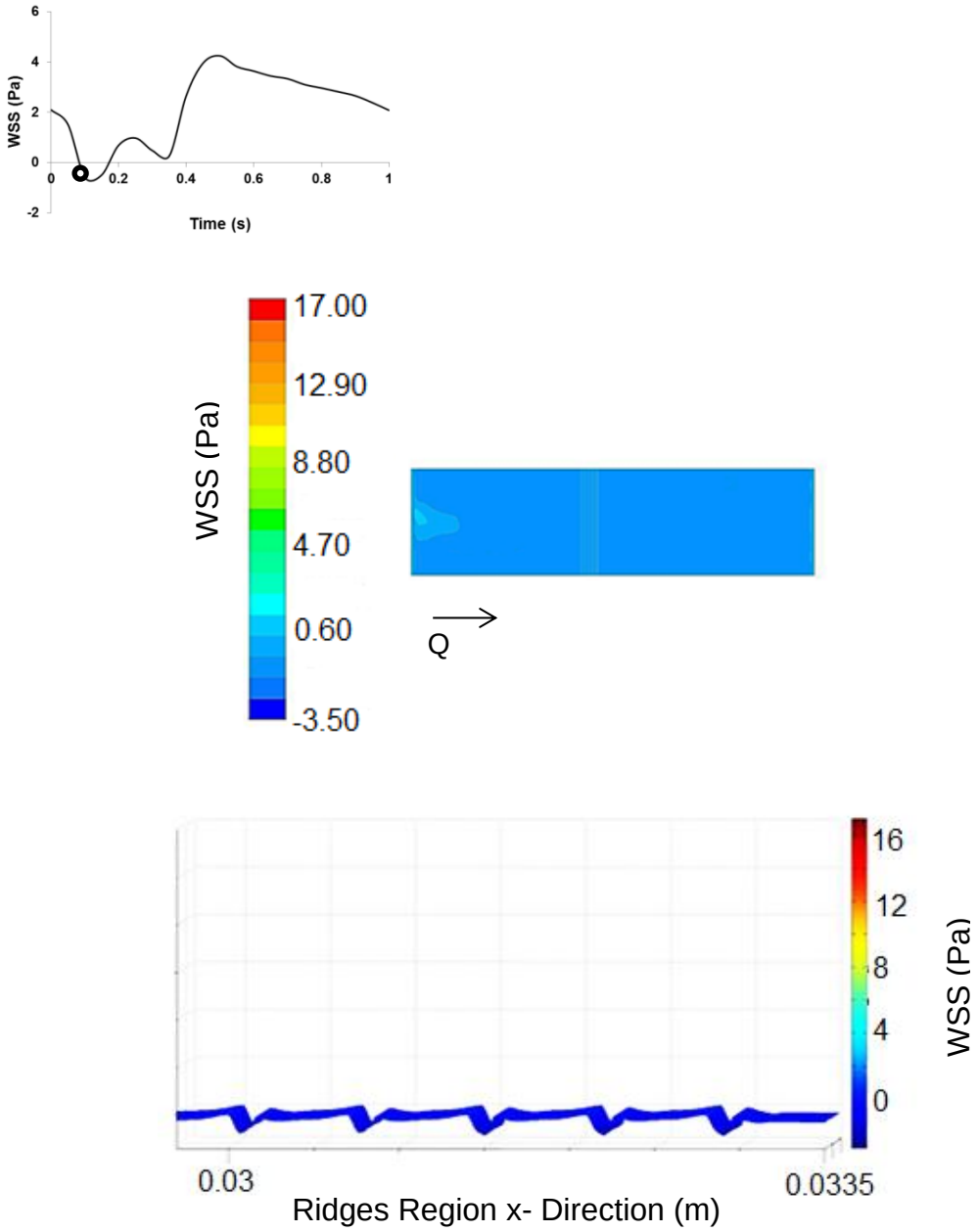

Figure 6.4a Contour plot of WSS distribution at 0.1s in the LAD waveform on entire cell culture surface area (Top) and at region with semi-circular ridges of cell-structure interaction model. Flow is from left to right. WSS magnitudes across the cell culture surface area are noted to be generally very low. This observation is as a result of very low volume flow rate at that instantaneous time.

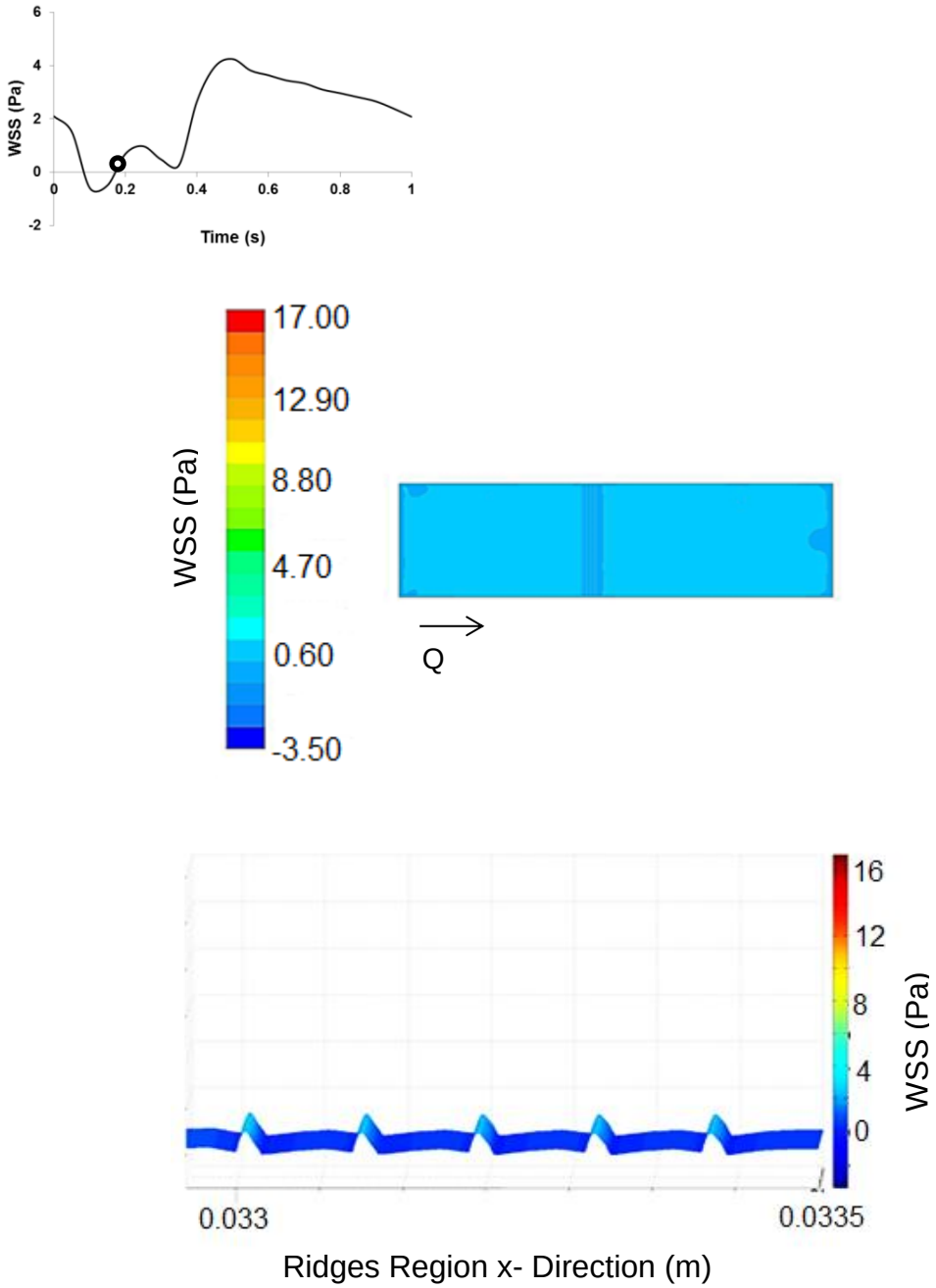

Figure 6.4b Contour plot of WSS distribution at t = 0.2s in the LAD waveform on entire cell culture surface area (Top) and at region with semi-circular ridges of cell-structure interaction model. Flow is from left to right. WSS magnitude across the culture surface area is noted to be low, however WSS on the top of the ridges are observed to be relatively high (~ 3 Pa).

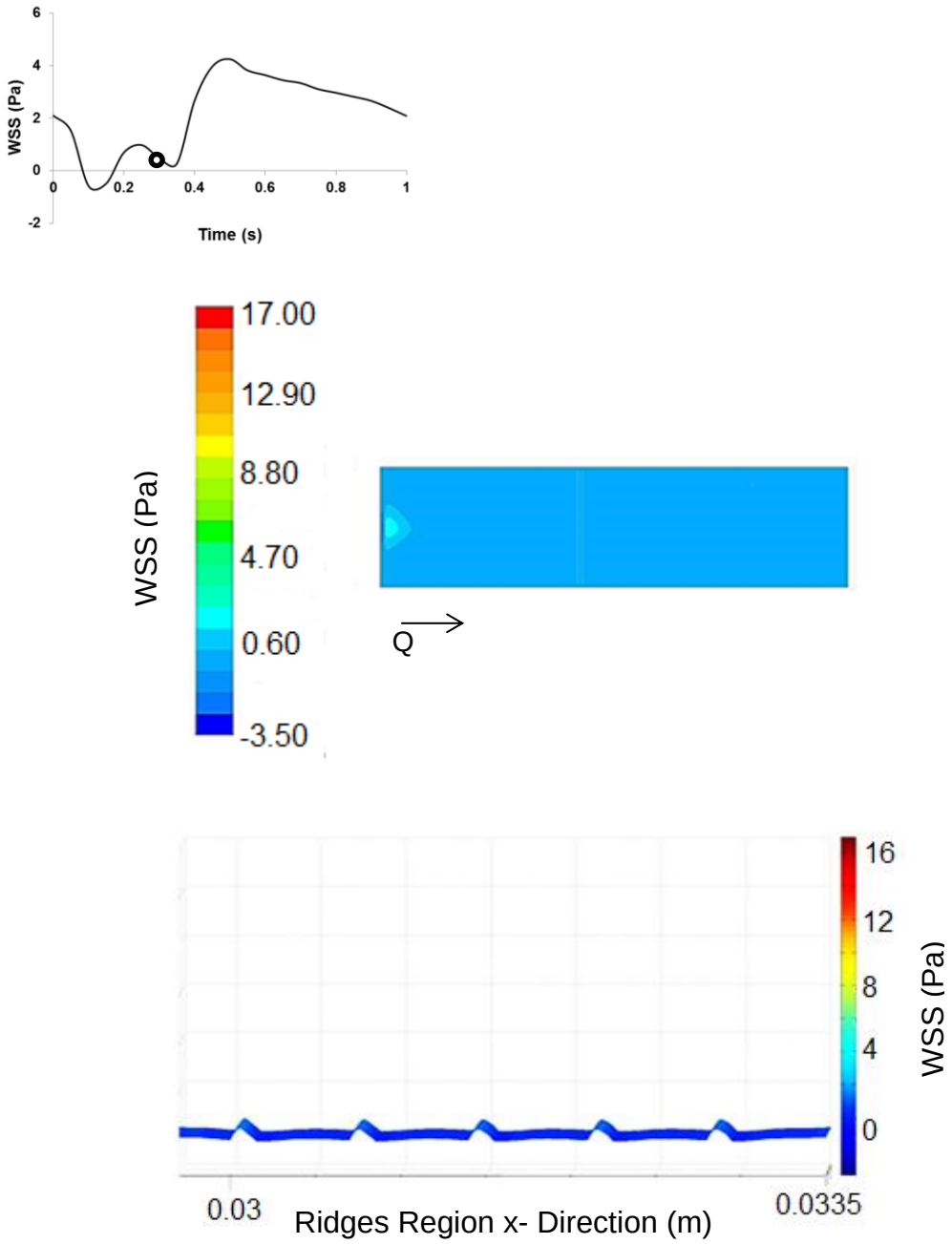

Figure 6.4c Contour plot of WSS distribution at t = 0.3s in the LAD waveform on entire cell culture surface area (Top) and at region with semi-circular ridges of cell-structure interaction model. Flow is from left to right. WSS magnitudes across the culture surface area are noted to be low. This is as a result of low flowrate at this waveform phase.

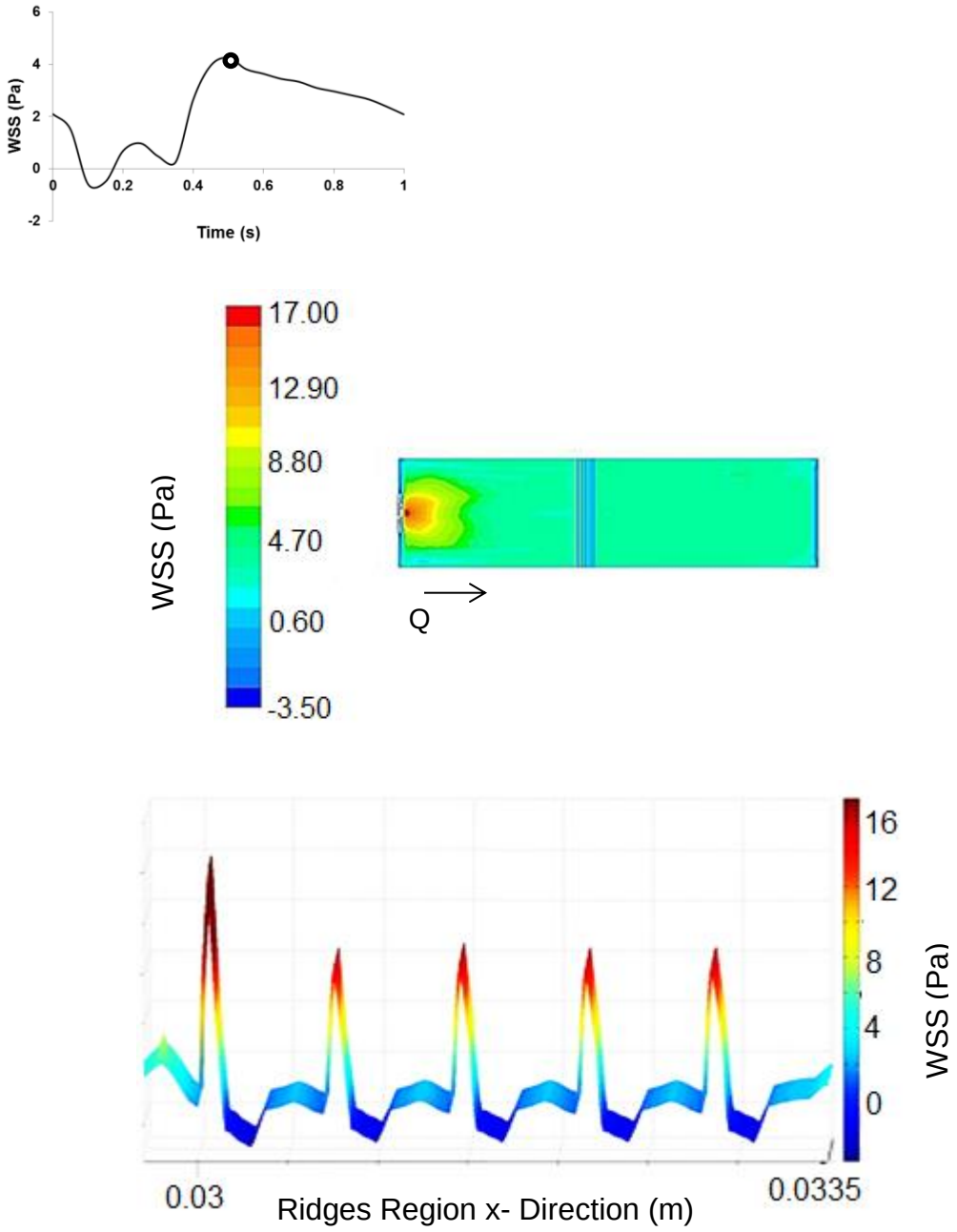

Figure 6.4d Contour plot of WSS distribution at t = 0.5s in the LAD waveform on entire cell culture surface area (Top) and at region with semi-circular ridges (Bottom). Flow is from left to right. Flow rate at this phase is highest hence high WSS magnitudes across culture surface area (~5 Pa). High WSSs (> 15 Pa) were recorded at the top of the ridges whilst WSSs at the peri-ridge regions ranged between 0 Pa to 3 Pa.

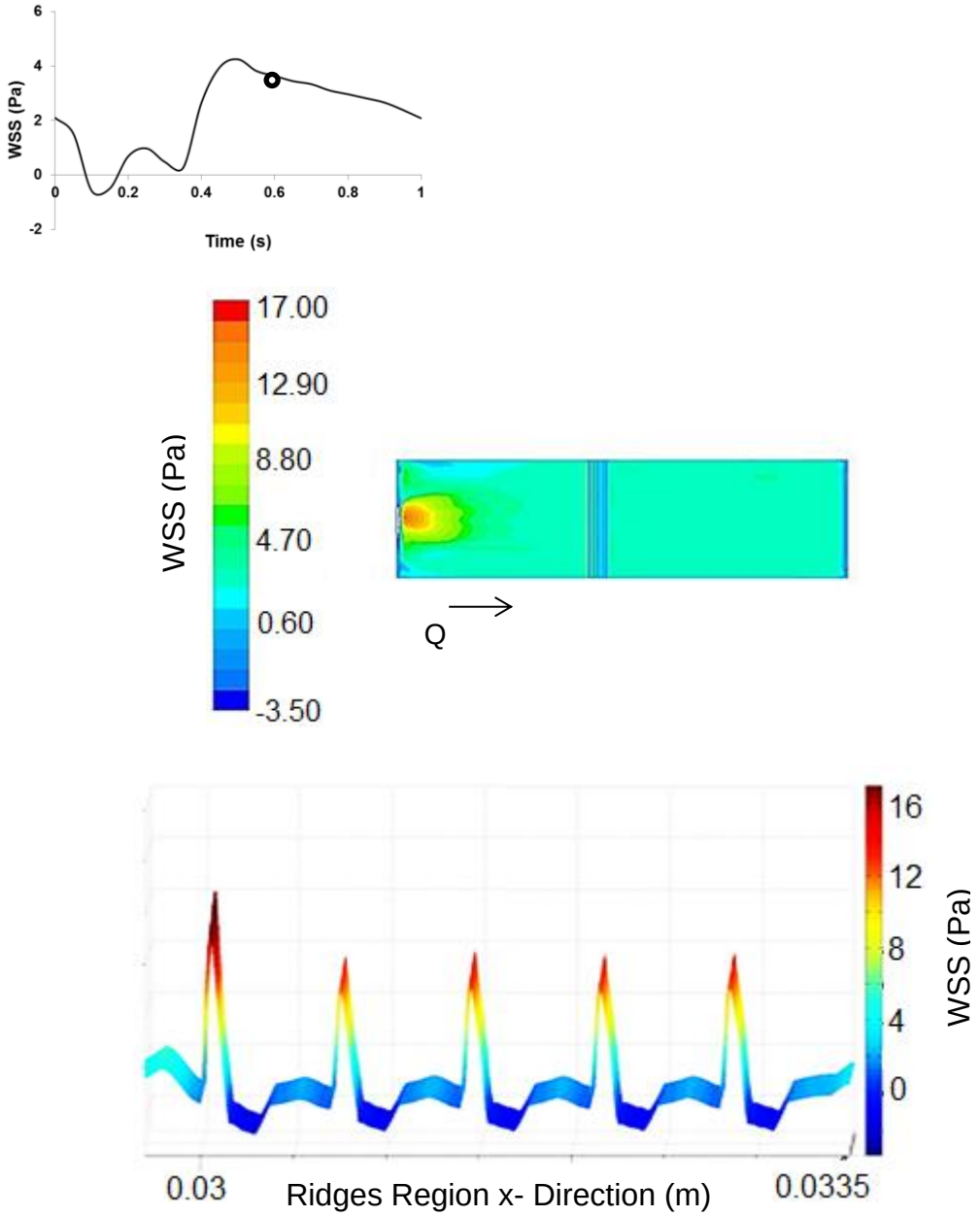

Figure 6.4e Contour plot of WSS distribution at 0.6s in the LAD waveform on entire cell culture surface area (Top) and at region with semi-circular ridges (Bottom). Flow is from left to right. In this figure as well as in figure 6.4d, WSS spikes are observed on the ridges whilst lowest WSSs are observed at immediate regions adjacent to the ridges. The WSS tend to increase with distance from the ridges and at its highest in the region furthest away from the ridge, with exception of the WSS on the ridges themselves.

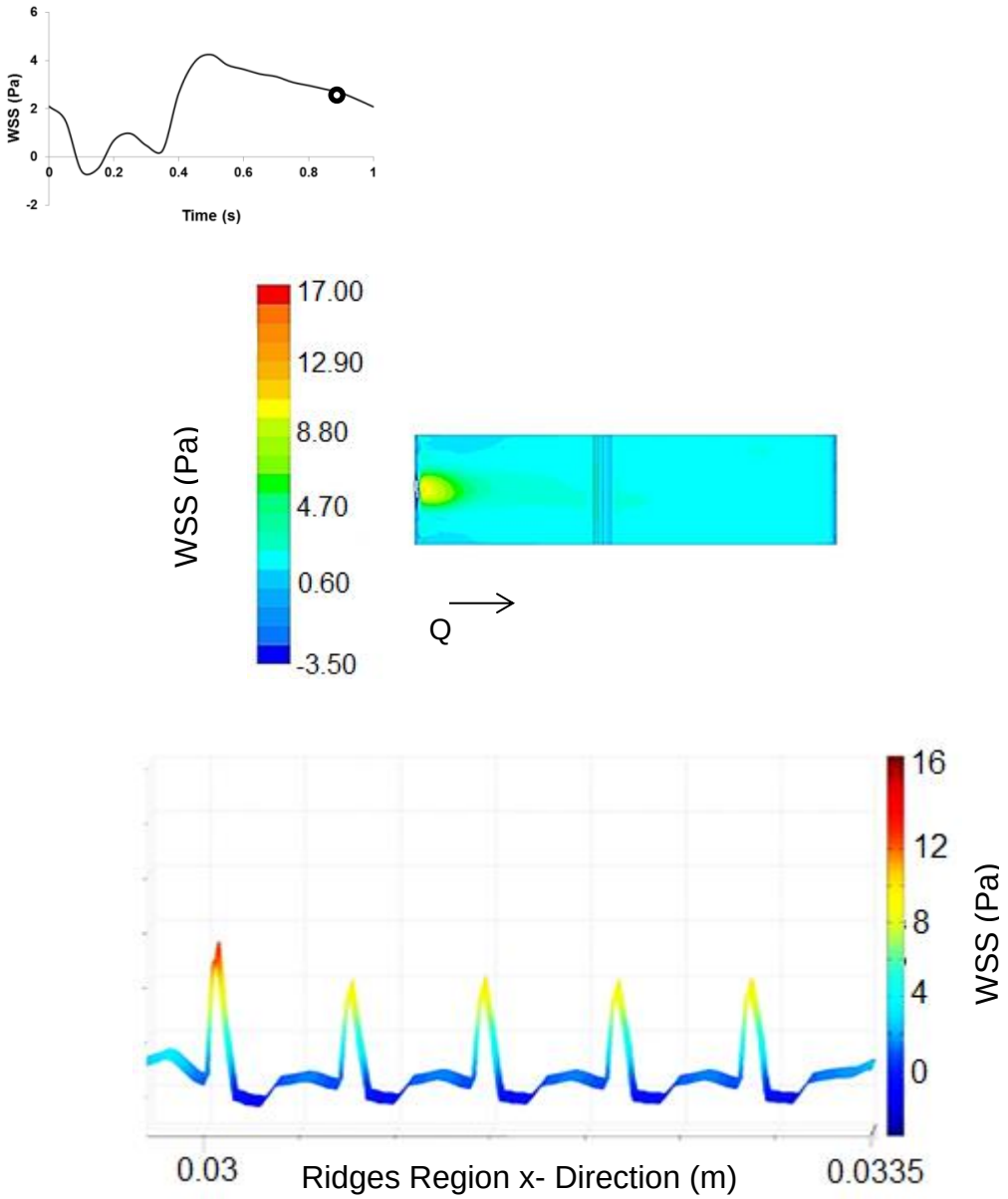

Figure 6.4f Contour plot of WSS distribution at t = 0.9s in the LAD waveform on entire cell culture surface area (Top) and at region with semi-circular ridges (Bottom). Flow is from left to right. WSSs experienced across the cell culture surface show similar WSS distribution trends as illustrated in figures 6.4d and 6.4e however with relatively lower WSS magnitudes. This occurrence is as a result of lower flowrate at this phase compared to that of t = 0.5s and t = 0.6s.

One of the main objectives of this project is to be able to map the mechanical stresses within the cell-structure interaction model to cells response. Thus CFD simulations serve as a tool to quantify these stresses and also help make decisions earlier in the experimental set up stages in relation to achieving desired results.

As discussed in chapter **4**, there have been many studies which have utilised parallel plate flow chamber in the investigation of WSS on ECs. Mostly in these studies, WSSs within parallel plate flow chambers have been calculated analytically using the formula given in equation **6.1** to obtain WSS from flow rate.

$$\tau_w = \frac{6\mu Q}{bh^2} \qquad 6.1$$

where τ_w is the instantaneous WSS, Q is the flow rate, μ is viscosity of flow medium and b and h are the width and height of the flow chamber respectively.

The use of this formula therefore obviates the need for CFD modelling. However this approach is only valid based on the assumptions that flow is fully developed spatially and temporal, laminar, Newtonian, two dimensional flow domain and no effect of side wall of the flow chamber on flow.

Being that the culture fluid used for the CFD simulation is Newtonian, as discussed earlier in this chapter, one of the above assumptions is satisfied. The assumption that flow domain is two dimensional is however clearly not satisfied in regions close to the flow chamber side walls. Nonetheless it has been suggested that as long as the width to height ratio of the parallel flow chamber is greater than 10:1, then this two-dimensional flow can be assumed [365]. The calculated width to height ratio of the modelled test flow chamber is approximately 42:1 and thus assumption that flow in the modelled test chamber is two-dimensional can be made.

From the CFD steady flow simulation presented in figure **6.3a**, uniform WSS magnitude at inlet and outlet region of flow domain was approximately 2 Pa. Hence using the flow and flow chamber parameters already stated in section **6.1**, and substituting those into equation **6.1**, one can calculate flow rate, ($Q = 2.4\ x\ 10^{-6}\ m^3/s$) needed to get a WSS of 2 Pa. This flow rate would result to an average flow velocity of $0.25\ m/s$. The Reynolds number, *Re,* of the flow can be calculated using the formula below:

$$Re = \frac{\rho \mu l}{\mu} \qquad 6.2$$

Substituting the average velocity, μ and taking h as the characteristic length scale, the Reynolds number of the fluid is 188.43. This flow is therefore classified as laminar as *Re* < 1000 [292]. Hence the assumption of laminar flow in the flow chamber is satisfied.

To justify that flow is developed spatially and temporally, it is reasoned that start up effects quickly dissipate under steady flow, hence flow is developed in time after few seconds of an experiment. To ascertain if flow becomes spatially developed in the flow chamber, the entrance length, Le is defined. Using the formula for calculating the entrance length for laminar flows between two parallel plates by Schlichting et al. [366] as shown below:

$$Le = 0.01h.Re \qquad 6.3$$

The entrance length in this flow chamber when the WSS is 2 Pa is therefore 0.90 mm, which is a negligible proportion of the entire chamber length ($\approx 70\ mm$). Flow is therefore assumed to be spatially developed after 0.90mm of the flow chamber entrance. This assumption is justified in figure **6.3a** as WSSs of the flow domain under steady flow simulation is observed to be relatively uniform after few distance from the entrance of the flow chamber. It should be noted nonetheless that although analytical methods

were used to predict approximately the WSS applied to cells within the test flow chamber, this method and assumptions made may not entirely be applicable for our custom designed flow chamber. This is because the assumption that led to the basis of equation **6.1** is thought to be more applicable for flow within a uniform space and non-disrupted flow. Therefore, since our custom designed flow chamber is not entirely of a uniform space and flow is slightly disrupted within some regions of the flow chamber due to the presence of the semi-circular ridges, the extent to which this assumption is applicable to our flow chamber is limited. CFD was therefore used to predict accurately the mechanical milieu experienced by the cells in the cell structure interaction experimental model.

Correlation between the WSS LAD waveform determined using analytical equation **6.1** and that predicted by CFD analysis is shown in figure **6.5**. It is observed that the WSS data produced from both methods compared relatively very close; thus the assumption made of the relationship between flow rate and WSS is plausible. Nonetheless, it is noted that there were at some time points where the WSS predicted by the analytical equation deviated slightly from that recorded by the CFD. This deviation implies that for complex flow, analytical equation many not be able to capture accurately the fluid dynamic present and thus the use of CFD is needed.

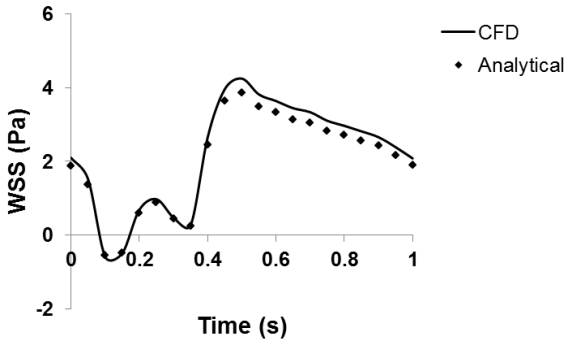

Figure 6.5 Graph showing the correlation between analytical WSS and CFD WSS over LAD waveform in flow chamber.

6.2.2 SPATIAL WALL SHEAR STRESS GRADIENT ANALYSIS

From the WSS results shown in figures **6.3a** – **6.4f** it is noted that WSSs at the inlet and outlet of the cell-structure model is relatively uniform. However at regions with the semi-circular ridges, there were varied WSSs as expected. The very high then low WSSs recorded at this region brings about a spatial WSS gradient. Figure **6.7** shows the SWSSG predicted to be experienced on the cell culture surface under the simulated steady flow and figures **6.8a** – **6.8d** show the SWSSG under the LAD pulsatile flow simulation at selected time points of the LAD waveform.

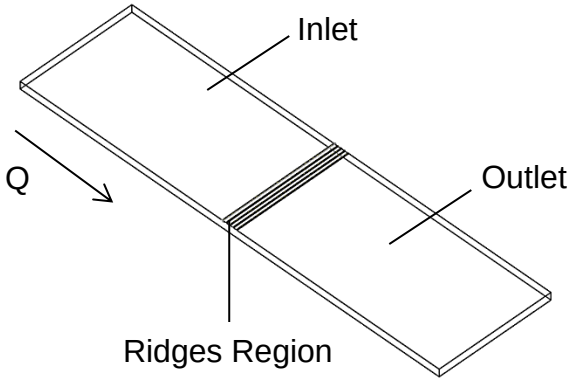

Figure 6.6 Labelled section of the cell culture surface area

Sections of the cell culture surface area were taken to show the SWSSG distributions under the two flow conditions. These sections were annotated as follows:

Inlet section is annotated with the letter ‘a’

Ridges Region is annotated with the letter ‘b’

Outlet Region is annotated with the letter ‘c’

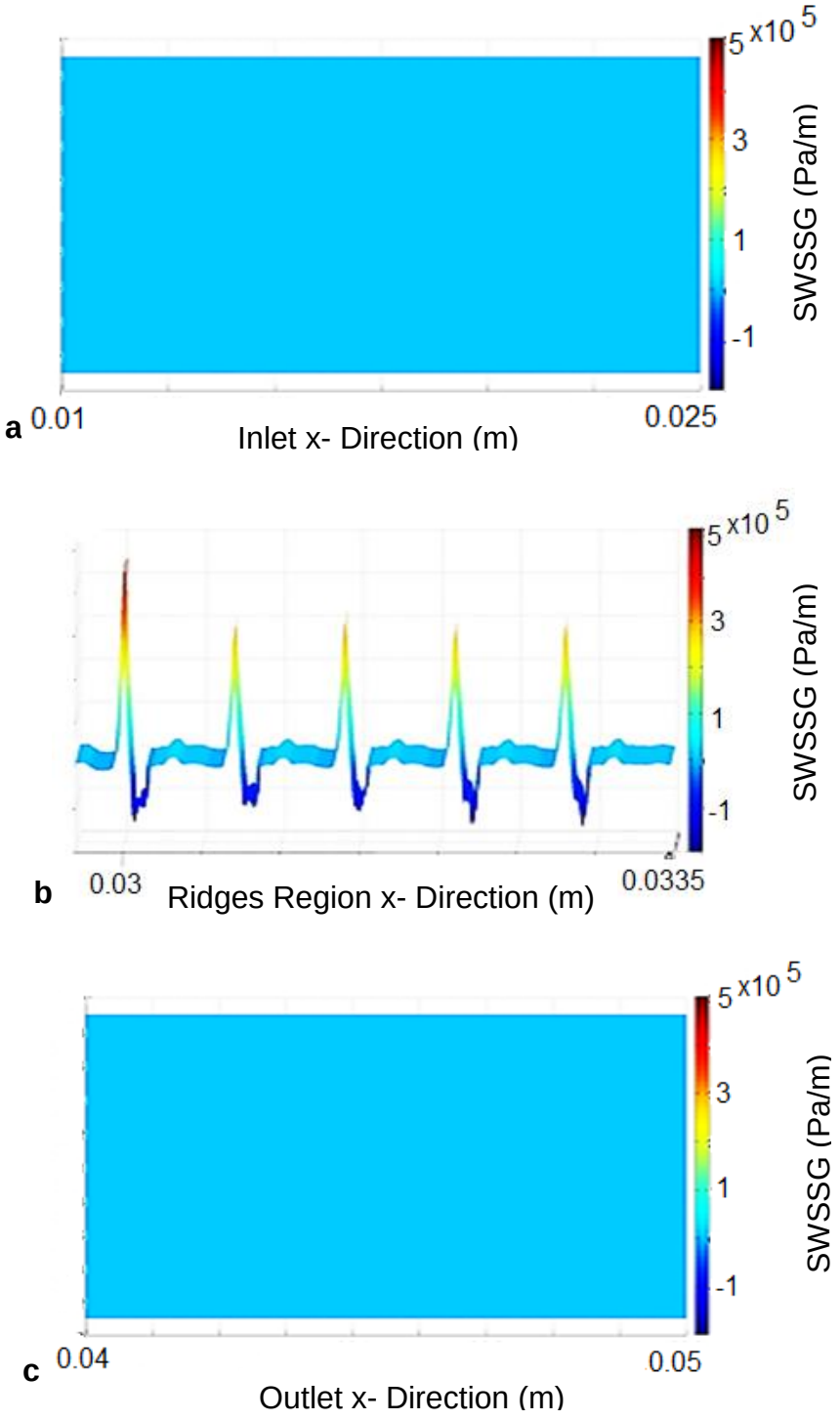

Figure 6.7 SWSSG (Pa/m) distribution under steady flow simulation. From this figure, there is no SWSSG (~ 0 Pa/m) at the inlet and outlet regions. SWSSG are however at the highest at immediate ridges region ($\geq 3.0 \times 10^5$ Pa/m). Also, SWSSG tend to decrease as we move further away from the ridges.

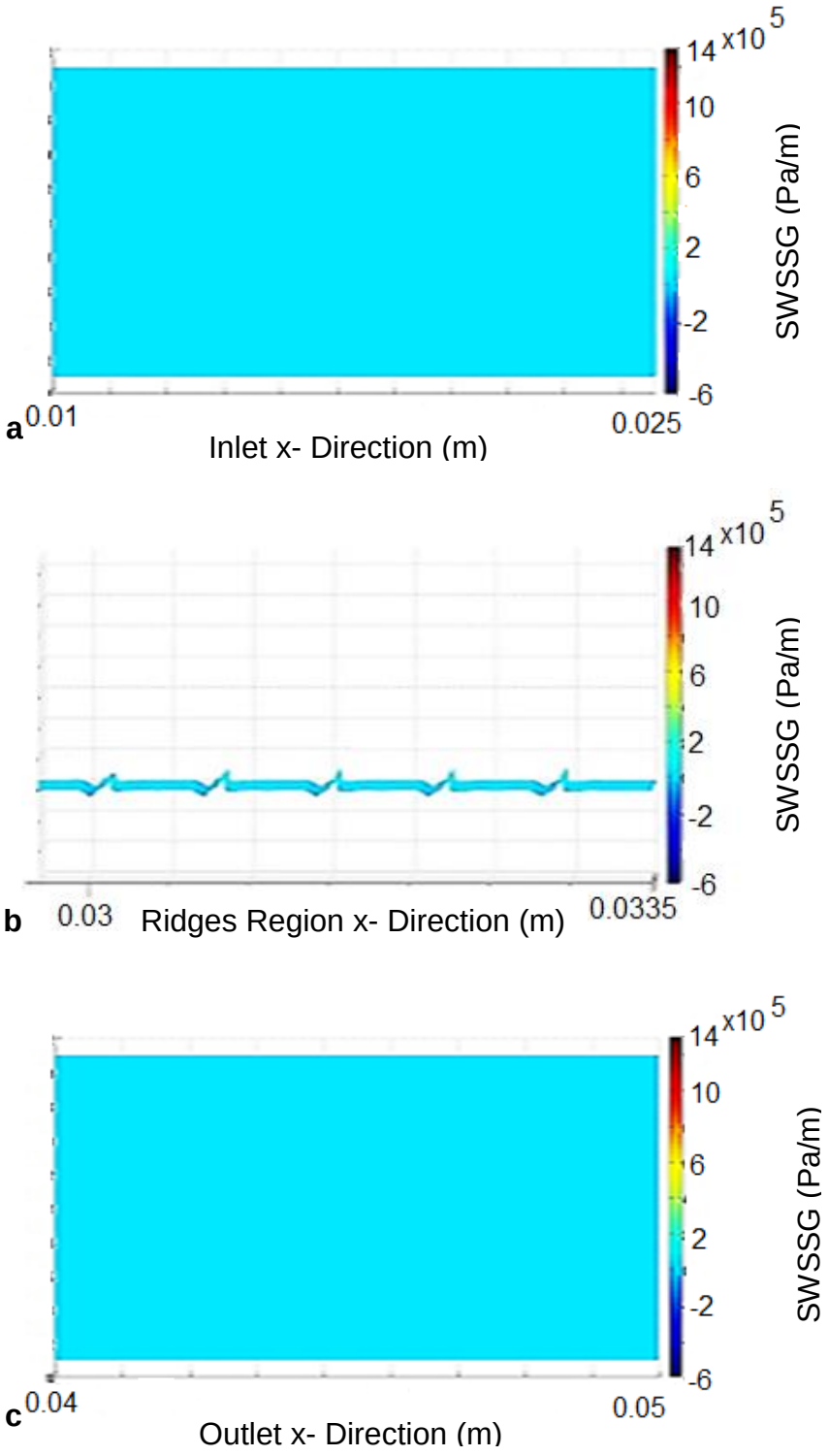

Figure 6.8a SWSSG (Pa/m) distribution under LAD flow simulation at t = 0.1s. As seen in this figure, there is on SWSSG across the inlet and outlet regions. However there is slight increase in SWSSG at immediate ridge regions.

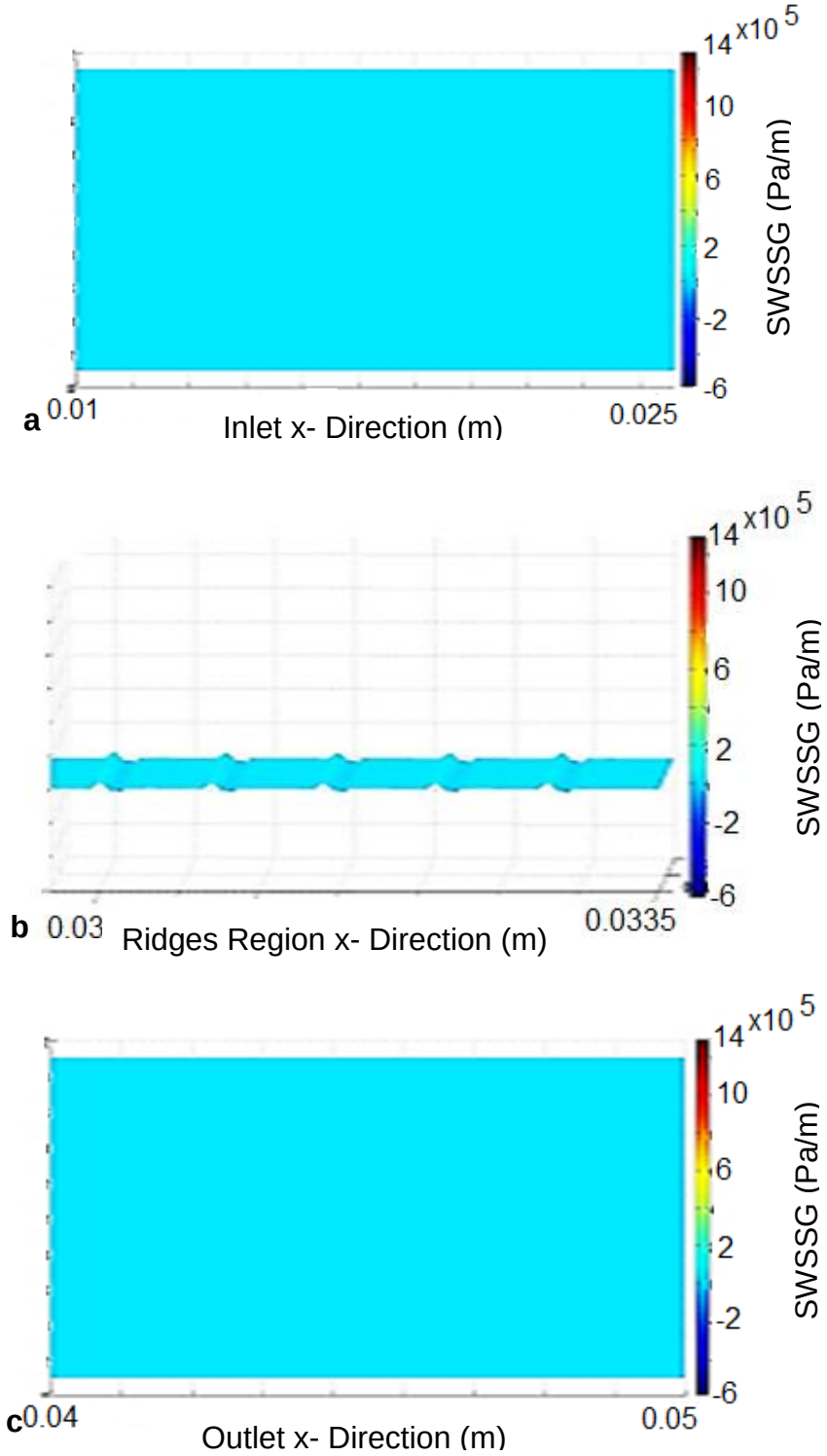

Figure 6.8b SWSSG (Pa/m) distribution under LAD flow simulation at t = 0.3s. As seen in this figure, there is on SWSSG across the inlet and outlet regions. However there is slight increase in SWSSG at immediate ridge regions.

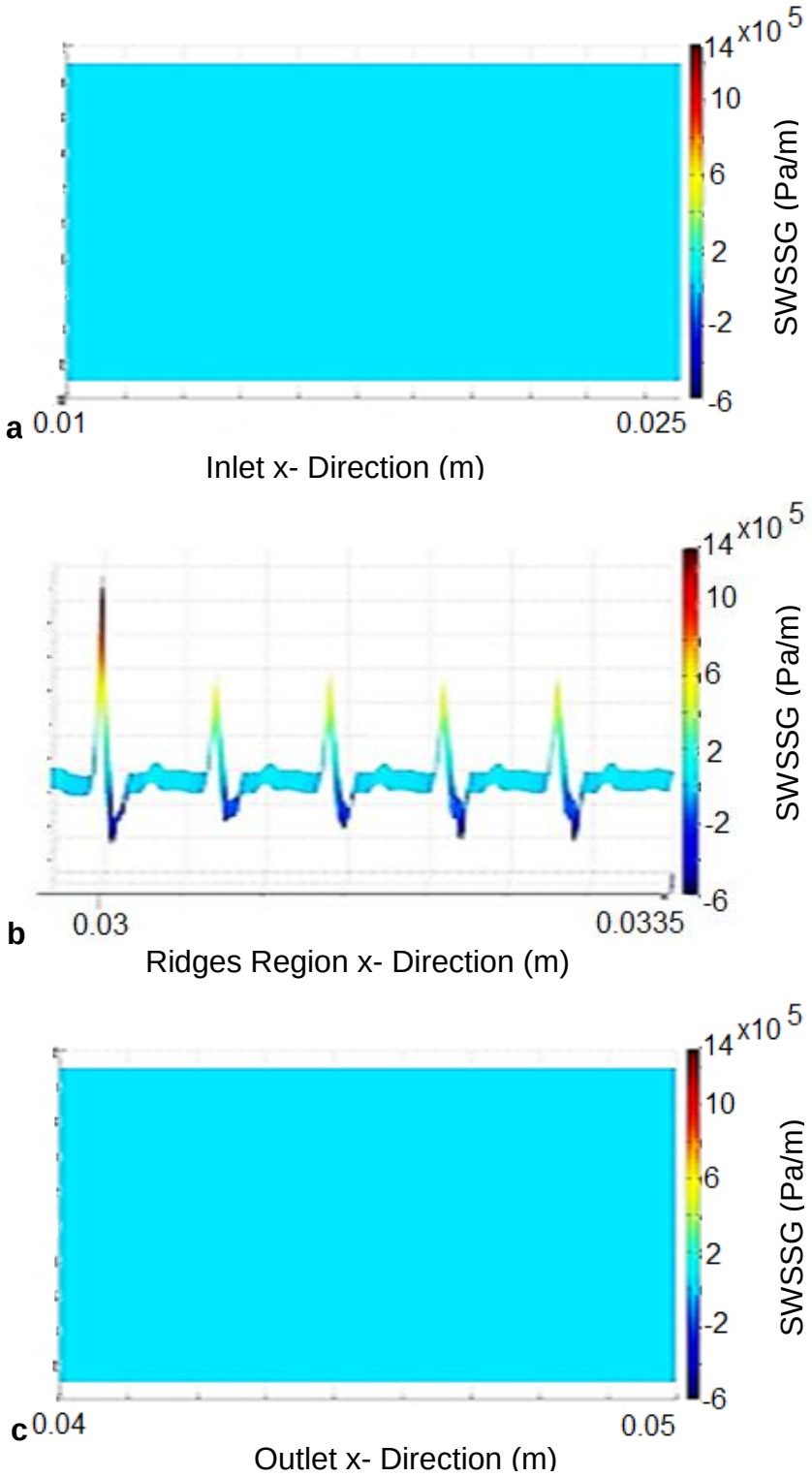

Figure 6.8c SWSSG (Pa/m) distribution under LAD flow simulation at t = 0.5s. As seen in this figure, there is on SWSSG across the inlet and outlet regions. However there is very high SWSSG at immediate regions around the ridges.

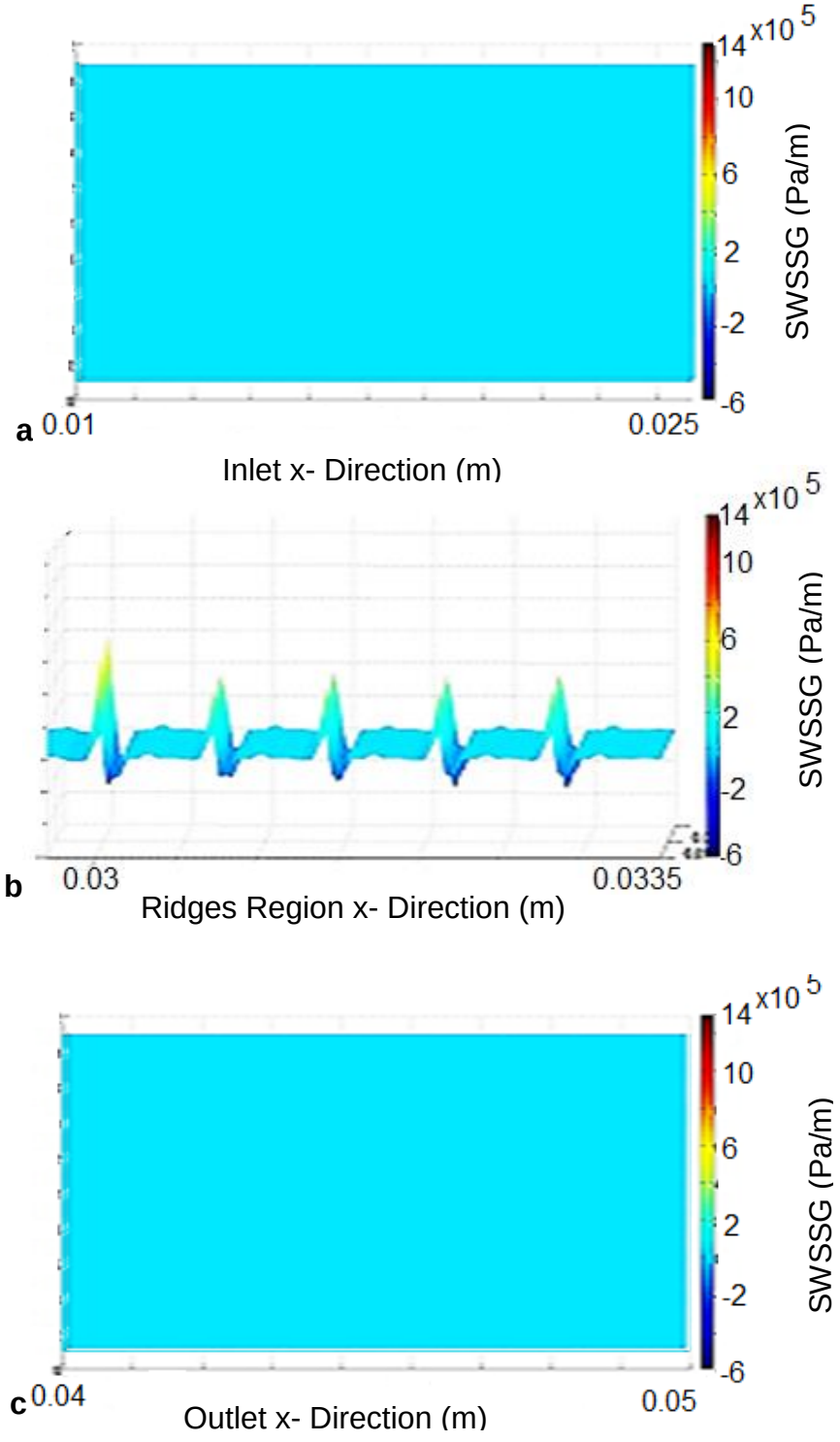

Figure 6.8d SWSSG (Pa/m) distribution under LAD flow simulation at t = 0.9s. This figure shows that at the inlet and outlet regions there are no SWSSG. Conversely, there is high SWSSG at immediate regions around the ridges.

The general observation made with regards to figures **6.7** – **6.8d**, is that there is zero or relatively minimal SWSSG at the inlet and outlet regions of the model under the steady and LAD pulsatile flow simulation performed. However, under steady flow simulation, SWSSG spikes are observed on the ridge regions and SWSSG valleys are observed at very immediate regions of ridges. Thereafter, the SWSSG levels tend to decrease with distance from the ridges. Under LAD pulsatile flow simulations, the SWSSG phenomenon at the ridges region at time phase t = 0.5s and t = 0.9s is similar to that observed under steady flow simulation. The reason for this similarity is that flowrate at these time points are comparable to that of the flowrate used for steady flow simulations. On the other hand, at time points t = 0.1s and t = 0.3s of the LAD waveform, flowrate is suggested to be very low. Hence SWSSGs magnitude at the ridge regions are not as pronounced as that observed with the steady flow simulations and at time phase t = 0.5s and 0.9s of the LAD pulsatile flow simulation. It is evidently seen in figures **6.8a** and **6.8b** that SWSSGs at the ridge regions are relatively very low.

6.2.3 OSCILLATORY SHEAR INDEX ANALYSIS

OSI, as previously discussed, is a measure that allows evaluating the local oscillatory effect within an artery which has been postulated to correlate with increased risk of stenotic lesions [330]. OSI values are within the range of 0 and 0.5 with the lowest value 0, representing a region in which there are no flow reversals; hence total instantaneous shear is in one direction. The highest value 0.5, indicates the region in which there are opposite flow directions and thus the oscillatory shear flow at this region results in a zero WSS. Regions of high OSIs have been suggested to be more prone to endothelium dysfunction [367]. Figure **6.9** shows the OSI distribution within the region with semi-circular ridges during one complete cardiac LAD cycle.

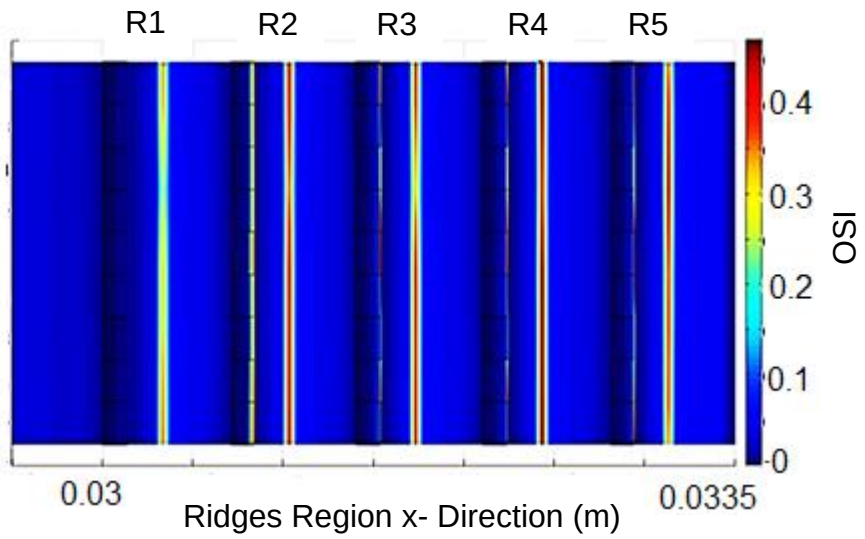

Figure 6.9 OSI distribution within ridges (R1, R2, R3, R4, R5) region during a complete LAD waveform cycle.

As shown in figure 6.9, high OSIs (≥ 0.3) are experienced some distance after the immediate ridge region which therefore meant that there were opposing flow directions at that area.

6.3 DISCUSSION

Of clinical relevance are 'site-specific' endothelial functional changes associated with particular flow dynamics and mechanical stresses that develop at arteries with certain geometrical characteristics such as curvature and bifurcations [104, 368]. On this premise, the mechanical stresses and flow characteristics at stented arteries associated with endothelial response are equally of high clinical importance as the presence of stents results in local geometric changes of the artery with flow conditions characterised by disturbed shear stresses [184]. Increasing evidence has led to the

suggestion that the number, shape, width and thickness of stent struts influence the arterial floor exposed to increased SWSSGs, TWSSGs, OSI and low WSSs that are associated with the spatial and sequential localisation of NIH and consequently in-stent restenosis [30, 216, 369-372].

CFD analysis allowed for evaluation of these individual mechanical stresses applied to ECs within a modified cell-structure interaction model which represented a simplified stented artery. The model was designed to apply combined stresses thus WSS, SWSSG, TWSSG and OSI to ECs. It is noted that at the immediate inlet regions of the model, there are some disturbed WSSs. This occurrence is as a result of flow being disturbed as it enters the cell-structure model from the flow tubing due to the significant geometrical difference between the flow tubing and the entrance of the model. Also, the "No Slip'' condition of the wall of the cell-structure model comes into effect when flow initially hits its boundary. Nonetheless, the flow is seen to develop quickly downstream from the inlet and have a uniform steady flow and thus majority of the ECs at the inlet region are suggested to be subjected to uniform WSSs. ECs at the very immediate region of the entrance region will not be taken into analysis due to this entrance effects. Figure **6.10** shows a line graph of the WSS and SWSSG distribution along the centreline of cell-structure model under steady flow simulations. Figures **6.11a** and **6.11b** show the WSS and SWSSG distributions respectively along the centreline of the cell-structure model under LAD pulsatile flow simulations at selected time points of the LAD waveform.

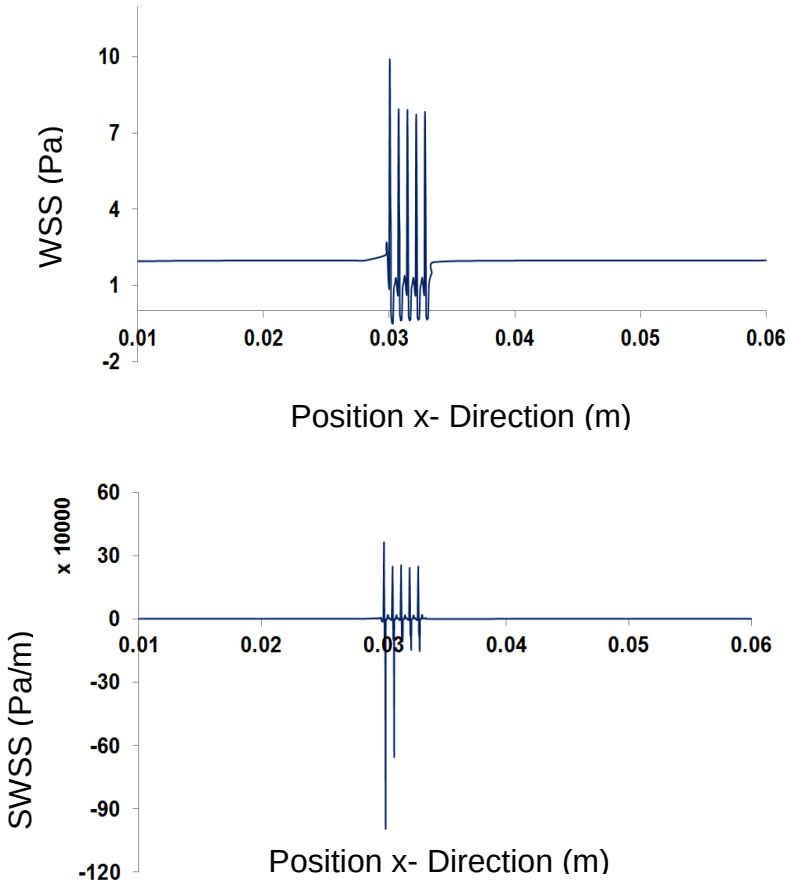

Figure 6.10 Line graphs showing WSS (top) and SWSSG (bottom) distributions on the centre of the cell-structure model under steady flow simulation.

From figure **6.10**, it is observed that areas where ridges were not present showed constant uniform WSSs and zero SWSSGs. However, ridge regions were characterised with WSS spikes on ridges and WSS valley around the immediate regions of the ridges. It is also noted that the first ridge in relation to the direction of flow (left to right) showed higher WSS magnitude. On the subsequent ridges however, WSS magnitudes reported were comparatively lower to that of the first ridge. Explanation to this occurrence is that flow over the first ridge is faster than the subsequent ridges. Hence from Bernoulli's equation pressure at the first ridge is lower than that of the subsequent ridges. The pressure difference across the ridge causes an increase in WSS and thus the lower pressure the higher the WSS produced.

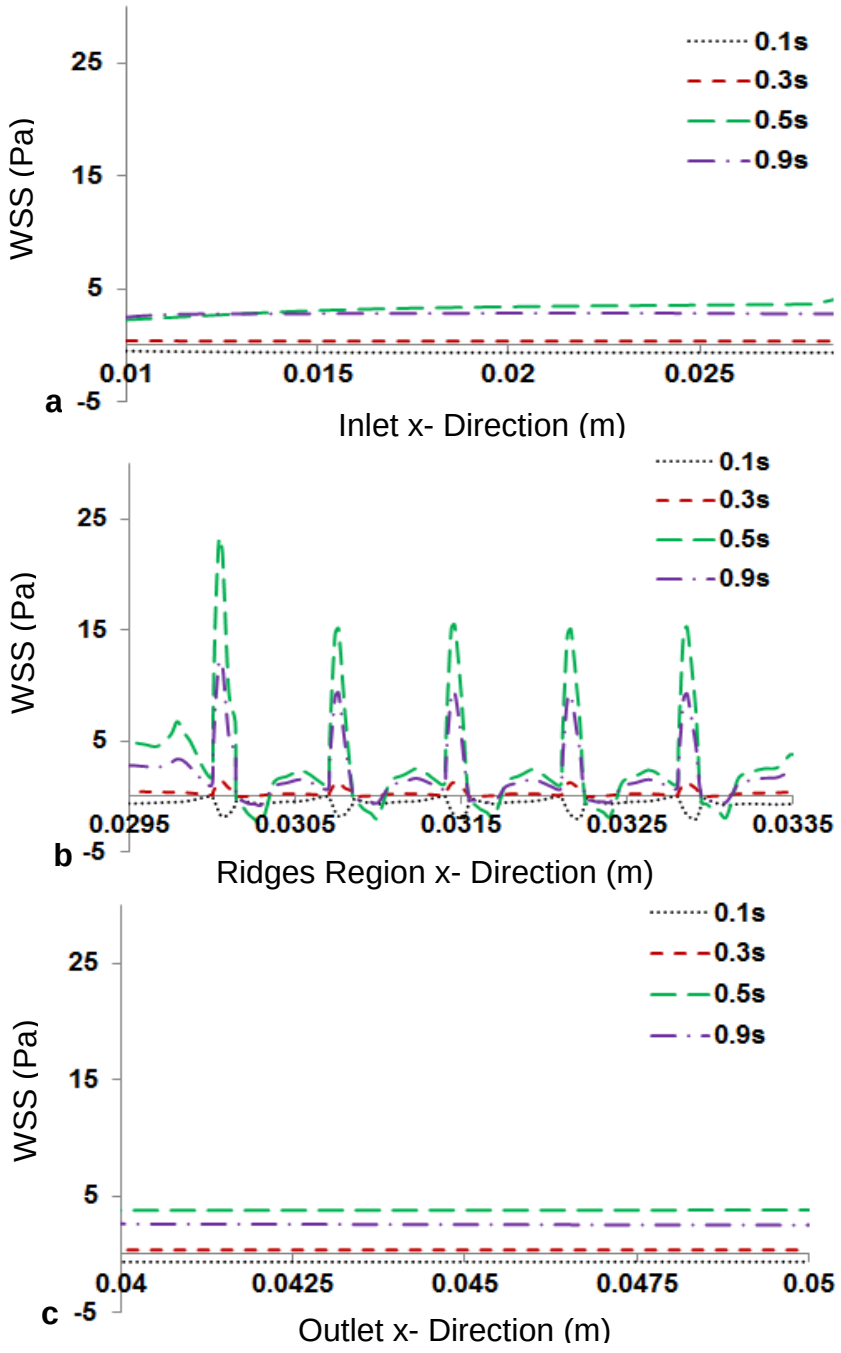

Figure 6.11a Line graphs showing WSS distributions at: (a) Inlet region, (b) Ridges region and (c) Outlet region of the cell-structure model under pulsatile LAD flow simulation at different time point (0.1s, 0.3s, 0.5s, 0.9s). WSSs at the inlet and outlet regions are characterised by uniform WSS whilst WSSs at ridge regions are marked by WSS spikes and WSS valleys.

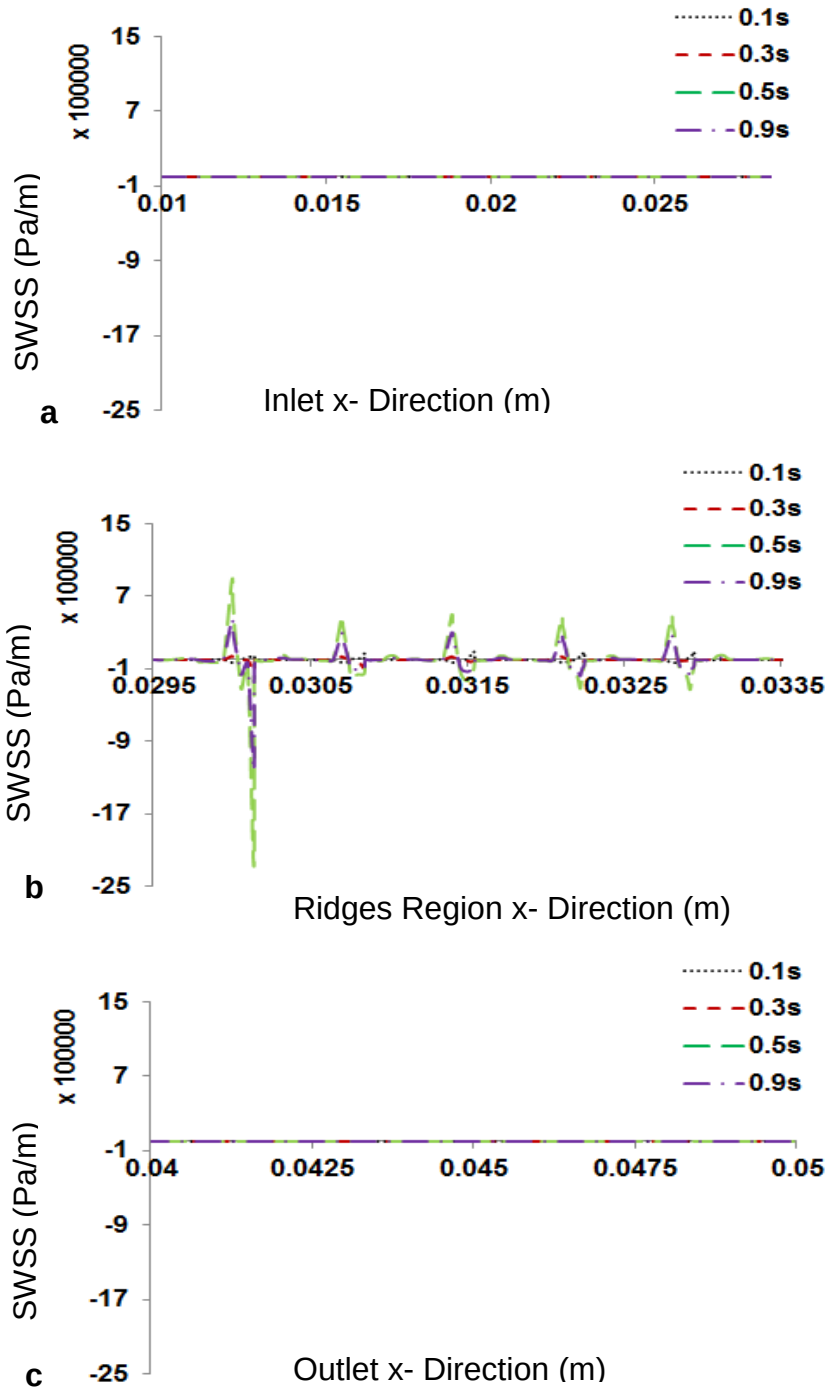

Figure 6.11b Line graphs showing WSS distributions at: (a) Inlet region, (b) Ridges region and (c) Outlet region of the cell-structure model under pulsatile LAD flow simulation at different time point (0.1s, 0.3s, 0.5s, 0.9s). From this figure it is observed that there is no SWSSG at the inlet and outlet regions. Conversely, there are high SWSSG at the very immediate ridge regions.

Consistent with the literature, it is observed that regions with spatially uniform WSS have no SWSSG; (inlet and outlet regions of the model) as opposed to regions where WSS is varied due to flow reversal, separation and reattachment regions (ridges region of the model), thus presenting spatial WSS gradient [11, 327, 373]. It is also noted that very high WSSs ($> 5\ Pa$) are recorded on the semi-circular ridges due the ridges disturbing the fluid flow and negative or low WSS ($< 1\ Pa$) at immediate regions near the ridges where recirculation flow vortices and flow separation are predicted. Flow is predicted to tend to recover from the flow disruption downstream from the location of the ridges as this region is characterised by increasing WSSs. This flow recovery is however hampered when flow goes past a subsequent semi-circular ridge. As noticed also, the WSS distributions are similar across the cell-structure interaction model regardless of the time point selected under the LAD pulsatile flow simulation. Conversely, the WSS magnitudes recorded are significantly different at the different time points selected and this occurrence could be explained by the direct proportionality relationship between flow rate and shear stress as indicated in equation **6.1**.

Detailed identification and quantification of local mechanical stresses distributions within stented arteries as similarly identified in the designed cell-structure model helps to predict arterial regions which may be more prone to restenosis. As discussed in earlier sections of this report, low and high WSS, SWSSG, TWSSG and oscillatory shear stress all have been proposed to influence the pathophysiology of diseased artery [97, 101, 327, 329, 330]. Although these findings have been validated by experimental data, it must be taken into account that it is not known specifically which of these mechanical stimuli is mediator of arterial disease. Thus it is thought by some researchers that the state of the disease may be as a result of the combined effect of these mechanical stimuli. Several studies have reported on the co-existence of increased WSS and positive SWSSG in complex arteries and have

postulated this co-existence relationship to trigger cerebral aneurysms [374-376]. Based on this premise, Dolan et al. [373] in a review on high WSS and SWSSG in vascular pathology presented findings to illuminate how these co-existing mechanical risk factors may influence the pathobiology of stenosis in arteries. To investigate this relationship of stresses within the cell-structure model, the WSSs predicted from the CFD analysis were compared with the recorded relative SWSSG and OSI. Figure **6.12** shows the correlation of the mechanical stress markers within the designed cell-structure interaction model where flow is mostly disturbed.

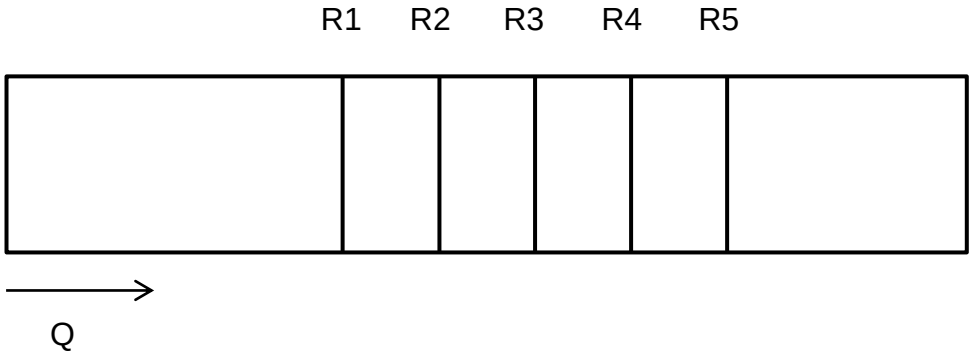

A schematic diagram (not drawn to scale) showing the cell culture surface area of the cell-structure interaction model with the five independent semi-circular ridges annotated by R1, R2, R3, R4 and R5. The arrow shows the direction of flow at flow rate, Q.

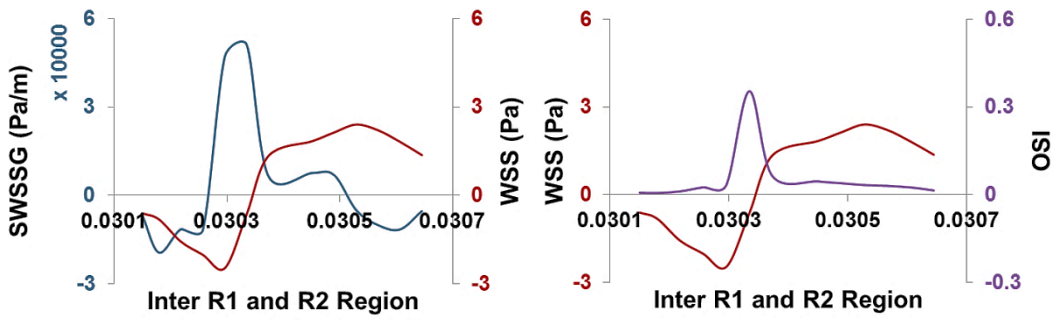

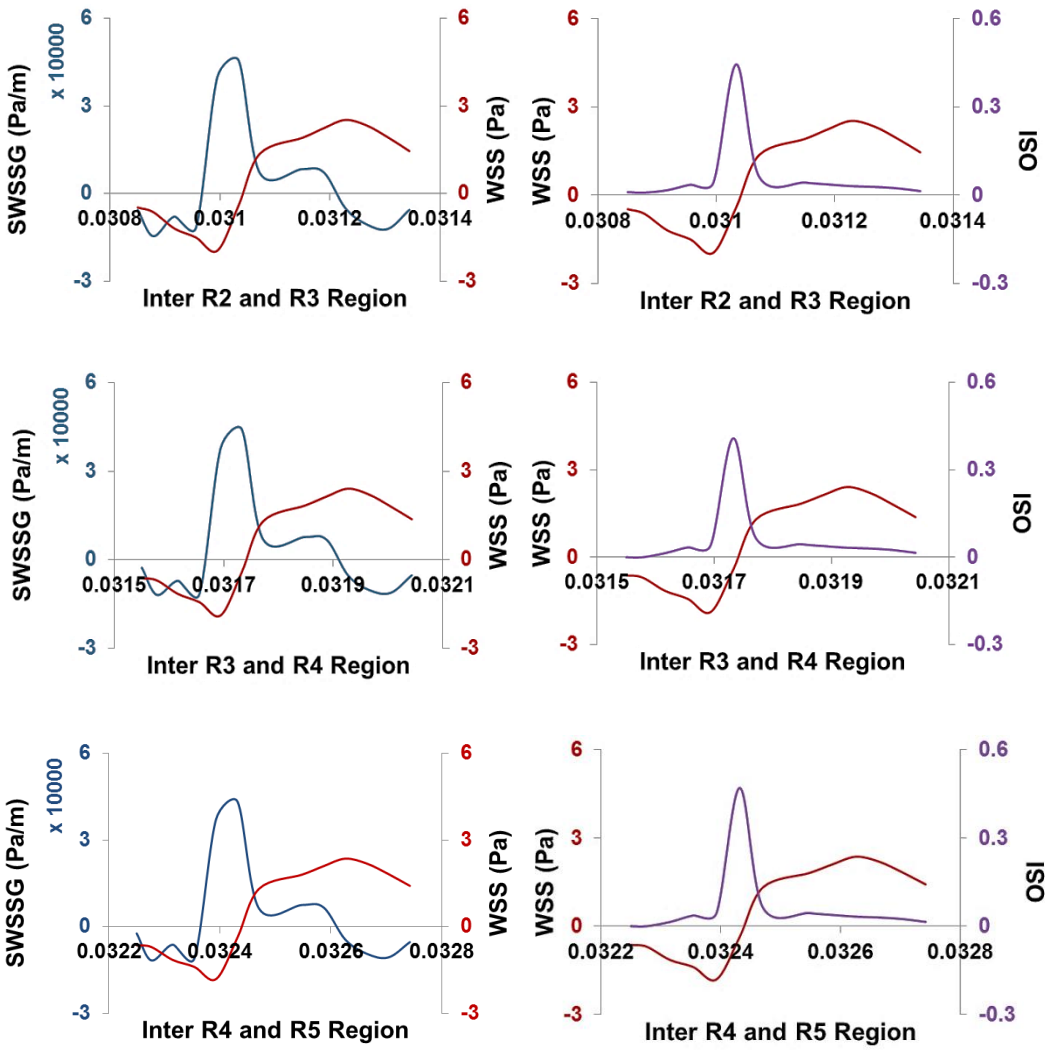

Figure 6.12 Line graphs showing the relationships between WSSs and SWSSGs (Left) and WSSs and OSIs (Right) within regions with ridges under LAD pulsatile flow simulation at time point 0.5s.

From figure **6.12**, it can be deduced that within the ridges, OSI is at its highest when WSS is relatively zero. Also increase in WSS led to decrease in OSI. Comparative analysis of WSS and SWSSG within ridges revealed that SWSSG tends to increase at the point where WSS within the ridge regions starts to increase. The SWSSG however subsequently decreased whilst WSS still increased.

The SWSSG and WSS relationship observed within the experimental model is similar to that reported by Schirmer et al. [377] in a study investigating the spatial and temporal hemodynamic changes within patient specific stenotic carotid artery. In the study, WSS increased at the throat of the stenotic artery whilst SWSSG changed from positive and negative past the throat of the stenotic artery. Furthermore, positive SWSSG was reported post stenotic region where endothelial erosion or plaque ulceration has been predicted to be most frequent [378, 379]. Rouleau et al. [11] findings of WSS and SWSSG distributions from a study on the effect of spatial wall shear stress gradient on ECs morphological response in an idealised in vitro stenotic artery was also consistent with that reported by Schirmer et al. [377]. It is thus interesting that in the cell-structure model similar observations are made as WSS is seen to increase at the ridge region and SWSSG changed from positive to negative past the ridge section. More so, a positive SWSSG is also observed post ridge region. The relationship between WSS and OSI is also demonstrated in the cell-structure model as high OSIs are recorded at proposed flow separation regions which are characterised by both negative and positive WSSs. In addition marked high OSI correlated to the post ridge region where positive SWSSG was recorded as shown in figure **6.13**. It is proposed that the choice of strut design could influence local flow conditions which may be conducive to the development of stent thrombosis or ISR.

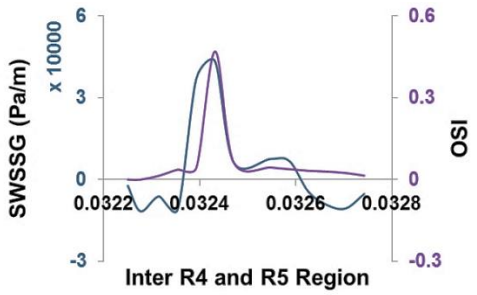

Figure 6.13 Line graphs showing the relationship between SWSSG and OSI within R4 and R5 region under LAD flow simulation at time point 0.5s.

Garasic et al. [301] investigation into the effect of stent and artery geometry on intimal thickening independent of arterial injury reported the existence of NIH within the centres of diamond shaped stent implanted in rabbit iliac arteries. Using a similar stent geometrical design LaDisa et al. [380] reported marked elevated SWSSGs and high WSS at these regions which were reported by Garasic et al. to have NIH. LaDisa et al. revelation seems to contradict the classic hypothesis that high WSS enables the athero-protective nature of EC [91, 92, 181]. In the study by LaDisa et al., on the circumferential vascular deformation after stent implantation, it was reported that vascular circumferential straightening as a result of stent implantation induced areas of high WSS between stent struts. This phenomenon was however absent in stented circular vessels. It was therefore concluded from the study that WSS distribution that may be linked to NIH onset may be influenced by the geometrical changes of the vessel after stent implantation.

The cell-structure interaction model designed represents a simplified idealised stented LAD artery; thus results presented should be interpreted within the constraint of the limitation of the model. The simulation results are of stented healthy arterial segment; however results may likely differ if simulations were of a stented diseased artery. The assumption of rigid arterial wall was made in the simulations presented. A study by LaDisa et al. [4] on the alteration of hemodynamic after stent implantation into the LAD arteries of 6 dogs reported a reduction of arterial compliance to zero at the stented region. Arterial compliance after stent implantation could however differ depending on the geometry of the vessel being investigated. Also, the arterial compliance of the proximal and distal regions to the stented segment could potentially alter vasodilation of the vasculature through the stented region. Thus to model this phenomenon would necessitate simulations using fluid-structure interactions.

6.4 CONCLUSION

The CFD results presented show regions within the cell-structure interaction model marked by reverse flow, flow separation and reattachment to have varied WSSs, high SWSSGs and OSIs whilst regions marked by relatively uniform flow exhibit uniform WSSs and negligible SWSSGs and OSIs. These results provide quantitative data that guides our experimental studies and understanding of the mechanical milieu within a stented artery and also the mechanical forces which might influence the onset of ISR.

CHAPTER 7

EXPERIMENTAL ANALYSIS OF ECs MORPHOLOGICAL RESPONSE TO PHYSIOLOGICAL RELEVANT FLUID DYNAMICS IN STENTED MODEL

7.1 INTRODUCTION

There have been, to the author's knowledge, no studies on in vitro examinations of the morphological and molecular responses of ECs within stented artery to a combination of physiologically relevant pulsatile flow waveform and pressure. The flow bioreactor system discussed in sections **4** and **5** is thus suggested suitable to study the effects of combined stresses on ECs exposed to physiological flow waveform and pressure. The bioreactor system designed is also suitable for the investigation of ECs response to steady flow. As the effects of steady flow on ECs responses have been well characterised, it is deemed that investigations using the designed bioreactor system could be validated by the confirmation of experimental results under steady flow being comparable to that reported in literature.

As discussed in earlier sections of this report, several studies have hypothesised the relationship between ECs response (morphological and molecular) and mechanical stresses such as WSS. Some of the classic hypotheses have been that cells experiencing physiological relevant levels of WSS elongate and align parallel to the direction of the fluid flow [11]. The degree of the cell alignment however depends up on the magnitude of the WSS and the time duration for which the cells have been subjected to the

WSS [180]. Conversely cells experiencing low or no WSS are cobblestone shaped and do exhibit random orientation [320]. As ECs distinctively alter their morphological shape (i.e. either elongated or cobblestone) in response to the type and strength of mechanical stimuli being applied to them, it is hence proposed that the morphology of the cells may be a focal indicator for predicting the arterial site prone to lesion growth. Low WSSs have been also postulated to upregulate vascular cell adhesion molecule (VCAM-1); a marker for plaque development [381]. Comprehensive in vitro and in vivo analyses have revealed a myriad of shear stress regulated genes [382]. Of these stress-regulated genes, 70% have been attributed to depend on Krüppel-like factor-2 (KLF-2) and nuclear factor erythroid 2-related factor (NrF2) which are mechano-sensitive transcription factors and suggested to be activated by shear stresses. These transcription factors play crucial roles in regulating pro-inflammatory, pro-thrombotic and pro-proliferation gene activation of the endothelial [383-385].

Despite the successes gained from having been able to map cellular responses and molecular responses of the ECs to mechanical stresses in vivo and in vitro; thus this knowledge have been used to infer the functional state of the artery, there still exist some pertinent challenges in interpreting clinical observations of diseased arteries and more especially stented arteries. Some of these challenges arise due to the disparities between some clinical results and experimental results. In most computational models (i.e. CFD) of stented arteries, simplification of the flow dynamics and/or the artery constituents are generally made. For example in many computational models of the artery, the arterial floor and blood is considered as a continuum thus disregarding the varied constituents of the blood (red blood cells, platelets) and the artery (smooth muscle cells, ECs) or the intercellular activities within constituents [382]. In recent studies however, a multi-scale modelling approach whereby mechanical stimuli and biological function at varied spatial

and transient scales are combined to provide a framework for analysing mechano-biology across scales have been employed in the study of ISR development [386-390]. Evans et al. [388] described a detailed formulation of a multi-scale model in analysing stenosis in stented coronary artery. This framework could potentially reveal the key mediators of clinical ISR and thus results achieved could be more comparable to clinical observations. However, whilst it is appreciated that multi-scale modelling approach could provide detailed insight into the predictors of disease progression in arteries, it is noted that most of the frameworks are modelled implicitly. Thus other molecular influences and/or reactions might have been neglected in the modelling due to the limited knowledge underpinning the relationship blood between mechanical stimuli and disease onset. Hence the main cause of ISR still remains elusive. Although there are some failings with the conventional computational modelling approach in correlating constituents and flow dynamics with cells response, this technique is a well-established and robust method. Thus it is suggested that if the appropriate processes of this technique are observed and results understood within the context of the model simulated and limitations of the model, results attained could be interpreted with some clinical relevance.

Many in vitro experimental studies to investigate ECs response to different mechanical stresses have mostly been performed under non-physiologically realistic flow waveforms (i.e. steady or sinusoidal) albeit physiologically realistic pulsatile flow dynamics could have a marked effect on the cells response. Although some studies have shown similar morphological changes of cells when exposed to physiological pulsatile flow dynamics or steady flow [98, 391], molecular and gene expressions of the cells however have been reported to differ [98, 392, 393]. Blackman et al. [98] in the in vitro examination of the effects of pulsatile arterial stress waveforms on ECs reported that ECs exposed to either arterial flow or equivalent steady flow

exhibited similar elongation and alignment, but the protein and cellular adhesion molecule expressions of the ECs differed with respect to the type of flow applied to the cells. It nonetheless should be made clear that the suggested similarity in morphological response of cells when exposed to either pulsatile or steady flow is only valid to a certain extent. Helmlinger et al. [391] investigated the influence of three types of pulsatile flow (i.e. non-reversing, reversing and pure oscillatory flow) and steady flow on bovine aortic endothelial cells (BAECs) shape and elongation. It was confirmed from the studies that there were differences in the elongation and also the duration it took for the ECs to change shape in respect to the flow waveform the cells were exposed to. It is therefore proposed that there is a distinctive responsiveness of ECs to any type of flow waveform irrespective of the similarities in results that may be observed. Thus to be able to explicitly compare in vitro results to in vivo results, then physiological parameters need to be employed in the experimental investigations.

7.2 METHOD

7.2.1 PRE-CELL CULTURE PREPARATION

The PDMS stamped glass microscope slides with the micro-structure semi-circular ridges were submerged into phosphate buffered saline (PBS) for at least seven days. This process ensured that uncured polymer resin was sufficiently leached out of the stamped glass slides. The stamped glass slides were then sterilised in 70% ethanol for at least two hours. The ridge sheaths fabricated as discussed in section **5.5** were also sterilised in 70% ethanol for at least two hours.

7.2.2 CELL CULTURE

T25 flasks were initially coated with sterile 0.1% bovine skin gelatin and incubated in a humidified cell culture incubator $(37℃, 5\%\ CO_2)$ for at least 45 minutes. This process ensured focal adhesion of cells to the base of the flasks. Frozen down human umbilical vein endothelial cells; HUVECs (Promocell, Germany) were revived at passage number 3 (P3) and seeded at sub-confluent density in the coated T25 flasks. The HUVECs were cultured with the cell growth medium M199 (Sigma-Aldrich) containing 20% foetal calf serum; FCS (BioSera, UK), $30ug/ml$ endothelial cell growth supplement; ECGS (Sigma-Aldrich, UK), $30ug/ml$ heparin (Sigma-Aldrich, UK), $2mM$L-Glutamine (Sigma-Aldrich), $100ug/ml$ Penicillin Streptomycin (Sigma-Aldrich). After every three days, the cell culture medium was aspirated from the cells and then after the cells were washed with Hank's balanced salt solution; HBSS (Sigma-Aldrich, UK) containing no calcium and magnesium to remove any dead cells before feeding the cells with new culture medium. When the cultured cells were about $90 - 100\%$ confluent, a routine cell passage was performed but this time the passaged cells were used for the flow experiment. Thus HUVECs were used at P4 for experiments.

7.2.3 CELL SEEDING

The sterilised PDMS stamped glass slides were washed thoroughly with sterile PBS three times to completely remove any ethanol from the slides and after the slides were placed in dry petri dishes. The surface of the sterile stamped slides with the micro-structure ridges were then each coated

with $1\ ml$ of $50\ ug/ml$ fibronectin solution and incubated for at least 1 hour. The fibronectin solution used was a mixture of $50\ ul$ fibronectin (Sigma-Aldrich, UK) and $950\ ul$ HBSS. After 1 hour of incubation, the fibronectin were aspirated from the stamped slides. Ridge sheaths were then carefully placed on top of the micro-structured ridges on the stamped slides after they have been washed thoroughly with sterile PBS. $1.5\ ml$ of HUVECs at P4 and a cell suspension of $330{,}000\ cells/ml$ were then seeded onto each stamped slides with care taken not to dislodge the ridge sheath from its position. This resulted in a cell seeding density of about $26{,}700\ cells/cm^2$ on the stamped slides. The now cell seeded stamped slides were carefully returned to the incubator for an added 3 hours to allow the cells to completely attach to the substrate, after which the ridge sheaths are removed and the cells flooded with $20\ ml$ of the cell growth culture medium. The flooded cells were then incubated for 24 hours to become confluent. In all the experimental investigations, HUVECs were seeded at a cell density of $26{,}700\ cells/cm^2$, used at P4 and incubated in a $5\%\ CO_2$ incubator at 37℃ unless otherwise stated.

7.2.4 CELL-STRUCTURE INTERACTION EXPERIMENT SETUP

The flow bioreactor system was setup to expose cells to:

- LAD physiological flow waveform with a mean fluid shear stress of $2\ Pa$ and a physiological hydrostatic pressure of $120/80\ mmHg$.
- Steady flow at a mean hydrostatic pressure of $100\ mmHg$ and fluid shear stress of $2\ Pa$.
- Hydrostatic pressure of $100\ mmHg$ and a fluid shear stress < $0.1\ Pa$.

Since the mean fluid shear stress applied to the cells were same for both the LAD pulsatile flow and steady flow, examinations of cells response under pulsatile and steady flow were run in parallel. To run the LAD pulsatile flow experiments the flow bioreactor system was assembled as described in figure **4.1**. To run the steady flow experiments however, the flow bioreactor was set up in a similar way to the pulsatile flow system but with the tubing connecting to the pulsatile simulator disconnected. The flow bioreactor circuits and gaskets were sterilised by autoclaving with the exception of the parallel plates of the test chamber which were sterilised using 0.1% peracetic acid in PBS for at least a day. Once the flow circuits were sterilised, the medium reservoirs were filled with the cell growth culture medium. In a sterile cell and tissue cabinet, the culture medium was run through the respective flow circuits without the test chambers (that is the cell-structure interaction model) connected to the flow systems to set the required pressure and flow waveform parameters. After the relevant parameters were set, the flow circuits were placed in the incubator and the culture medium primed throughout the flow circuits at a low flow rate of $10\,ml/min$ for at least 2 hours.

During the priming of the cell culture media, the test chambers were then assembled. To completely mount a test chamber, the stamped slide with the seeded HUVECs was initially washed with warm HBSS and then carefully placed into the groove of the sterilised bottom plate of the test chamber. The gasket was then placed on the bottom plate and carefully $1\,ml$ of warm culture media was pipetted onto the cells without spilling the culture media anywhere on the bottom plate. Finally, the top plate of the test chamber was placed on top of the bottom plate and firmly and securely affixed with machine screws. Warm culture medium was then gently introduced into the test chamber whilst making sure that there were no trapped air bubbles in the test chamber. After priming of the cell media, the flow circuits were

moved back into the sterile tissue cabinet where the test chambers were now connected to them. To connect the test chambers to the flow circuits, either sides of the tubing where the test chambers would be connected were initially clamped. Then after connecting the tubing to the inlets and outlets of the test chambers the clamps were removed. The now completed flow bioreactor system is moved to the incubator. Before the desired experiments were started, the flow rate was gradually increased after every 5 minutes starting from $5\,ml/min$ and doubling the flow rate thereafter until the required flow rate is reached. Once the required flow rate had been reached the cam driven physiologic flow simulator is switched on to add the desired pulsatile component onto the flow waveform.

HUVECs were exposed to either LAD pulsatile and steady flow at a mean flow rate of $144\,ml/min$. This resulted in a mean WSS of $2\,Pa$ experienced by the cells. In examining HUVECs under only hydrostatic pressure, the cells were subjected to a steady flow rate of $7\,ml/min$ which resulted in a WSS of approximately $0.07\,Pa$. Initial experiments investigating the hydrostatic pressure effects on HUVECs was done at a cell density of approximately $10{,}114\,cells/cm^2$. It was suggested that fluid flow rate at $7\,ml/min$ to yield a shear stress < $0.1\,Pa$ had negligible fluid stress effects on the cells but rather allowed for adequate perfusion of cell growth medium to the cells [313]. All three main experiments were run for 6, 12 and 24 hours.

7.2.5 CELLS STAINING

After exposure of the cells to the combined pressure and flow stimuli or pressure stimulus only for the desired time duration, the flow bioreactor system was stopped. The test chambers were then disconnected from the

flow circuit in a sterile tissue cabinet and the stamped slides carefully taken from the test chambers into petri dishes. The cells were washed once in $20\,ml$ of HBSS and then twice with PBS before fixing them in $20\,ml$ of 3.7% formaldehyde for 20 minutes. The cells were then stained for their actin cytoskeleton, nuclei and some inflammatory molecules and to ensure good staining of the cells this was done in a dark tissue cabinet.

7.2.5.1 STAINING FOR CYTOSKELETON AND NUCLEI

After the cells had been fixed, they were washed three times with PBS for 5 minutes each. After the third wash, the PBS was aspirated and then the cells permeabilised by adding 1% Triton X-100 for 3 minutes. The cells were washed again three times with PBS for 5 minutes each after being permeabilised. After this step, 1% bovine serum albumin (BSA) in PBS solution was added to the cells for 1 hour to block nonspecific binding. The staining solution was then made by adding $100\,ul$ of a $5mg/ml$ concentration FITC conjugated Phalloidin (Sigma-Aldrich, UK) and a $10\,ul$ of $0.1\,ug/ml$ aliquoted DAPI into $10\,ml$ of 1% BSA in PBS. The BSA was aspirated from the cells after the 1 hour and $1\,ml$ of the stain solution was put on the cells for 1 hour. The cells were then washed once with PBS after the staining for 1 hour and then preserved in PBS before visualised with a fluorescence upright LSM510 Meta confocal microscope. The actin cytoskeleton of the cells were stained green when labelled with the FITC conjugated Phalloidin. This fluorophore was able to be seen using $488nm$ excitation laser with an emission filter of $500-550nm$ setting on the confocal microscopy. The DAPI stained the nuclei of the cells blue and this was also observed by setting the emission filter of the microscopy to $435-485nm$.

7.2.6 CELLS SEGMENTATION

HUVECs stained with fluorophores after exposure to the mechanical stimuli and results obtained with confocal light microscopy system help provide qualitative assessment of the changes in cell morphology and orientation. This method of obtaining cell results for assessment is relatively better than the use of conventional optical microscope as the former provides enhanced distinctive features of the cell [394]. Whilst the use of this modern technique to produce excellent epifluorescent cell images is well appreciated, it is noted that achieving detailed quantitative data with this method can be very challenging.

Previous investigators have quantitatively analysed epifluorescent cell images by manually counting and assessing the cell morphological features [395]. This type of quantitative analysis is however severely influenced by the operator and thus results are highly not repeatable, may not be set to the same standards and have high inaccuracies. To overcome this problem, researchers have developed computational image processing programmes capable of producing unbiased and repeatable quantitative cell data [396-399]. It should however be noted that the choice of a cell image processing programme could be inadequate for analysing complex data and also the robustness of statistical methods of the image programme could influence results [396, 400]. Thus care should be taken when choosing appropriate image processing programme for cell data analysis.

A modular image processing software called CellProfiler was used to quantitatively analyse the cell data produced in this report. This software is a robust, high - throughput and free open-source image analysis programme that provides frameworks to measure standard biological assays (i.e. cell size and count) and complex morphological assays (i.e. cell shape and

protein staining) [396, 401]. The algorithm of this image analysis is built on a MatLab platform with the adoption of watershed transform methods which allows for accurate cell identification and measurements on crowded cell samples [401]. This software has been validated to solve several realistic biological problems with high accuracy [402, 403].

7.2.6.1 WORKFLOW OF CELL SEGMENTATION

Segmentation of the stained cells was performed using a pipeline (a sequential set of image analysis algorithms) constructed using CellProfiler version 2.1.0 software package. The sequential flow to segmenting the stained cells is illustrated in figure **7.1** below.

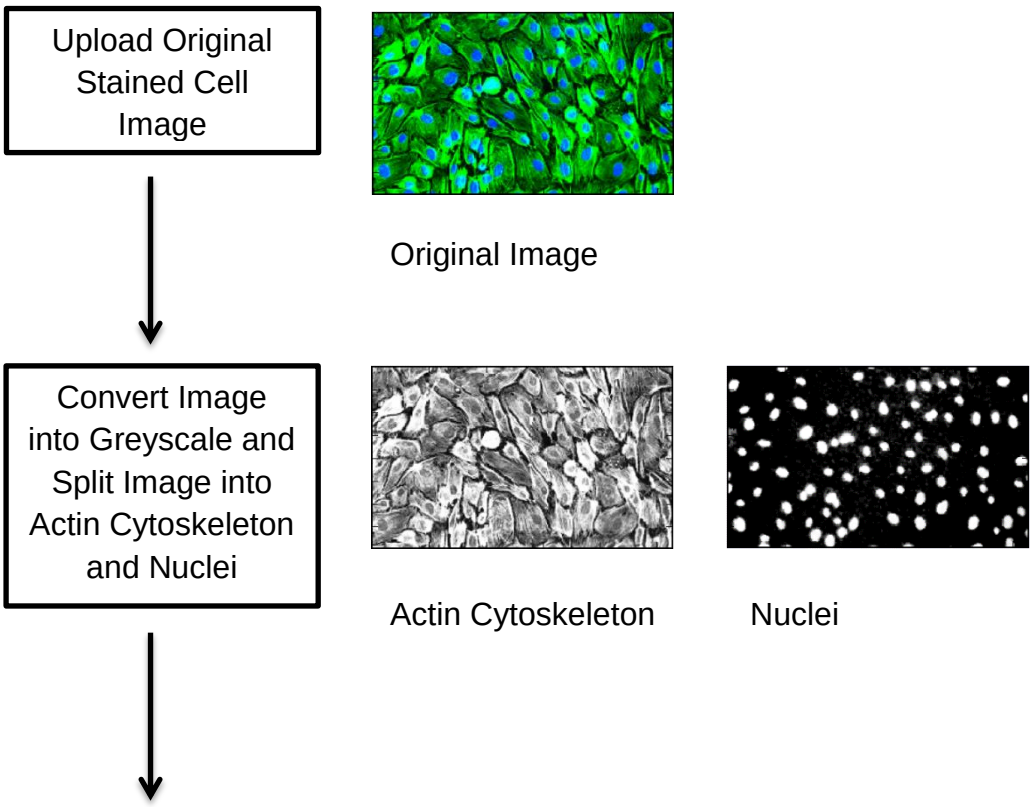

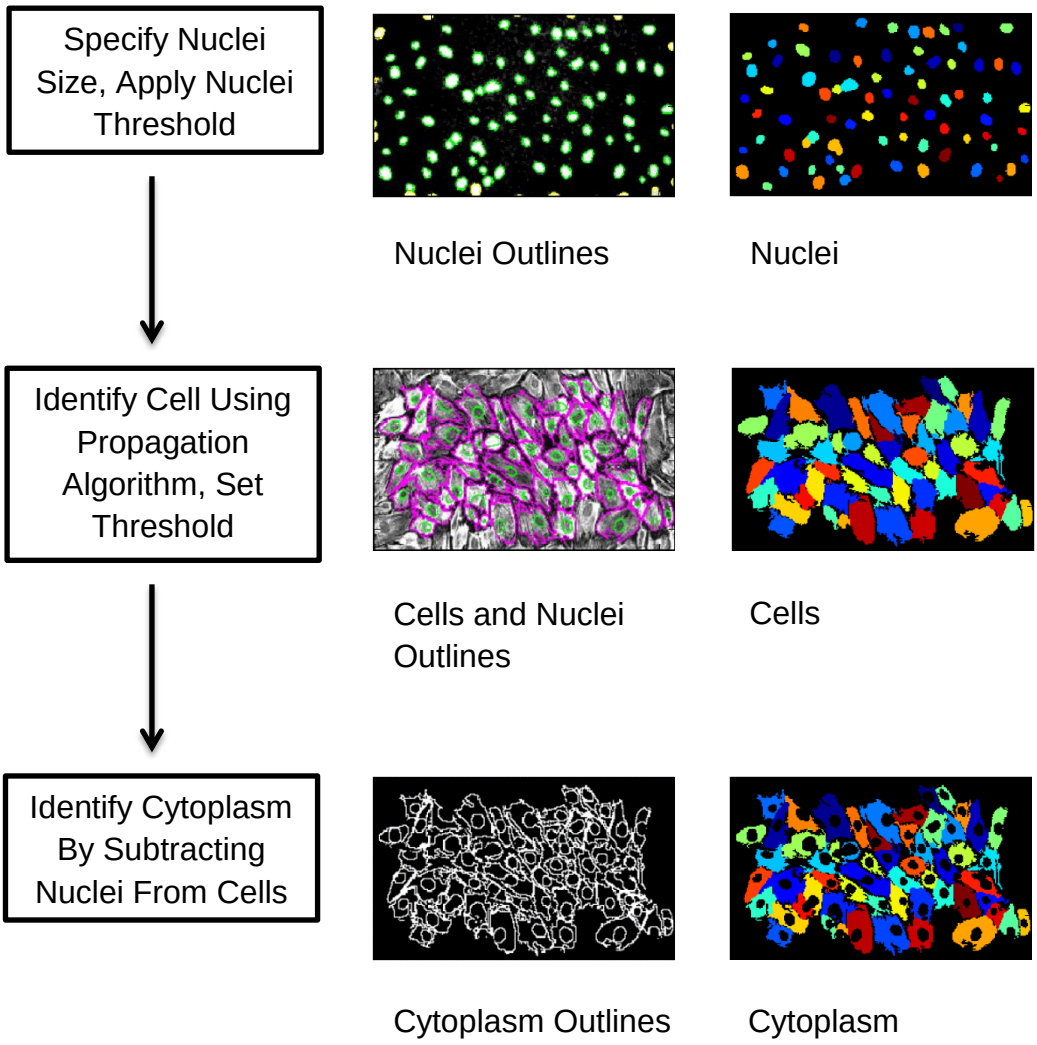

Figure 7.1 Flowchart of cell segmentation. Each cell and its nucleus is colour coded to facilitate easy identification quantification of the cell and nucleus.

The propagation alogorithm was used to identify cells as this method was an improvement on the conventional watershed transform method and appropriate for cell images with small gaps [404]. The propagation algorithm works by considering the identified nuclei as seed points and determines the Voronoi region of each given seed point on a Riemann manifold with a metric defined in the local image plane [404]. Cells and nuclei touching the image boundary are negated in the process of segmenting the cells as they may not

be segmented in their entirety and could compromise accuracy of results. This is shown with nuclei touching the image boundary outlined with yellow hue and the cells touching the image boundary not outlined.

7.2.6.2 QUANTIFICATION OF SEGMENTATION DATA

Once the cells had been segmented, the morphology such as the shape, size, aspect ratio and orientation of the cell and nuclei could now be quantified. Thus a MatLab script was written to analyse the segmented data. Figure **7.2** illustrates some of the morphological parameters obtained from the segmentation process. The maximum ferret diameter (a) and the minimum ferret diameter (b) show the length and width respectively of the cell. Taking that flow (Q) direction is from left to right; the orientation of the cell is calculated by finding the angle (θ) between the major axis of the cell and the axis parallel to the flow direction. Nucleus localisation (upstream or downstream) in respect to the flow direction was determined by taking the distance between the centroid of the cell (C_1) and that of the nucleus (C_2).

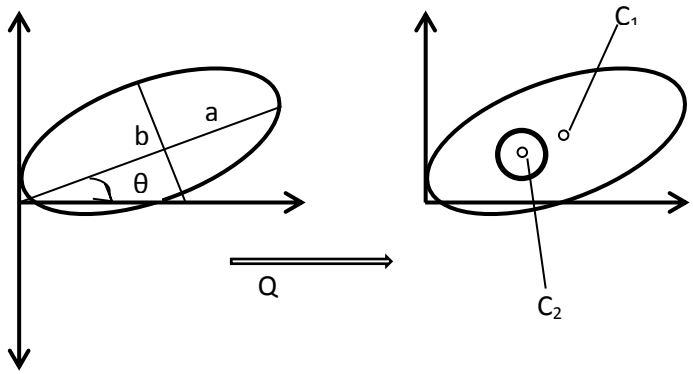

Figure 7.2 Morphological parameters produced from cell segmentation

The aspect ratio of the cell can also be calculated by dividing the minor ferret diameter by the major ferret diameter. Calculating the aspect ratio by this method produces a conceptual binary result; thus 1 represents a fully rounded cell and 0 represents a fully elongated cell.

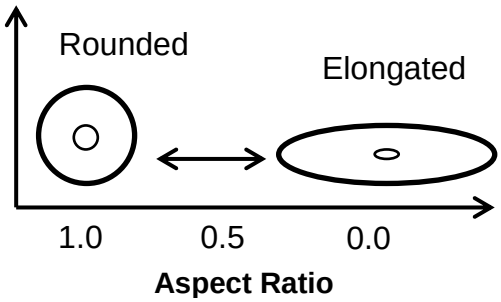

Figure 7.3 A schematic diagram to explain aspect ratio. The cell is assumed to be fully elongated when aspect ratio is 0.0 and cobblestone when the aspect ratio is 1.0

7.3 RESULTS

Images of all stained cells taken were at the centre plane of the stamped glass slides. This ensured that results were then comparable. Additionally all images were taken with a x10 objective lens of the confocal microscopy and a standard scale bar of $200\ um$ was set on the images.

7.3.1 CELLS EXPOSED TO HYDROSTATIC PRESSURE

Results presented in figure **7.4** shows HUVECs response to $100\ mmHg$ hydrostatic pressure only seeded at a cell density of $10{,}114\ cells/cm^2$ for time durations 0, 6, 12 and 24 hours.

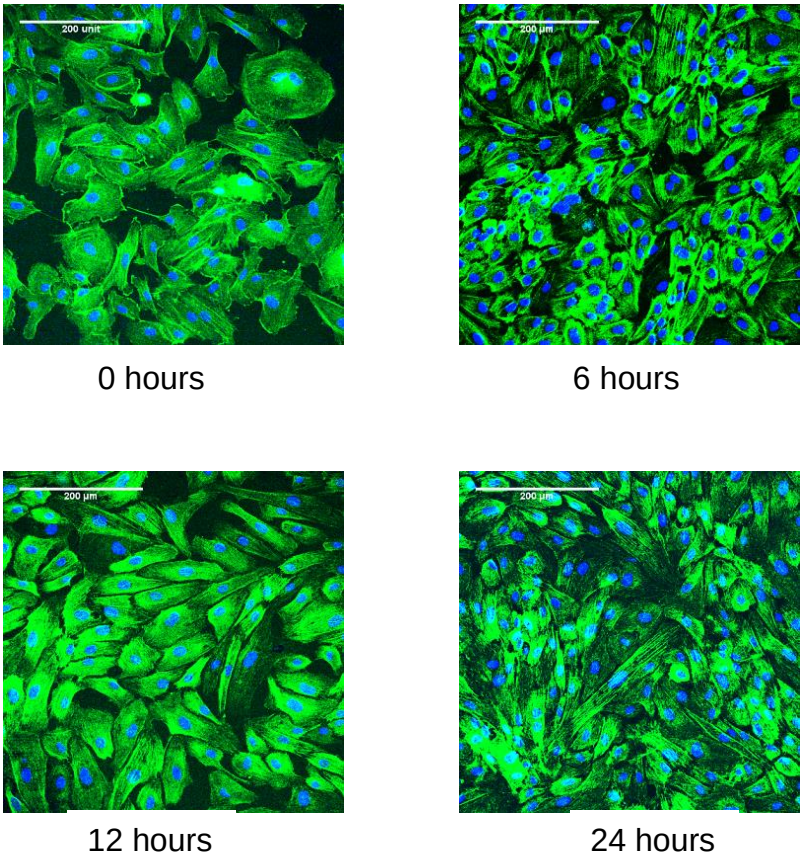

Figure 7.4 Images of stained HUVECs after exposure to sustained hydrostatic pressure 100mmHg and fluid stress of 0.07 Pa for 0, 6, 12 and 24 hours. Direction of fluid stress is from left to right.

As observed in figure **7.4**, local cell density of cell increased with increasing time when cells were exposed to sustained hydrostatic pressure.

HUVECs morphological response to the hydrostatic pressure when seeded at a cell density of $26{,}700\ cells/cm^2$ is shown in figure **7.5** below. Cell images shown here are in respect to specific locations on the cell-structure interaction model.

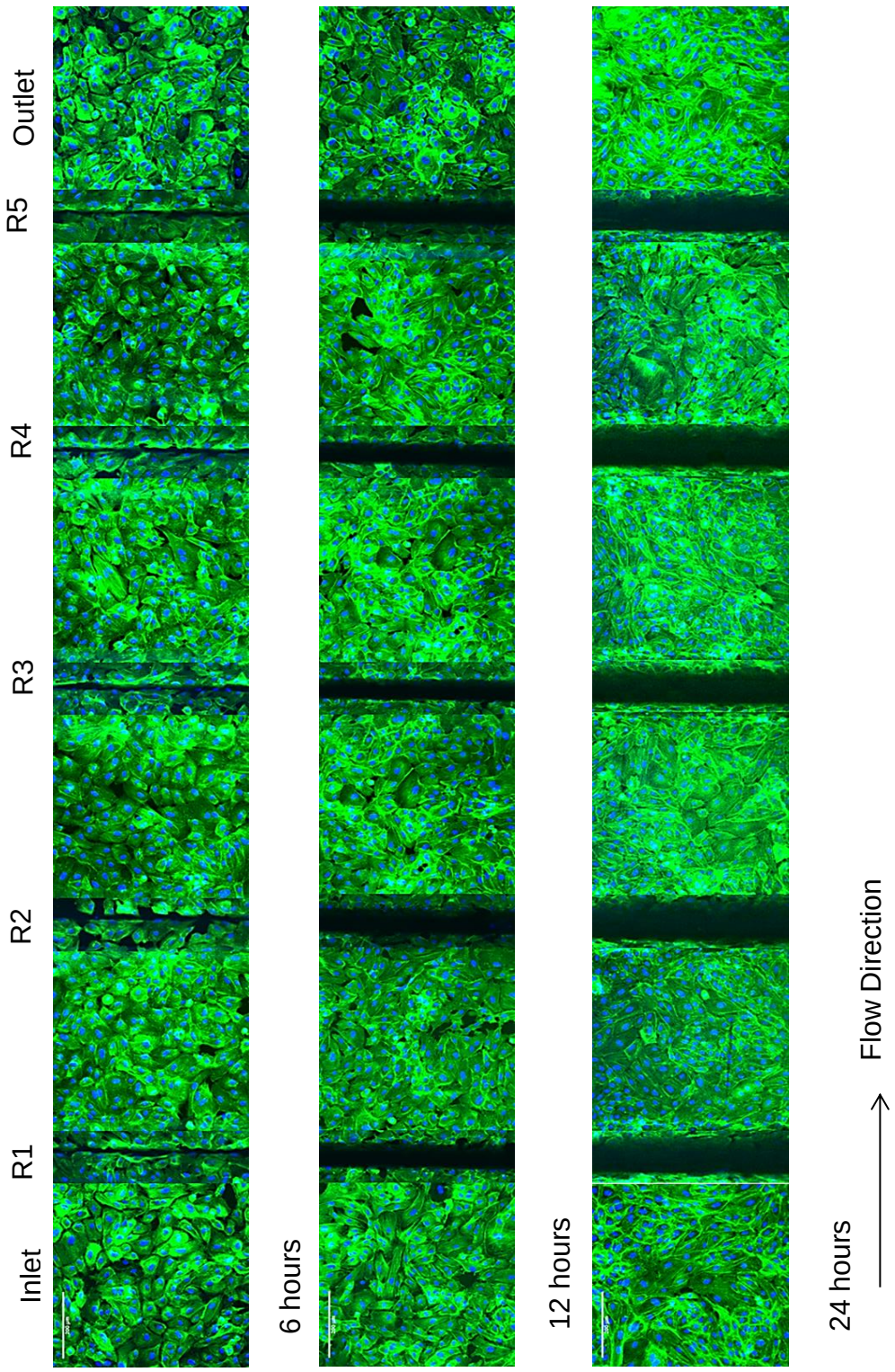

Figure 7.5 Stained HUVECs after exposure to sustained hydrostatic pressure 100mmHg and fluid stress of 0.07 Pa for 6, 12 and 24 hours.

It is observed in figure **7.5** that HUVECs subjected to hydrostatic pressure increase in local cell density with increase in time. Also cells show random orientation and are cobblestone shaped.

7.3.2 CELLS EXPOSED TO COMBINED FLUID STRESS AND HYDROSTATIC PRESSURE

The results presented in figure **7.6a** shows HUVECs morphological response when subjected to combined mechanical stimuli that is LAD pulsatile flow with a mean shear stress of $2\ Pa$ and physiological hydrostatic pressure of $120/80\ mmHg$.

In figure **7.6b**, the stained cell images are of the morphological changes of HUVECs when subject to steady laminar flow that yields a shear stress of $2\ Pa$ and hydrostatic pressure of $100\ mmHg$.

The results shown in figure **7.6a** and **7.6b** were of the experiments with cells seeded at a cell density of $26{,}700\ cells/cm^2$ and run for different time durations of 6, 12 and 24 hours.

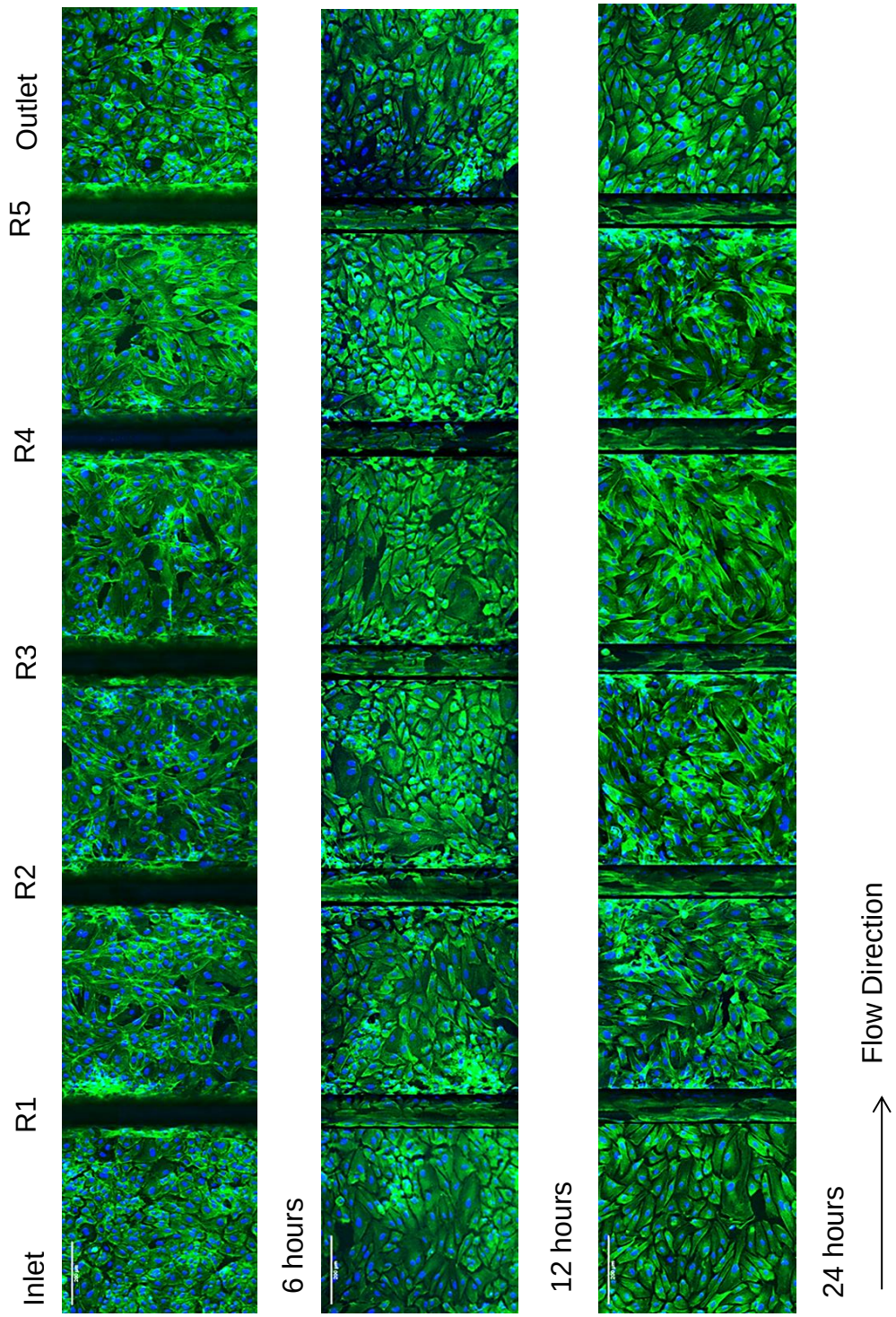

Figure 7.6a Stained HUVECs after exposure to LAD pulsatile flow and hydrostatic pressure 120/80 mmHg for 6, 12 and 24 hours. Cells appear to elongate and align more in flow direction at 12 and 24 hours in the inlet and outlet regions. Cells at 6 hours appear less elongated at the inlet and outlet.

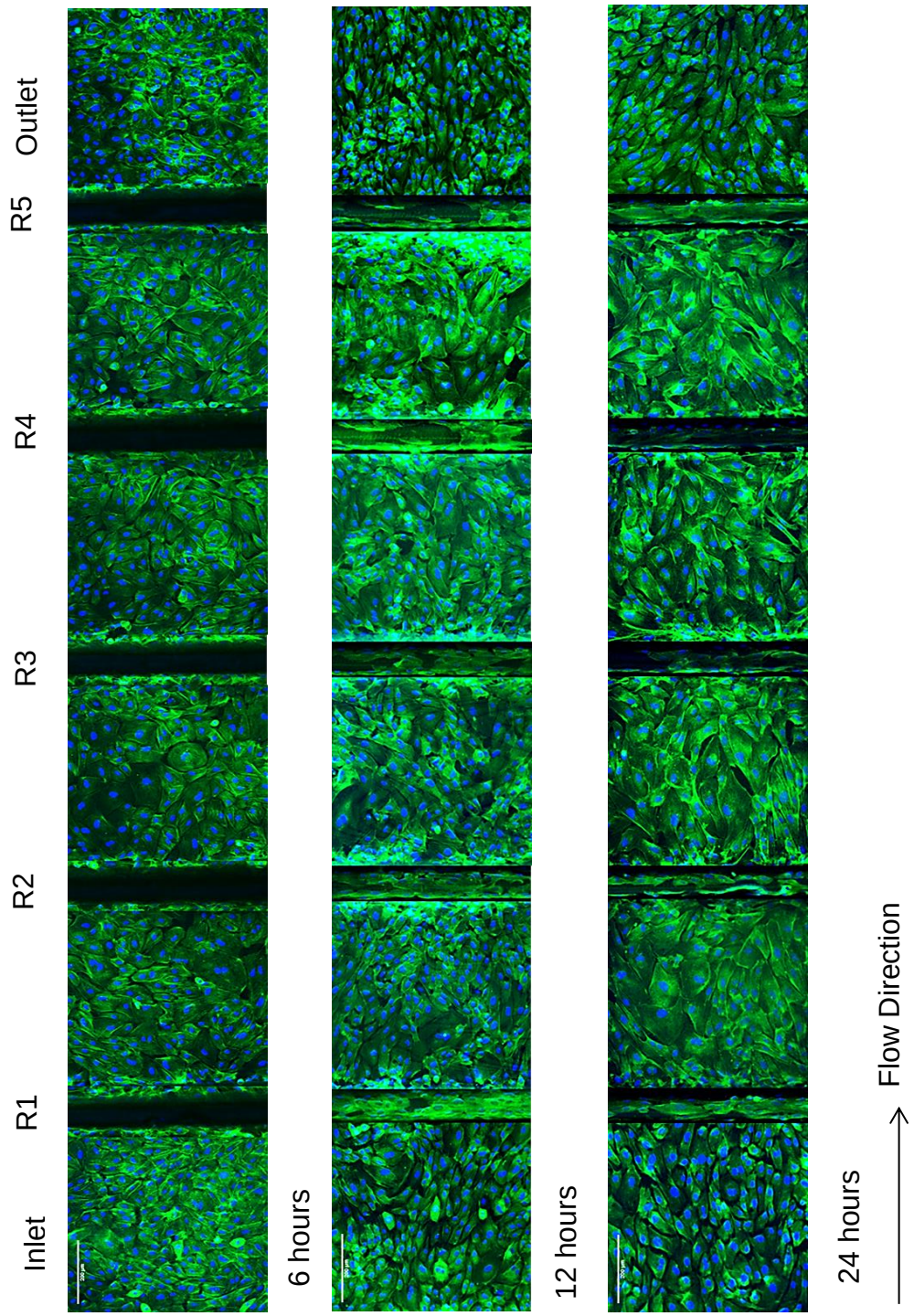

Figure 7.6b Stained HUVECs after exposure to steady flow and hydrostatic pressure 100 mmHg for 6, 12 and 24 hours. Cells appear to elongate and align more in flow direction at time 12 hours and 24 hours in the inlet and outlet regions. Cells within the ridges regions however are less aligned to flow direction. Cells are also observed on top of ridges at 12 and 24 hours.

7.3.3 MORPHOLOGICAL QUANTIFICATION

Quantifying the morphology of cells after been exposed to the desired mechanical stimuli included cell orientation distribution, aspect ratio, average nuclei and cell size, local cell density and nucleus localisation. Statistical analyses of results were expressed as the mean $\pm$ SEM (standard error mean). Statistical significance was assessed by analysis of a 2 tailed, unpaired, Student's T test with critical values of $P < 0.05$ considered significant. The number of repeat for each specific test is denoted by the letter '***n***'.

7.4 RESULT ANALYSIS II

In this section, the change in morphology of sub-confluent and confluent cultured HUVECs when exposed to only sustained hydrostatic pressures are analysed.

7.4.1 SUB-CONFLUENT CULTURED CELLS EXPOSED TO ONLY HYDROSTATIC PRESSURE

The data presented here are of the experiments conducted with cell density of $10{,}114\ cells/cm^2$ and cells exposed to hydrostatic pressure of $100\ mmHg$.

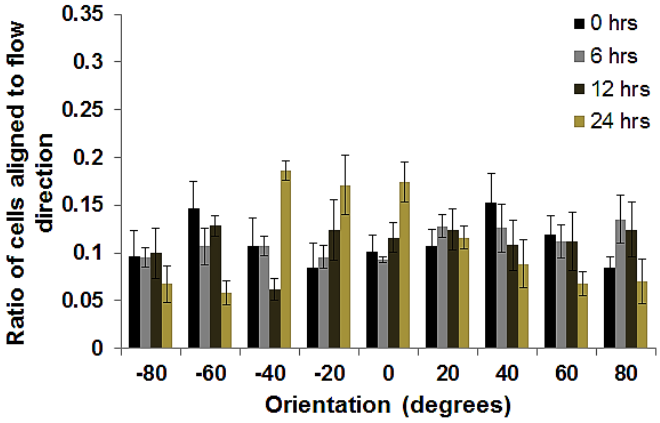

Figure 7.7a Histogram graph showing orientation of sub-confluent cultured cells exposed to hydrostatic pressure of 100 mmHg for 0, 6, 12 and 24hrs. n = 1. Error bars show SEM of 6 images. From this graph, it can be reported that HUVECs randomly orientate when subjected only to hydrostatic pressure.

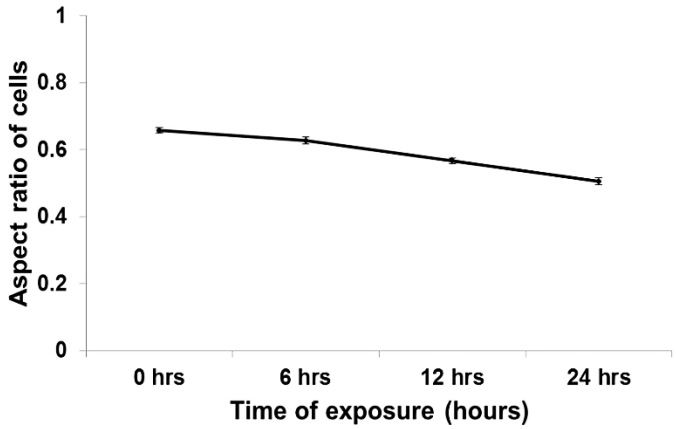

Figure 7.7b Line graph showing average aspect ratio of cells exposed to hydrostatic pressure of 100 mmHg for 0hrs, 6hrs, 12hrs and 24hrs. n = 1. Error bars show SEM of 6 images.

Analysing the graph of figure **7.7b** it could be deduced that HUVECs subjected to only hydrostatic pressure elongate. This deduction is made based on the decrease of cell aspect ratio with time under the stipulated condition.

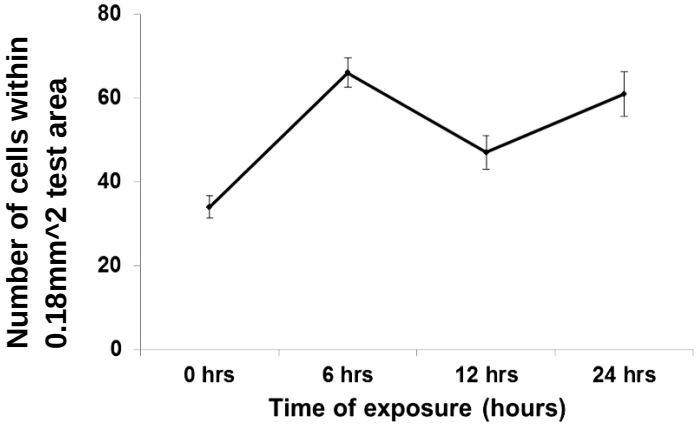

Figure 7.7c Line graph showing average number of cells within a local area of 0.18m^2 after exposure to hydrostatic pressure of 100 mmHg for 0hrs, 6hrs, 12hrs and 24hrs. n = 1. Error bars show SEM of 6 images.

From figure **7.7c**, it is realised that HUVECs only under hydrostatic pressure, first increase in density (0 to 6 hours) and then later decrease (6 to12 hours). There is however a surge in cell density again (12 to 24 hours).

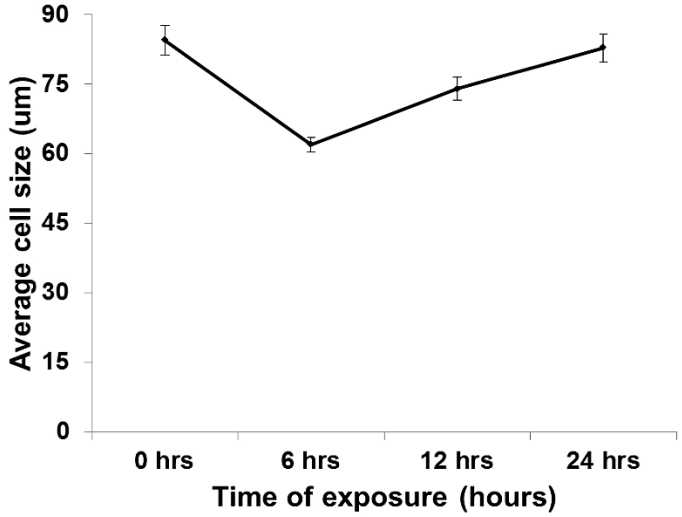

Figure 7.7d Line graph showing average cell size in microns of cells exposed to hydrostatic pressure of 100 mmHg for 0hrs, 6hrs, 12hrs and 24hrs. n = 1. Error bars show SEM of 6 images.

From the graph shown in figure **7.7d**, it is seen that cells initially decrease in size and thereafter increase in size with respect to time when subjected to only hydrostatic pressure.

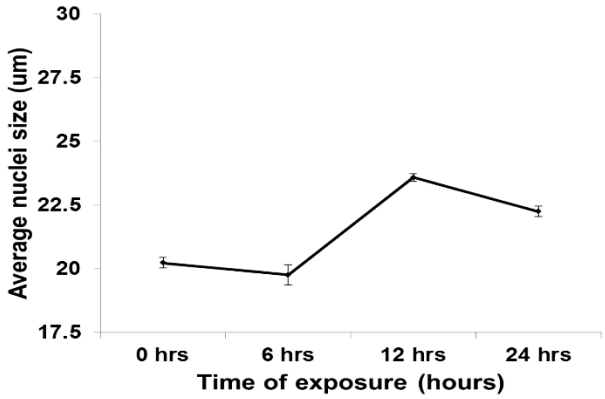

Figure 7.7e Line graph showing average nuclei size in microns of cells exposed to hydrostatic pressure of 100 mmHg for 0hrs, 6hrs, 12hrs and 24hrs. n = 1. Error bars show SEM of 6 images.

From figure **7.7e**, it is observed that there is a relative change in nuclei size when subjected only to hydrostatic pressure for different timescales.

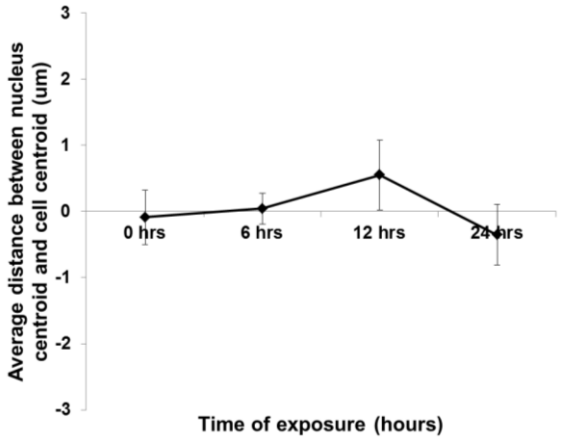

Figure 7.7f Line graph showing average distance between centroid of nucleus and cell centroid after cells exposed to hydrostatic pressure of100 mmHg for 0hrs, 6hrs, 12hrs and 24hrs. n = 1. Error bars show SEM of 6 images.

From the graphs shown in figure **7.7f**, it is observed that there is an increase in the average distance between the nucleus centroid and cell centroid of cell between 0 – 12 hours. This then tend to decrease at time 12 hours to 24 hours.

7.4.2 CONFLUENT CELLS EXPOSED TO ONLY HYDROSTATIC PRESSURE

The data below are of the experiments conducted with cell density of $26{,}700\ cells/cm^2$ and cells exposed to hydrostatic pressure of $100\ mmHg$.

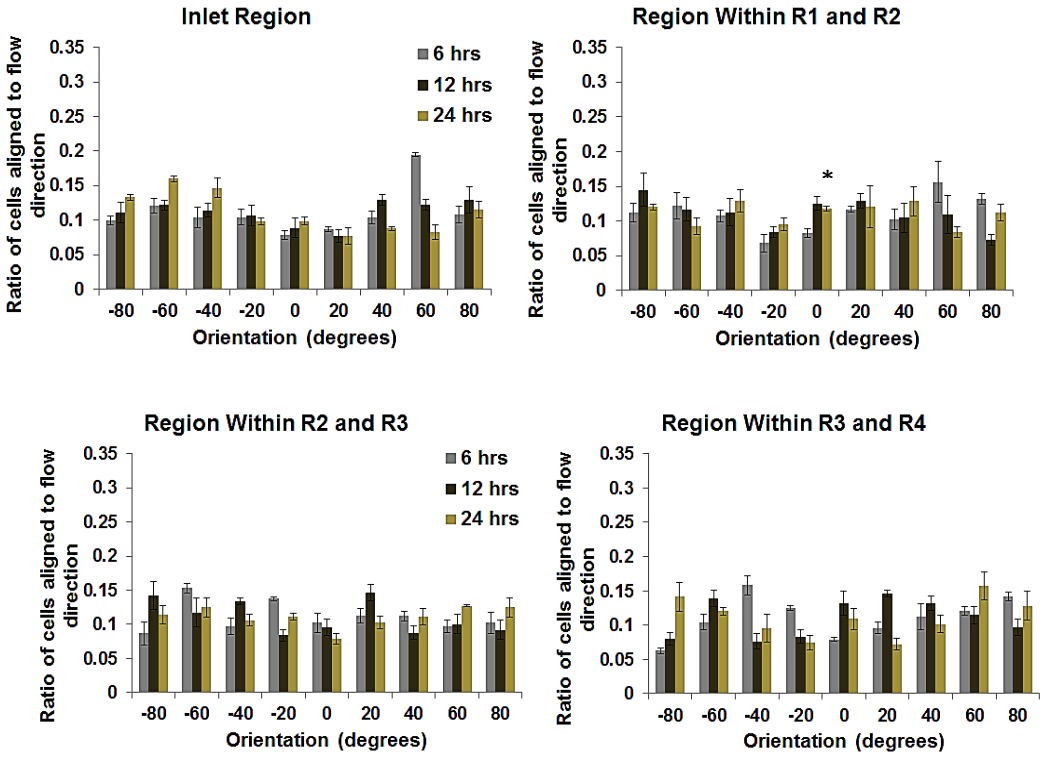

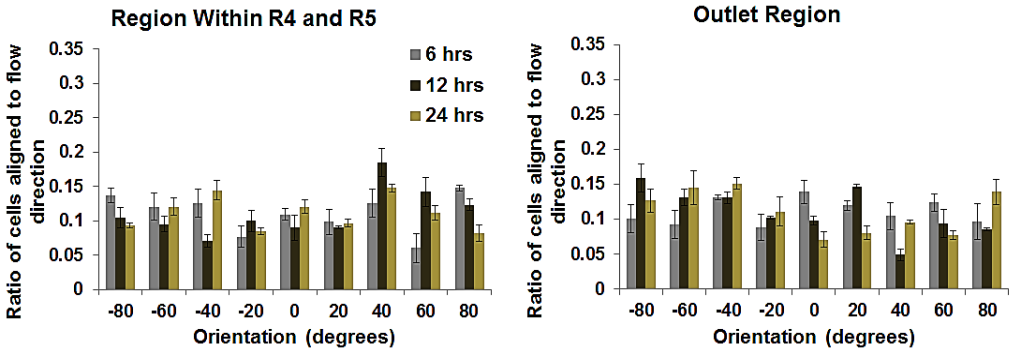

Figure 7.8a Histogram showing orientation of cells exposed to hydrostatic pressure of 100 mmHg for 6hrs, 12hrs and 24hrs. n = 3. Error bars show SEM of 3 images. * $p < 0.05$ vs. 6 hrs and ** $p < 0.05$ vs. 12 hrs.

From the histogram graph presented in figure **7.8a**, it is seen that confluent cultured cells tend to orientate randomly when subjected to only hydrostatic pressure for different timescales.

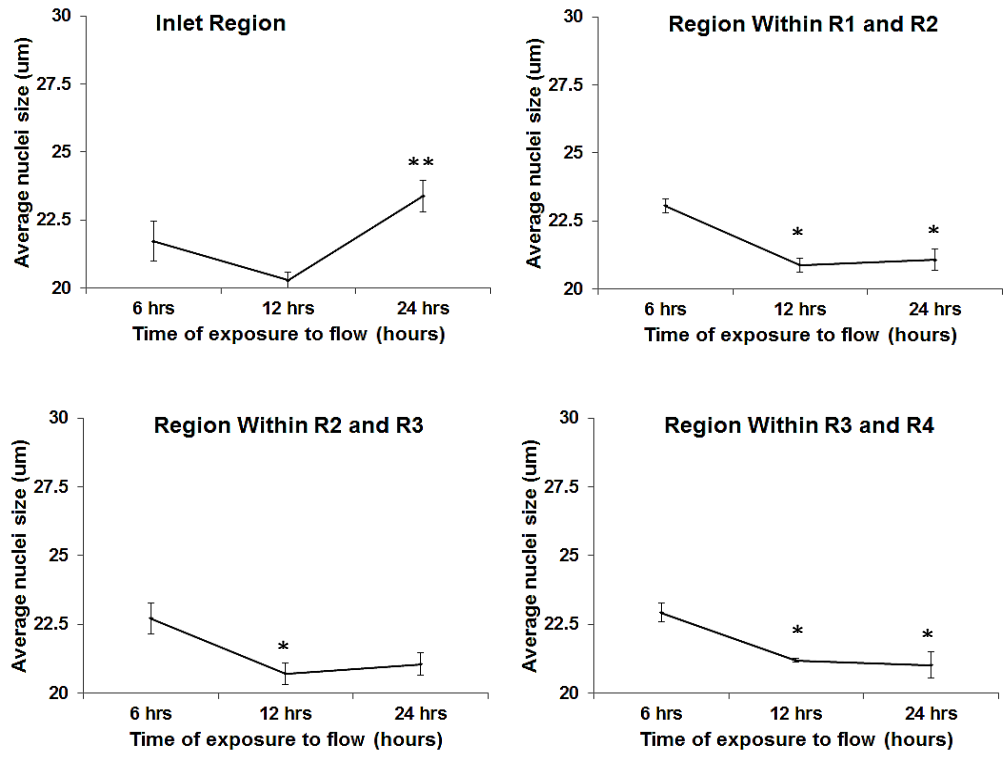

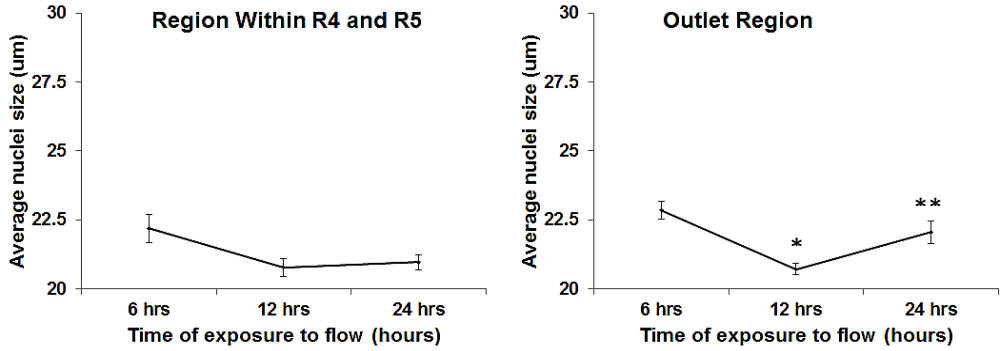

Figure 7.8b Line graph showing average nuclei size in microns of cells exposed to hydrostatic pressure of 100 mmHg for 6hrs, 12hrs and 24hrs. n = 3. Error bars show SEM of 3 images. * $p < 0.05$ vs. 6 hrs and ** $p < 0.05$ vs. 12 hrs.

It is observed from the above graph that the nuclei size of confluent cells generally tend to decrease when exposed to only hydrostatic pressure with increase timescales.

Analysis of the density of the cells when HUVECs were exposed to hydrostatic pressure for 6 hours, 12 hours and 24 hours are presented below.

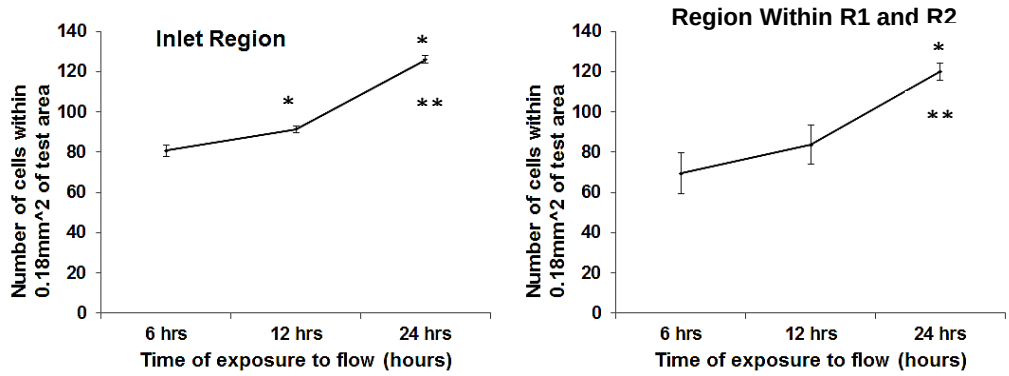

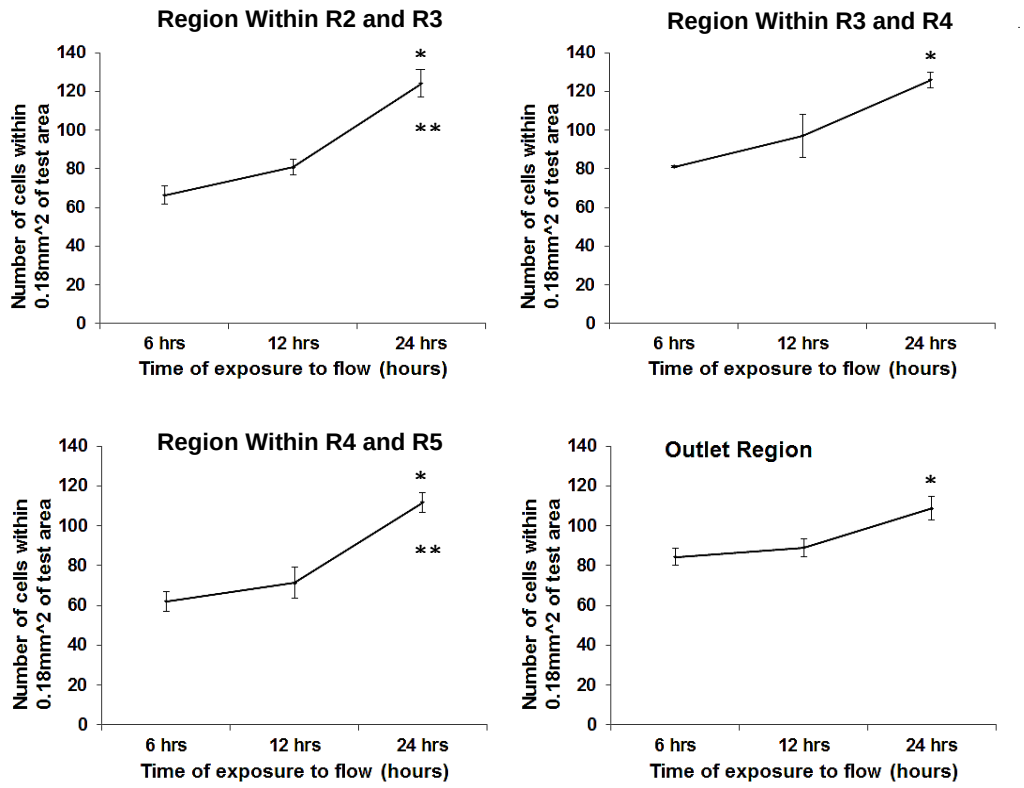

Figure 7.8c Line graph showing average number of cells within a local area of 0.18mm^2 after exposure to hydrostatic pressure of 100 mmHg for 6hrs, 12hrs and 24hrs. n = 3. Error bars show SEM of 3 images. * $p < 0.05$ vs. 6 hrs and ** $p < 0.05$ vs. 12 hrs.

Analysis of the graphs in figure **7.8c** show a general increase in cell density with increasing time periods when cells are subjected to hydrostatic pressure.

7.5 DISCUSSION TO RESULT ANALYSIS II

7.5.1 HUVECs EXPOSED TO SUSTAINED HYDROSTATIC PRESSURE

Most studies investigating into the effects of hydrostatic pressure on ECs

morphology have reached similar conclusions that ECs elongate without prime cell orientation upon exposure to sustained hydrostatic pressure in a time dependent manner [313, 405]. Also, the actin cytoskeleton is reported to rearrange to form a multilayer structure. So it was as expected when results of HUVECs seeded under both sub-confluent $(10{,}114\ cells/cm^2)$ and confluent $(26{,}700\ cells/cm^2)$ conditions and exposed to hydrostatic pressure of $100\ mmHg$ exhibited similar behaviour. The random orientations of cells when subjected to hydrostatic pressure are shown in figures **7.7a** and **7.8a** respectively. In figure **7.9**, cell elongation is marked by decrease in aspect ratio. Below is a comparative quantitative analysis of HUVECs aspect ratio under sub-confluent and confluent conditions for 6, 12 and 24 hours.

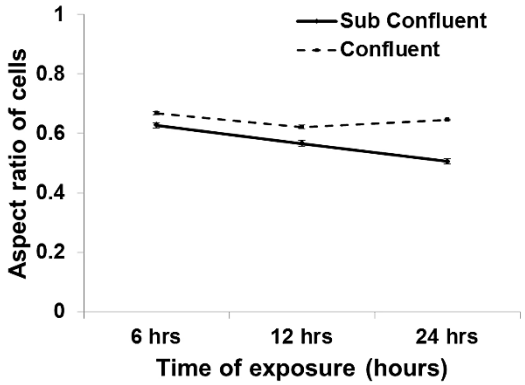

Figure 7.9 Line graph of average aspect ratio of HUVECs exposed to sustained hydrostatic pressure of 100 mmHg for 6, 12 and 24 hours. Cells under confluent condition before exposure to stimulus (dashed lines) and cells under sub-confluent conditions before exposure to stimulus (straight line). Error bars show SEM of 6 images.

From figure 7.9 it is shown that there is a general decrease of cell aspect ratio with increase in time when subjected to hydrostatic pressure. This decrease in aspect ratio of cell can be related to as cell elongation. Thus

continuous exposure of cells to hydrostatic pressure may cause cells to elongate. It is important however to note that morphology and cell function of sub confluent ECs could differ to those of confluent conditions [406, 407]. Hence results of ECs under different confluency and exposed to hydrostatic pressure were careful analysed.

Under sub-confluent conditions, HUVECs were inferred to elongate as the aspect ratio of the cells were quantified to decrease with time (average aspect ratio of ~ 0.65 at 0 hours to ~0.55 at 24 hours) as shown in figure **7.7b**. Also in figure **7.7c**, local density of cells within a 0.18mm^2 area is observed to increase with time with only a slight decrease in local density at 12 hours. However results from the cells seeded under confluent conditions and exposed to same hydrostatic pressure level showed a general increase in local cell density from 6 hours to 24 hours. This data is presented in figure **7.8c**. From these results, it is implied that hydrostatic pressure promotes ECs proliferation, a deduction which has been made in several similar investigations [313, 405, 408, 409]. The hypothesis that the confluency level of ECs could affect experimental findings was justified when HUVECs seeded at confluent conditions were qualitatively demonstrated to form multilayers as opposed to ECs under sub-confluent condition at 24 hours. Shown below are the figures of stained HUVECs exposed to hydrostatic pressure for 24 hours when seeded under two different confluent levels. Multilayering of HUVECs is suggested in the image 'A' of figure **7.10** as distinct features of the cells actin cytoskeletons reported to be only present in multi-layered cell form were noticed.

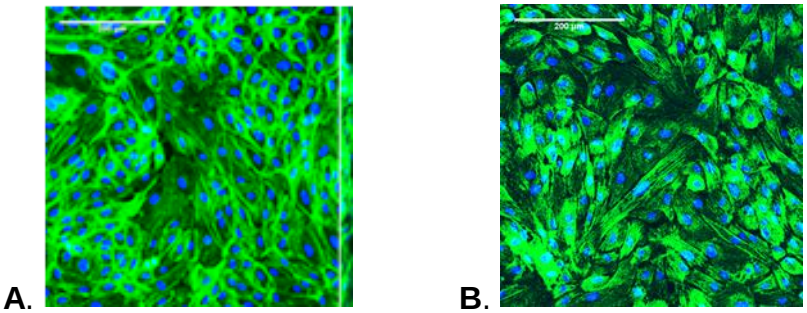

Figure 7.10 HUVECs exposed to sustained hydrostatic pressure of 100 mmHg for 24 hours. Cells under confluent conditions (A) and cells under sub-confluent conditions (B) before exposure to stimulus.

The multi-layered cells were observed to have more apparent thicker and central actin filaments (shown by the very bright green fluorescence around the cells) and formed a web-like structure. Additionally, cells further away from the substrate level are seen to exhibit cobblestone morphology characteristics. It is also realised that the dense peripheral band around the cells were lost and thus the shape of the cells were not evidently defined. These observations are analogous to that reported by Salwen et al. [410]. In contrast to these observations, the non-confluent cell result showed ECs which were more elongated, had parallel actin fibres and thin actin filaments. Salwen et al. [410] also reported similar ECs characteristics of non-confluent cells exposed to hydrostatic pressures of $1.5\ cmH_2O, 5\ cmH_2O, 10\ cmH_2O$ respectively for 7 days at substrate level.

Furthermore, it is observed that the nuclei size of the confluent cells exposed to the sustained pressure tend to decrease (from ~ 23um to ~ 21um) whilst that of the non-confluent cell increased (~ 20.5um to ~ 22.5um) with time. This is evidently shown in figures **7.8b** and **7.7e** respectively. It would therefore be of great interest in future to investigate if these changes in the nuclear form would evoke different and/or similar gene activities of the cells. Thus this investigation might provide some insight into the influence of

pressure on endothelialisation after PCI. It is thought that as the nucleus is a mechanosensor, its nuclear form just like the cytoskeleton of the cell is induced by mechanical stimuli. Thus understanding the changes to the nucleus morphology as a result of stress could be indicative of the process by which cells respond to physical stimuli; for instance cell migration. In fact, the roles played by cytoskeleton and nucleus in ECs mechanotransduction are not mutually exclusive and may be interrelated through complex cellular pathways [411].

To further quantify the nuclei response to mechanical stimuli and in this case sustained hydrostatic pressure, the average distance between the centroid of cell and its respective nucleus was determined. Figure **7.11** shows a schematic line graph representation of this measured average distance between the cell and nucleus at 6, 12 and 24 hours.

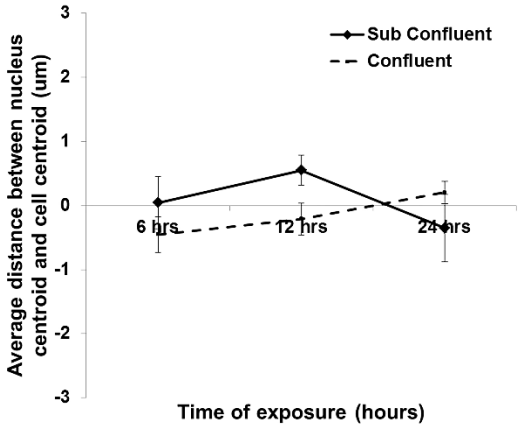

Figure 7.11 Line graph showing average distance between the centroid of cells and nucleus for HUVECs under confluent condition (dashed lines) and HUVECs under sub-confluent conditions (straight line) exposed to hydrostatic pressure of 100 mmHg for 6, 12 and 24 hours. Error bars show SEM of 6 images.

A negative distance is defined as the centroid of the nucleus displaced downstream to the centroid of the entire cell. From figure **7.11** it is thus

observed that nuclei centroid of HUVECs under confluent conditions tend to move from the downstream of the cell (~ -0.45um) at 6 hours to the upstream of the cell (~ 0.20um) at 24 hours. On the other hand, HUVECs under the non-confluent condition showed the centroid of the nuclei to initially move upstream (~ 0.3um at 6 hours to ~ 0.5um at 12 hours) before being located downstream of the cell (~ -0.35 um) at 24 hours.

7.6 RESULT ANALYSIS III

In this section, the change in cell morphology when exposed to a combination of fluid stress and hydrostatic pressure is analysed

7.6.1 CELLS EXPOSED TO COMBINED LAD FLUID STRESS AND HYDROSTATIC PRESSURE

The data below are of the experiments conducted with cell density of $26{,}700\ cells/cm^2$ and cells exposed to LAD pulsatile flow waveform with a mean shear stress of $2\ Pa$ and hydrostatic pressure of $120/80\ mmHg$.

The following set of data show the statistical analysis of cell orientation to flow direction within $\pm\ 10°$ and $\pm\ 20°$ respectively. In addition to these data provided, analyses of the other morphological features of cells such as cell size and aspect ratio are also presented.

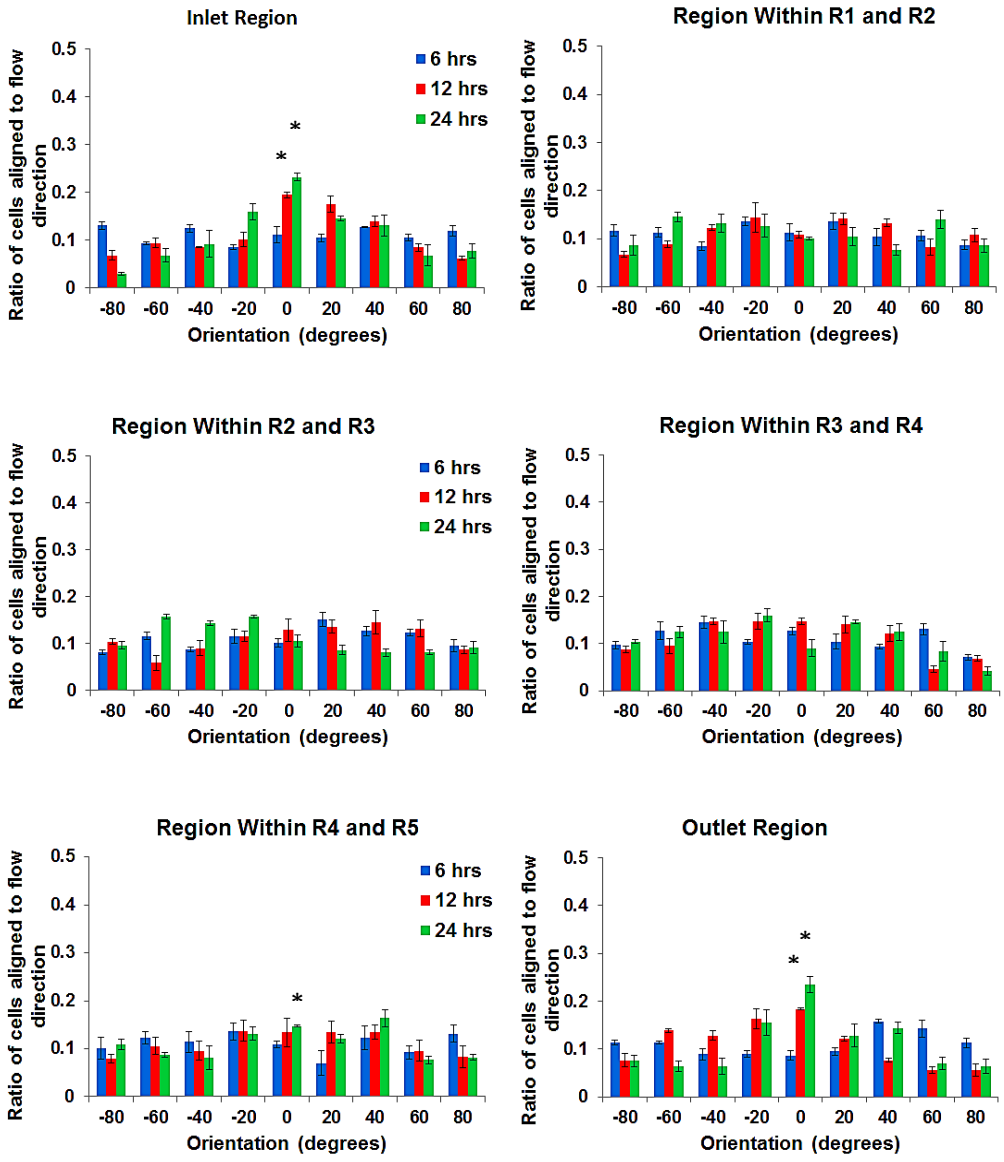

Figure 7.12ai Histogram showing orientation of cells exposed to LAD pulsatile flow and hydrostatic pressure of 120/80 mmHg for 6hrs, 12hrs and 24hrs. n = 3. SEM of 3 images. Statistical significance of cells aligned in $\pm$ 10° of flow direction; * $p < 0.05$ vs. 6 and ** $p < 0.05$: 24 hrs vs. 12 hrs.

Analyses of the graphs in figure **7.12ai** show that cells align more in the $\pm$ 10° of flow direction with increase time period under LAD pulsatile flow simulation at the inlet and outlet regions. However, cell alignment to $\pm$ 10°

of flow direction within inter-ridges regions are not pronounced but generally are more randomly aligned.

The analysis of cell alignment to $\pm 20°$ of flow direction under LAD pulsatile flow is presented below.

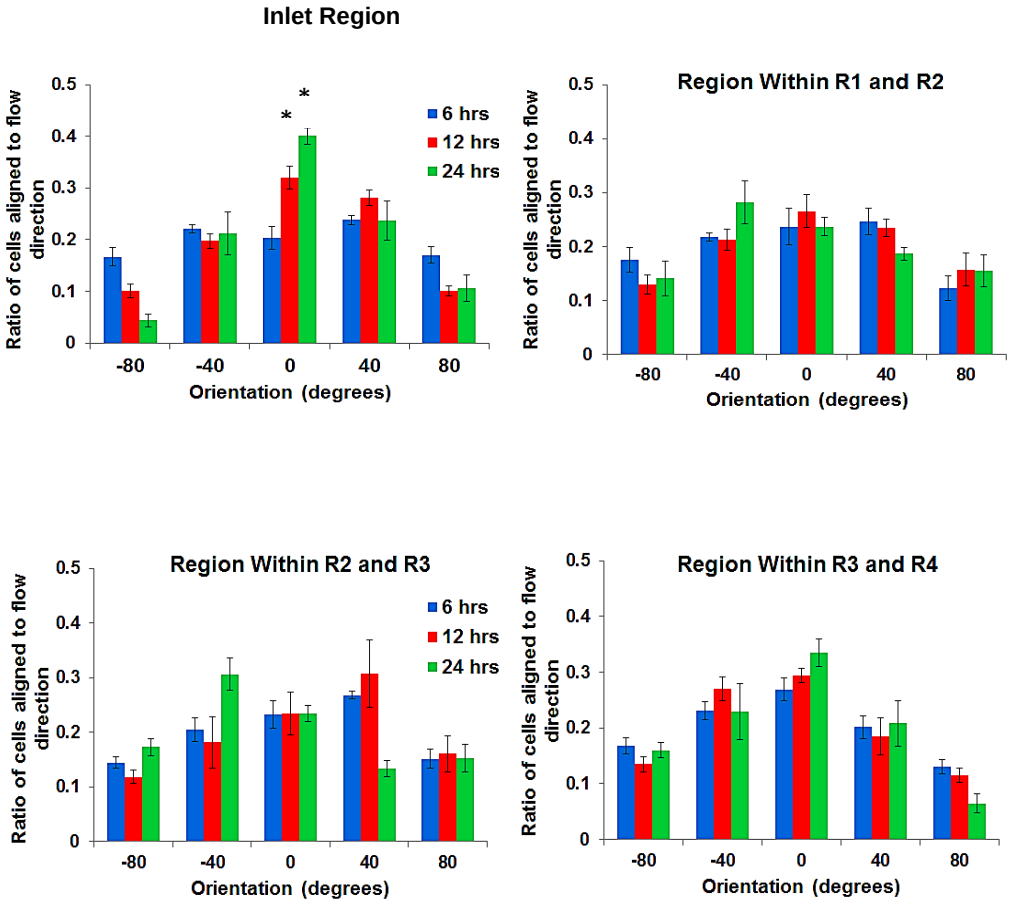

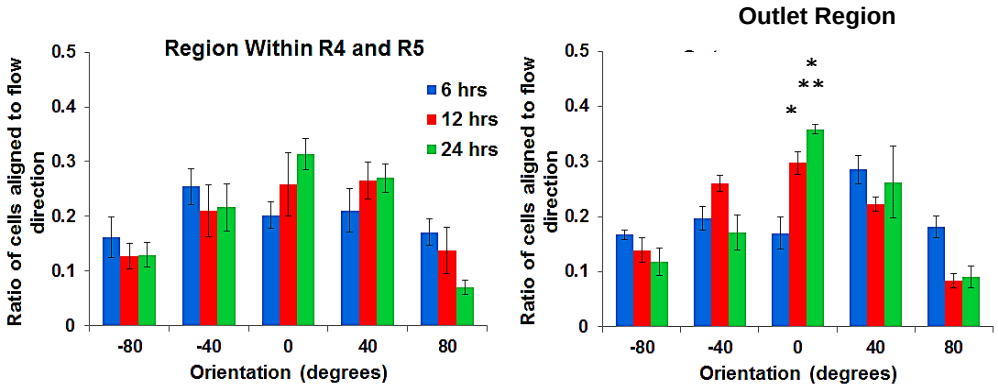

Figure 7.12aii Histogram showing orientation of cells exposed to LAD pulsatile flow and hydrostatic pressure of 120/80 mmHg for 6hrs, 12hrs and 24hrs. n = 3. SEM of 3 images. Statistical significance of cells aligned in $\pm$ 20° of flow direction; * p < 0.05 vs. 6 hrs and ** p < 0.05: 24 hrs vs. 12 hrs.

Analyses of the graphs in figure **7.12aii** show that cells tend to align more in the $\pm$ 20° of flow direction with increase time period under LAD pulsatile flow simulation at the inlet and outlet regions. More so, this time dependent increase in the cell alignment to the $\pm$ 20° of flow direction is statistically significant. Conversely, although there may be a time dependent increase of cells aligned to $\pm$ 20° of flow direction within inter-ridges regions, these increments are not statistically significant.

The next set of data show the aspect ratio of cells when subjected to a combination of LAD pulsatile fluid shear stress and hydrostatic pressure of $120/80\ mmHg$.

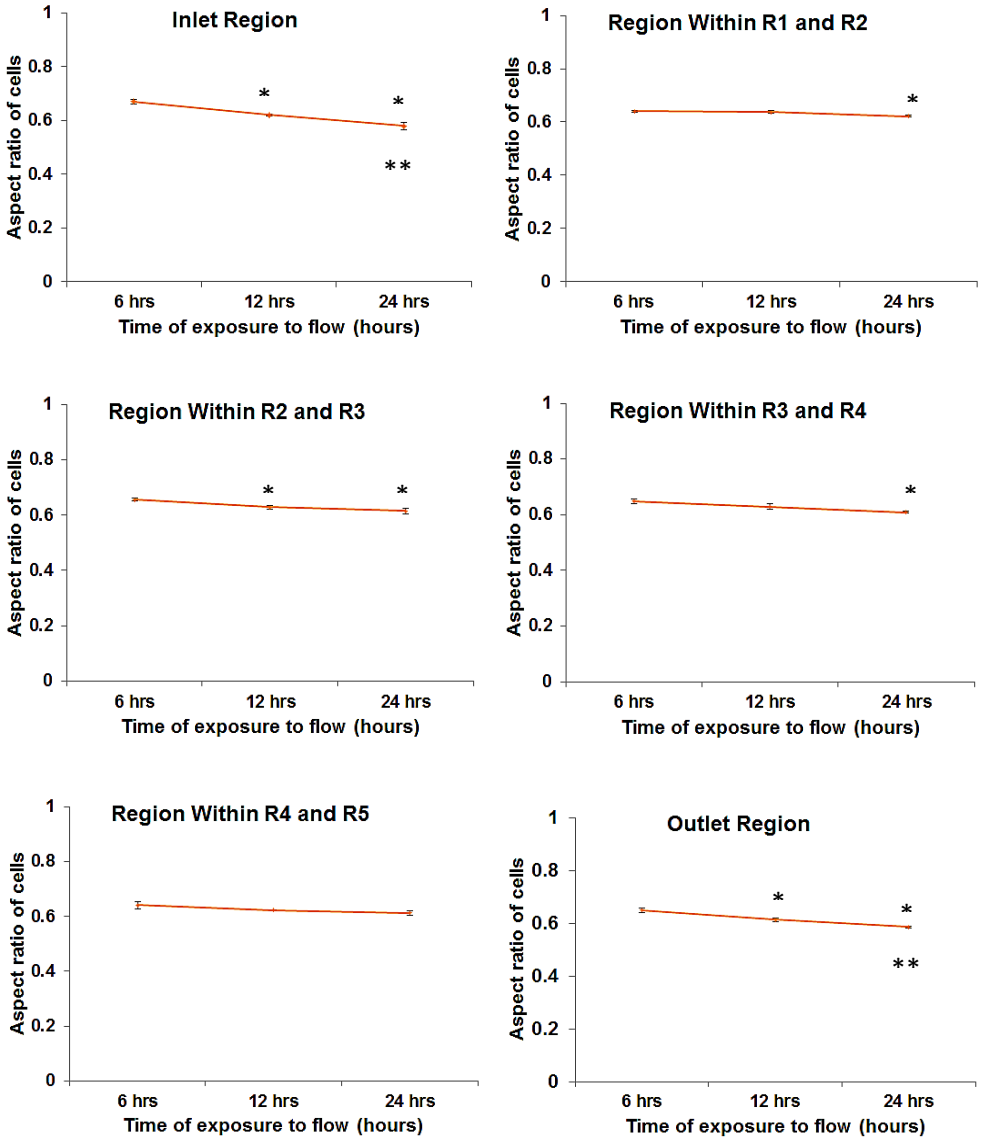

Figure 7.12b Line graph showing average aspect ratio of cells exposed to LAD pulsatile flow and hydrostatic pressure of 120/80 mmHg for 6hrs, 12hrs and 24hrs. n = 3. SEM of 3 images. * $p < 0.05$ vs. 6 hrs and ** $p < 0.05$: 24 hrs vs. 12 hrs.

It is observed from figure **7.12b**, that there is a time dependent gentle decrease of aspect ratio of cells. However at the inlet and outlet regions, the decrease in aspect ratio of cell with respect to time is generally statistically significant.

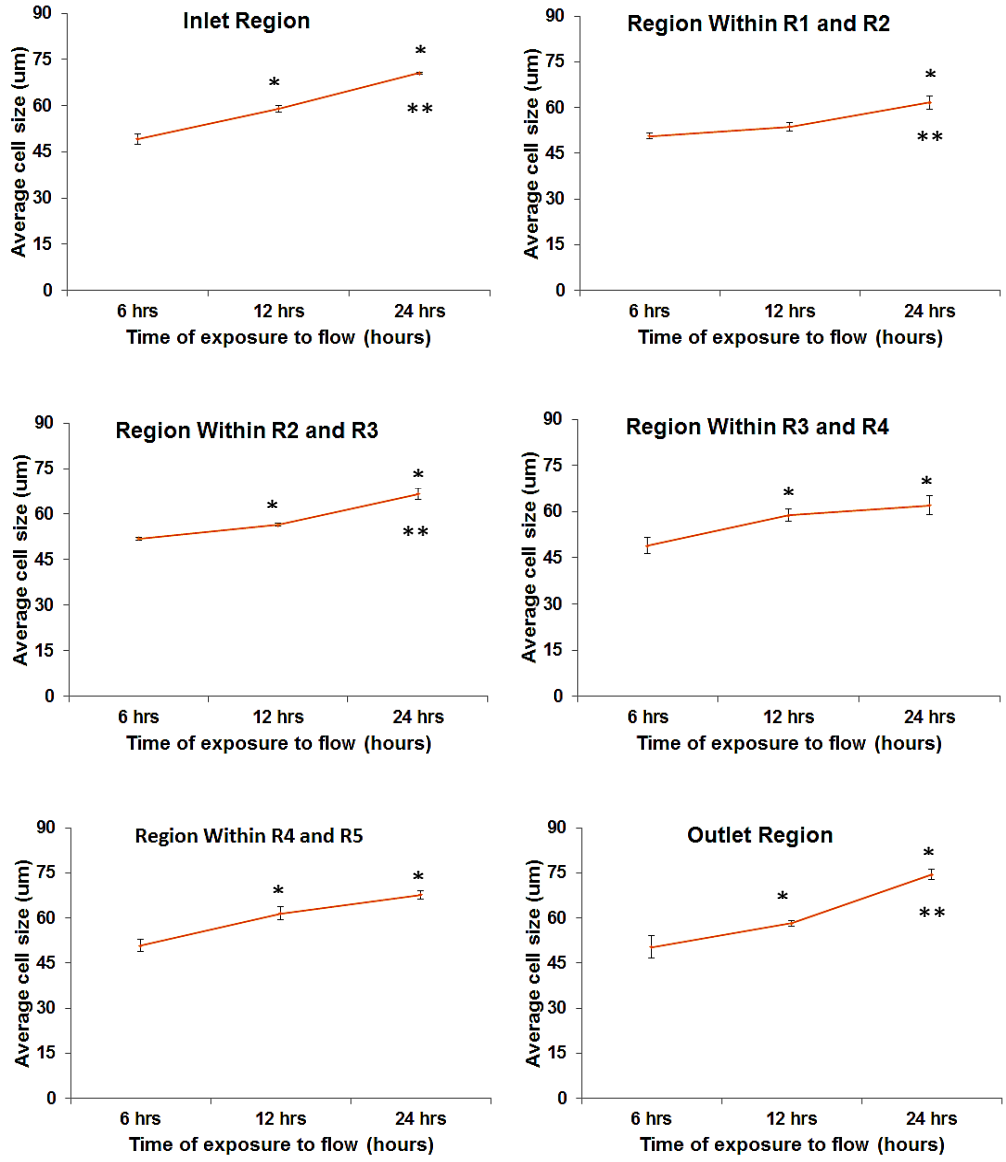

Figure 7.12c Line graph showing average cell size in microns of cells exposed to LAD pulsatile flow and hydrostatic pressure of 120/80 mmHg for 6hrs, 12hrs and 24hrs. n = 3. Error bars show SEM of 3 images. * $p < 0.05$ vs. 6 hrs and ** $p < 0.05$: 24 hrs vs. 12 hrs.

It is noted from figure **7.12c** that there is a general statistically significant time dependent increase of cell size across the experimental model when subjected to the stipulated fluid stress and hydrostatic pressure.

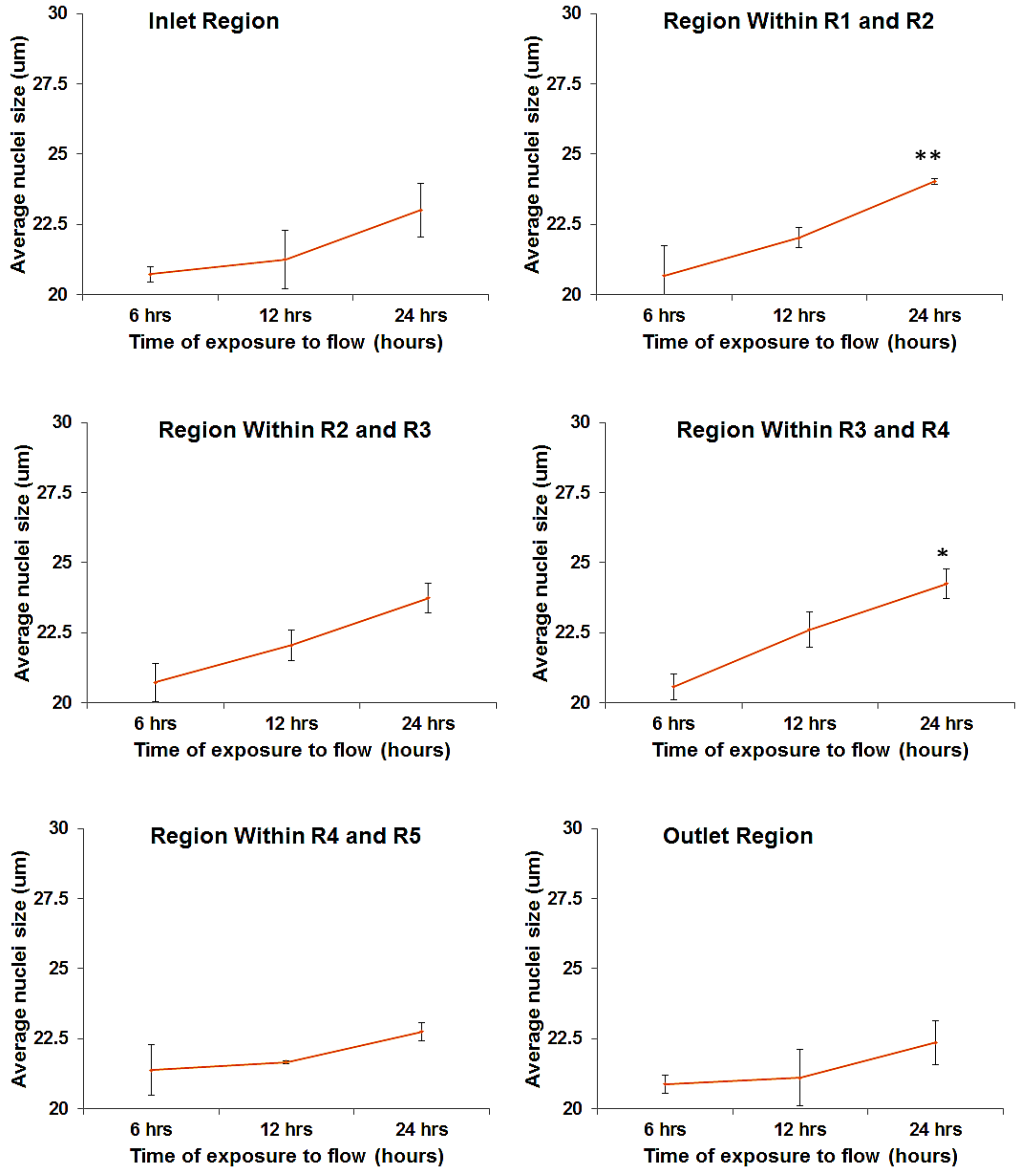

Figure 7.12d Line graph showing average nuclei length size in microns of cells exposed to LAD pulsatile flow and hydrostatic pressure of 120/80 mmHg for 6hrs, 12hrs and 24hrs. n = 3. Error bars show SEM of 3 images. * $p < 0.05$ vs. 6 hrs and ** $p < 0.05$: 24 hrs vs. 12 hrs.

The graphs presented in figure 7.12d show an increase in nuclei size with increase in time period although generally not statistically significant when subjected to stipulated fluid stress and hydrostatic pressure.

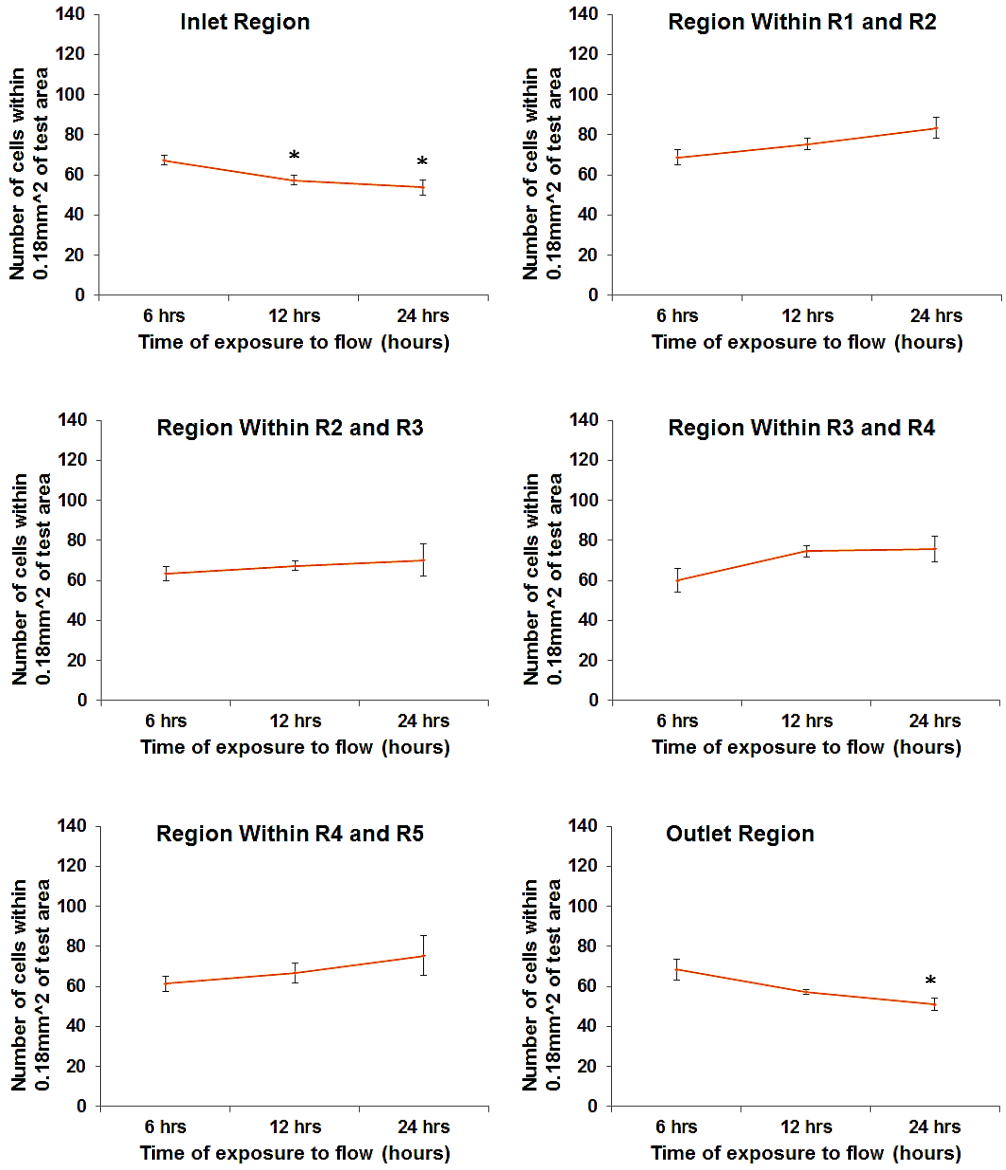

Figure 7.12e Line graph showing average number of cells within a local area of 0.18mm^2 after exposure to LAD pulsatile flow and hydrostatic pressure of 120/80 mmHg for 6hrs, 12hrs and 24hrs. n = 3. Error bars show SEM of 3 images. * $p < 0.05$ vs. 6 hrs and ** $p < 0.05$: 24 hrs vs. 12 hrs.

It is noticed from the graphs presented in figure **7.12e** that local cell density tend to decrease at the inlet and outlet regions whilst there is a gentle increase in local cell density within the inter-ridges regions.

7.6.2 CELLS EXPOSED TO COMBINED STEADY FLUID STRESS AND HYDROSTATIC PRESSURE

The data below are of the experiments conducted with cell density of $26{,}700\ cells/cm^2$ and cells exposed to steady laminar flow of a shear stress of $2\ Pa$ and hydrostatic pressure of $100\ mmHg$.

The following set of data show the statistical analysis of cell orientation to flow direction within $\pm 10°$ and $\pm 20°$ respectively. In addition to these data provided, analyses of the aspect ratio of cells and cell size are also presented.

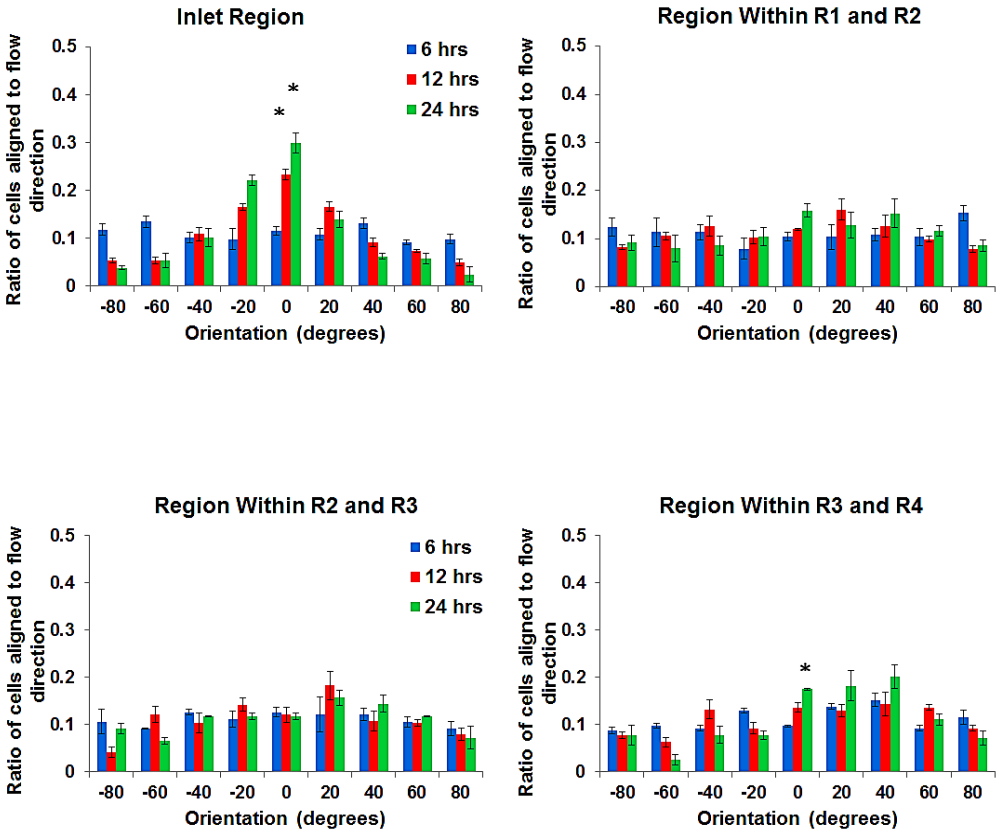

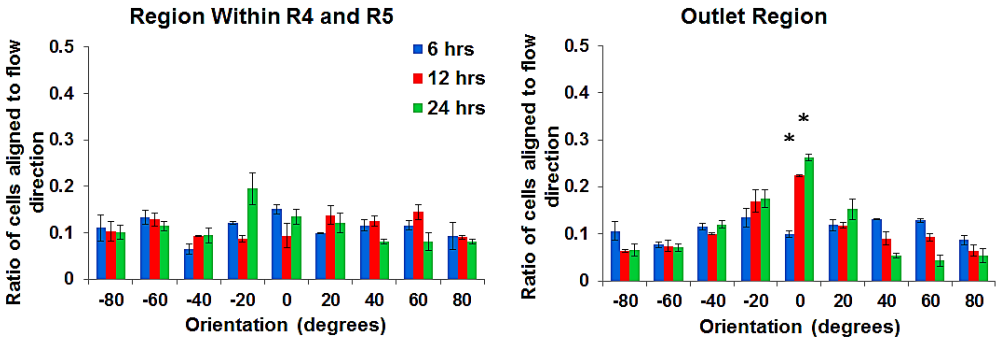

Figure 7.13ai Histogram showing orientation of cells exposed to steady flow and hydrostatic pressure of 100 mmHg for 6hrs, 12hrs and 24hrs. n = 3. SEM of 3 images. Statistical significance of cells aligned in $\pm 10°$ of flow direction; * $p < 0.05$ vs. 6 hrs and ** $p < 0.05$: 24 hrs vs. 12 hrs.

Analyses of the graphs in figure **7.13ai** show that cells tend to align more in the $\pm 10°$ of flow direction in a time dependent manner at the inlet and outlet regions under steady flow simulation. However, cell within ridges regions are noticed to be generally randomly aligned.

The analysis of cell alignment to $\pm 20°$ of flow direction under steady flow is presented below.

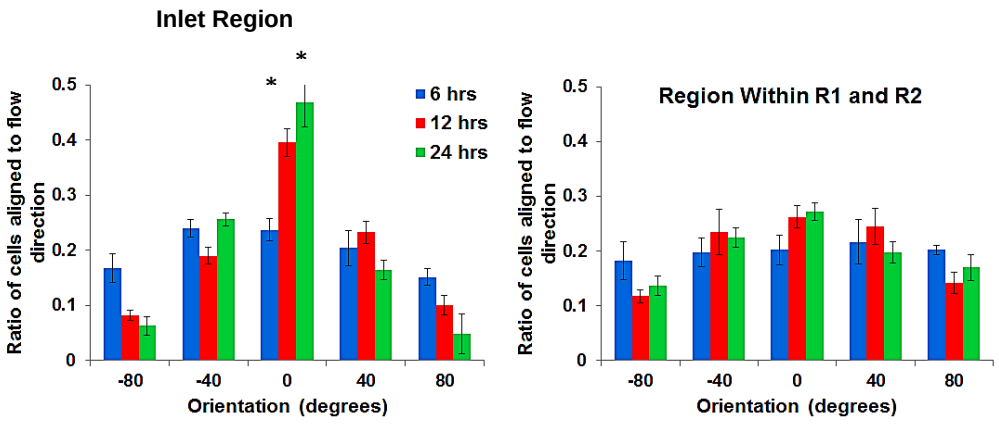

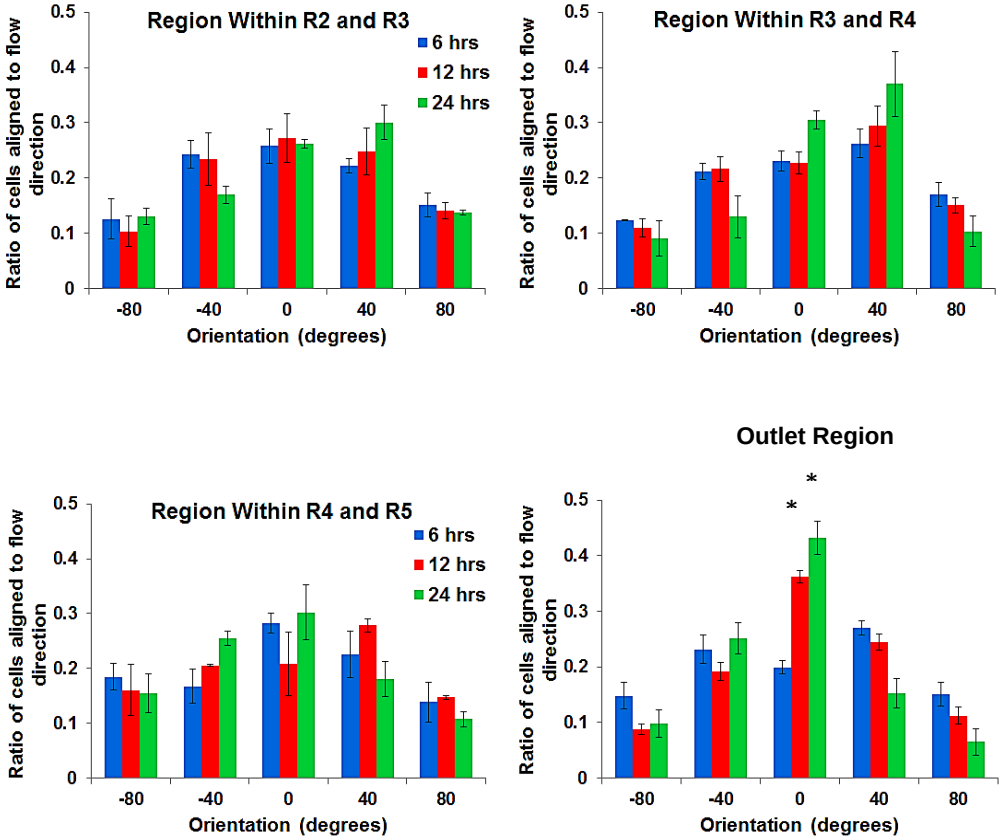

Figure 7.13aii Histogram showing orientation of cells exposed to steady flow and hydrostatic pressure of 100 mmHg for 6hrs, 12hrs and 24hrs. n = 3. SEM of 3 images. Statistical significance of cells aligned in $\pm 20°$ of flow direction; * $p < 0.05$ vs. 6 hrs and ** $p < 0.05$: 24 hrs vs. 12 hrs.

Analyses of the graphs in figure **7.13aii** show that cells tend to align more in the $\pm 20°$ of flow direction with increasing timescale under steady flow simulation at the inlet and outlet regions. More so, this time dependent increase in the cell alignment to the $\pm 20°$ of flow direction is statistically significant. Conversely, although there may be a time dependent increase of cells aligned to $\pm 20°$ of flow direction within inter-ridges regions, this increment is not statistically significant.

The next set of data show the aspect ratio of cells when subjected to a combination of steady fluid stress and hydrostatic pressure of $120/80\ mmHg$.

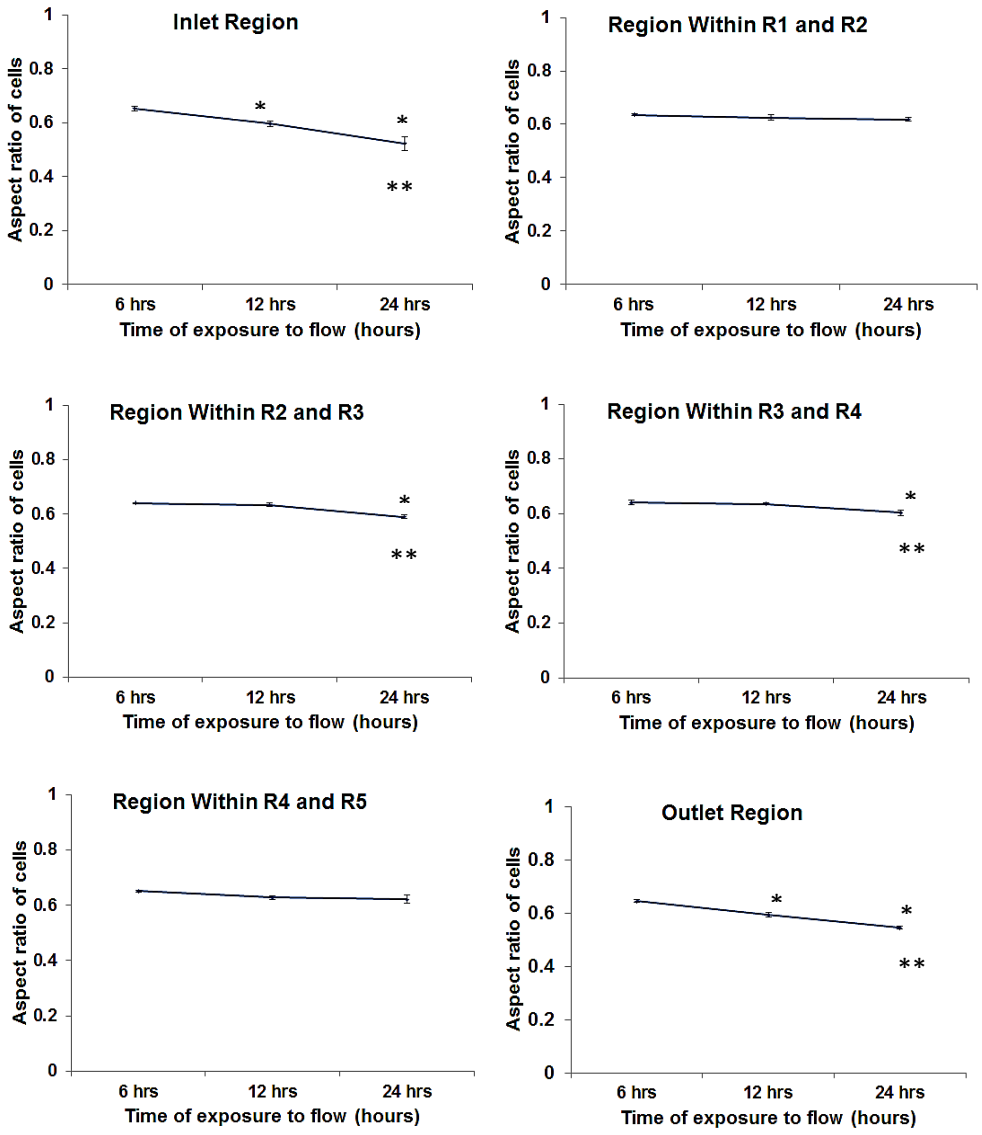

Figure 7.13b Line graph showing average aspect ratio of cells exposed to steady flow and hydrostatic pressure of 100 mmHg for 6hrs, 12hrs and 24hrs. n = 3. SEM of 3 images. * $p < 0.05$ vs. 6 hrs and ** $p < 0.05$: 24 hrs vs. 12 hrs. From figure **7.13b** it is noted that generally there is a time dependent decrease of cell aspect ratio. Nonetheless, this decrease in cell

aspect ratio is slightly more pronounced at inlet and outlet regions.

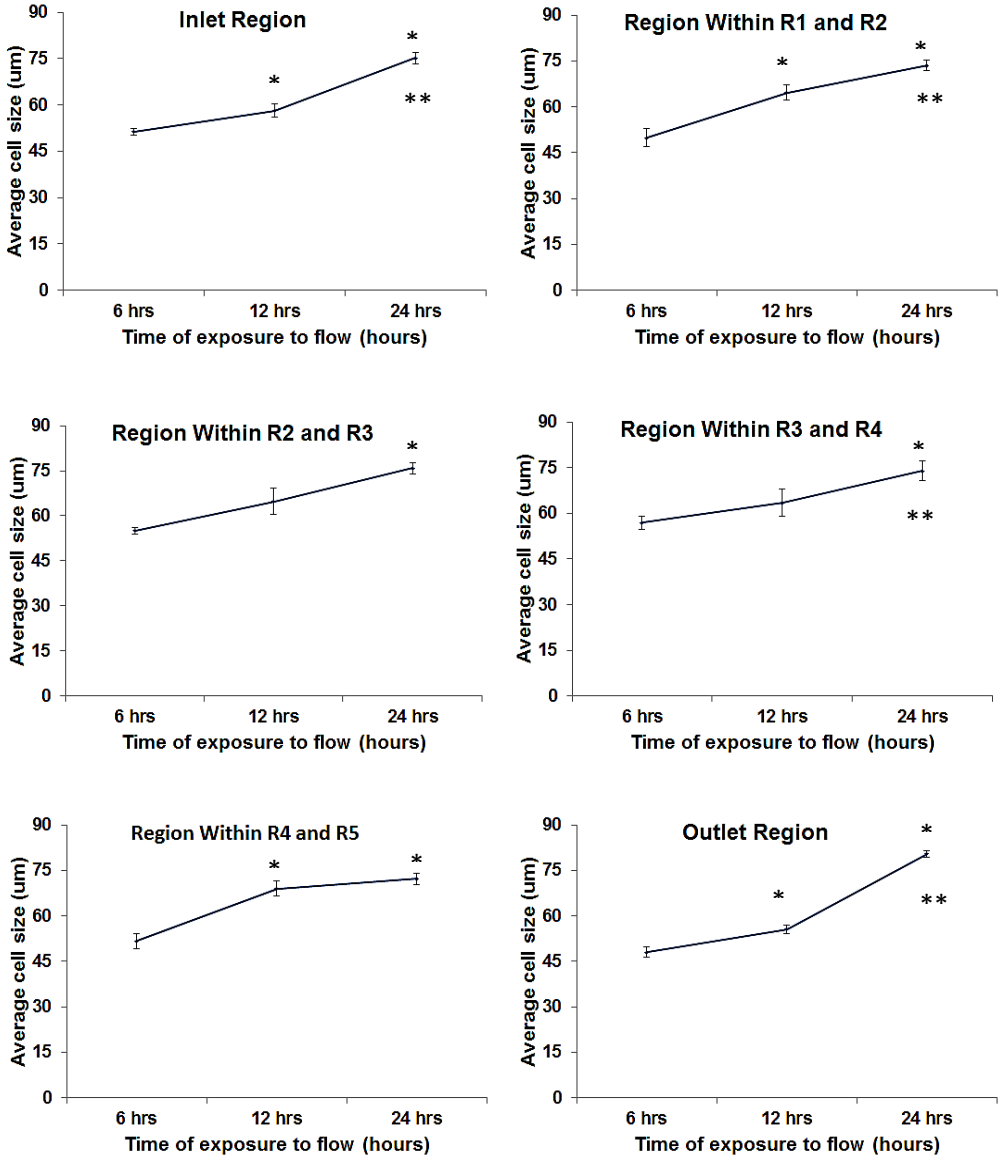

Figure 7.13c Line graph showing average cell size in microns of cells exposed to steady flow and hydrostatic pressure of 100 mmHg for 6hrs, 12hrs and 24hrs. n = 3. Error bars show SEM of 3 images. * $p < 0.05$ vs. 6 hrs and ** $p < 0.05$: 24 hrs vs. 12 hrs.

From data produced in figure **7.13c**, it is generally seen that average cell size tend to increase with increasing timescale under steady flow simulation. This cell size increment with time is statistically significant.

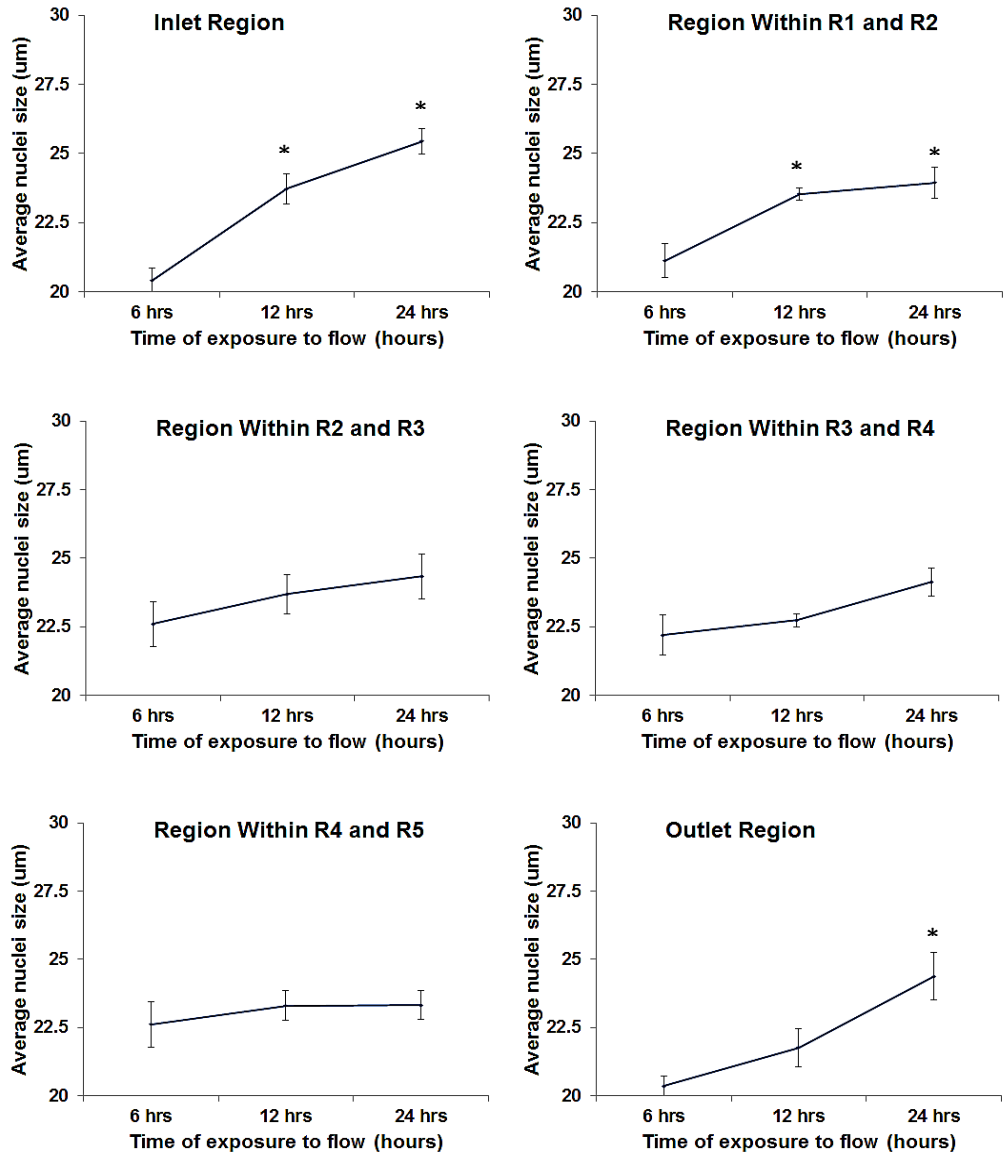

Figure 7.13d Line graph showing average nuclei length size in microns of cells exposed to steady flow and hydrostatic pressure of 100 mmHg for 6hrs, 12hrs and 24hrs. n = 3. Error bar show SEM of 3 images. * $p < 0.05$ vs. 6 hrs

and ** $p < 0.05$: 24 hrs vs. 12 hrs.

From the graphs presented in figure 7.13d, increase in nuclei size is seen to be time dependent although this phenomenon is more pronounced at the inlet and outlet regions.

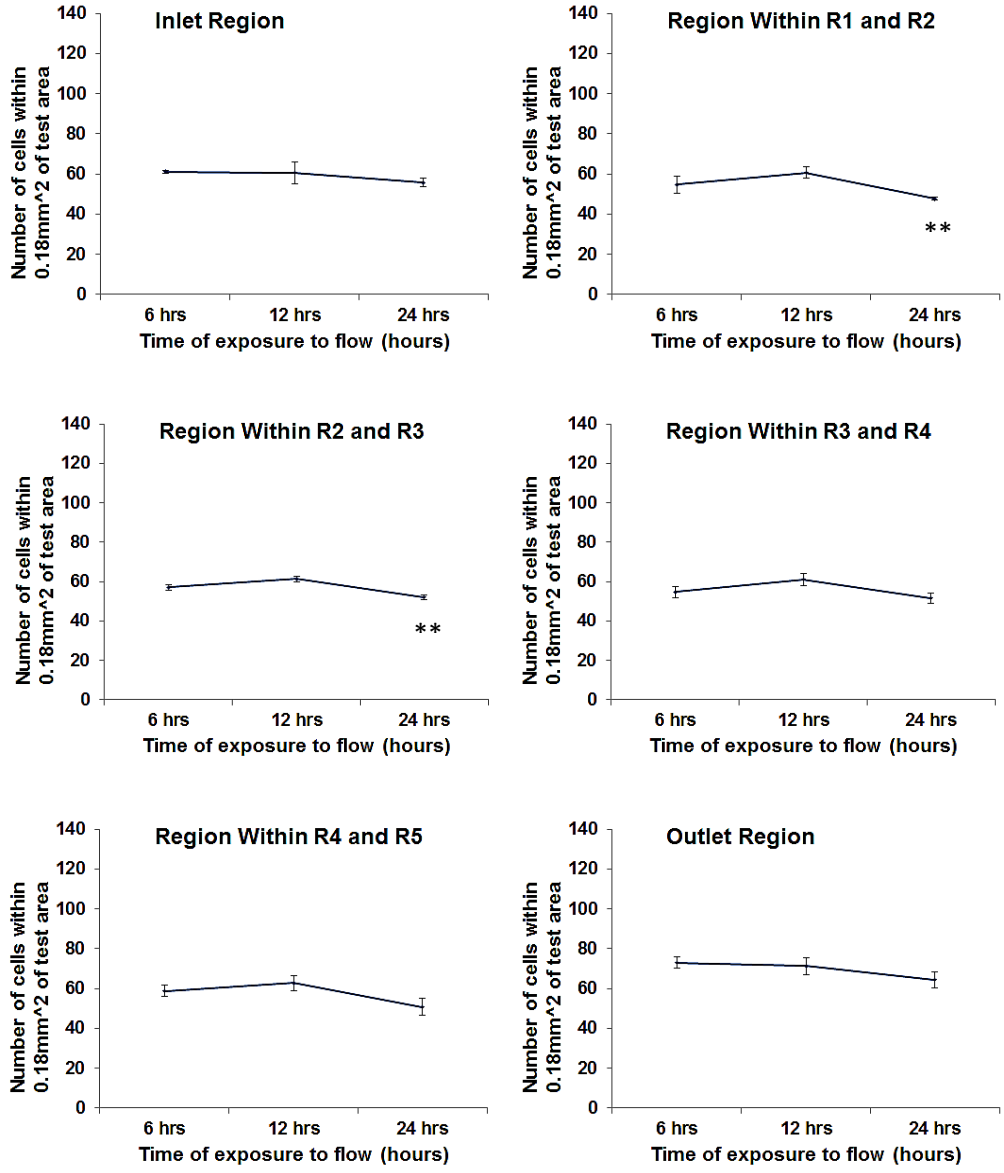

Figure 7.13e Line graph showing average number of cells within a local area

of 0.18mm^2 after exposure to steady flow and hydrostatic pressure of 100 mmHg for 6hrs, 12hrs and 24hrs. n = 3. Error bars show SEM of 3 images. * $p < 0.05$ vs. 6 hrs and ** $p < 0.05$: 24 hrs vs. 12 hrs.

From the data presented in figure **7.13e**, the local cell density is seen to somewhat decrease with increase in time. This decrement however is generally not statistically significant.

7.6.3 RESULTS COMPARING STEADY FLOW VS. LAD PULSATILE FLOW VS. HYDROSTATIC PRESSURE CONDITIONS

The data below are of the experiments conducted with cell density of $26{,}700\ cells/cm^2$ and cells exposed to different flow and pressure conditions as discussed in this section.

Comparative statistical analysis of cell orientation to flow direction within $\pm 10°$ with respect to the different flow conditions at various time points is demonstrated in addition to the analysis of the morphological features of cells.

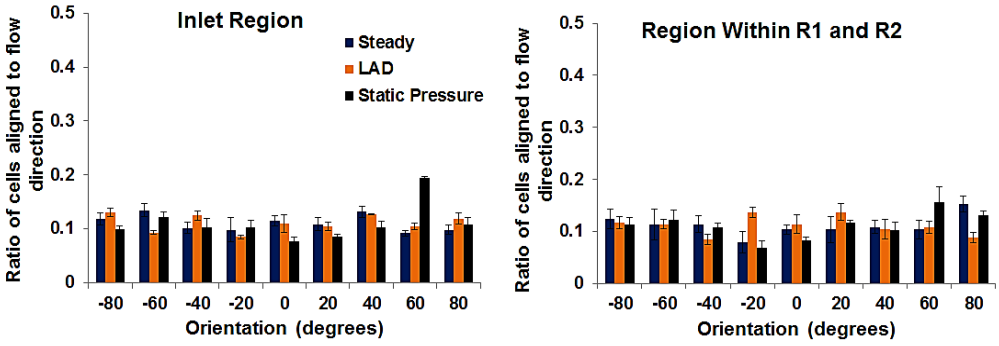

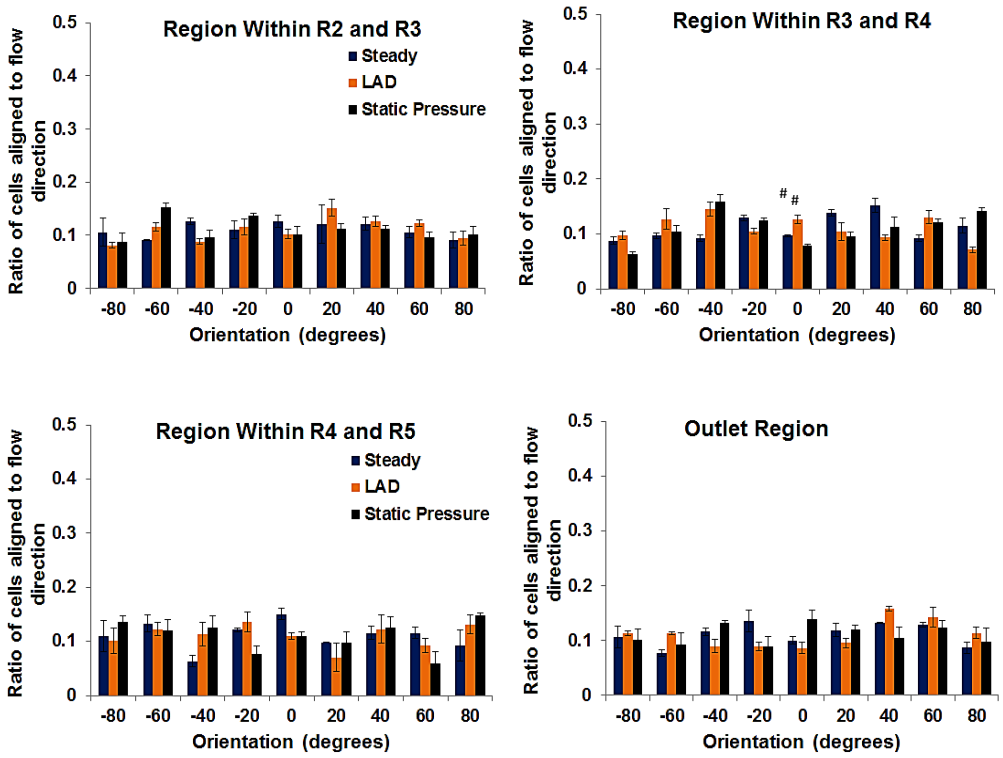

Figure 7.14ai Histogram showing orientation of cells exposed to steady, LAD pulsatile flows and sustained hydrostatic pressure for 6hrs. n = 3. SEM of 3 images. Statistical significance of cells aligned in $\pm$ 10° of flow direction; $^{\#}$ $p < 0.05$ vs. static and $^{\#\#}$ $p < 0.05$: steady vs. LAD.

It is observed from figure **7.14ai** that cells subjected to either LAD, steady or sustained hydrostatic pressure for 6 hours exhibit random orientation and do not predominantly align in the $\pm$ 10° of flow direction.

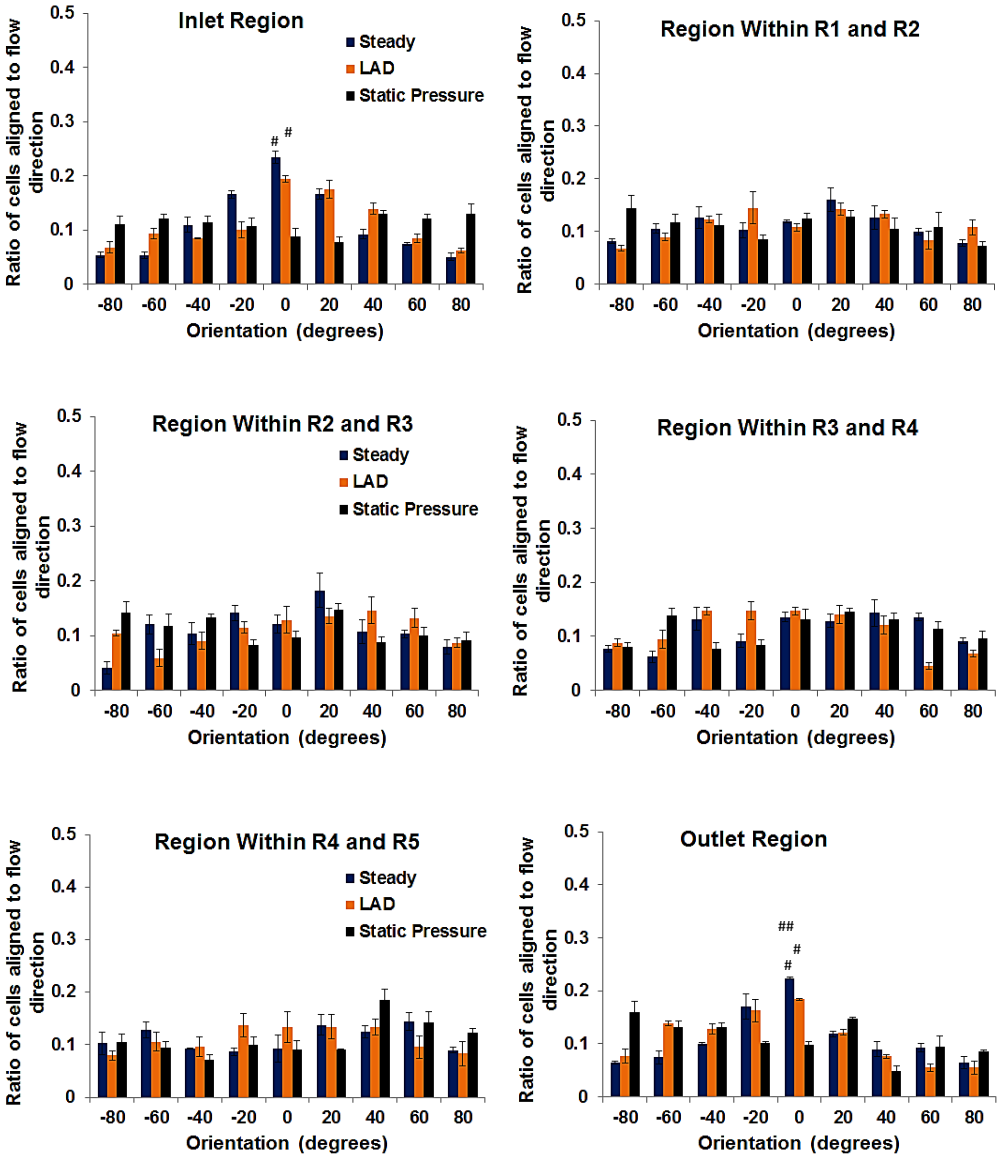

Figure 7.14aii Histogram showing orientation of cells exposed to steady, LAD pulsatile flows and sustained hydrostatic pressure for 12hrs. n = 3. SEM of 3 images. Statistical significance of cells aligned in $\pm$ 10° of flow direction; $^{\#}$ $p < 0.05$ vs. static and $^{\#\#}$ $p < 0.05$: steady vs. LAD.

From the above data it is observed that cells at inlet and outlet regions subjected to steady flow of 12 hours show more pronounced alignment in $\pm$ 10° of flow direction compared to that of LAD flow and hydrostatic

pressure for the same time duration. On the other hand, cells within the ridges regions do not show any strong alignment to flow $\pm 10°$ direction regardless of the type of flow or pressure subjected to them.

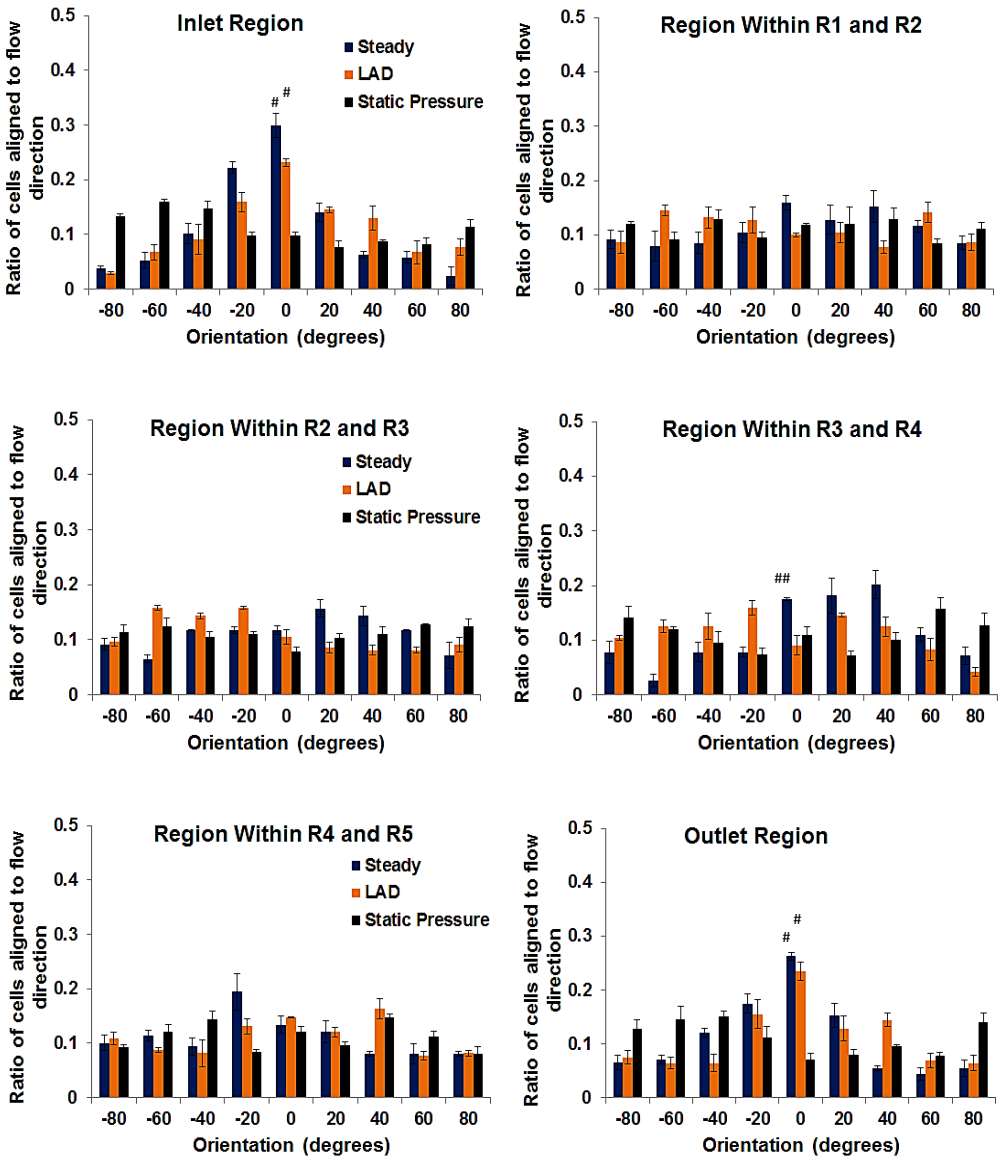

Figure 7.14aiii Histogram showing orientation of cells exposed to steady, LAD pulsatile flows and sustained hydrostatic pressure for 24hrs. n = 3. SEM of 3 images. Statistical significance of cells aligned in $\pm 10°$ of flow direction;

[#] $p < 0.05$ vs. static and [##] $p < 0.05$: steady vs. LAD.

Figure **7.14aiii** shows that there is statistically significant difference between the number of cells aligning within $\pm 10°$ flow direction at inlet and outlet regions when comparing steady flow, LAD pulsatile flow and hydrostatic pressure after 24 hours. However, although there are evidently slight differences in the cell proportion aligned within $\pm 10°$ flow direction when comparing steady flow with LAD flow at the inlet and outlet regions, these differences are not statistically significant. On the other hand, cells within the inter-ridges regions generally do not show strong alignment within $\pm 10°$ of flow direction regardless of the type of stimulus subjected to cells. Also, there are generally no statistically significant difference between the cells aligned within the 10 degrees at the inter-ridges region with the exception of steady flow stimulated cells within ridges 3 and 4 which are statistically significant when compared to that of the LAD flow stimulated cells.

The next data presented shows comparative analysis of aspect ratio of cells when subjected to steady and LAD flow waveform

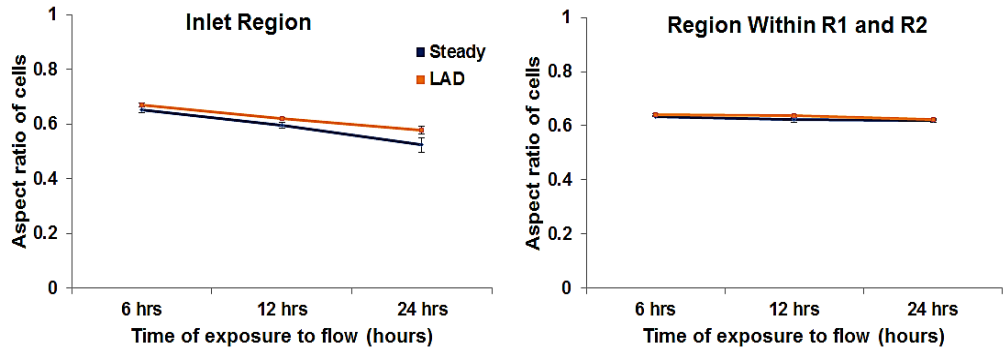

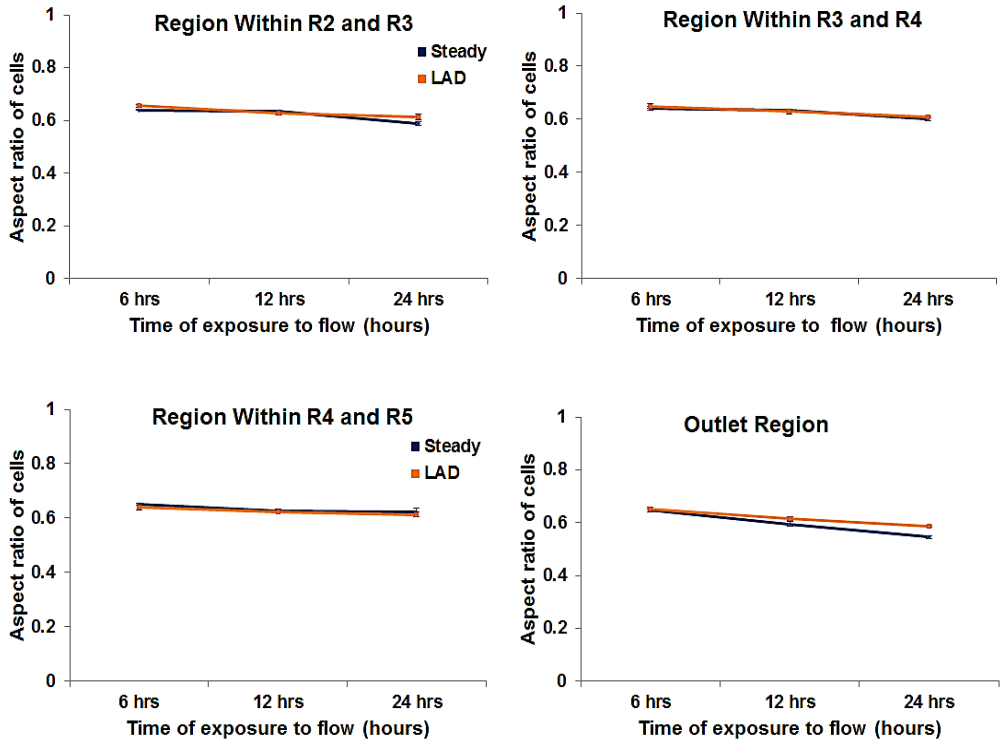

Figure 7.14b Line graph showing average aspect ratio of cells exposed to steady and LAD pulsatile flows for 6hrs, 12hrs and 24hrs. n = 3. SEM of 3 images. $^{\#\#}$ $p < 0.05$ vs. LAD flow.

It is observed from figure **7.14b** that cells to either steady flow or LAD pulsatile flow exhibit a time dependent decrease of cell aspect ratio. These decrease in cell aspect ratio are however very minimal and there is no statistical significance of cell aspect ratio with respect to the type of flow stimulus the cells were subjected to.

Comparative analysis of the average cell sizes when HUVECs were subjected to either steady or LAD pulsatile flow is presented below.

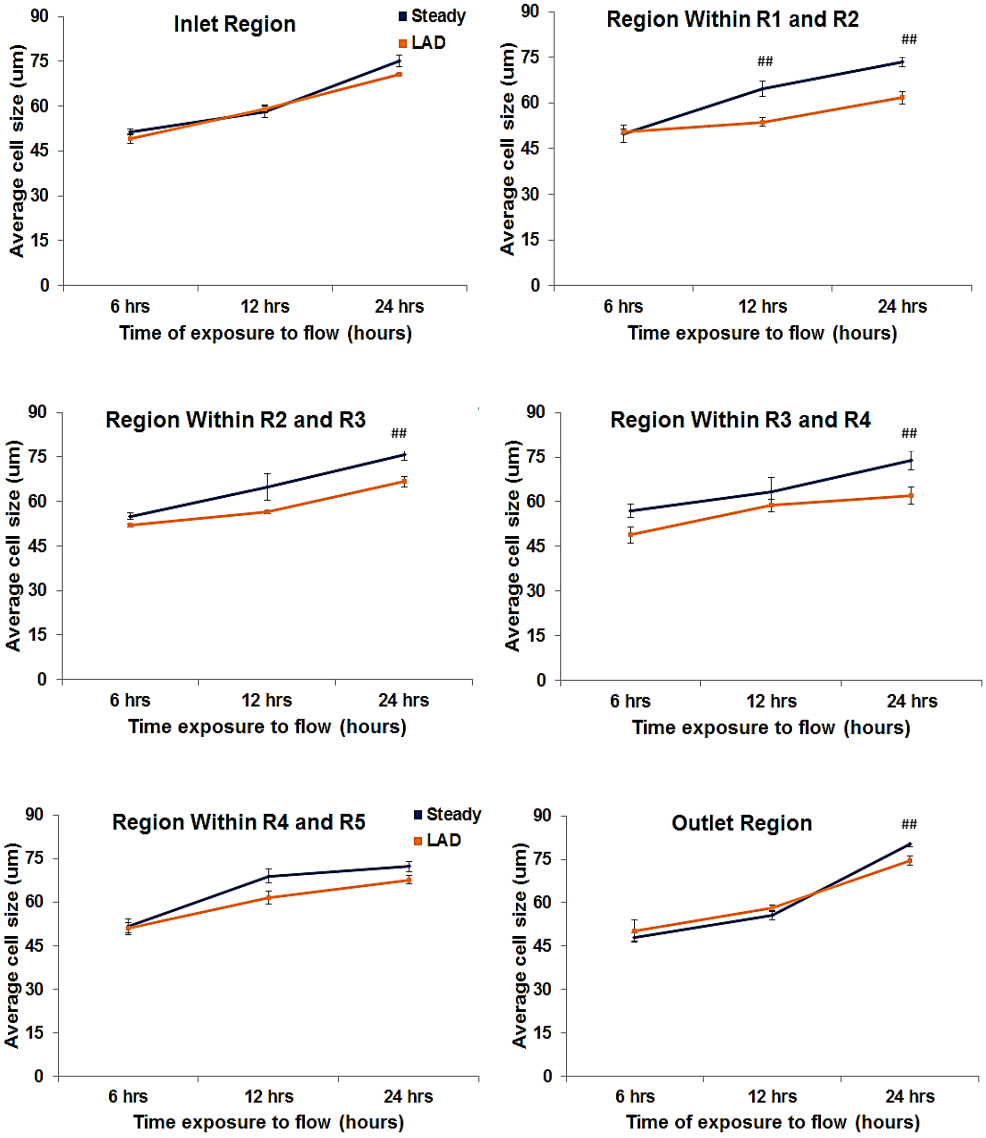

Figure 7.14c Line graph showing average cell size of cells exposed to steady and LAD pulsatile flows for 6hrs, 12hrs and 24hrs. n = 3. SEM of 3 images. $^{\#\#}$ $p < 0.05$ vs. LAD flow.

From figure **7.14c**, a general trend of increase in cell size with respect to time when cells are subjected to either steady or LAD flow is observed. It is however noted that cells within the inter-ridges region and subjected to steady flow show greater increase in cell size than when subjected to LAD pulsatile flow.

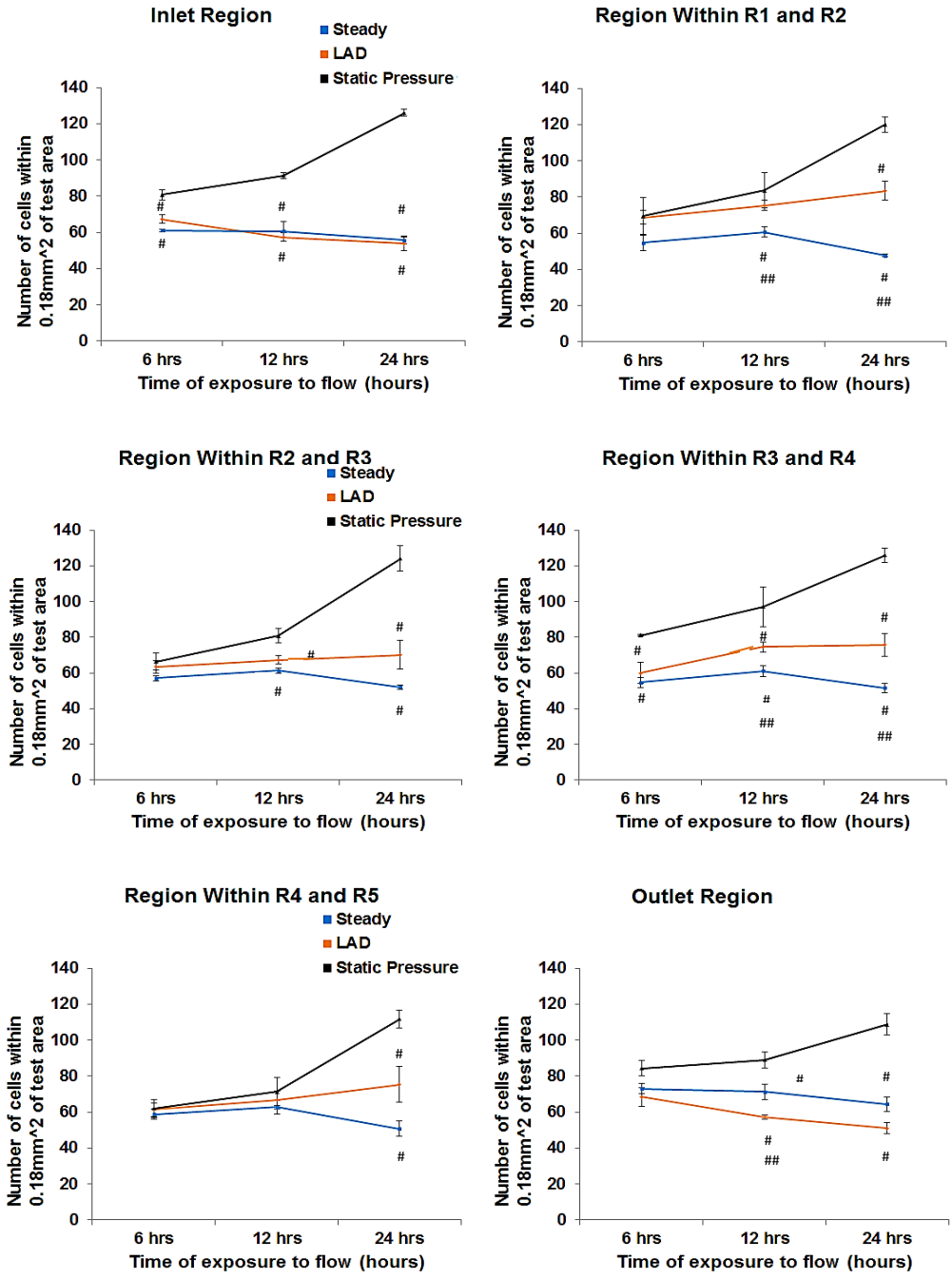

Figure 7.14d Line graph showing average number of cells within a local area of 0.18mm^2 after exposure to steady, LAD pulsatile flows and sustained hydrostatic pressure for 6hrs, 12hrs and 24hrs. n = 3. SEM of 3 images. $^{\#}$ $p < 0.05$ vs. static and $^{\#\#}$ $p < 0.05$: steady vs. LAD.

As shown in figure **7.14d**, HUVECs were subjected to either steady, LAD pulsatile flow or sustained hydrostatic pressure. From the graphs presented in this figure, it is clearly seen that cells subjected to sustained hydrostatic pressure show greater increase in cell density with respect to time. Cells subjected to steady flow show a relatively slow increase in cell density within the inter-ridges regions and decrease in cell density at the inlet and outlet regions. On the other hand, cell subjected to LAD pulsatile flow tend to decrease in cell density at the inter-ridges regions and also inlet and outlet regions. More so, comparative analysis of the effect of sustained hydrostatic pressure, steady flow and LAD pulsatile flow on the local density of cell was showed to be statistically significant.

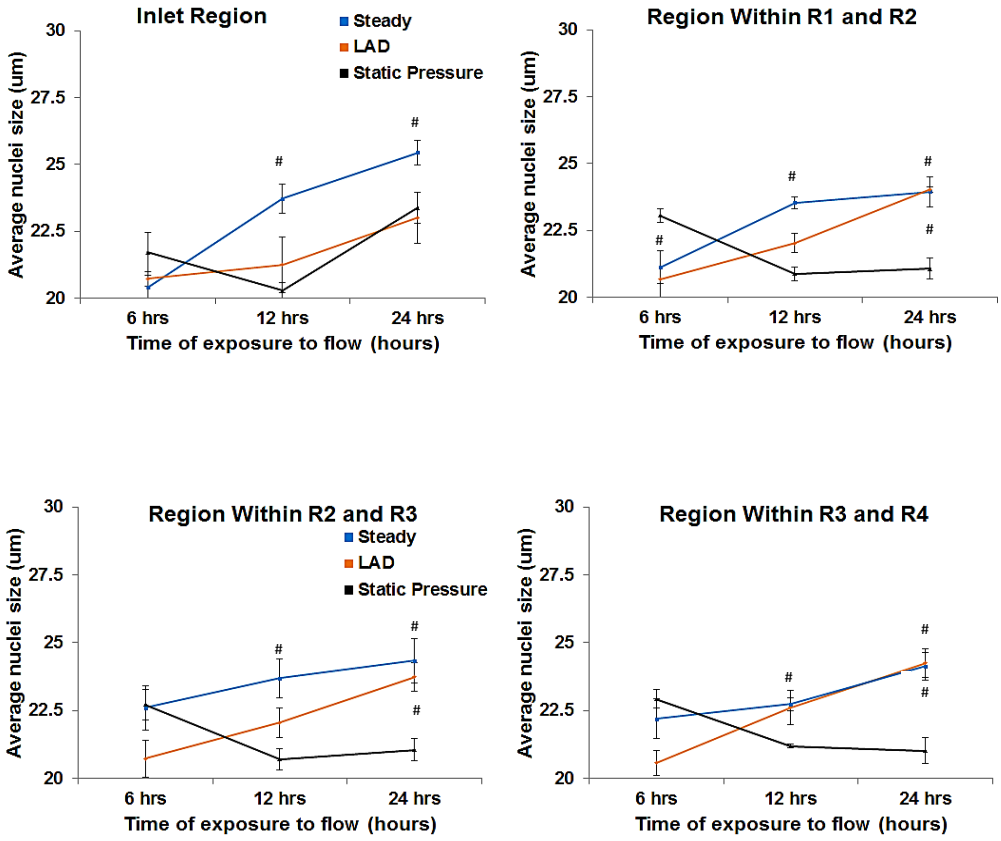

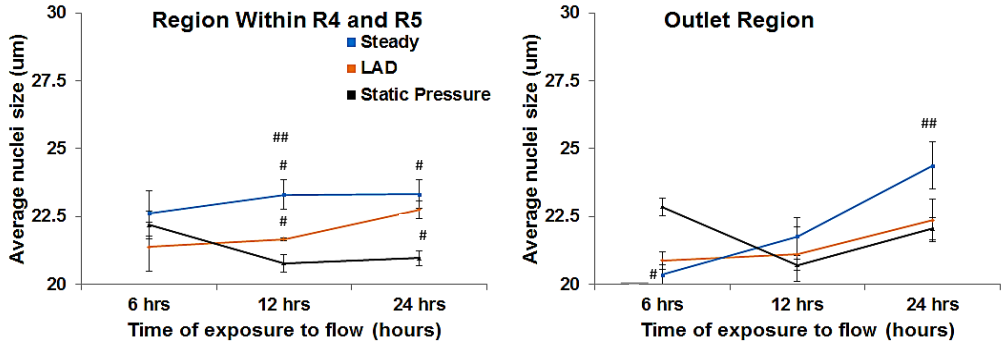

Figure 7.14e Line graph showing average nuclei length size after exposure to steady, LAD pulsatile flows and sustained hydrostatic pressure for 6hrs, 12hrs and 24hrs. n = 3. $^{\#}$ $p < 0.05$ vs. static and $^{\#\#}$ $p < 0.05$: steady vs. LAD.

The average nuclei size of cells subjected to sustained hydrostatic pressure tend to decrease with time whilst that of cells subjected to either LAD pulsatile flow or steady flow increase with time as shown in figure **7.14e**. It however suggested that steady flow does have stronger effect on the nuclei size of cells compared to LAD pulsatile flow. This suggestion is made based on the results presented in figure 7.14e which showed greater increase in nuclei size of cells subjected to steady flow to cells subjected to LAD pulsatile flow.

The average distances between nucleus centroid and cell centroid when cells are subjected to either steady or LAD pulsatile flow is analysed and results presented below. This analysis was grouped under cells that were subjected to steady uniform shear stress, steady non-uniform shear stress, LAD shear stress and LAD non-uniform shear stress.

Classification of non-uniform shear stress was based on the shear stress dynamics within ridge regions. As reported in chapter **6**, WSS dynamics at ridge regions are marked by WSS spikes on ridges and WSS valleys between the ridges and thus WSS at ridges region is non-uniform. Hence steady shear stress and LAD pulsatile shear stress at these regions are

categorised as steady non-uniform shear stress and LAD non-uniform shear stress respectively. Also, it is reported in chapter **6**, that WSS at inlet and outlet regions of the experimental designed model were relatively uniform. So, steady stress and LAD stress at these regions are also categorised as steady uniform shear stress and LAD uniform shear stress respectively.

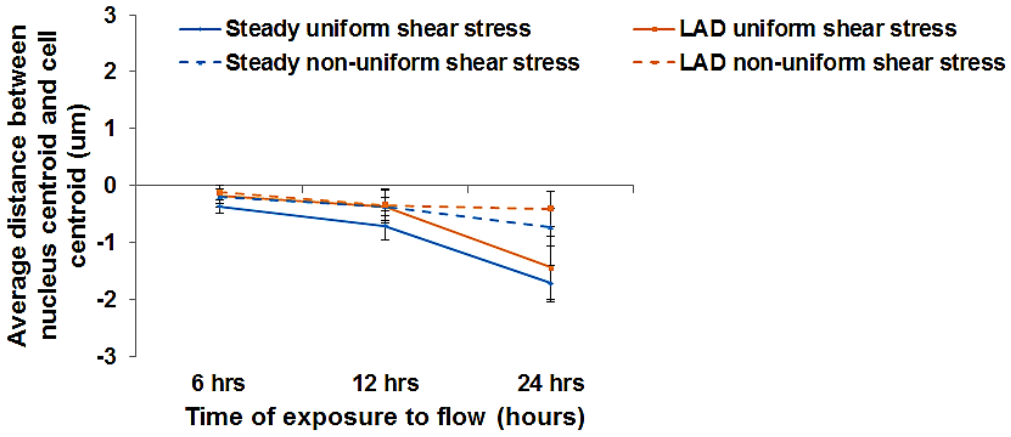

Figure 7.14f Line graph showing average distance between centroid of nucleus and cell centroid after cells exposed to steady and LAD pulsatile flows for 6hrs, 12hrs and 24hrs. n = 3. Error bars show SEM of 6 images. $^{\#}$ $p < 0.05$: steady uniform stress vs. steady non-uniform stress and $^{\#\#}$ $p < 0.05$: LAD uniform stress vs. LAD non-uniform stress.

A negative distance is defined as the centroid of the nucleus displaced downstream to the centroid of the entire cell. As shown in figure **7.14f**, it is observed that steady uniform stress and LAD pulsatile uniform stress both have greater effect on nuclei centroid downstream displacement over increased timescale compared to steady and LAD pulsatile non-uniform shear stresses. Comparatively, steady uniform stress showed stronger effect on the nuclei centroid downstream displacement when compared to that of LAD uniform stress although not statistically significant.

7.7 DISCUSSION TO RESULT ANALYSIS III

Biomechanical cues arising in the cellular milieu have generally been hypothesised to play major role in regulating EC function. Thus physical forces induced on ECs could lead to change in cell morphology and phenotype [61, 89, 289, 412-415]. It has been postulated that changes in cell shape does influence gene expression and cell cycle progression, albeit the precise mechanism and/or mechanisms which brings about this phenomenon remains unclear. It is however assumed that these cellular effects due to mechanical forces are mediated at least partly by changes in the actin cytoskeleton and nuclear structure of the cell [411, 412, 416]. Hence, it is imperative to understand how mechanical stimuli could bring about alterations in the cytoskeleton, nucleus and the cell in general. Understanding of how mechanical stimuli influence cell behaviour could be indicative to having better insight into the predictors of some arterial diseases such as restenosis. It is well documented from in vitro and in vivo experiments that ECs elongate together with rearrangement of the cytoskeleton with increasing shear stress and align parallel to the dominant flow direction [180]. ECs are therefore considered as high resolution localised flow sensors and their morphology used to classically describe the shear stress patterns that may be present. Indeed whilst it is appreciated the knowledge gained in correlating shear stress to cell morphology and thus helped predict arterial disease prone sites, it is important that the nuclear form is not overlooked. This is because it has been realised that the nucleus of the cell plays an important role in the regulation of protein-gene expression and transcriptional activity [417]. In fact the nucleus itself has been suggested to be a mechanosensor as it elongates and aligns in the direction of imposed flow [418]. More so, some studies have proposed the nuclei to modulate cellular phenotype and have a stronger correlation to diseased states [419, 420]. For example, a study into the nuclear

organisation of breast cancer cells after being exposed to a level of shear stress found a striking correlation between cancer cells phenotype and nucleus morphology compared to that of cellular morphology and the cancerous cells [419]. It is therefore suggested that greater strides could be made in the quest of establishing mechanisms involved in the onset and/or progression of restenosis and subsequently better ISR treatment strategies if the role of the nucleus in the cell function is thoroughly examined.

ECs in arteries are known not to be only exposed to shear stress due to blood flow dynamics but also hydrostatic pressure as a result of blood pressure. These stresses could therefore have independent or contributory effect on cells response. As shown in the results section of this chapter, ECs exposed only to hydrostatic pressure and combined stresses thus fluid stress and hydrostatic pressure resulted in marked cellular morphological differences. It is these differences and the effects of the physical stimuli on the cell state which would be elaborated in this chapter.

7.7.1 HUVECs EXPOSED TO COMBINED PRESSURE AND SHEAR STRESS

HUVECs exposed to combined stresses; thus steady WSSs and hydrostatic pressure of $100\ mmHg$ and also LAD pulsatile shear stress and hydrostatic pressure of $120/80\ mmHg$, in the cell-structure interaction experimental model showed ECs distinctive response to different type of stresses. HUVECs were observed to elongate and align predominately in the flow direction at the inlet and outlet regions of the model in a time dependent manner as shown in figures **7.12ai**, **7.12aii**, **7.12b**, **7.13ai**, **7.13aii** and **7.13b**. WSSs at these regions were proposed to be relatively uniform with an average stress magnitude of $2\ Pa$ as indicated by the CFD simulations in

chapter **6**. These observations are analogous to the findings reported in several in vitro and in vivo studies that ECs subjected to unidirectional WSS elongate and align in the direction of the imposed flow [61, 180, 304, 395, 421, 422]. Analysis of the number of ECs aligned within $\pm 10°$ and $\pm 20°$ to the impinged flow directions over increasing timescales at the inlet and outlet regions indicated statistical significant differences. This statistical significant difference of time-dependent ECs alignment to flow is shown in figure **7.12ai**, **7.12aii**, **7.13ai** and **7.13aii**. Nonetheless, although there were increased number of ECs aligned within $\pm 10°$ and $\pm 20°$ of flow direction at 24 hours than at 12 hours under exact same flow conditions, this difference in number of ECs alignment between the two timescales was not statistically significant. In general steady flow was observed to induce more ECs to align within the $\pm 10°$ of the flow directions when compared to that of LAD pulsatile flow conditions as shown in figures **7.14aii** and **7.14aiii**. However the difference in number of ECs aligned to flow direction between the two flow conditions was generally not statistically significant. It is noted nonetheless that ECs alignment to flow direction at the outlet region at 12 hours between the steady and LAD pulsatile flow conditions was statistically significant whereas the inlet region of the same experiment showed otherwise. Plausible explanation for this observation could be that local cell density at the selected outlet region might have been slightly different from that of the inlet region. Hence the type of fluid stress subjected to the cells could have a profound effect on the number of cells aligned to the imposed flow direction. This variation in local cell density may be as a result of normal experimental procedural inconsistencies. However studies have demonstrated that steady, non-reversing pulsatile and reversing pulsatile flow conditions all have different effects on ECs morphological response [318, 423]. Steady flow conditions have been reported to influence strongly cell morphological response whilst that of reverse pulsatile flow conditions triggered weaker morphological response [318]. So as the experimental LAD pulsatile flow

condition included a small reversing component, it is possible that the associated stresses due to the LAD flow type such as OSIs, and also slight increase of SWSSG at the outlet region as shown in chapter **6** could cause weaker alignment of cells to the flow direction and thus bring about the statistical difference recorded. Further examination into this occurrence is therefore needed to clarify clearly if the observed outcome was more as a result of experimental inconsistencies or mechanical stress related. As explained earlier, different type of fluid stress have different effects on cells morphological response and this statement is justified as steady flow is shown to induce greatly an increase in cell aspect ratio when compared to that of the LAD pulsatile flow at the inlet and outlet regions.

Conversely in the regions where flow was “disturbed” thus regions marked with flow recirculation, flow separations and flow recovery, HUVECs were by qualitative inspection seen to be somewhat of a polygonal shaped as shown in figures **7.6a** and **7.6b**. This disturbed flow phenomenon occurred at the inter-ridges regions and from the CFD analysis discussed in chapter **6,** these regions were characterised with SWSSG, OSIs and both low (~ -2.5 Pa) and high (~ 2.5 Pa) WSSs. This observation presents the evidence that the application of disturbed stresses to ECs in vitro have distinct influence on ECs shape compared to the effects of uniform stresses on ECs shape. This said evidence is supported by results from other similar investigations [319, 424]. Comparative quantitative analysis on the effects of “disturbed steady shear stress” and “disturbed LAD pulsatile shear stress” on ECs average aspect ratio showed similar results as illustrated in figure **7.14b**. However, this quantitative data tends to obviate the proposed hypothesis that different types of fluid stress (i.e. steady and pulsatile) do have different effects on ECs. To ascertain if this observation holds true for other morphological parameters of the ECs under the two stipulated disturbed stresses, further quantitative examinations of cell morphology was performed. Investigation

into the effect of disturbed stresses on cell size length revealed that steady disturbed shear stress stimulated greater increase in cell size than that of disturbed LAD pulsatile stress as shown in figure **7.14c**. Furthermore, there were recorded statistical significant differences in the cell sizes between ECs exposed to the two disturbed stresses at timescales of 12 hours and 24 hours. Qualitative evidence of difference in cell size is shown in figure **7.15**.

A. 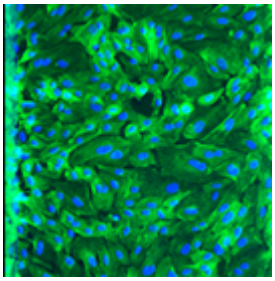 **B.** 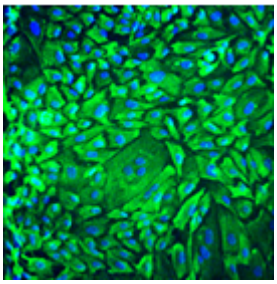

Figure 7.15 HUVECs exposed to disturbed steady shear (A) and disturbed LAD pulsatile shear (B) for 12 hours.

This additional data helps clarify the inference made about the similar morphological disposition (i.e. aspect ratio) of HUVECs exposed to both disturbed steady and LAD pulsatile stresses. It is therefore suggested that although ECs exposed to different disturbed stresses may have the same average aspect ratio, the size of the cells could differ greatly, hence the said hypothesis stills holds true.

Additionally, cells exposed to disturbed flow regimens were noticed to be more randomly aligned to the $\pm 10°$ flow directions irrespective to the stress exposure duration as shown in figures **7.12ai** and **7.13ai**. However there were observed slight major alignment of cells to the $\pm 20°$ flow directions although this observation was not consistent across all the disturbed flow locations as also shown in figures **7.12aii** and **7.13aii**. Estrada et al. [425] in a study investigating ECs morphological response to disturbed flow conditions also reported similar observations. Saksamoto et al. [185] also

reported a weaker alignment of ECs to imposed flow direction and attributed this occurrence to high SWSSG present. Thus from our CFD simulations which showed high SWSSGs at the disturbed flow regions, this conclusion reached by Saksamoto et al. [185] tends to support our experimental observation.

Regardless of the type of combined fluid stress and pressure exposed to the cells, a general observation of the cells being able to maintain their monolayer integrity was made. Thus the effect of the hydrostatic pressure of cells to cause the cells to form multilayer structure is void. It is therefore suggested that in the presence of hydrostatic force and shear stress, shear stress becomes the overriding force that tends influence the morphology of the ECs.

As previously discussed, hydrostatic pressure is reported to stimulate increase in ECs proliferation whereas studies have demonstrated uniform shear stress inhibits ECs proliferation [423, 426, 427]. On the contrary, disturbed shear stresses which may give rise to shear gradients, more specifically temporal shear gradient have been attributed to enhance ECs proliferation [24, 428]. White et al. [24] concluded from their investigations on the effect of temporal gradient in shear and spatial gradient in shear on EC proliferation that temporal shear gradient induced ECs proliferation. Spatial shear stress gradient on the other hand was suggested to affects ECs proliferation similarly to that of a uniform shear stress. If increase in local cell density is implied to as increase in ECs proliferation, then these hypotheses are suggested to be in accord with the results achieved from our experimental studies. This is because it has been demonstrated clearly that ECs subjected to predominant hydrostatic pressure of $100\ mmHg$ enhanced increase of local cell density per unit area. The local cell density of HUVECs exposed to steady flow where observed to decrease even at regions where flow was classified disturbed. Since steady flow has no transient

characteristics, the effect of TWSSG on HUVECs may be very minimal or non-existent. This hence explains why there was no increase in local cell density at the disturbed flow region under steady flow simulation. On the other hand, the local cell density of cells exposed to LAD pulsatile flow decreased at regions where shear stress was classified uniform (inlet and outlet regions) and increased at disturbed stress regions (inter-ridges regions). It is reasoned that due to the transient nature of the LAD flow waveform, disturbed LAD flow brings into effect strongly the influence of TWSSG on HUVECs present and thus elucidate the observation made.

It is also important to take into account the effect of the different type of fluid stress on the nucleus morphology. The shape of EC nuclei is well defined as an ellipse and aligns in the direction of an imposed uniform flow as reported by Flaherty et al. [429] The nucleus is also reported to elongate upon exposure to shear stress. In the analysis of the nucleus morphology after HUVECs had been exposed to both LAD pulsatile and steady shear stress, it is observed that the latter had a dominant time dependent effect on the nuclei length size. Interestingly, this effect on nuclei size was generally not statistically significant when compared to that of the LAD pulsatile stress as shown in figure **7.14e**. If the increased in nuclei length size is thus inferred to as elongation of the nuclei since the shape of nuclei is generally well defined, then it could be suggested that cells exposed to both flow conditions (i.e. steady and LAD pulsatile) caused elongation of the nucleus. This deduction of nuclei elongation thus tends to support Flaherty et al. [429] experimental findings on nuclei elongation due to shear stress. Bond et al. [318] in a study of endothelial nuclei elongation around mouse aortic branches reported that steady flow had more dominant effect on ECs nuclei elongation than the corresponding reverse pulsatile flow. This conclusion by Bond et al. [318] therefore supports our evidence of HUVECs nuclei elongation under the stipulated flow conditions. Conversely, HUVECs exposed to sustained

hydrostatic pressure showed a general time-dependent decrease of nucleus length size.

In a study conducted by Tkachenko et al. [418] into the sensory role played by the nucleus of ECs, a hypothesis that ECs upon sensing the direction of shear stress through hydrodynamic drag induce the nucleus to polarise downstream of the cell was proposed. To confirm this hypothesis in our experiments, an investigation into the effect of steady and LAD pulsatile flows on the downstream displacement of the nuclei within HUVECs was conducted. In the study by Tkachenko et al. [418], cells were only subjected to uniform steady shear flow, thus results of nuclei displacement within cells was that of cells under steady flow conditions. In our experimental model however, cells were exposed to both physiological relevant shear (LAD pulsatile WSS) and steady WSS. Also, due to the design of the experimental model there were regions where ECs were exposed to uniform shear stress (inlet and outlet regions) and other regions where ECs were exposed to disturbed shear stress (ridge regions). The localisation of the nuclei within HUVECs when exposed to uniform and disturbed LAD pulsatile WSS and also uniform and disturbed steady WSS are shown in figures **7.16** and **7.17** respectively.

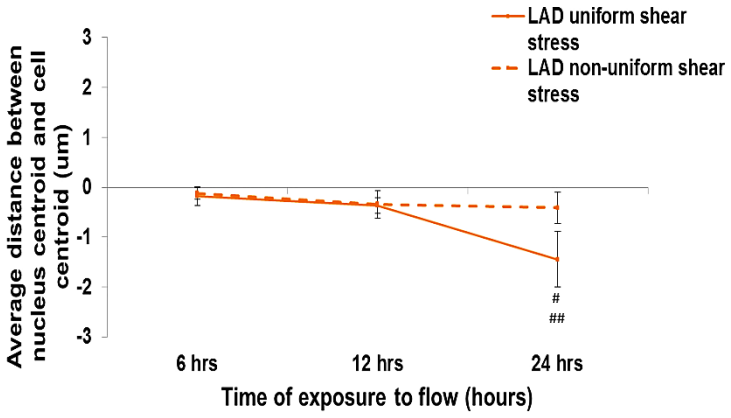

Figure 7.16 Line graph showing average distance between nucleus and cell

centroids after exposure to stimuli for 6hrs, 12hrs and 24hrs. n = 3. Error bars show SEM of 6 images. # $p < 0.05$ vs. 6 hrs and ## $p < 0.05$: 12 hrs vs. 24 hrs.

Cells localised at the inlet and outlet regions are predicted to experience constant uniform shear stress across these regions. It is thus suggested that LAD shear stress at these areas is uniform and this suggestion is supported by the evidences presented in chapter 6. On the other hand WSS at the ridges region are marked by WSS peaks and valleys and because of the irregularities of WSSs at this region, LAD shear stress at this region is classified as non-uniform shear stress. From figure 7.16, it is observed that from time duration of 6 hours to 12 hours, cells being subjected to either LAD uniform shear stress or LAD non-uniform shear stress both show a similarly gradual negative displacement of nuclei centroid. However after 12 hours, there is a sharp increase in the negative displacement of nuclei centroid with cells that were subjected to LAD uniform shear stress whilst cells subjected to LAD non-uniform shear stress maintained a gradual increase in negative displacement of the cell nuclei centroid.

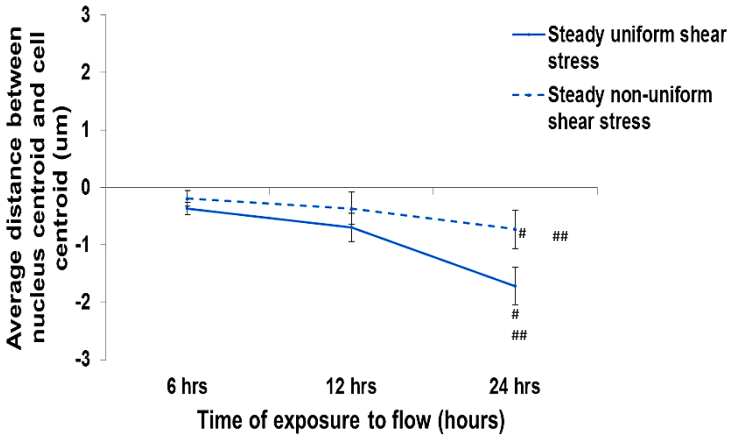

Figure 7.17 Line graph showing average distance between nucleus and cell centroids after cells exposed to stimuli for 6hrs, 12hrs and 24hrs. n = 3. SEM of 6 images. # $p < 0.05$ vs. 6 hrs and ## $p < 0.05$: 12 hrs vs. 24 hrs.

The nuclei centroid displacement of cells when subjected to steady uniform shear stress and steady non-uniform shear stress show similar behaviour to that observed for the LAD pulsatile shear stresses in figure **7.16**.

A negative distance is defined as the centroid of the nucleus displaced downstream to the centroid of the entire cell. As could be seen from figures **7.16** and **7.17**, both flow conditions induced a downstream displacement of the nucleus within HUVECs, thus our findings support the hypothesis proposed by Tkachenko et al. [418]. It is however noted that the uniform shear stress had greater effect of the nuclei displacement when compared to that of the disturbed shear stress. Also there were time dependent statistical significant differences of the nuclei displacement when subjected to uniform shear stresses. Of interest, whilst disturbed steady shear brought about a time dependant statistical significant differences in nucleus displacements, disturbed LAD pulsatile shear on the other hand showed no statistical significant difference. Additionally, comparative analysis of the nuclei localisation between HUVECs exposed to steady and LAD pulsatile flow conditions revealed steady flow conditions to induce more the downstream localisation of the nucleus. This steady flow effect on the nucleus displacement was however not statistically significant when compared to that under LAD pulsatile flow condition as shown in figure **7.14f**. Nonetheless, these experimental evidences reiterate the earlier stated hypothesis that different fluid stresses have different effects on endothelial cellular response.

Another important observation made about the response of HUVECs exposed to the stated combined mechanical stresses within the experimental model was the presence of HUVECs on the fabricated micro-structure ridges at 12 hours and 24 hours. During the experimental seeding procedure, the ridges were covered with a sheath to prevent HUVECs from being seeded onto the ridges before being subjected to fluid stresses and pressure. Upon exposure of the stresses on the cells for a duration of 6 hours there were no

observed cells on the ridges, however at time points 12 hours and 24 hours, there were cell present on the ridges as shown in figures **7.6a** and **7.6b**. Several possible explanations to this phenomenon could include that some cells might have been seeded on the ridges during the seeding process due to experimental procedure negligence. This explanation although reasonable is considered not probable as the ridge sheath covered fully the ridges and was taken off until the cells had fully bedded down. Additionally this explanation does not tend to justify the non-existence of HUVECs on the ridges after exposure to the stated stimuli for 6 hours. So, another plausible explanation to this phenomenon could be that the mechanical stresses subjected to HUVECs induced cells to "migrate" and hence led to the cells covering the ridges. This latter explanation is deemed more appropriate for the observed occurrence. In a study by Ostrowski et al. [430] on ECs migration, it was reported that gradient in shear due to fluid flow stimulated ECs to migrate against the impinged flow direction and concentrate in region of high WSS. As shown in our CFD simulation in chapter **6**, high WSSs (> 10 Pa) were recorded on top of the ridges and also high SWSSGs were recorded at the inter-ridges region. So in relating to Ostrowski et al. [430] explanation on ECs migration, it is proposed that HUVECs within the inter-ridges region upon sensing gradient in shear stress migrated towards the region of increased WSSs (i.e. the top of the ridge).

An in vivo study by Sprague et al. [431] into the impact of parallel micro-engineered stent grooves on ECs migration and function produced results that further supported our experimental observations. Sprague et al. [431], reported that parallel microgrooves stent within coronary artery of a swine induced cell migration and positive cell function which consequently inhibited the NI formation.

7.8 SUMMARY

From the discussions presented in this chapter, it can be concluded that the type of fluid stimuli or hydrostatic pressure subjected to cells show marked difference in the morphological response of cell. Cells subjected to either LAD pulsatile flow or steady flow tend to align more to the direction of flow with increase time periods whilst cells subjected to only hydrostatic pressures show random orientation. However, cells subjected to unstable flow regimes which are characterised by WSS peaks and valleys tend to show random alignment to flow direction. Additionally whilst exposure of cells to only hydrostatic pressure caused strong increase in local cell density, the effect of steady and LAD pulsatile flow on cell density was opposite. Thus, cell density decreased when cells were exposed to steady flow. Cells exposed LAD pulsatile flow however showed a gentle increase in cell density within the ridge regions whilst at the inlet and outlet regions cell density decreased. It is also noticed that cells within the inter-ridges region and exposed to steady flow showed increased average cell size when compared to that of cells exposed to LAD pulsatile flow.

7.4.3 LIMITATIONS

It is notable from the results produced of HUVECs exposed to independent and combined stresses that the designed flow bioreactor system is capable of supporting healthy cultured ECs for experimental investigations for at least 24 hours. Qualitative and quantitative analyses of the HUVECs response when subjected to defined mechanical environment are in parallel agreement to similar studies reported by other researchers. Thus these scientific studies have been the benchmark for which our experimental results have been

compared and validated. Additionally, results observed in the designed cell-structure interaction experimental model demonstrates the feasibility of studying HUVECs response to mechanical stimuli that may be present within stented arteries.

Despite experimental results of cells response to a given stimuli which has been shown to be analogous to that observed in vivo, one should nonetheless be very careful when interpreting the results achieved for clinical relevance. This is because the timescales for which the cells experiments were conducted, although sufficiently long to induce significant cell morphological response, was relatively short compared to the timescales for which cells may be experiencing same stimuli in vivo. It is known that ECs in stented arteries characteristically experience mechanical stimuli relevant to restenosis and/or ISR for timescales of many months or even years [432, 433]; a system which cannot practically be repeated in vitro. Thus practical experimental considerations dictate the duration of in vitro experiments performed and that certain cellular responses occurring at later stages might have been overlooked.

The common use of HUVECs in the investigation of cells response to mechanical stresses have been well documented and with results suggested to represent in vivo arterial occurrences [424, 434-436]. However, it must be made clear that HUVECs are not arterial cell type and thus the phenotype of cell could influence differently the cells response to stimuli. It should therefore be considered that results achieved from the experiments may not be an entirely accurate indicator of arterial cells response to mechanical stimuli. Albuquerque et al. [437] reported a weak correlation between HUVECs response to steady laminar shear and human coronary arterial endothelial cells response to the same shear. It is therefore of importance that future work would involve the use of arterial ECs to compare and validate results documented.

CHAPTER 8

EXPERIMENTAL ANALYSIS OF ECs MOLECULAR RESPONSE TO PHYSIOLOGICAL RELEVANT FLUID DYNAMICS IN STENTED MODEL

8.1 INTRODUCTION

As previously discussed in chapter **7**, the choice of stress applied to cells could influence significantly the cells morphology. Moreover, the ability of cells to discriminate between flow types is dependent on the shear-induced molecular mechanochemical signal transduction [415]. The complex interplay and processes involved in the shear induced signalling molecules tend to alter transcription factors which modulate endothelial gene expression and thus results in differential cell function [438]. Amongst the transcriptional factors being altered is the nuclear factor kappa B (NF-kB). NF-kB is thought to play a very important role in controlling inflammation, cell adhesion molecules and proliferation and if activated becomes the bane of the arterial system [439]. A mechanobiological modelling of restenosis in stented artery by Boyle et al. [389] suggested that inflammation accounted for restenosis in stented artery. Studies have demonstrated that $p50/p65$ NF-kB heterodimer lies dormant in the cell cytoplasm complexed to IkB, its inhibitory element [440]. Upon stimulation of the cells by cytokines or low/disturbed shear stress, NF-kB tend to dissociates from IkB and translocates into the nucleus, thus becomes active [100, 440, 441]. The activation of NF-kB therefore promotes inflammation and other adverse gene transcription which

subsequently evokes arterial disease. It should however be noted that not all genes modulated by NF-kB is deleterious to the arterial system [442]. One of the many cytokines regulated by NF-kB is the tumour necrosis factor-alpha (tnf-α). Tnf-α is considered a critical mediator of inflammatory process that occurs during atherosclerosis and known to promote the expression of adhesion molecules such as intercellular adhesion molecule-1 (ICAM-1), vascular cell adhesion molecule-1 (VCAM-1) and endothelial selectin (E-selectin) [443]. Although studies have reported inflammation to play critical roles in atherosclerosis and restenosis development, it is still necessary to clarify that inflammatory pathway leading to each stated disease could be different. Hence investigations into restenosis based on atherosclerosis and the role played by inflammation in the development of atherosclerosis could be entirely flawed. It is therefore suggested that the role of inflammation in restenosis should be explicitly investigated. In addition to cytokines inducing inflammatory genes and expression of adhesion molecules, fluid shear stress has also been reported to modulate ECs adhesion molecules [444].

Nonetheless, as it is suspected that inflammation may play a pivotal role in linking arterial injury to the eventual consequence of restenosis, it is proposed that key inflammatory molecules be investigated. The main objective of this chapter is therefore to gain better understanding of how combined stresses thus fluid stress and hydrostatic pressure affect the expression of ICAM-1 and NF-kB.

8.2 METHOD

Pre cell culture preparation and cell seeding process for this experiment was similar to that discussed in sections **7.2.2** and **7.2.3** respectively but with the difference that cells were seeded under low density ($\approx 13{,}000\ cells/cm^2$)

so as to attain confluency within 4 days. Cells were seeded under low confluence so as to allow cells enough time to regenerate new membrane proteins which may have been damaged when cells were initially trypsinized.

Initial experiment performed with the now confluent cells involved stimulating the cells with the cell growth media containing human recombinant tumour necrosis factor alpha; tnf-α (Life Technologies, UK) of different concentrations; thus $100\ units/ml, 200\ units/ml$ and $300\ units/ml$ for 1 hour and kept under static flow conditions in the incubator. This experiment was to determine the most appropriate tnf-α dose level to cause translocation of $p65$ subunit of NF-kB from the cytoplasm of HUVECs to the nucleus. A positive control did not involve any stimulation of the cells; however the cells were kept under static flow conditions in the incubator for equal duration. After the cells had been stimulated with tnf-α for an hour, the cells were then washed once in $20\ ml$ of HBSS and then twice with PBS before fixing them in $20\ ml$ of 3.7% formaldehyde for 20 minutes. The unstimulated cells were also fixed in the exact manner as the stimulated cells. Both stimulated and unstimulated cells were then stained for the location of NF-kB.

Subsequent experiments involved the investigation of the effect of the stipulated combined stresses on NF-kB and ICAM-1 expressions. In the experiment to investigate NF-kB expression due to stress conditions, this experiment involved similar flow setup as discussed in section **7.2.4** but this time the confluent cells were exposed to combined flow and pressure conditions for 1 hour. Investigation of ICAM-1 expression also involved same experimental flow setup as illustrated in **7.2.4** at different timescales of 6 hours, 12 hours and 24 hours. Negative controls of the ICAM-1 investigation involved stimulating confluent HUVECs for 6 hours, 12 hours and 24 hours respectively with cell growth media containing tnf-α at a concentration of

$200\ units/ml$ under static culture. On the contrary, positive controls of this investigation involved HUVECs not being stimulated under static culture for also 6 hours, 12 hours and 24 hours.

8.2.1 CELLS STAINING

8.2.1.1 STAINING FOR NF-kB

After the cells had been fixed, they were washed three times with PBS for 5 minutes each. After the third wash, the PBS was aspirated and then the cells permeabilised by adding 1% Triton X-100 for 3 minutes. The cells were washed again three times with PBS for 5 minutes each after being permeabilised. After this step, 1% bovine serum albumin (BSA) in PBS solution was added to the cells for 1 hour to block nonspecific binding. A primary antibody solution containing $40ul$ of a $200ug/ml$ concentration anti-NF-kB/$p65$ goat polyclonal IgG (Santa Cruz Biotechnology, Santa Cruz) in $4\ ml$ of 1% BSA-PBS was pipetted onto the cells and left for 1 hour at room temperature. After an hour, the primary antibody solution was aspirated from the cells and the cells washed three times in PBS with each wash lasting for 5 minutes. The cells were then incubated with a secondary antibody solution made of $10ul$ of a $1.5mg/ml$ concentration biotinylated anti-goat IgG (Vector Laboratories, UK) in $10\ ml$ of 1% BSA-PBS for 1 hour at room temperature. The cells were then washed three times with PBS again after the 1 hour had elapsed and then stained with a fluorophore solution containing $40ul$ of a $1mg/ml$ concentration fluorescein streptavidin (Vector Laboratories, UK) in $4\ ml$ of 1% BSA-PBS for 30 minutes at room temperature. Then after, the cells were washed twice with PBS before being

stained with the DAPI solution for 10 minutes. The cells were for the final time washed with PBS after being stained with DAPI and visualised using confocal microscopy. The fluorophore stain for the NF-kB was able to be seen using the same confocal settings used with the FITC conjugated Phalloidin.

8.2.1.2 STAINING FOR ICAM-1

HUVECs were stained for ICAM-1 expression after stimulations with the stipulated combined stresses and also tnf-α. After having initially fixed the stimulated cells, the cells were then washed three times with PBS and each wash lasted for 5 minutes. After the third wash, the PBS was aspirated and the cells then permeabilised by adding 1% Triton X-100 for 3 minutes. After the 3 minutes had elapsed, the cells were washed again three times with PBS. After the third wash, 1% bovine serum albumin (BSA) in PBS solution was added to the cells for 1 hour to block nonspecific binding. A primary antibody solution containing $20ul$ of a $0.5mg/ml$ concentration purified anti-human CD54 ICAM-1 (Affymetrix eBioscience, UK) in $10\,ml$ of 1% BSA-PBS was pipetted onto the cells and left overnight in a $4℃$ fridge. After the cells have been left in the fridge overnight, the primary antibody solution was then aspirated from the cells. The cells were again washed three times with PBS and each wash lasted for 5 minutes. The cells were later incubated with a secondary antibody solution made of $20ul$ of goat anti-mouse IgG, Alexa fluor 633 (Life Technologies, UK) in $20\,ml$ of 1% BSA-PBS for 1 hour at room temperature. The cells were then washed three times and the cytoskeleton and nuclei stained with FITC conjugated Phalloidin (Sigma-Aldrich, UK) and DAPI solution respectively. The cells were then washed for the final time with PBS and after visualised using confocal microscopy. The

fluorophore stain for ICAM-1 was able to be seen using $632nm$ excitation laser with an emission filter of $647nm$ setting on the confocal microscopy.

8.3 RESULTS

Images of all stained cells taken were at the centre plane of the stamped glass slides. Additionally all images were taken with a x10 objective lens of the confocal microscopy and a standard scale bar of $200\ um$ was set on the images.

8.3.1 CELLS STAINED FOR NF-kB

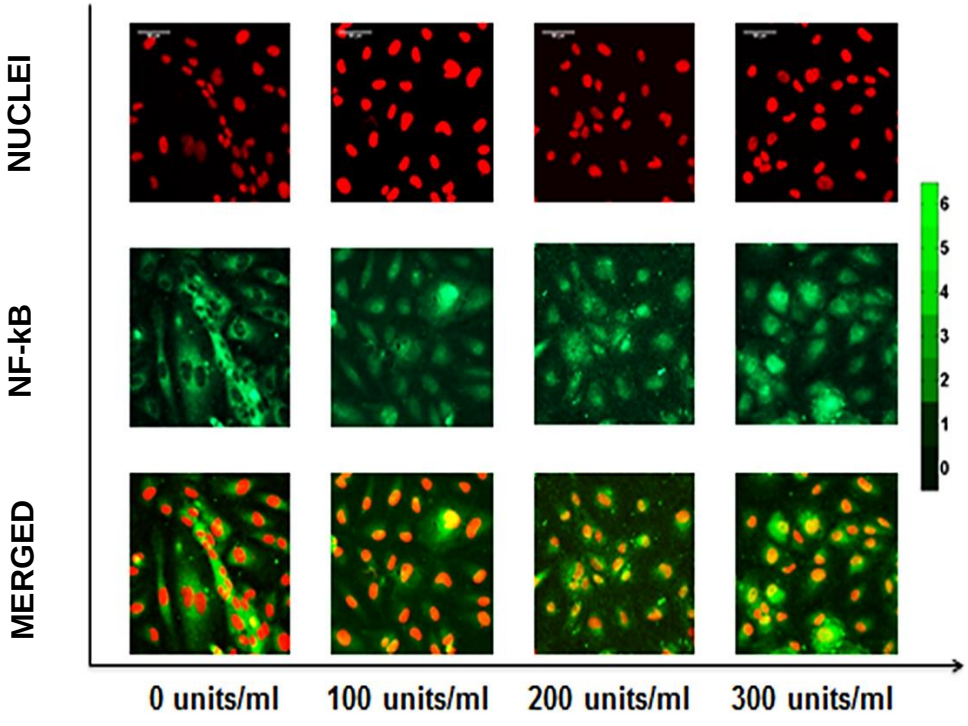

Figure 8.1 Image showing localisation of NF-kB after static culture simulation of human recombinant Tnf-α at different concentrations for 1 hour. Scale bar (0 – 6) shows activation level of NF-kB in nuclei. n = 1.

As seen in figure **8.1**, when NF-kB is inactive, the nucleus form within the cell and the cytoplasm is clearly identified and defined. However when NF-kB is active; the structure of the cytoplasm becomes less defined.

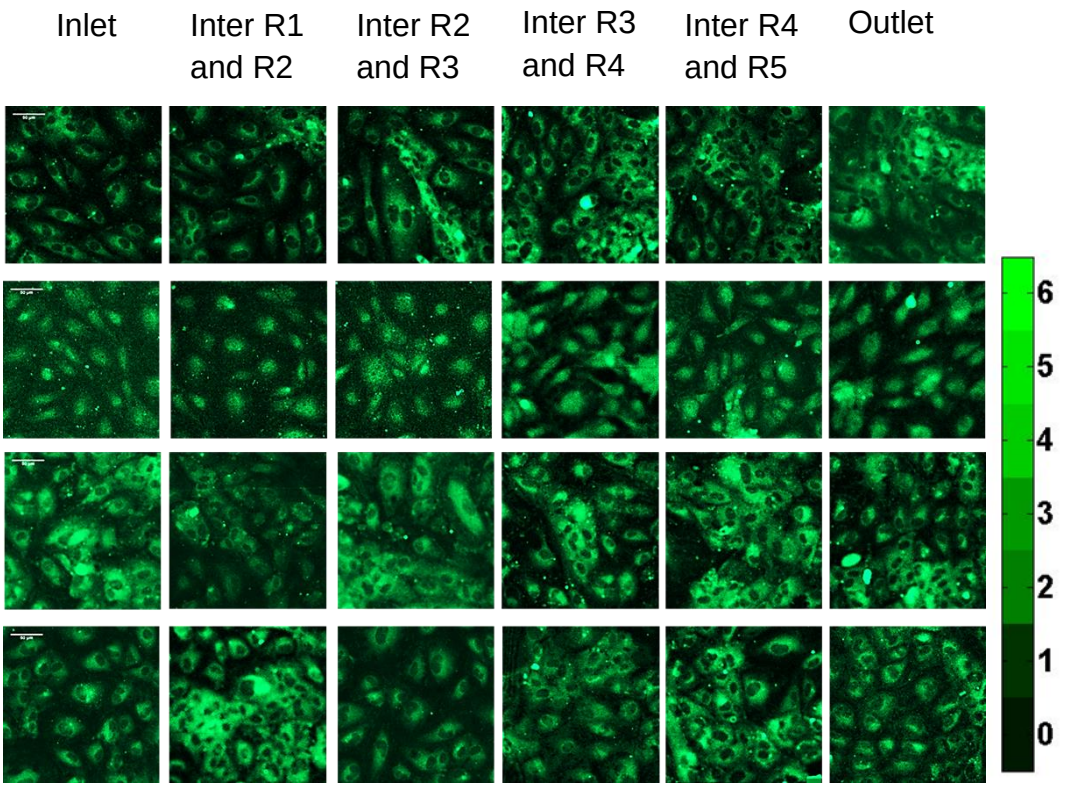

Figure 8.2 Image showing localisation of NF-kB in HUVECs after stimulation for 1 hour. Static culture stimulation; positive Control (Top row), stimulation with human recombinant Tnf-α at concentration of 200 units/ml under static control (2nd row), combination of steady flow and hydrostatic pressure of 100mmHg (3rd row), combination of LAD pulsatile flow and hydrostatic pressure of 120/80mmHg (4th row). Scale bar (0 – 6) shows activation level of NF-kB in nuclei. n = 1. As illustrated in figure **8.2**, cells subjected to LAD and steady flow showed no activation of NF-kB. However, NF-kB was activated when cells were stimulated with Tnf-α.

8.3.2 CELLS STAINED FOR ICAM-1

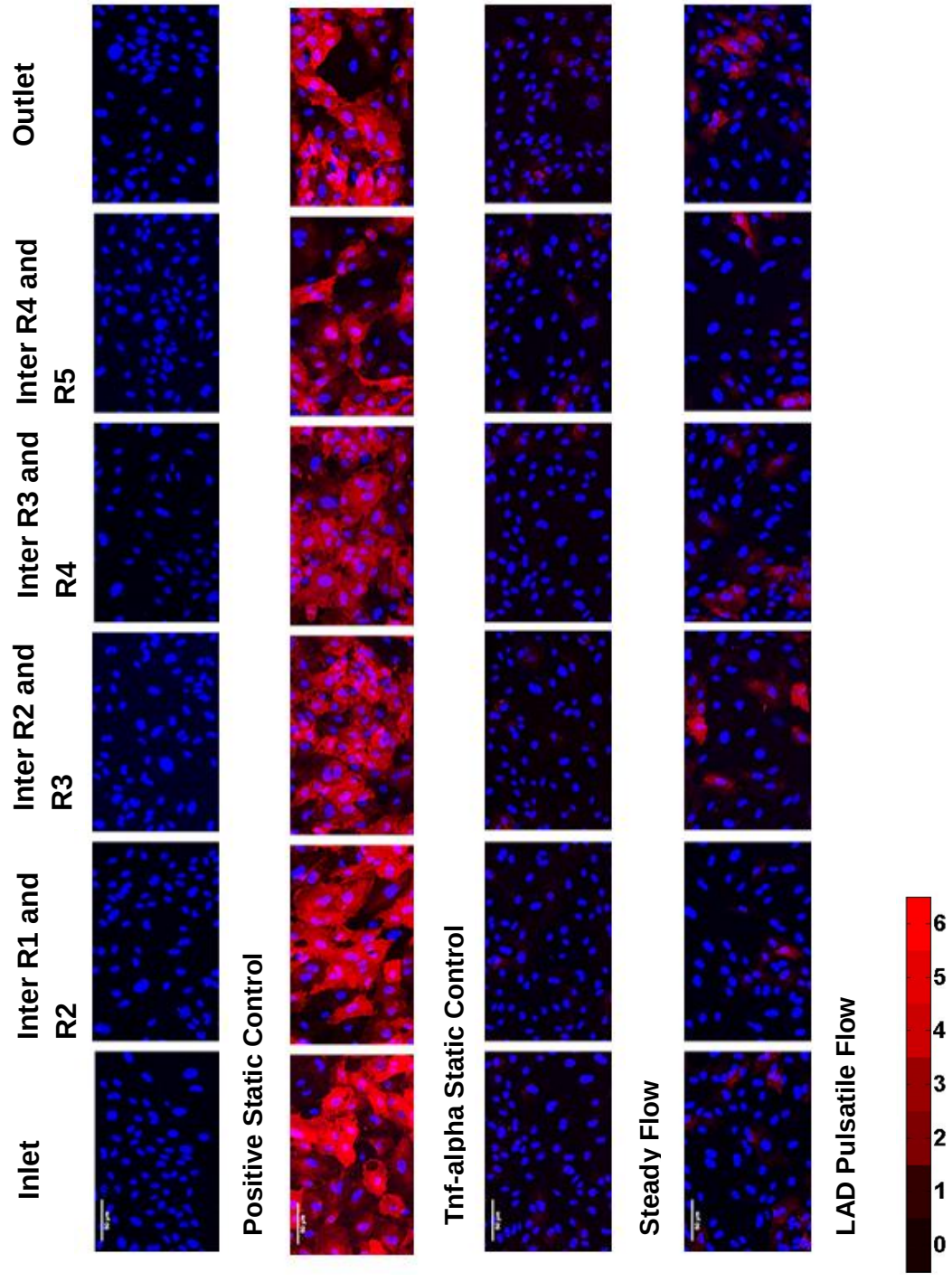

Figure 8.3 Images showing expression of ICAM-1 (Red stain) and stained nucleus (Blue) in HUVECs after stimulation for 6 hours. Static culture

stimulation; positive control (Top row), stimulation with human recombinant Tnf-α at concentration of 200 units/ml under static control (2nd Row), combination of steady flow and hydrostatic pressure of 100mmHg (3rd Row), combination of LAD pulsatile flow and hydrostatic pressure of 120/80mmHg (4th Row). Scale bar (0 – 6) shows expression level of ICAM-1 with 0 being least or no expression of ICAM-1 and 6 being fully expressed ICAM-1. n = 1.

Stimulation of HUVECs with human recombinant Tnf-α for 6 hours caused an increased level of ICAM-1 expression as shown in figure 8.3. However it is noticed that HUVECs exposed to both steady and LAD pulsatile flow exhibited selective expression of ICAM-1 in HUVECs for same time duration.

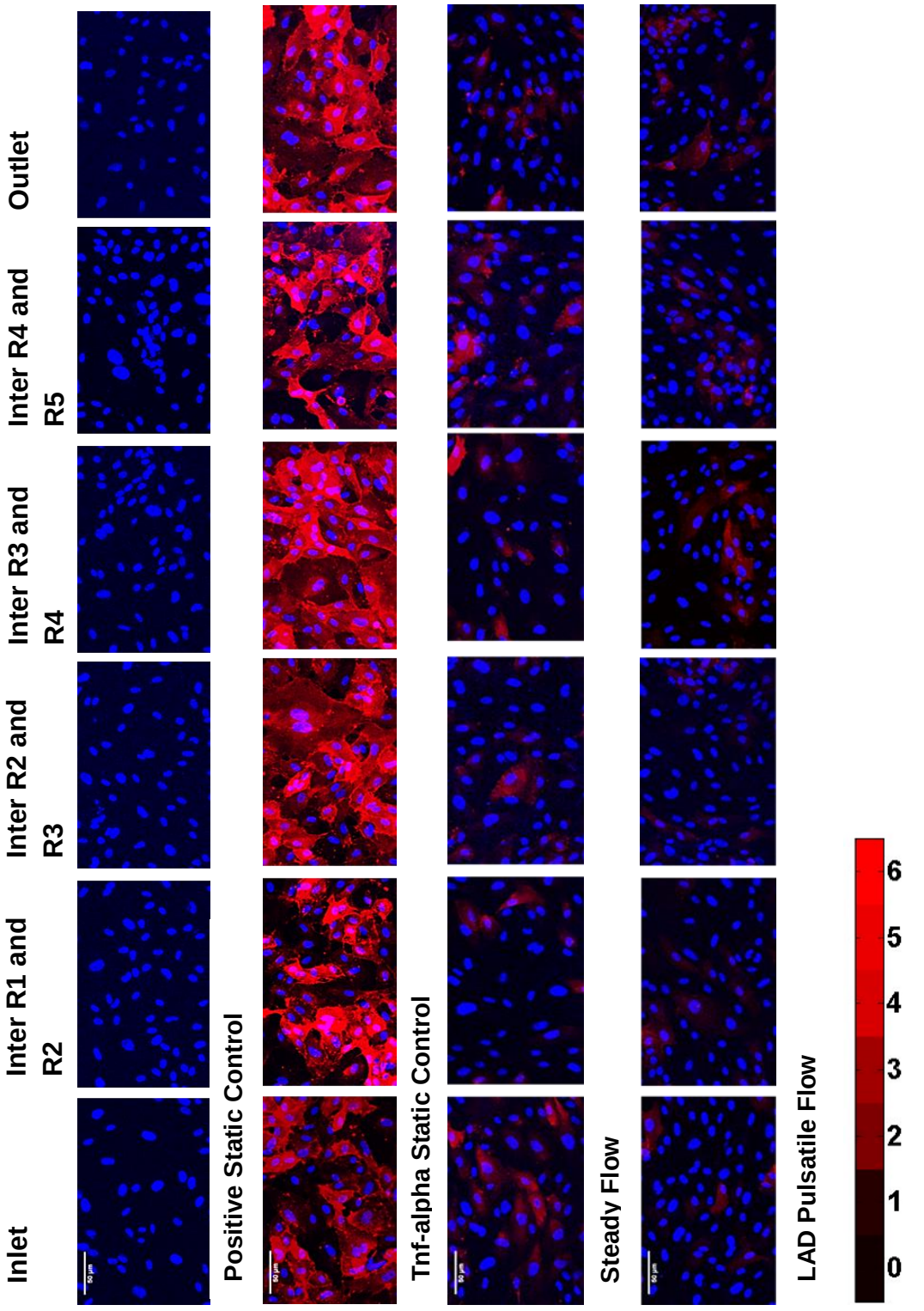

Figure 8.4 Images showing expression of ICAM-1 (Red stain) and stained nucleus (Blue) in HUVECs after stimulation for 12 hours. Static culture stimulation; positive control (Top row), stimulation with human recombinant

Tnf-α at concentration of 200 units/ml under static control (2nd row), combination of steady flow and hydrostatic pressure of 100mmHg (3rd row), combination of LAD pulsatile flow and hydrostatic pressure of 120/80mmHg (4th row). Scale bar (0 – 6) shows expression level of ICAM-1 with 0 being the least or no expression of ICAM-1 and 6 being fully expressed ICAM-1. n = 1.

Stimulation of HUVECs with human recombinant Tnf-α for 12 hours caused an increased level of ICAM-1 expression in HUVECs as shown in figure **8.4**. However it is noticed that HUVECs exposed to both steady and LAD pulsatile flow exhibited selective expression of ICAM-1 in HUVECs for same time duration.

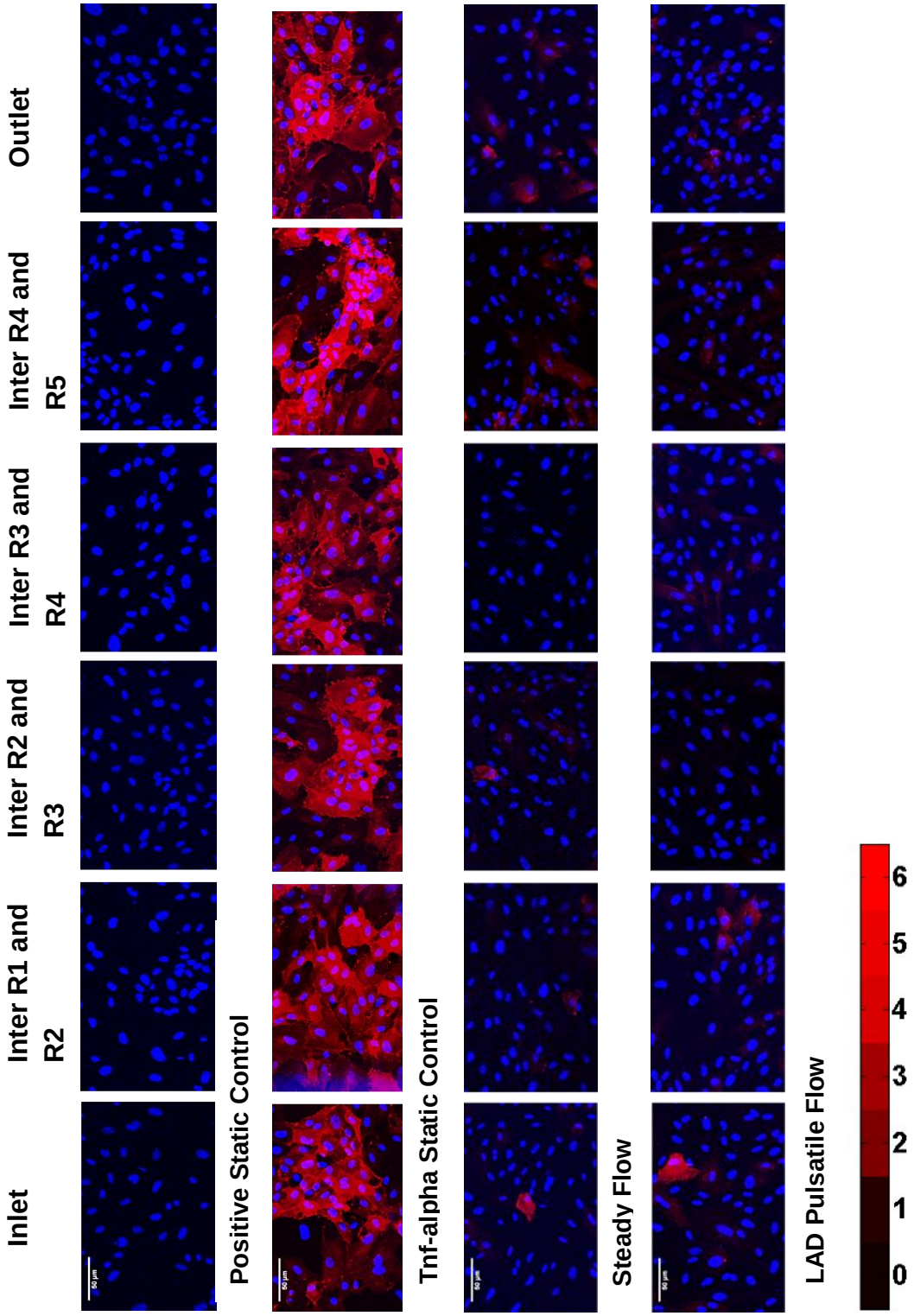

Figure 8.5 Images showing expression of ICAM-1 (Red stain) and stained nucleus (Blue) in HUVECs after stimulation for 24 hours. Static culture

stimulation; positive control (Top row), stimulation with human recombinant Tnf-α at concentration of 200 units/ml under static control (2nd row), combination of steady flow and hydrostatic pressure of 100mmHg (3rd row), combination of LAD pulsatile flow and hydrostatic pressure of 120/80mmHg (4th row). Scale bar (0 – 6) shows expression level of ICAM-1 with 0 being the least or no expression of ICAM-1 and 6 being fully expressed ICAM-1. n = 1.

Stimulation of HUVECs with human recombinant Tnf-α for 24 hours showed increased levels of ICAM-1 expression in HUVECs as illustrated in figure **8.5**. However it is noticed that HUVECs exposed to both steady and LAD pulsatile flow exhibited selective expression of ICAM-1 in HUVECs for same time duration.

8.4 DISCUSSION

ECs in the arterial vasculature are constantly being subjected to different combined stresses such as shear stress, cyclic strain and hydrostatic pressure. The effect of combined shear stress and hydrostatic pressure at physiological levels on HUVECs has been discussed to elicit marked changes of cell morphology; thus change in nuclear and actin cytoskeleton forms. Several studies have proposed that ECs predisposed to disturbed or low shear were more prone to atherogenesis [90, 413]. In most cases of arterial disease development, inflammation has been suggested to play a notable mediating role of disease [389, 445]. Many studies have reported low and disturbed shear induced NF-kB to cause adhesion molecules and inflammatory cytokines to be upregulated [441, 446-448]. However, there are few studies which have considered the role of combined hydrostatic pressure and shear stress on the regulation of NF-kB and subsequently on the

expression of NF-kB dependent adhesion molecules.

In vitro experiment presented in this chapter shows the activation of NF-kB and expression of ICAM-1 in HUVECs exposed to combined stresses (i.e. steady shear stress and hydrostatic pressure of 100 mmHg; and LAD pulsatile shear stress and hydrostatic pressure of 120/80 mmHg). Due to the design of the experimental model, fluid stresses were characterised by unidirectional mean shear stress of $2\,Pa$ and disturbed shear stress of approximately $-2\,Pa$ to $2.5\,Pa$. Activation of NF-kB as previously discussed is marked by the translocation of the $p65$ subunit NF-kB from the cytoplasm into the nucleus. The reason why HUVECs were stimulated for 1 hour in the investigation of NF-kB activation and no longer was that studies have reported ECs subjected to high shear stress to exhibit a biphasic response of NF-kB [449, 450]. Thus, stimulation of ECs to high shear stress causes an initial increase of NF-kB expression level followed by a steady decrease to a level at which NF-kB cannot be detected. Lan et al. [450] reported maximum activation of $p65$ subunit NF-kB at 1 hour of BAECs being subjected to only shear stress of $1.2\,Pa$ and then a decrease in activation thereafter. Based on the conclusion reached by Lan et al. [450], it was considered appropriate that the investigation of NF-kB activation in HUVECs when subjected to the stipulated stresses be for a duration of 1 hour. Qualitative analysis of HUVECs exposed to these combined stresses for 1 hour showed no activation of NF-kB as the nuclei of HUVECs appeared “black”. However, HUVECs stimulated with tnf-α for the same duration showed full activation of NF-kB as the nuclei this time appeared “green” as shown in figure **8.2**. This observation made however conflicts with that reported by Lan et al. [450] and more so with Nagel et al. [446] report which suggested disturbed shear to promote NF-kB activation. Reason to these differences in results could be due to the added stress; thus the hydrostatic pressure in our experiment.

We can draw some parallels of results on the effect of combined stresses on HUVECs in the activation of NF-kB presented here to that of Nakadate et al. [316] studies on the effect of combined hydrostatic pressure and shear stress on ECs expression of adhesion molecules. In the study by Nakadate et al. [316], it was reported that cells subjected to combined stresses induced different gene expression compared to the genes expressed by the cells subjected to only individual stress. The report further concluded that not only does the type of stress and/or combined stresses applied to the cells have an effect on the type of gene expressed but also the magnitude of these stresses also account for the difference in the gene expressed. It should be noted however that results presented are of a singular experiment and thus should only be considered as an indication of the possible response of cells exposed to a combination of shear stress and hydrostatic pressure on NF-kB activation. Further experiments are therefore needed to validate results.

HUVECs exposed to the stipulated combined stress conditions for ICAM-1 expression showed sporadic expression ICAM-1 at 6 hour, 12 hours and 24 hours whilst HUVECs stimulated with tnf-α showed maximum ICAM-1 expressions at the same timescales as shown figures **8.3** – **8.5**. Due to the experimental model design, there were regions where HUVECs were exposed to uniform shear and other regions they were exposed to 'disturbed' shear. Quantification of the levels of ICAM-1 expression of HUVECs exposed to uniform steady shear and uniform LAD pulsatile shear are shown in figure **8.6**. Also the level of ICAM-1 expression of HUVECs exposed to disturbed steady shear and disturbed LAD pulsatile shear are shown in figure **8.7**.

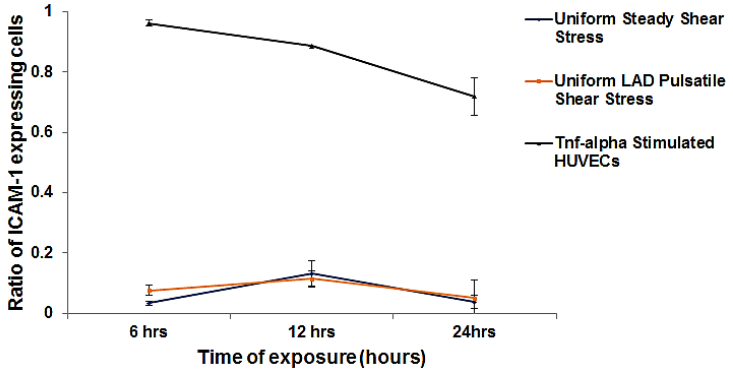

Figure 8.6 Line graph showing ICAM-1 expression level of HUVECs stimulated under stipulated combined stresses and Tnf-alpha. SEM = 3 images. n = 1.

As shown in figure **8.6**, HUVECs stimulated with tnf-alpha show high expression levels of ICAM-1 when compared to HUVECs stimulated under LAD pulsatile and steady flow. However, the level of ICAM-1 expressed by cells stimulated with tnf-alpha is seen to decrease with time. On the other hand, there is a gentle increase in the expression levels of ICAM-1 when cells were exposed to either steady or LAD pulsatile uniform stress from time 6 hours to 12 hours and then decreased from 12 hours to 24 hours.

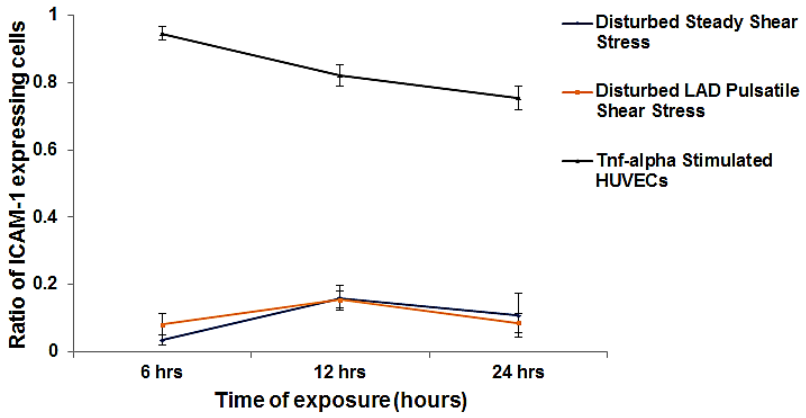

Figure 8.7 Line graph showing ICAM-1 expression level of HUVECs stimulated under stipulated combined stresses and Tnf-alpha. SEM = 3 images. n = 1.

As shown in figure **8.7**, HUVECs exposed to disturbed steady and LAD pulsatile shear stress exhibit a time dependent ICAM-1 expression. Therefore, there is an increase in ICAM-1 expression of cells subjected to disturbed steady and LAD pulsatile shear stress from 6 to 12 hours and then a decrease in the level of ICAM-1 expression from 12 to 24 hours. On the other hand, HUVECs stimulated by tnf-alpha do exhibit generally a time dependent decrease of ICAM-1 expression levels.

Quantitative analysis of ICAM-1 expression levels of HUVECs exposed to combined stress (i.e. steady shear stress and hydrostatic pressure of 100 mmHg; and LAD pulsatile shear stress and hydrostatic pressure of 120/80 mmHg) was performed by using the image toolbox in ImageJ to identify and count cells with ICAM-1 molecules stained as red. Whilst it is assumed that identification and count of ICAM-1 cells with ImageJ were accurate, it should be noted that form of analysis is operator dependent and therefore it is to be expected that results may be variable between operators. However, the human brain is very capable of recognising and interpreting images and thus it should be expected that analysis performed is sufficiently accurate.

From the quantitative data shown in figures 8.6 and 8.7, the local ICAM-1 expression levels are seen to increase up to 12 hours and then decrease until 24 hours when HUVECs are subjected to combined stress. This result is comparable to the results presented by Nakadate et al. [316] after exposing human aortic endothelial cells to combined stress of steady shear stress of $1.5\ Pa$ and hydrostatic pressure of $100\ mmHg$ and also pulsatile flow with a shear stress of $1.2/1.8\ Pa$ and hydrostatic pressure of $120/80\ mmHg$. It is however suggested that to validate results further experimental analysis is needed.

8.5 CONCLUSION

HUVECs were subjected to either a combination of shear stress and hydrostatic pressure conditions or stimulated with human recombinant Tnf-α to investigate the effects of these stimuli on ICAM-1 and NF-kB activation of the cells. It is observed that NF-kB and ICAM-1 are fully activated when HUVECS is stimulated with Tnf-α as shown in figures 8.2 to 8.7. Taking into consideration the design and CFD analysis of our cell-structure interaction model, cells were predicted to experience either a uniform or 'disturbed' shear stress depending on the localisation of the cells within the model. It was therefore interesting to observe that regardless of the localisation of the cells within the model, cells subjected to combined shear and hydrostatic pressure (i.e. LAD pulsatile shear and 120/80 mmHg or steady shear and 100 mmHg) for a given duration showed no activation of NF-kB. There was however a decreased level time-dependent selective expression of ICAM-1 when HUVECs were subjected to afore mentioned combined shear stress and hydrostatic pressure as shown in figures 8.6 and 8.7. These data suggest that combination of shear stress and hydrostatic pressure may play significant role in genes that could be expressed in ECs.

CHAPTER 9

CONCLUSIONS AND FUTURE WORK

9.1 CONCLUSIONS

This thesis sought to provide insights into the interrelation between physical forces arising in a stented arterial model and ECs response to elucidate the occurrence of restenosis within stented coronary artery. To achieve this purpose, the objectives as discussed in Chapter **1** were needed to be executed. Summarised below were the work done to achieve the following objectives of this thesis.

1. Establishing appropriate rheological blood model to be used in CFD analysis of fluid dynamics within straight stented artery: To achieve this objective the three most commonly used rheological blood models were investigated (i.e. Newtonian model, Non-Newtonian Power Law model and Carreau model) as discussed in Chapter **3**. Based on the specific geometrical dimensions of the stented model simulated, fluid dynamics analysis based on Newtonian model were seen to be >80% comparable to non-Newtonian blood dynamics based on Carreau model. It was thus suggested that analysing blood dynamics within a stented model using Newtonian fluid model in this case was acceptable.

2. Establishing a computational model of a 2D cell-stent interaction design: This objective was to mimic an in vivo 2D stented artery and

consequently investigate the mechanical forces created within the local stented artery. The classic hemodynamic factors such as WSSs, OSIs, SWSSGs and TWSSGs proposed in many experimental (in vivo and in vitro) and computational studies to play critical roles in the development and progression of CADs were also considered in the investigation. As demonstrated in Chapter **6**, the proximal and distal regions of the stented region were characterised with uniform shear and no shear gradients. However, within the stented regions were marked high shear gradients, disturbed WSSs and high OSIs.

3. Develop a flow bioreactor system capable of applying physiologically relevant parameters and producing appropriate mechanical milieu within stented artery model: This objective was achieved as the flow system developed was able to produce physiologically realistic LAD pulsatile flow waveforms and also physiological hydrostatic pressure of $120/80\ mmHg$. As further elaborated in Chapter **4**, data produced from the flow bioreactor system was comparable with that of analytical data. The design of the test section; thus the cell-interaction structure model, of the flow bioreactor system as discussed in depth in Chapter **5**, helped elicit the characteristic fluid flow dynamics experienced within a stented artery. Indeed, the application of the flow bioreactor system and the designed test section produced the WSSs, SWSSGs and OSIs illustrated in Chapter **6** at approximately physiological levels. Thus the CFD analysis performed in Chapter **6** was used to quantify the mechanical environment applied to the cells in the test section of the flow bioreactor system. More importantly, this flow bioreactor system was capable of maintain cells under sterile conditions.

4. Quantitatively analyse ECs morphological response to either combined or individual stress: As demonstrated in Chapter **7**, ECs subjected to a specific type of stress resulted in a marked change in the morphology of cultured cells. HUVECs subjected to uniform shear stress elongated and aligned to flow direction whilst HUVECs subjected to varied shear stresses exhibited random orientation to flow direction. These morphological changes were then quantified using commercial image programming software called CellProfiler. Results of morphological cells response reported in this thesis were similar to that reported by other researchers undertaking similar experimental investigations.

5. Investigate into shear-induced molecules expressed by the ECs: As discussed in Chapter **8**, HUVECs exposed to shear stresses and hydrostatic pressures created within the cell-structure interaction model did not activate the inflammatory molecule NF-kB. However, ICAM-1 was selectively expressed in respect to stimulation duration. To the author's knowledge there has been no investigation into the effects of cells exposed to a combination of shear stress and hydrostatic pressure on NF-kB activation.

Based up on the above observations, the following conclusions were reached:

1. The mechanical milieu within a stented artery is marked by varied WSSs, high SWSSGs and High OSIs due to flow disturbances at local site. WSS spikes are observed on top of stent struts whilst WSSs at the immediate regions of stent struts are very low.

2. There is a relationship between WSS, SWSSG and OSI present within stent struts regions. It was elucidated in chapter 6 that regions within stent struts which were predicted to experience flow separations were not only marked by high OSIs but both negative and positive WSSs and also high SWSSGs.

3. HUVECs subjected to steady and LAD pulsatile shear stress although may show qualitatively very similar response to shear stress may be quantitatively different. As discussed in chapter 7, HUVECs subjected to increase LAD SWSSGs showed slight increase in cell density whilst those subjected to increase steady SWSSG exhibited a decrease in cell density for the same time duration. Plausible reasoning to this observation is that TWSSGs may induce cell proliferation. Thus as steady flow has no transient characteristics, the effect of TWSSG on cells may be minimal or non-existent. Also as discussed in chapter 7, HUVECs subjected to steady and LAD pulsatile flow all show cell elongation and alignment to flow direction. More so there were no statistical differences in the number of cells that aligned to flow direction depending on the type of shear stress the cells were subjected. However, as evidently shown in figures 7.14aii and 7.14aiii, steady flow induced more cells to align to the flow direction compared to LAD pulsatile flow. Hence the type of stress subjected to cells may have a more distinctive effect compared to the other.

4. Most studies have focused on the individual stress effects of on ECs response albeit the effects of combined stress on ECs response more specifically on the type of genes being expressed could be different. It is thus proposed that investigations based on individual stress may not yield sufficient data to clarify clinical incidence of restenosis.

5. The modular design of the flow bioreactor system allows for easy addition and/or alteration of components such as the test sections and pulsatile cams. Thus permits a wide range of investigations into different types of combined stresses that may be applied to cells.

9.2 FUTURE WORK

Results presented in this thesis has provided some insights into how semi-circular struts dictate the fluid flow dynamics experienced on cells and how this stimuli influence cells response. It is however suggested that different strut designs may cause different fluid flow dynamics. Hence it is proposed that for future works, cells are subjected to different fluid flow dynamics dictated by the different stent strut designs and the cells response under each flow dynamics investigated to determine which strut design provides fluid dynamics more favourable to cells physiological behaviour.

It was also realised that combined stress and individual stress may influence differently the type of genes that are expressed. Hence future work may involve the investigation of various genes and signalling molecules that may be induced by different types of stress.

As previously stated the modular design of the flow bioreactor system allows for addition of other enabling technologies. It is therefore envisaged that a video camera could be incorporated to the bioreactor system so as to capture in real-time how cells respond to specific mechanical stimuli.

APPENDIX A

This appendix contains stimulated HUVECs stained for ICAM-1 expressions and also showing the stained cytoskeleton of the cell.

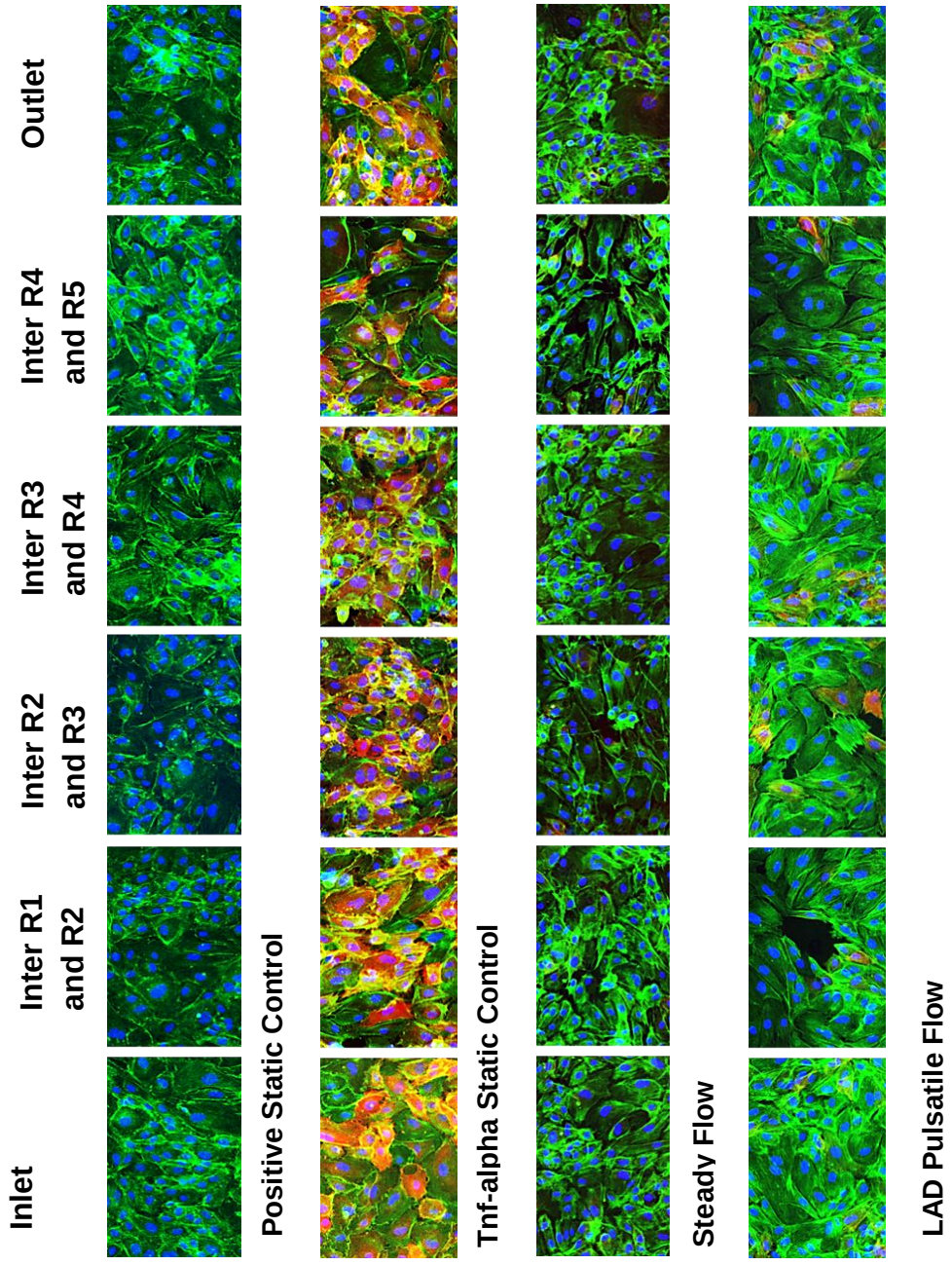

Figure 1 Images showing expression of ICAM-1 (Red stain), stained nucleus (Blue) and stained cytoskeleton (Green) in HUVECs after stimulation for 6 hours. Static culture stimulation; positive control (Top row), stimulation with human recombinant Tnf-α at concentration of 200 units/ml under static control (2^{nd} row), combination of steady flow and hydrostatic pressure of 100mmHg (3^{rd} row), combination of LAD pulsatile flow and hydrostatic pressure of 120/80mmHg (4^{th} Row).

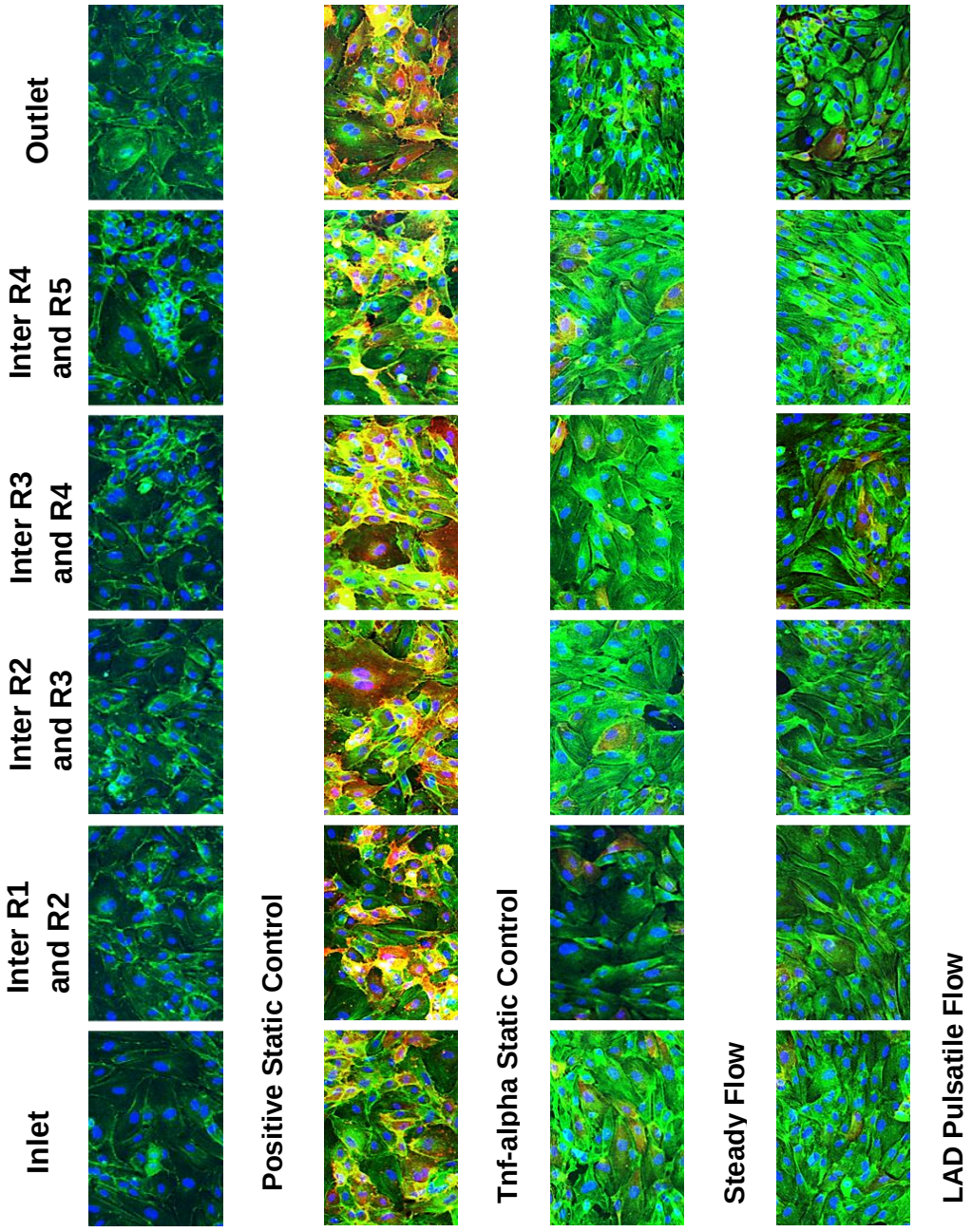

Figure 2 Images showing expression of ICAM-1 (Red stain), stained nucleus (Blue) and stained cytoskeleton (Green) in HUVECs after stimulation for 12 hours. Static culture stimulation; positive control (Top row), stimulation with human recombinant Tnf-α at concentration of 200 units/ml under static control (2nd row), steady flow and pressure of 100mmHg (3rd row), LAD flow and pressure of 120/80mmHg (4th row).

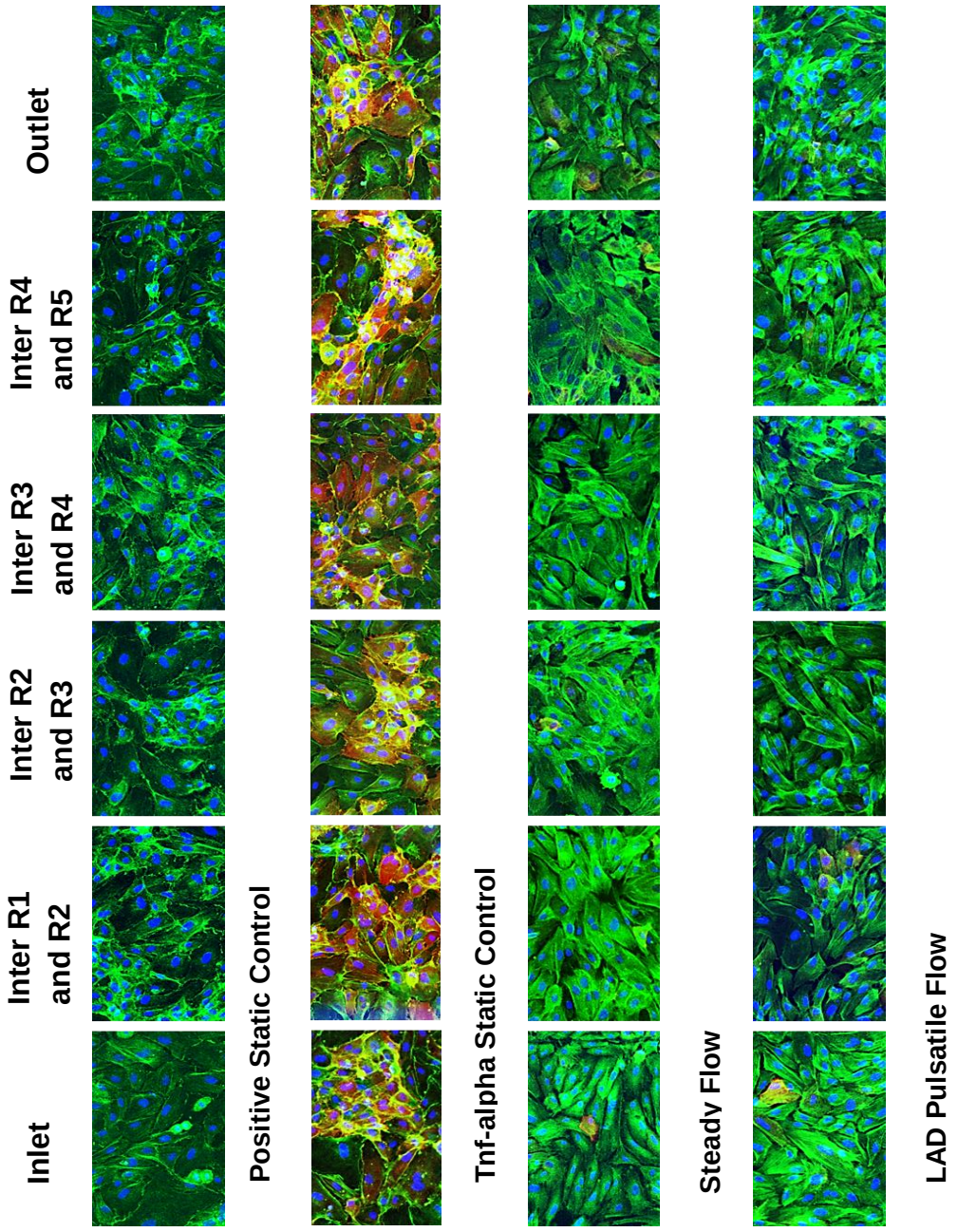

Figure 3 Images showing expression of ICAM-1 (Red stain), stained nucleus (Blue) and stained cytoskeleton (Green) in HUVECs after stimulation for 24 hours. Static culture stimulation; positive control (Top row), stimulation with human recombinant Tnf-α at concentration of 200 units/ml under static control (2nd row), steady flow and pressure of 100mmHg (3rd row), LAD flow and pressure of 120/80mmHg (4th Row).

REFERENCES

1. Service, N.H. *Coronary Heart Disease*. 2010 [cited 2012 13 June]; Available from: http://www.nhs.uk/conditions/coronary-heart-disease/Pages/Introduction.aspx.
2. Association, A.H., *AHA Statistical Update.* Circulation, 2010. **123**: p. 18.
3. Okrainec K., Eisenberg M.J., and Banerjee D.K., *Coronary artery disease in the developing world.* American Heart Journal, 2004. **148**(1): p. 7-15.
4. LaDisa J.F. Jr., et al., *Stent implantation alters coronary artery hemodynamics and wall shear stress during maximal vasodilation.* Journal of Applied Physiology, 2002. **93**(6): p. 1939-1946.
5. Voskuil M., et al., *Coronary hemodynamics of stent implantation after suboptimal and optimal balloon angioplasty.* JACC, 2002. **39**(9): p. 1513-1517.
6. Berry J.L., et al., *Experimental and Computational Flow Evaluation of Coronary Stents.* Ann Biomed Eng, 2000. **28**: p. 386-398.
7. Dehlaghi V., Najarian S., and Shadpour M.T., *Effect of Stent Geometry on Phase Shift between Pressure and Flow Waveforms in Stented Human Coronary Artery.* Am J App Sc, 2008. **5**(4): p. 340-346.
8. Ku D., et al., *Pulsatile flow and atherosclerosis in the human carotid bifurcation: positive correlation between plaque and low and oscillating shear stress.* Atherosclerosis, 1985. **5**: p. 293–302.
9. Zarins C.K., et al., *Carotid bifurcation atherosclerosis. Quantitative correlation of plaque localization with flow velocity profiles and wall shear stress.* Arterioscler Thromb Vasc Biol., 1983. **53**: p. 502-514.
10. Friedman M.H., et al., *Correlation between intimal thickness and fluid shear in human arteries* arteriosclerosis, 1981. **39**: p. 425-436.
11. Rouleau, L., et al., *Endothelial cell morphologic response to asymmetric stenosis hemodynamics: effects of spatial wall shear stress gradients.* Journal of Biomechanical Engineering, 2010. **132**(8): p. 081013.
12. Koskinas, K.C., et al., *Role of endothelial shear stress in stent restenosis and thrombosis: pathophysiologic mechanisms and implications for clinical translation.* Journal of the American College of Cardiology, 2012. **59**(15): p. 1337-1349.
13. Schirmer, C.M. and A.M. Malek, *Wall shear stress gradient analysis within an idealised stenosis using non-Newtonian flow.* Neurosurgery, 2007. **61**(4): p. 853-864.
14. Fujimoto, M., et al., *Temporal correlation between wall shear stress and in-stent stenosis after Wingspan stent in swine model.* American Journal of Neuroradiology, 2014. **35**(5): p. 994-998.
15. Kibos, A., A. Campeanu, and I. Tintoiu, *Pathophysiology of coronary artery in-stent restenosis.* Acute cardiac care, 2007. **9**(2): p. 111-119.
16. Samady, H., et al., *Coronary artery wall shear stress is associated with progression and transformation of atherosclerotic plaque and arterial remodeling in patients with coronary artery disease.* Circulation, 2011. **124**(7): p. 779-788.

17. Eshtehardi, P., et al., *Association of coronary wall shear stress with atherosclerotic plaque burden, composition, and distribution in patients with coronary artery disease.* Journal of the American Heart Association, 2012. **1**(4): p. e002543.
18. Taxon M., *Hemodynamic basis of atherosclerosis with critique of the cholesterol-heart disease hypothesis*. 1995, Wallingford, U.K.: Begell House. 48-49.
19. Misra S., et al., *Increased shear stress with upregulation of VEGF-A and its receptors and MMP-2, MMP-9, and TIMP-1 in venous stenosis of hemodialysis grafts* Am J Physiol Heart Circ Physiol, 2008. **294**: p. H2219-H2230.
20. Ford, M.D., et al., *PIV-measured versus CFD-predicted flow dynamics in anatomically realistic cerebral aneurysm models.* Journal of Biomechanical Engineering, 2008. **130**(2): p. 021015.
21. Xiong, F. and C. Chong, *PIV-validated numerical modeling of pulsatile flows in distal coronary end-to-side anastomoses.* Journal of Biomechanics, 2007. **40**(13): p. 2872-2881.
22. Oyre, S., et al., *Quantitation of circumferential subpixel vessel wall position and wall shear stress by multiple sectored three-dimensional paraboloid modeling of velocity encoded cine MR.* Magnetic Resonance in Medicine, 1998. **40**(5): p. 645-655.
23. Chaichana, T., Z. Sun, and J. Jewkes, *Computational fluid dynamics analysis of the effect of plaques in the left coronary artery.* Computational and mathematical methods in medicine, 2012. **2012**.
24. White, C.R., et al., *Temporal gradients in shear, but not spatial gradients, stimulate endothelial cell proliferation.* Circulation, 2001. **103**(20): p. 2508-2513.
25. Gundert T. J., et al., *A Rapid and Computationally Inexpensive Method to Virtually Implant Current and Next-Generation Stents into Subject-Specific Computational Fluid Dynamics Models.* Annals of Biomedical Engineering, 2011. **39**(5): p. 1423-1437.
26. Murphy J. and Boyle F., *Predicting neointimal hyperplasia in stented arteries using time-dependant computational fluid dynamics: A review.* Computers in Biology and Medicine, 2010. **40**(4): p. 408-418.
27. Dehlaghi V., Shadpoor M. T., and Najarian S., *Analysis of wall shear stress in stented coronary artery using 3D computational fluid dynamics modeling.* Journal of Materials Processing Technology, 2008. **197**(1-3): p. 174-181.
28. Berry J. L., et al., *Experimental and computational flow evaluation of coronary stents.* Annals of Biomedical Engineering, 2000. **28**(4): p. 386-398.
29. Benard N., Perrault R., and Coisne D., *Computational approach to estimating the effects of blood properties on changes in intra-stent flow.* Annals of Biomedical Engineering, 2006. **34**(8): p. 1259-1271.
30. Mejia J., et al., *Evaluation of the effect of stent strut profile on shear stress distribution using statistical moments.* Biomedical Engineering Online, 2009. **8**.
31. Liu B. and Tang D., *Computer simulations of atherosclerotic plaque growth in coronary arteries.* Molecular & Cellular Biomechanics, 2010. **7**(4): p. 193-202.
32. Johnston B. M., et al., *Non - Newtonian blood flow in human right coronary arteries: Transient simulations.* J Biomech, 2005. **39**: p. 1116 - 1128.
33. Kirpalani A., et al., *Velocity and wall shear stress patterns in the human right coronary artery.* Journal of Biomechanical Engineering, 1993. **121**: p. 709 - 720.
34. Perktold K. and Resch M., *Numerical flow studies in human carotid artery bifurcations: basic discussion of geometry factor in atherogenesis.* Journal of Biomechanical Engineering, 1990. **12**: p. 111 - 123.
35. Soulis J. V., et al., *Non-Newtonian models for molecular viscosity and wall shear stress in a 3D reconstructed human left coronary artery.* Medical Engineering & Physics, 2008. **30**(1): p. 9-19.

36. Liepsch D., *An introduction to biofluid mechanics—basic models and applications.* Journal of Biomechanics, 2002. **35**: p. 415–435.
37. Matsuo S., et al., *Phasic coronary artery flow velocity determined by Doppler flowmeter catheter in aortic stenosis and aortic regurgitation.* The American Journal of Cardiology, 1988. **62**(1): p. 917–922.
38. Fujii K., et al., *Stent underexpansion and residual reference segment stenosis are related to stent thrombosis after sirolimus-eluting stent implantation.* J Am Coll Cardiol, 2005. **45**: p. 995-998.
39. Finn A.V., et al., *Pathological correlates of late drug-eluting stent thrombosis: strut coverage as a marker of endothelialization.* Circulation, 2007. **115**: p. 2435-2441.
40. Cook S., et al., *Incomplete Stent Apposition and Very Late Stent Thrombosis After Drug-Eluting Stent Implantation.* Circulation, 2007. **115**: p. 2426-2434.
41. Briguori C., et al., *In-stent restenosis in small coronary arteries: Impact of strut thickness.* JACC, 2002. **40**(3): p. 403-409.
42. Soucy N.V., et al., *Strut tissue coverage and endothelial cell coverage: a comparison between bare metal stent platforms and platinum chromium stents with and without everolimus-eluting coating.* EuroIntervention, 2010. **6**(5): p. 630-637.
43. Jiménez, J.M. and P.F. Davies, *Hemodynamically driven stent strut design.* Annals of Biomedical Engineering, 2009. **37**(8): p. 1483-1494.
44. Karas S. P., et al., *Coronary intimal proliferation after balloon injury and stenting in swine - An animal model of restenosis.* Journal of the American College of Cardiology, 1992. **20**(2): p. 467-474.
45. Farb A., et al., *Morphological predictors of restenosis after coronary stenting in humans.* Circulation, 2002. **105**(25): p. 2974-2980.
46. Wentzel, J.J., et al., *Relationship between neointimal thickness and shear stress after Wallstent implantation in human coronary arteries.* Circulation, 2001. **103**(13): p. 1740-1745.
47. Frangos, J., L. McIntire, and S. Eskin, *Shear stress induced stimulation of mammalian cell metabolism.* Biotechnology and Bioengineering, 1988. **32**(8): p. 1053-1060.
48. Estrada, R., et al., *Endothelial cell culture model for replication of physiological profiles of pressure, flow, stretch, and shear stress in vitro.* Analytical chemistry, 2011. **83**(8): p. 3170-3177.
49. Bao, X., C. Lu, and J.A. Frangos, *Mechanism of temporal gradients in shear-induced ERK1/2 activation and proliferation in endothelial cells.* American Journal of Physiology-Heart and Circulatory Physiology, 2001. **281**(1): p. H22-H29.
50. White, C.R., et al., *Temporal gradients in shear, but not spatial gradients, stimulate ERK1/2 activation in human endothelial cells.* American Journal of Physiology-Heart and Circulatory Physiology, 2005. **289**(6): p. H2350-H2355.
51. Yee, A., et al., *A validated system for simulating common carotid arterial flow in vitro: alteration of endothelial cell response.* Annals of Biomedical Engineering, 2006. **34**(4): p. 593-604.
52. Breen, L.T., et al., *Development of a novel bioreactor to apply shear stress and tensile strain simultaneously to cell monolayers.* Review of Scientific Instruments, 2006. **77**(10).
53. Madhavan, M.V., et al., *Coronary artery calcification: Pathogenesis and prognostic implications.* Journal of the American College of Cardiology, 2014. **63**(17): p. 1703-1714.
54. Zhu H., et al., *Comparison of coronary artery dynamics pre- and post-stenting.* Journal of Biomechanics, 2003. **36**: p. 689-697.

55. Gittard S. and Narayan R.J., *Laser direct writing of micro- and nano-scale medical devices.* Expert Rev Med Devices, 2010. **7**(3): p. 343-356.
56. Koskela J.E., et al., *Two-photon microfabrication of poly(ethylene glycol) diacrylate and a novel biodegradable photopolymer—comparison of processability for biomedical applications.* Polym Adv. Technol, 2011. **23**(6): p. 992-1001.
57. Bailey R. *Coronary Artery*. 2011 [cited 2012 12 June]; Available from: http://biology.about.com/od/anatomy/ss/Coronary-Arteries.htm.
58. Marcus, J.T., et al., *Flow profiles in the left anterior descending and the right coronary artery assessed by MR velocity quantification: effects of through-plane and in-plane motion of the heart.* Journal of computer assisted tomography, 1999. **23**(4): p. 567-576.
59. Langille, B.L. and F. O'Donnell, *Reductions in arterial diameter produced by chronic decreases in blood flow are endothelium-dependent.* Science, 1986. **231**(4736): p. 405-407.
60. Rudic, R.D., et al., *Direct evidence for the importance of endothelium-derived nitric oxide in vascular remodeling.* Journal of Clinical Investigation, 1998. **101**(4): p. 731.
61. Davies, P.F., *Flow-mediated endothelial mechanotransduction.* Physiological reviews, 1995. **75**(3): p. 519-560.
62. Epstein, F.H., G.H. Gibbons, and V.J. Dzau, *The emerging concept of vascular remodeling.* New England Journal of Medicine, 1994. **330**(20): p. 1431-1438.
63. Kohler, T.R., et al., *Increased blood flow inhibits neointimal hyperplasia in endothelialized vascular grafts.* Circulation Research, 1991. **69**(6): p. 1557-1565.
64. Bandosz P., et al., *Decline in mortality from coronary heart disease in Poland after socioeconomic transformation: modelling study.* BMJ, 2012. **344**: p. 1-10.
65. Beller G.A., *Coronary heart disease in the first 30 years of the 21st century: Challenges and opportunities.* Circulation, 2001. **103**: p. 2428-2435.
66. Drewnowski A. and Popkin B.M., *The nutrition transition: new trends in the global diet.* Nutr Rev, 1997. **55**(2): p. 31-43.
67. Kumar R., et al., *Urbanization and coronary heart disease: a study of urban-rural differences in northern India.* Indian Heart J., 2006. **58**(2): p. 126-130.
68. Muna W.F., *Cardiovascular disorders in Africa.* World Health Stat Q., 1993. **46**(2): p. 125-133.
69. Rani M., et al., *Tobacco use in India: prevalence and predictors of smoking and chewing in a national cross sectional household survey.* Tob Control BMJ, 2003. **12**(4): p. 1-8.
70. Gupta R., et al., *Epidemiology and causation of coronary heart disease and stroke in India.* Heart, 2008. **94**: p. 16-26.
71. Dawber, T.R., F.E. Moore, and G.V. Mann, *II. Coronary heart disease in the Framingham study.* American Journal of Public Health and the Nations Health, 1957. **47**(4_Pt_2): p. 4-24.
72. Aboyans V., Lacroix P., and Criqui M.H., *Large and small vessels atherosclerosis: Similarities and differences.* Progress in Cardiovascular Diseases, 2007. **50**(2): p. 112-125.
73. Stary, H.C., *Natural history and histological classification of atherosclerotic lesions an update.* Arteriosclerosis, thrombosis, and vascular biology, 2000. **20**(5): p. 1177-1178.
74. Stary, H.C., et al., *A definition of initial, fatty streak, and intermediate lesions of atherosclerosis. A report from the Committee on Vascular Lesions of the Council on Arteriosclerosis, American Heart Association.* Arteriosclerosis, thrombosis, and vascular biology, 1994. **14**(5): p. 840-856.
75. Ross, R., *The pathogenesis of atherosclerosis: a perspective for the 1990s.* 1993.

76. Friedman M.H., et al., *Correlation between wall shear and intimal thickness at a coronary artery branch.* Atheroscleosis, 1987. **68**: p. 27-33.
77. Caro C.G., Fitz-Gerald J.M., and Schroter R.C., *Atheroma and Arterial Wall Shear Observation, Correlation and Proposal of a Shear Dependent Mass Transfer Mechanism for Atherogenesis.* Proceedings of the Royal Society of London B Biological Science, 1971. **177**(46): p. 109-159.
78. Chen J. and Lu X., *Numerical investigation of the non-Newtonian blood flow in a bifurcation model with a non-planar branch.* Journal of Biomechanics, 2004. **37**: p. 1899-1911.
79. Dvir D., et al., *Degrees of severe stenoses in sigma-shaped versus c-shaped right coronary arteries.* Am J Cardiol, 2003. **92**: p. 294-297.
80. Dvir D., et al., *Relation of amounts of narrowing to the length of the right coronary artery.* Am J Cardiol, 2002. **90**: p. 46-48.
81. Hochman, J.S., et al., *The distribution of atherosclerotic lesions in the coronary arterial tree: relation to cardiac risk factors.* American heart journal, 1988. **116**(5): p. 1217-1222.
82. El Fawal, M., et al., *Sudden coronary death in Glasgow: the severity and distribution of chronic coronary atherosclerotic stenoses.* British heart journal, 1987. **57**(5): p. 420-426.
83. McGill, H.C., et al., *Effects of coronary heart disease risk factors on atherosclerosis of selected regions of the aorta and right coronary artery.* Arteriosclerosis, Thrombosis, and Vascular Biology, 2000. **20**(3): p. 836-845.
84. C, W.R. and A.J. A, *Quantification of coronary arterial narrowing at necropsy in acute transmural myocardial infarction. Analysis and comparison of findings in 27 patients and 22 controls.* Circulation, 1980. **61**(4): p. 786-790.
85. Warnes, C.A. and W.C. Roberts, *Comparison at necropsy by age group of amount and distribution of narrowing by atherosclerotic plaque in 2995 five-mm long segments of 240 major coronary arteries in 60 men aged 31 to 70 years with sudden coronary death.* American heart journal, 1984. **108**(3): p. 431-435.
86. Schmermund, A., et al., *Usefulness of topography of coronary calcium by electron-beam computed tomography in predicting the natural history of coronary atherosclerosis.* The American journal of cardiology, 2000. **86**(2): p. 127-132.
87. Strong J.P., *Atherosclerotic lesions. Natural history, risk factors, and topography.* Arch Pathol Lab Med, 1992. **116**(12): p. 1268-1275.
88. Gazetopoulos N., et al., *Short left coronary artery trunk as a risk factor in the development of coronary atherosclerosis. Pathological study.* British Heart Journal, 1976. **38**: p. 1160-1165.
89. Chien S., *Mechanotransduction and endothelial cell homeostasis: the wisdom of the cell.* Am J Physiol Heart Circ Physiol, 2007. **292**: p. H1209-H1224.
90. Cunningham K.S. and Gotlieb A.I., *The role of shear stress in the pathogenesis of atherosclerosis.* Lab Inves, 2005. **85**: p. 9-23.
91. Traub O. and Berk B.C., *Laminar Shear Stress, Mechanisms by Which Endothelial Cells Transduce an Atheroprotective Force.* Arterioscler Thromb Vasc Biol., 1998. **18**: p. 677-685.
92. Chatzizisis Y.S. and Giannoglou G.D., *Pulsatile flow: A critical modulator of the natural history of atherosclerosis.* Medical Hypotheses, 2006. **67**: p. 338-340.
93. Shaaban A.M. and Duerinckx A.J., *Wall shear stress and early atherosclerosis: A review.* AJR, 2000. **174**(6): p. 1657-1665.
94. Ohashi T. and Sato M., *Remodeling of vascular endothelial cells exposed to fluid shear stress: experimental and numerical approach.* Fluid Dynamic Research, 2005. **37**: p. 40-59.

95. Zarins, C.K., et al., *Carotid bifurcation atherosclerosis. Quantitative correlation of plaque localization with flow velocity profiles and wall shear stress.* Circulation Research, 1983. **53**(4): p. 502-514.
96. Glagov, S., et al., *Hemodynamics and atherosclerosis. Insights and perspectives gained from studies of human arteries.* Archives of Pathology & Laboratory Medicine, 1988. **112**(10): p. 1018-1031.
97. Ku D.N., *Blood flow in arteries.* Annu Rev. Fluid Mech, 1997. **29**: p. 399 - 434.
98. Blackman B.R., Garcia-Cardena G., and Gimbrone M.A. Jr., *A new in vitro model to evaluate differential responses of endothelial cells to simulated arterial shear stress waveforms.* J Biomech Eng., 2002. **124**: p. 397–407.
99. Ziegler T., et al., *Influence of oscillatory and unidirectional flow environments on the expression of endothelin and nitric oxide synthase in cultured endothelial cells.* Arterioscler Thromb Vasc Biol., 1998. **18**: p. 686–692.
100. Bao X., Lu C., and Frangos J.A., *Temporal gradient in shear but not steady shear stress induces PDGF-A and MCP-1 expression in endothelial cells: role of NO, NF kappa B, and egr-1.* Arterioscler Thromb Vasc Biol., 1999. **19**: p. 996–1003.
101. Morrisett J.D., *The role of lipoprotein[a] in atherosclerosis.* Curr Atheroscler Rep, 2000. **2**(3): p. 243-250.
102. Ku, D.N., et al., *Pulsatile flow and atherosclerosis in the human carotid bifurcation. Positive correlation between plaque location and low oscillating shear stress.* Arteriosclerosis, thrombosis, and vascular biology, 1985. **5**(3): p. 293-302.
103. Peiffer, V., S.J. Sherwin, and P.D. Weinberg, *Does low and oscillatory wall shear stress correlate spatially with early atherosclerosis? A systematic review.* Cardiovascular research, 2013: p. cvt044.
104. Steinman, D.A., et al., *Reconstruction of carotid bifurcation hemodynamics and wall thickness using computational fluid dynamics and MRI.* Magnetic Resonance in Medicine, 2002. **47**(1): p. 149-159.
105. Joshi, A.K., et al., *Intimal thickness is not associated with wall shear stress patterns in the human right coronary artery.* Arteriosclerosis, thrombosis, and vascular biology, 2004. **24**(12): p. 2408-2413.
106. Gijsen, F.J., et al., *A new imaging technique to study 3-D plaque and shear stress distribution in human coronary artery bifurcations in vivo.* Journal of Biomechanics, 2007. **40**(11): p. 2349-2357.
107. Augst, A., et al., *Analysis of complex flow and the relationship between blood pressure, wall shear stress, and intima-media thickness in the human carotid artery.* American Journal of Physiology-Heart and Circulatory Physiology, 2007. **293**(2): p. H1031-H1037.
108. van der Giessen, A.G., et al., *3D fusion of intravascular ultrasound and coronary computed tomography for in-vivo wall shear stress analysis: a feasibility study.* The international journal of cardiovascular imaging, 2010. **26**(7): p. 781-796.
109. Wentzel, J.J., et al., *Geometry guided data averaging enables the interpretation of shear stress related plaque development in human coronary arteries.* Journal of Biomechanics, 2005. **38**(7): p. 1551-1555.
110. Yusuf S., *Two decades of progress in preventing vascular disease.* Lancet, 2002. **360**(9326): p. 2-3.
111. Garg S. and Serruys P.W., *Coronary stents: Current status.* J Am Coll Cardiol, 2010. **56**: p. s1-s42.
112. Brener S.J., et al., *Propensity analysis of long-term survival after surgical or percutaneous revascularization in patients with multivessel coronary artery disease and high-risk features.* Circulation, 2004. **109**: p. 2290-2295.

113. Pell J.P., et al., *Comparison of survival following coronary artery bypass grafting vs. percutaneous coronary intervention in diabetic and non-diabetic patients: retrospective cohort study of 6320 procedures.* Diabet Med, 2004. **21**: p. 790-792.
114. Van Domburg R.T., et al., *Late outcome after stenting or coronary artery bypass surgery for the treatment of multivessel disease: a single-center matched-propensity controlled cohort study.* Ann Thorac Surg, 2005. **79**: p. 1563-1569.
115. Serruys P. W., et al., *Percutaneous coronary intervention versus coronary-artery bypass grafting for severe coronary artery disease.* New England Journal of Medicine, 2009. **360**(10): p. 961-972.
116. Lamy A., Natarajan M., and Yusuf S., *Medical treatment, PCI, or CABG for coronary artery disease? The three approaches should complement one another, not compete.* BMJ, 2011. **342**(966): p. 1-2.
117. Holmes D. R., *Debate: PCI vs CABG: a moving target, but we are gaining.* Current Controlled Trials in Cardiovascular Medicine, 2001. **2**(6): p. 263-265.
118. British Journal Cardio Staff., *PCI in the UK: the continuing journey.* The British Journal of Cardiology, 2010. **17**: p. 5-8.
119. Stouffer III G.A. and Karlheinz P., *Percutaneous coronary intervention.* Medscape, 2011. **1**: p. 1-7.
120. Mack M.J., et al., *Current status and outcomes of coronary revascularization 1999 to 2002: 148,396 surgical and percutaneous procedures.* The Annals of Thoracic Surgery, 2004. **77**(3): p. 761-768.
121. Ulrich M.R., Brock D.M., and Ziskind A.A., *Analysis of trends in coronary artery bypass grafting and percutaneous coronary intervention rates in Washington state from 1987 to 2001.* Am J Cardiol, 2003. **92**(7): p. 836-839.
122. Gerber Y., et al., *Coronary revascularization in the community. A population-based study, 1990 to 2004.* J Am Coll Cardiol, 2007. **50**(13): p. 1223-1229.
123. F, L.P., et al. *National audit of percutaneous coronary interventional procedures public report: Annual public report January 2012 - December 2012*. 2014.
124. Defeyter P. J., Dejaegere P. P. T., and Serruys P. W., *Incidence, predictors, and management of acute coronary-occlusion after coronary angioplasty.* American Heart Journal, 1994. **127**(3): p. 643-651.
125. Sigwart U., et al., *Emergency stenting for acute occlusion after coronary balloon angioplasty.* Circulation, 1988. **78**: p. 1121 - 1127

126. SC NG. *The heart of the matter* Understanding balloon angioplasty 2006 [cited 2012 03 April]; Available from: http://hmatter.blogspot.co.uk/2006/01/understanding-balloon-angioplasty.html.
127. Sigwart U., et al., *Intravascular stents to prevent occlusion and restenosis after trans-luminal angioplasty.* New England Journal of Medicine, 1987. **316**(12): p. 701-706.
128. Serruys P. W., et al., *A comparison of balloon-expandable stent implantation with balloon angioplasty in patients with coronary artery disease.* New England Journal of Medicine, 1994. **331**(8): p. 489-495.
129. Fischman D. L., et al., *A randomized comparison of coronary-stent placement and balloon angioplasty in the treatment of coronary artery disease.* New England Journal of Medicine, 1994. **331**(8): p. 496-501.
130. King S. B., *The development of interventional cardiology.* Journal of the American College of Cardiology, 1998. **31**(4): p. 64B-88B.
131. Serruys P. W., Kutryk M. J. B., and Ong A. T. L., *Drug therapy - Coronary-artery stents.* New England Journal of Medicine, 2006. **354**(5): p. 483-495.

132. Gordon P. C., et al., *Mechanisms of restenosis and redilation within coronary stents—Quantitative angiographic assessment.* Journal of the American College of Cardiology, 1993. **21**(5): p. 1166-1174.
133. Hoffmann R., et al., *Patterns and Mechanisms of In-Stent Restenosis. A Serial Intravascular Ultrasound Study.* Circulation, 1996. **94**: p. 1247-1254.
134. McBride W., Lange R.A., and Hillis L.D., *Restenosis after successful coronary angioplasty. Pathophysiology and prevention.* N Engl J Med, 1988. **318**: p. 1734-1737.
135. Versaci F., et al., *A comparison of coronary-artery stenting with angioplasty for isolated stenosis of the proximal left anterior descending coronary artery.* N Engl J Med, 1997. **336**: p. 817-822.
136. Moliterno D. J., *Healing achilles - Sirolimus versus paclitaxel.* New England Journal of Medicine, 2005. **353**(7): p. 724-727.
137. Serruys, P.W., M.J.B. Kutryk, and A.T.L. Ong, *Drug therapy - Coronary-artery stents.* New England Journal of Medicine, 2006. **354**(5): p. 483-495.
138. Birkenhauer P., Yang Z., and Gander B., *Preventing restenosis in early drug-eluting stent era: recent developments and future perspectives.* J Pharm Pharmacol, 2004. **56**: p. 1339-1356.
139. Serruys P.W., et al., *Angiographic follow-up after placement of a self-expanding coronary-artery stent.* N Engl J Med, 1991. **324**: p. 13-17.
140. Arjomand H., et al., *Percutaneous coronary intervention: historical perspectives, current status and future directions.* Am Heart J, 2003. **146**: p. 787-796.
141. Cutlip D.E., et al., *Stent thrombosis in the modern era: a pooled analysis of multicenter coronary stent clinical trials.* Circulation, 2001. **103**: p. 1967-1971.
142. Bertrand M.E., et al., *Randomized multicenter comparison of conventional anticoagulation versus antiplatelet therapy in unplanned and elective coronary stenting. The full anticoagulation versus aspirin and ticlopidine (fantastic) study.* Circulation, 1998. **98**: p. 1597-1603.
143. de Feyter P.J., Vos J., and Rensing B.J., *Anti-restenosis trials.* Curr Interv Cardiol Rep, 2000. **2**: p. 326-331.
144. Kobayashi Y., et al., *Stented segment length as an independent predictor of restenosis.* J Am Coll Cardiol, 1999. **34**: p. 651-659.
145. Hoffmann R. and Mintz G.S., *Coronary in-stent restenosis - predictors, treatment and prevention.* Eur Heart J, 2000. **21**: p. 1739-1749.
146. Greenberg D., Bakhai A., and Cohen D.J., *Can we afford to eliminate restenosis? Can we afford not to?* J Am Coll Cardiol, 2004. **43**: p. 513-518.
147. Chen M.S., et al., *Bare metal stent restenosis is not a benign clinical entity.* American Heart Journal, 2006. **151**(6): p. 1260-1264.
148. Walters D. L., et al., *Acute coronary syndrome is a common clinical presentation of in-stent restenosis.* American Journal of Cardiology, 2002. **89**(5): p. 491-494.
149. Woods T. C. and Marks A. R., *Drug-eluting stents.* Annual Review of Medicine, 2004. **55**: p. 169-178.
150. Yokoi H., Kimura T., and Nakagawa Y., *Long-term clinical and quantitative angiographic follow-up after the Palmaz-Schatz stent restenosis.* J Am Coll Cardiol, 1995. **27**: p. 224A.
151. Lemos P.A., Serruys P.W., and Sousa J.E., *Drug-eluting stents: cost versus clinical benefit.* Circulation, 2003. **107**: p. 3003-3007.
152. Nobuyoshi M., et al., *Restenosis After Percutaneous Transluminal Coronary Angioplasty: Pathologic Observations in 20 Patients.* JACC, 1991. **17**: p. 433-439.

153. Austin G.E., et al., *Intimal proliferation of smooth muscle cells as an explanation for recurrent coronary artery stenosis after percutaneous transluminal coronary angioplasty.* JACC, 1985. **6**(2): p. 369-375.
154. Clowes A.W. and Schwartz S.M., *Significance of quiescent smooth muscle migration in the injured rat carotid artery.* Circulation, 1985. **56**: p. 139-145.
155. O'Brien E.R., et al., *Proliferation in primary and restenotic coronary atherectomy tissue. Implications for antiproliferative therapy.* Circulation, 1993. **73**: p. 223-231.
156. Lafont A., et al., *Restenosis After Experimental Angioplasty: Intimal, Medial, and Adventitial Changes Associated With Constrictive Remodeling.* Circulation, 1995. **76**: p. 996-1002.
157. Post M.J., Borst C., and Kuntz R.E., *The relative importance of arterial remodeling compared with intimal hyperplasia in lumen renarrowing after balloon angioplasty. A study in the normal rabbit and the hypercholesterolemic Yucatan micropig* Circulation, 1994. **89**: p. 2816-2821.
158. Mintz G.S., et al., *Arterial Remodeling After Coronary Angioplasty: A Serial Intravascular Ultrasound Study.* Circulation, 1996. **94**: p. 35-43.
159. Kastrati, A., et al., *Restenosis after coronary placement of various stent types.* The American Journal of Cardiology, 2001. **87**(1): p. 34-39.
160. Hoffmann R., et al., *Patterns and Mechanisms of In-Stent Restenosis: A Serial Intravascular Ultrasound Study.* Circulation, 1996. **94**: p. 1247-1254.
161. Komatsu R., et al., *Neointimal Tissue Response at Sites of Coronary Stenting in Humans: Macroscopic, Histological, and Immunohistochemical Analyses.* Circulation, 1998. **98**: p. 224-233.
162. Schoenhagen, P., et al., *Arterial remodeling and coronary artery disease: the concept of "dilated" versus "obstructive" coronary atherosclerosis.* Journal of the American College of Cardiology, 2001. **38**(2): p. 297-306.
163. Marx, S.O., H. Totary-Jain, and A.R. Marks, *Vascular smooth muscle cell proliferation in restenosis.* Circulation: Cardiovascular Interventions, 2011. **4**(1): p. 104-111.
164. Hoffmann R., et al., *Chronic Arterial Responses to Stent Implantation: A Serial Intravascular Ultrasound Analysis of Palmaz-Schatz Stents in Native Coronary Arteries.* JACC, 1996. **28**: p. 1134-1139.
165. Kornowski R., et al., *In-stent restenosis: contributions of inflammatory responses and arterial injury to neointimal hyperplasia* JACC, 1998. **31**: p. 224-230.
166. Schwartz R.S., et al., *Restenosis and the Proportional Neointimal Response to Coronary Artery Injury : Results in a Porcine Model.* JACC, 1992. **19**(2): p. 267-274.
167. Komatsu, R., et al., *Neointimal tissue response at sites of coronary stenting in humans macroscopic, histological, and immunohistochemical analyses.* Circulation, 1998. **98**(3): p. 224-233.
168. Mitra A.K. and Agrawal D.K., *In stent restenosis: bane of the stent era.* J Clin Pathol, 2006. **59**: p. 232-239.
169. Lowe H.C., Oesterle S.N., and Khachigian L.M., *Coronary in-stent restenosis: Current status and future strategies* JACC, 2001. **39**(2): p. 183-193.
170. Ong A.T.L., et al., *Classification and Current Treatment Options of In-Stent Restenosis: Present Status and Future Perspectives.* Herz, 2004. **29**: p. 187-194.
171. Lopez-Palop R., et al., *Utility of the fractional flow reserve in the evaluation of angiographically moderate in-stent restenosis.* Eur Heart J, 2004. **25**: p. 2040-2047.
172. Gottsauner-Wolf M., et al., *Restenosis - An Open File.* Clin Cardiol, 1996. **19**: p. 347-356.
173. Ojha M., et al., *Distribution of intimal and medial thickning in the human right coronary artery: A study of 17 RCAs.* Atheroscleosis, 2001. **158**: p. 147.

174. Velican C. and Velican D., *The precursors of coronary atherosclerotic plaques in subjects up to 40 years old.* Atherosclerosis, 1980. **37**: p. 33.
175. Dangas G.D., et al., *In-Stent Restenosis in the Drug-Eluting Stent Era.* JACC, 2010. **56**: p. 1897-1907.
176. Blouza A., Dumas L., and M'Baye I., *Multiobjective optimization of a stent in a fluid-structure context*, in *GECCO '08*. 2008, ACM: Atlanta, Georgia, USA. p. 2055-2060.
177. Gijsen F.J.H., et al., *The influence of the non-Newtonian properties of blood on the flow in large arteries: unsteady flow in a 90°curved tube.* Journal of Biomechanics, 1999. **32**: p. 705-713.
178. Lally C., Dolan F., and Prendergast P.J., *Cardiovascular stent design and vessel stresses: a finite element analysis.* Journal of Biomechanics, 2004. **38**: p. 1574-1581.
179. Tahir H., et al., *Multi-scale simulations of the dynamics of in-stent restenosis: impact of stent deployment and design.* The Royal Society, 2011: p. 1-12.
180. Levesque M.J. and Nerem R.M., *The elongation and orientation of cultured endothelial cells in response to shear stress.* J Biomech Eng., 1985. **107**(4): p. 341-347.
181. Levesque M.J., et al., *Correlation of endothelial cell shape and wall shear stress in a stenosed dog aorta.* Arterioscler Thromb Vasc Biol., 1986. **6**: p. 220-229.
182. Sanmartín, M., et al., *Influence of shear stress on in-stent restenosis: in vivo study using 3D reconstruction and computational fluid dynamics.* Revista Española de Cardiología (English Edition), 2006. **59**(1): p. 20-27.
183. LaDisa Jr, J.F., et al., *Three-dimensional computational fluid dynamics modeling of alterations in coronary wall shear stress produced by stent implantation.* Annals of Biomedical Engineering, 2003. **31**(8): p. 972-980.
184. Duraiswamy, N., et al., *Stented artery flow patterns and their effects on the artery wall.* Annu. Rev. Fluid Mech., 2007. **39**: p. 357-382.
185. Sakamoto, N., et al., *Effect of spatial gradient in fluid shear stress on morphological changes in endothelial cells in response to flow.* Biochemical and biophysical research communications, 2010. **395**(2): p. 264-269.
186. Ghriallais, R.N., L. McNamara, and M. Bruzzi, *Comparison of in vitro human endothelial cell response to self-expanding stent deployment in a straight and curved peripheral artery simulator.* Journal of The Royal Society Interface, 2013. **10**(81): p. 20120965.
187. Passerini, A.G., et al., *Coexisting proinflammatory and antioxidative endothelial transcription profiles in a disturbed flow region of the adult porcine aorta.* Proceedings of the National Academy of Sciences of the United States of America, 2004. **101**(8): p. 2482-2487.
188. Wang G., et al., *The change of local wall shear stress accelerates intima hyperplasia and atherosclerosis.* IEEE, 2007.
189. Rodkiewicz C. M., Sinha P., and Kennedy J.S., *On the application of a constitutive equation for whole human blood* Journal of Biomechanical Engineering, 1990. **112**: p. 198 - 206.
190. Walburn F.J. and Schneck D.J., *A constitutive equation for whole humanblood.* Biorheology, 1976. **13**: p. 201-210.
191. Cho Y. I. and Kensey K.R., *Effects of the non-Newtonian viscosity of blood on flows in a diseased arterial vessel. Part 1: Steady flows. .* Biorheology 1991. **28**: p. 241-262.
192. Ballyk P.D., Steinman D.A., and Ethier C.R., *Simulation of non-Newtonian blood flow in an end-to-end anastomosis.* Biorheology, 1994. **31**(5): p. 565-586.
193. Johnston B.M., et al., *Non-Newtonian blood flow in human right coronary arteries:Transient simulations.* journal of Biomechanics, 2006. **39**: p. 1116-1128.

194. Pant S., et al., *Multiobjective design optimisation coronary stents.* Journal of Biomaterials, 2011. **32**: p. 7755-7773.
195. Wahle A., et al., *Four–dimensional coronary morphology and computational hemodynamics.* Soc. Photo-Optical Instru Eng, 2001. **4322**: p. 743-753.
196. Serruys P.W., *Fourth annual american college of cardiology international lecture: a journey in the interventional field.* J Am Coll Cardiol, 2006. **47**: p. 1754-1768.
197. Sousa J.E., Serruys P.W., and Costa M.A., *New frontiers in cardiology: drug-eluting stents: Part II.* Circulation, 2003. **107**: p. 2383-2389.
198. Morice M.C., et al., *RAVEL Study Group. Randomized study with the sirolimus-coated bx velocity balloon-expandable stent in the treatment of patients with de novo native coronary artery lesions. A randomized comparison of a sirolimus-eluting stent with a standard stent for coronary revascularization.* N Engl J Med, 2002. **346**: p. 1773-1780.
199. Moses J.W., et al., *SIRIUS Investigators. Sirolimus-eluting stents versus standard stents in patients with stenosis in a native coronary artery.* N Engl J Med, 2003. **349**: p. 1315-1323.
200. Schampaert E., et al., *C-SIRIUS Investigators. The Canadian study of the sirolimus-eluting stent in the treatment of patients with long de novo lesions in small native coronary arteries (C-SIRIUS).* J Am Coll Cardiol, 2004. **43**: p. 1110-1115.
201. Grube E., et al., *TAXUS I: six- and twelve-month results from a randomized, double-blind trial on a slow-release paclitaxel-eluting stent for de novo coronary lesions.* Circulation, 2003. **107**: p. 38-42.
202. Colombo A., et al., *TAXUS II Study Group. Randomized study to assess the effectiveness of slow- and moderate-release polymer-based paclitaxel-eluting stents for coronary artery lesions.* Circulation, 2003. **108**: p. 788-794.
203. Stone G.W., et al., *TAXUS-IV Investigators. A polymer-based, paclitaxel-eluting stent in patients with coronary artery disease.* N Engl J Med, 2004. **350**.
204. Stone G.W., et al., *TAXUS V Investigators. Comparison of a polymer-based paclitaxel-eluting stent with a bare metal stent in patients with complex coronary artery disease: a randomized controlled trial.* JAMA, 2005. **294**: p. 1215-1223.
205. Dawkins K.D., et al., *TAXUS VI Investigators. Clinical efficacy of polymer-based paclitaxel-eluting stents in the treatment of complex, long coronary artery lesions from a multicenter, randomized trial: support for the use of drug-eluting stents in contemporary clinical practice.* Circulation, 2005. **112**: p. 3306-3313.
206. Grube E. and Buellesfeld L., *Paclitaxel-eluting stents: current clinical experience.* Am J Cardiovasc Drugs, 2004. **4**: p. 355-360.
207. Sousa J.E., et al., *Two-year angiographic and intravascular ultrasound follow-up after implantation of sirolimus-eluting stents in human coronary arteries.* Circulation, 2003. **107**: p. 381-383.
208. Schomig A., et al., *A meta-analysis of 16 randomized trials of sirolimus-eluting stents versus paclitaxel-eluting stents in patients with coronary artery disease.* J Am Coll Cardiol, 2007. **50**: p. 1373-1380.
209. Kandzari D.E., et al., *Frequency, predictors, and outcomes of drug-eluting stent utilization in patients with high-risk non-ST-segment elevation acute coronary syndromes.* Am J Cardiol, 2005. **96**: p. 750-755.
210. Jazi S.M.H., et al., *The effects of bare metal versus drug-eluting stent implantation on circulating endothelial cells following percutaneous coronary intervention.* J Res Med Sci, 2011. **16**(5): p. 605-610.
211. Esmon C.T. and Esmon N.L., *The link between vascular features and thrombosis.* Annu Rev Physiol, 2011. **73**: p. 503-514.

212. van Leeuwen E.B., et al., *Scanning electron microscopic analysis of endothelial cell coverage and quality in large vessels from multi-organ donors: effects of preservation on endothelial cell integrity.* Clin Transplant, 2000. **14**(3): p. 246-251.
213. Pant S., et al., *Multiobjective design optimisation of coronary stents.* Biomaterials, 2011. **32**(31): p. 7755-7773.
214. Seo T., Schachter L.G., and Barakat A.I., *Computational study of fluid mechanical disturbance induced by endovascular stents.* Ann Biomed Eng, 2005. **33**(4): p. 444-456.
215. Robaina, S., et al., *Platelet adhesion to simulated stented surfaces.* Journal of Endovascular Therapy, 2003. **10**(5): p. 978-986.
216. LaDisa, J., J. F., L. E. Olson, H. A. Douglas, D. C. Warltier, J. R. Kersten, and P. S. Pagel, *Alterations in wall shear stress predict sites of neointimal hyperplasia after stent implantation in rabbit iliac arteries.* Am. J. Physiol. Heart, 2005. **288**: p. H2465 - H2475.
217. Berry, J.L., et al., *Hemodynamics and wall mechanics of a compliance matching stent: in vitro and in vivo analysis.* Journal of Vascular and Interventional Radiology, 2002. **13**(1): p. 97-105.
218. Kastrati A., et al., *Intracoronary Stenting and Angiographic Results: Strut Thickness Effect on Restenosis Outcome (ISAR-STEREO) trial.* Circulation, 2001. **103**: p. 2816-2821.
219. Kereiakes D.J., et al., *Usefulness of a cobalt chromium coronary stent alloy.* Am J Cardiol, 2003. **92**: p. 463-466.
220. Menown I.B.A., et al., *The platinum chromium element stent platform: from alloy, to design, to clinical practice.* Adv Ther, 2010. **27**: p. 1219-141.
221. Krucoff, M.W., et al., *A novel bioresorbable polymer paclitaxel-eluting stent for the treatment of single and multivessel coronary disease. Primary results of the COSTAR (Cobalt Chromium Stent With Antiproliferative for Restenosis) II Study.* Journal of the American College of Cardiology, 2008. **51**(16): p. 1543-1552.
222. Kim J.W., et al., *A prospective, randomized, 6-month comparison of the coronary vasomotor response associated with a zotarolimus- versus a sirolimus-eluting stent: differential recovery of coronary endothelial dysfunction.* J Am Coll Cardiol, 2009. **53**: p. 1653-1659.
223. Kim J-S., et al., *Evaluation in 3 months duration of neointimal coverage after zotarolimus-eluting stent implantation by optical coherence tomography: the ENDEAVOR OCT trial.* J Am Coll Cardiol Intv, 2009. **2**: p. 1240-1247.
224. Awata M., et al., *Angioscopic comparison of neointimal coverage between zotarolimus- and sirolimus-eluting stents.* J Am Coll Cardiol, 2008. **52**: p. 789-790.
225. Fajadet J., et al., *Randomized, double-blind, multicenter study of the Endeavor zotarolimus-eluting phosphorylcholine-encapsulated stent for treatment of native coronary artery lesions: clinical and angiographic results of the ENDEAVOR II trial.* Circulation, 2006. **114**: p. 798-806.
226. Latib, A., et al., *Clinical outcomes after unrestricted implantation of everolimus-eluting stents.* JACC: Cardiovascular Interventions, 2009. **2**(12): p. 1219-1226.
227. Joner M., et al., *Endothelial cell recovery between comparator polymer-based drug-eluting stents* JACC, 2008. **52**(5): p. 333-342.
228. Virmani, R., et al., *Drug eluting stents: are human and animal studies comparable?* Heart, 2003. **89**(2): p. 133-138.
229. PRNewswire -- Boston Scientific Corporation. *Boston Scientific's PROMUS Element™ Platinum chromium stent demonstrates excellent outcomes in patients with long coronary lesions*. 2011 [cited 2012 12 April]; Available from: http://www.prnewswire.com/news-releases/boston-scientifics-promus-element-

platinum-chromium-stent-demonstrates-excellent-outcomes-in-patients-with-long-coronary-lesions-133439633.html.
230. Camenzind E., Steg P.G., and Wijns W., *Controversies in cardiovascular medicine: A cause for concern.* Circulation, 2007. **115**: p. 1440-1455.
231. Spaulding C., et al., *A pooled analysis of data comparing sirolimus-eluting stents with bare-metal stents.* N Engl J Med, 2007. **356**: p. 989-997.
232. Kastrati A., et al., *Analysis of 14 Trials Comparing Sirolimus-Eluting Stents with Bare-Metal Stents.* The New England Journal of Medicine, 2007. **356**: p. 1030-1039.
233. Stone G.W., et al., *Safety and efficacy of sirolimus- and paclitaxel-eluting coronary stents.* N Engl J Med, 2007. **356**: p. 998-1008.
234. Brodie B.R., et al., *Outcomes and complications with off-label use of drug-eluting stents: results from the STENT (Strategic Transcatheter Evaluation of New Therapies) group.* J Am Coll Cardiol Intv, 2008. **1**: p. 405-414.
235. Beohar N., et al., *Outcomes and complications associated with off-label and untested use of drug-eluting stents.* J A M A, 2007. **297**: p. 1992-2000.
236. Serruys P.W. and Daemen J., *Are drug-eluting stents associated with a higher rate of late thrombosis than bare metal stents? Late stent thrombosis: a nuisance in both bare metal and drug-eluting stents.* Circulation, 2007. **115**: p. 1433-1439.
237. Ong A.T. and Serruys P.W., *Drug-eluting stents: current issues.* Tex Heart Inst J, 2005. **32**: p. 372-377.
238. Virmani R., et al., *Localized hypersensitivity and late coronary thrombosis secondary to a sirolimus-eluting stent: should we be cautious?* Circulation, 2004. **109**: p. 701-705.
239. Ong A.T., et al., *Thirty-day incidence and six-month clinical outcome of thrombotic stent occlusion after bare-metal, sirolimus, or paclitaxel stent implantation.* J Am Coll Cardiol, 2005. **45**: p. 947-953.
240. Iakovou I., et al., *Incidence, predictors, and outcome of thrombosis after successful implantation of drug-eluting stents.* JAMA, 2005. **293**: p. 2126-2130.
241. McFadden E.P., et al., *Late thrombosis in drug-eluting coronary stents after discontinuation of antiplatelet therapy.* Lancet, 2004. **364**: p. 1519-1521.
242. Waters R.E., et al., *Late thrombosis following treatment of in-stent restenosis with drug-eluting stents after discontinuation of antiplatelet therapy.* Catheter Cardiovasc Interv, 2005. **65**: p. 520-524.
243. Mueller H., et al., *The effects of intra-aortic counterpulsation on cardiac performance and metabolism in shock associated with acute myocardial infarction.* J Clin Invest, 1971. **50**(9): p. 1885-1900.
244. Hwang, C.-W., D. Wu, and E.R. Edelman, *Physiological transport forces govern drug distribution for stent-based delivery.* Circulation, 2001. **104**(5): p. 600-605.
245. Eisenstein E.L., et al., *Clopidogrel use and long-term clinical outcomes after drug-eluting stent implantation.* JAMA, 2007. **297**(2): p. 159-168.
246. Brar S.S., et al., *Long-Term Outcomes by Clopidogrel Duration and Stent Type in a Diabetic Population With De Novo Coronary Artery Lesions.* JACC, 2008. **51**: p. 2220-2227.
247. Mehta S.R., et al., *Effects of pretreatment with clopidogrel and aspirin followed by long-term therapy in patients undergoing percutaneous coronary intervention: the PCI-CURE study.* Lancet, 2001. **358**: p. 527-533.
248. Steinhubl S.R., et al., *Early and sustained dual oral antiplatelet therapy following percutaneous coronary intervention: a randomized controlled trial.* J A M A, 2002. **288**: p. 2411-2420.

249. Yusuf S., et al., *Effects of clopidogrel in addition to aspirin in patients with acute coronary syndromes without ST-segment elevation.* N Engl J Med, 2001. **345**: p. 494-502.
250. Bhatt D.L., et al., *Patients with prior myocardial infarction, stroke, or symptomatic peripheral arterial disease in the CHARISMA trial.* JACC, 2007. **49**: p. 1982-1988.
251. Yusuf S., et al., *Early and late effects of clopidogrel in patients with acute coronary syndromes.* . Circulation, 2003. **107**: p. 966-972.
252. Moscucci M., et al., *Predictors of major bleeding in acute coronary syndromes: the Global Registry of Acute Coronary Events (GRACE).* . Eur Heart J, 2003. **24**: p. 1815-1823.
253. Park D., et al., *Stent Thrombosis, Clinical Events, and Influence of Prolonged Clopidogrel Use After Placement of Drug-Eluting Stent: Data From an Observational Cohort Study of Drug-Eluting Versus Bare-Metal Stents.* JACC, 2008. **1**(5): p. 495-502.
254. Tanzilli G., et al., *Effectiveness of Two-Year Clopidogrel and Aspirin in Abolishing the Risk of Very Late Thrombosis After Drug-Eluting Stent Implantation (from the TYCOON [Two-Year ClOpidOgrel Need] Study).* Am J Cardiol, 2009. **104**: p. 1357-1361.
255. Karvouni E., Korovesis S., and Katritsis D.G., *Very late thrombosis after implantation of sirolimus eluting stent.* Heart, 2005. **91**: p. e45.
256. Zhijian W., et al., *e0504 Chronic kidney disease and the risk of stent thrombosis after percutaneous coronary intervention with drug-eluting stents.* Heart, 2010. **96**: p. A157.
257. van Werkum J.W., et al., *Predictors of coronary stent thrombosis: the Dutch Stent Thrombosis Registry.* J Am Coll Cardiol, 2009. **53**: p. 1399-1409.
258. Sardi G., et al., *Left ventricular ejection fraction as a predictor of restenosis and stent thrombosis after percutaneous coronary intervention.* J. Am. Coll. Cardiol., 2011. **57**: p. e1639.
259. Park D.W., et al., *Frequency of and risk factors for stent thrombosis after drug-eluting stent implantation during long term follow-up.* Am J Cardiol, 2006. **98**: p. 352-356.
260. Kuchulakanti P.K., et al., *Correlates and long-term outcomes of angiographically proven stent thrombosis with sirolimus- and paclitaxel-eluting stents.* Circulation, 2006. **113**: p. 1108-1113.
261. Nguyen T.A., Diodati J.G., and Pharand C., *Resistance to Clopidogrel: A Review of the Evidence.* JACC, 2005. **45**(8): p. 1157-1163.
262. Muller I., et al., *Prevalence of clopidogrel non-responders among patients with stable angina pectoris scheduled for elective coronary stent placement.* Thromb Haemost, 2003. **89**: p. 783-787.
263. Barragan P., et al., *Resistance to thienopyridines: clinical detection of coronary stent thrombosis by monitoring of vasodilator-stimulated phosphoprotein phosphorylation.* Catheter Cardiovasc Interv, 2003. **59**: p. 295-302.
264. Matetzky S., et al., *Clopidogrel resistance is associated with increased risk of recurrent atherothrombotic events in patients with acute myocardial infarction.* Circulation, 2004. **109**: p. 3171-3175.
265. Angiolillo D.J., et al., *Variability in Individual Responsiveness to Clopidogrel: Clinical Implications, Management, and Future Perspectives.* JACC, 2007. **49**(14): p. 1505-1516.
266. Heestermans A.A.C.M., et al., *Acute and subacute stent thrombosis after primary percutaneous coronary intervention for ST-segment elevation myocardial infarction:*

incidence, predictors and clinical outcome. J Thromb Haemost, 2010. **8**: p. 2385-2393.

267. Hougaard M., et al., *Impact of lesion length on outcomes after revascularization with everolimus and sirolimus eluting stents. A Substudy of the SORT OUT IV TRIAL*, in *ACC-i2 with TCT*. 2012, JACC: McCormick Place South, Hall A. p. E195.
268. Nebeker J.R., et al., *Hypersensitivity cases associated with drug-eluting coronary stents: A review of available cases from the research on adverse drug events and reports (RADAR) project.* Journal of the American College of Cardiology, 2006. **47**: p. 176-181.
269. Gurbel P.A., et al., *Clopidogrel for coronary stenting: response variability, drug resistance, and the effect of pretreatment platelet reactivity.* Circulation, 2003. **107**: p. 2908-2913.
270. Gurbel P.A., et al., *Could stent design affect platelet activation? Results of the platelet activation in stenting (PAST) study.* J Invasive Cardiol., 2002. **14**: p. 584-589.
271. Nordmann A.J., Briel M., and Bucher H.C., *Mortality in randomized controlled trials comparing drug-eluting vs. bare metal stents in coronary artery disease: a meta-analysis.* Eur Heart J, 2006. **2.3**: p. 2784-2814.
272. Pfisterer M., et al., *Late clinical events after clopidogrel discontinuation may limit the benefit of drug-eluting stents: an observational study of drug-eluting versus bare-metal stents.* J Am Coll Cardiol, 2006. **48**: p. 2584-2591.
273. Lagerqvist B., et al., *Long-term outcomes with drug-eluting stents versus bare-metal stents in Sweden.* The New England Journal of Medicine, 2007. **356**: p. 1009-1018.
274. Stettler C., et al., *Outcomes associated with drug-eluting and bare-metalstents: acollaborativenetworkmeta-analysis.* The Lancet, 2007. **370**(9591): p. 937-948.
275. Kirtane A.J., et al., *Safety and efficacy of drug-eluting and bare metal stents comprehensive meta-analysis of randomized trials and observational studies.* Circulation, 2009. **119**: p. 3198-3206.
276. Hariharan, P., et al., *Multilaboratory particle image velocimetry analysis of the FDA benchmark nozzle model to support validation of computational fluid dynamics simulations.* (1528-8951 (Electronic)).
277. Marossy, A., et al., *Hemorheology and circulation.* Clinical hemorheology and microcirculation, 2009. **42**(4): p. 239-258.
278. Marrero, V.L., et al., *Numerical Study of Purely Viscous Non-Newtonian Flow in an Abdominal Aortic Aneurysm.* Journal of Biomechanical Engineering, 2014. **136**(10): p. 101001.
279. Mejia, J., R. Mongrain, and O.F. Bertrand, *Accurate prediction of wall shear stress in a stented artery: Newtonian versus non-Newtonian models.* Journal of Biomechanical Engineering, 2011. **133**(7): p. 074501.
280. Isobe N., et al., *Comparison of the Rheologic Parameters in Left Internal Thoracic Artery Grafts With Those in Saphenous Vein Grafts.* Circulation Journal, 2005. **69**(6): p. 700-706.
281. Baskurt O.K. and Meiselman H.J., *Blood Rheology and Hemodynamics.* Semin Thromb Hemost 2003. **29**(5): p. 435-450.
282. Cho, Y.I. and K.R. Kensey, *Effects of the non-Newtonian viscosity of blood on flows in a diseased arterial vessel. Part 1: Steady flows.* Biorheology, 1991(28): p. 241-62.
283. Chien, S., et al., *Effects of hematocrit and plasma proteins on human blood rheology at low shear rates.* Journal of Applied Physiology, 1966. **21**(1): p. 81-87.
284. Sharma K. and Bhat S.V., *Non-Newtonian rheology of leukemic blood and plasma: are n and k parameters of power law model diagnostic?* Physiol Chem Phys Med NMR, 1992. **24**: p. 307-312.

285. Hassan, T., et al., *Computational simulation of therapeutic parent artery occlusion to treat giant vertebrobasilar aneurysm.* American Journal of Neuroradiology, 2004. **25**(1): p. 63-68.
286. Versteeg, H.K. and W. Malalasekera, *An introduction to computational fluid dynamics: the finite volume method*. 2007: Pearson Education.
287. Bhaskaran, R. and L. Collins, *Introduction to CFD basics.* Cornell University-Sibley School of Mechanical and Aerospace Engineering, 2002.
288. Prakash, S. and C.R. Ethier, *Requirements for mesh resolution in 3D computational hemodynamics.* Journal of Biomechanical Engineering, 2001. **123**(2): p. 134-144.
289. Garin, G. and B.C. Berk, *Flow-mediated signaling modulates endothelial cell phenotype.* Endothelium, 2006. **13**(6): p. 375-384.
290. Patankar, S.V. and D.B. Spalding, *A calculation procedure for heat, mass and momentum transfer in three-dimensional parabolic flows.* International Journal of Heat and Mass Transfer, 1972. **15**(10): p. 1787-1806.
291. He, X. and D.N. Ku, *Pulsatile flow in the human left coronary artery bifurcation: average conditions.* Journal of biomechanical engineering, 1996. **118**(1): p. 74-82.
292. Kam, P. and I. Power, *Principles of Physiology for the Anaesthetist*. 2012: CRC Press.
293. Banerjee, M.K., R. Ganguly, and A. Datta, *Effect of pulsatile flow waveform and Womersley number on the flow in stenosed arterial geometry.* ISRN Biomathematics, 2012. **2012**.
294. Kajiya, F., et al., *Velocity profiles and phasic flow patterns in the non-stenotic human left anterior descending coronary artery during cardiac surgery.* Cardiovascular research, 1993. **27**(5): p. 845-850.
295. Liu B. and Tang D., *Influence of non-Newtonian properties of blood on the wall shear stress in human atherosclerotic right coronary arteries.* Mol Cell Biomech., 2011. **8**(1): p. 73-90.
296. Johnston B.M., et al., *Non-Newtonian blood flow in human right coronary arteries: steady state simulations.* Journal of Biomechanics, 2003. **37**: p. 709-720.
297. Razavi, A., E. Shirani, and M. Sadeghi, *Numerical simulation of blood pulsatile flow in a stenosed carotid artery using different rheological models.* Journal of Biomechanics, 2011. **44**(11): p. 2021-2030.
298. Rogers, C. and E.R. Edelman, *Endovascular stent design dictates experimental restenosis and thrombosis.* Circulation, 1995. **91**(12): p. 2995-3001.
299. Sadasivan, C., et al., *An original flow diversion device for the treatment of intracranial aneurysms evaluation in the rabbit elastase-induced model.* Stroke, 2009. **40**(3): p. 952-958.
300. Pant, S., et al., *The influence of strut-connectors in stented vessels: a comparison of pulsatile flow through five coronary stents.* Annals of Biomedical Engineering, 2010. **38**(5): p. 1893-1907.
301. Garasic J. M., et al., *Stent and artery geometry determine intimal thickening independent of arterial injury.* Circulation, 2000. **101**: p. 812 - 818.
302. Neuhaus, K.L., et al., *Videodensitometric measurement of coronary flow*, in *Angiocardiography*, H. Just and P.H. Heintzen, Editors. 1986, Springer Berlin Heidelberg. p. 383-388.
303. Cooke, J., et al., *Flow activates an endothelial potassium channel to release an endogenous nitrovasodilator.* Journal of Clinical Investigation, 1991. **88**(5): p. 1663.
304. Dewey, C., et al., *The dynamic response of vascular endothelial cells to fluid shear stress.* Journal of biomechanical engineering, 1981. **103**(3): p. 177-185.
305. Warboys, C.M., et al., *Acute and chronic exposure to shear stress have opposite effects on endothelial permeability to macromolecules.* American Journal of Physiology-Heart and Circulatory Physiology, 2010. **298**(6): p. H1850-H1856.

306. Weinberg, P.D., *Rate-limiting steps in the development of atherosclerosis: the response-to-influx theory.* Journal of vascular research, 2004. **41**(1): p. 1-17.
307. Dekker, R.J., et al., *Prolonged fluid shear stress induces a distinct set of endothelial cell genes, most specifically lung Krüppel-like factor (KLF2).* Blood, 2002. **100**(5): p. 1689-1698.
308. Galbraith, C., R. Skalak, and S. Chien, *Shear stress induces spatial reorganization of the endothelial cell cytoskeleton.* Cell motility and the cytoskeleton, 1998. **40**(4): p. 317-330.
309. Ghriallais, R.N., L. McNamara, and M. Bruzzi, *Comparison of in vitro human endothelial cell response to self-expanding stent deployment in a straight and curved peripheral artery simulator.* Journal of The Royal Society Interface, 2013. **10**(81).
310. Breen, L.T., P.E. McHugh, and B.P. Murphy, *Multi-axial mechanical stimulation of HUVECs demonstrates that combined loading is not equivalent to the superposition of individual wall shear stress and tensile hoop stress components.* Journal of biomechanical engineering, 2009. **131**(8): p. 081001.
311. Cecelja, M. and P. Chowienczyk, *Role of arterial stiffness in cardiovascular disease.* JRSM cardiovascular disease, 2012. **1**(4): p. 11.
312. Chiastra, C., et al., *On the necessity of modelling fluid–structure interaction for stented coronary arteries.* Journal of the mechanical behavior of biomedical materials, 2014. **34**: p. 217-230.
313. Ohashi, T., et al., *Hydrostatic pressure influences morphology and expression of VE-cadherin of vascular endothelial cells.* Journal of Biomechanics, 2007. **40**(11): p. 2399-2405.
314. Akimoto, S., et al., *Laminar shear stress inhibits vascular endothelial cell proliferation by inducing cyclin-dependent kinase inhibitor p21Sdi1/Cip1/Waf1.* Circulation Research, 2000. **86**(2): p. 185-190.
315. Xu, Q., *Disturbed flow-enhanced endothelial turnover in atherosclerosis.* Trends in cardiovascular medicine, 2009. **19**(6): p. 191-195.
316. Nakadate, H., H. Minamitani, and S. Aomura. *Combinations of hydrostatic pressure and shear stress influence morphology and adhesion molecules in cultured endothelial cells*. in *Engineering in Medicine and Biology Society (EMBC), 2010 Annual International Conference of the IEEE*. 2010. IEEE.
317. Bond, A.R., et al., *Morphological evidence for a change in the pattern of aortic wall shear stress with age.* Arteriosclerosis, thrombosis, and vascular biology, 2011. **31**(3): p. 543-550.
318. Bond, A.R., et al., *Intimal cushions and endothelial nuclear elongation around mouse aortic branches and their spatial correspondence with patterns of lipid deposition.* American Journal of Physiology-Heart and Circulatory Physiology, 2010. **298**(2): p. H536-H544.
319. Chiu, J.-J. and S. Chien, *Effects of disturbed flow on vascular endothelium: pathophysiological basis and clinical perspectives.* Physiological reviews, 2011. **91**(1): p. 327-387.
320. Malek, A.M. and S. Izumo, *Mechanism of endothelial cell shape change and cytoskeletal remodeling in response to fluid shear stress.* Journal of Cell Science, 1996. **109**(4): p. 713-726.
321. Krams, R., et al., *Evaluation of endothelial shear stress and 3D geometry as factors determining the development of atherosclerosis and remodeling in human coronary arteries in vivo. Combining 3D reconstruction from angiography and IVUS (ANGUS) with computational fluid dynamics.* Arterioscler Thromb Vasc Biol, 1997. **17**(10): p. 2061-5.

322. Wentzel, J.J., et al., *Extension of increased atherosclerotic wall thickness into high shear stress regions is associated with loss of compensatory remodeling.* Circulation, 2003. **108**(1): p. 17-23.
323. Chatzizisis, Y.S., et al., *Prediction of the localization of high-risk coronary atherosclerotic plaques on the basis of low endothelial shear stress an intravascular ultrasound and histopathology natural history study.* Circulation, 2008. **117**(8): p. 993-1002.
324. Taylor, C.A., T.J. Hughes, and C.K. Zarins, *Finite element modeling of three-dimensional pulsatile flow in the abdominal aorta: relevance to atherosclerosis.* Annals of Biomedical Engineering, 1998. **26**(6): p. 975-987.
325. Buchanan, J.R., Jr., et al., *Relation between non-uniform hemodynamics and sites of altered permeability and lesion growth at the rabbit aorto-celiac junction.* Atherosclerosis, 1999. **143**(1): p. 27-40.
326. Olgac, U., et al., *Patient-specific three-dimensional simulation of LDL accumulation in a human left coronary artery in its healthy and atherosclerotic states.* Am J Physiol Heart Circ Physiol, 2009. **296**(6): p. 27.
327. DePaola, N., et al., *Vascular endothelium responds to fluid shear stress gradients.* Arteriosclerosis, thrombosis, and vascular biology, 1992. **12**(11): p. 1254-1257.
328. Lei, M., C. Kleinstreuer, and G. Truskey, *Numerical investigation and prediction of atherogenic sites in branching arteries.* Journal of Biomechanical Engineering, 1995. **117**(3): p. 350-357.
329. LaMack, J.A., et al., *Interaction of wall shear stress magnitude and gradient in the prediction of arterial macromolecular permeability.* Annals of Biomedical Engineering, 2005. **33**(4): p. 457-464.
330. Zhang, C., et al., *Flow patterns and wall shear stress distribution in human internal carotid arteries: the geometric effect on the risk for stenoses.* J Biomech, 2012. **45**(1): p. 83-9.
331. Chakraborty, A., et al., *Effects of biaxial oscillatory shear stress on endothelial cell proliferation and morphology.* Biotechnology and Bioengineering, 2012. **109**(3): p. 695-707.
332. Ohashi, T., N. Sakamoto, and M. Sato. *Biomedical approach to endothelial cell responses to fluid shear stress and hydrostatic pressure*. in *Future Medical Engineering Based on Bionanotechnology: Proceedings of the Final Symposium of the Tohoku University 21st Century Center of Excellence Program, Sendai International Center, Japan 7-9 January 2007*. 2006. Imperial College Press.
333. Vara, D.S., et al., *The effect of shear stress on human endothelial cells seeded on cylindrical viscoelastic conduits: an investigation of gene expression.* Biotechnology and applied biochemistry, 2006. **45**(3): p. 119-130.
334. Conklin, B.S., et al., *A simple physiologic pulsatile perfusion system for the study of intact vascular tissue.* Medical Engineering & Physics, 2000. **22**(6): p. 441-449.
335. Dolan, J.M., et al., *High fluid shear stress and spatial shear stress gradients affect endothelial proliferation, survival, and alignment.* Annals of Biomedical Engineering, 2011. **39**(6): p. 1620-1631.
336. Punchard, M., et al., *Endothelial cell response to biomechanical forces under simulated vascular loading conditions.* Journal of Biomechanics, 2007. **40**(14): p. 3146-3154.
337. Dardik, A., et al., *Differential effects of orbital and laminar shear stress on endothelial cells.* Journal of Vascular Surgery, 2005. **41**(5): p. 869-880.
338. Lane, W.O., et al., *Parallel-plate flow chamber and continuous flow circuit to evaluate endothelial progenitor cells under laminar flow shear stress.* J Vis Exp, 2012. **17**(59).

339. Usami, S., et al., *Design and construction of a linear shear stress flow chamber.* Annals of Biomedical Engineering, 1993. **21**(1): p. 77-83.
340. DeVerse, J.S., et al., *On-chip endothelial inflammatory phenotyping.* Journal of visualized experiments: JoVE, 2012(65).
341. Moore Jr, J.E., et al., *A device for subjecting vascular endothelial cells to both fluid shear stress and circumferential cyclic stretch.* Annals of Biomedical Engineering, 1994. **22**(4): p. 416-422.
342. Elliott, J., et al. *Targeted Drug Delivery with PEGylated Immuno-Niosomes*. in *25th Southern Biomedical Engineering Conference 2009, 15–17 May 2009, Miami, Florida, USA*. 2009. Springer.
343. Bao, X., C.B. Clark, and J.A. Frangos, *Temporal gradient in shear-induced signaling pathway: involvement of MAP kinase, c-fos, and connexin43.* American Journal of Physiology-Heart and Circulatory Physiology, 2000. **278**(5): p. H1598-H1605.
344. Hsu, P.-P., et al., *Effects of flow patterns on endothelial cell migration into a zone of mechanical denudation.* Biochemical and Biophysical Research Communications, 2001. **285**(3): p. 751-759.
345. Nakadate, H., et al., *A new in vitro pulsatile perfusion system that mimics physiological transmural pressure and shear stress in any size of in vivo vessel.* Journal of Biomechanical Science and Engineering, 2008. **3**(1): p. 25-37.
346. El-Kurdi, M.S., J.S. Vipperman, and D.A. Vorp, *Control of circumferential wall stress and luminal shear stress within intact vascular segments perfused ex vivo.* Journal of Biomechanical Engineering, 2008. **130**(5): p. 051003.
347. Calvert, J.R. and R.A. Farrar, *An engineering data book*. 1999: Palgrave Macmillan.
348. Chetwynd, D., K. Worden, and G. Manson, *An application of interval-valued neural networks to a regression problem.* Proceedings of the Royal Society A: Mathematical, Physical and Engineering Science, 2006. **462**(2074): p. 3097-3114.
349. Melchels, F.P.W., *Preparation of advanced porous structures by stereolithography for application in tissue engineering*. 2010: University of Twente.
350. Brulle, Y., et al., *Industrial photochemistry XXI. Chemical, transport and refractive index effects in space-resolved laser photopolymerization.* Journal of photochemistry and photobiology A: Chemistry, 1994. **83**(1): p. 29-37.
351. Spangenberg, A., et al., *Recent advances in two-photon stereolithography.* 2013.
352. LaFratta, C.N., et al., *Multiphoton fabrication.* Angewandte Chemie International Edition, 2007. **46**(33): p. 6238-6258.
353. Sun, H.-B., et al., *Scaling laws of voxels in two-photon photopolymerization nanofabrication.* Applied physics letters, 2003. **83**(6): p. 1104-1106.
354. Wu S., Serbin J., and Gu M., *Two-photon polymerisation for three-dimensional micro-fabrication.* Journal of Photochemistry and Photobiology, 2006. **181**(1): p. 1-11.
355. Zhang, Y.-L., et al., *Designable 3D nanofabrication by femtosecond laser direct writing.* Nano Today, 2010. **5**(5): p. 435-448.
356. Odde D.J. and Renn M.J., *Laser-guided directwriting for applications in biotechnology.* Trends in Biotechnology, 1999. **17**(10): p. 385-389.
357. Ke K., Hasselbrink E.F., and Hunt A.J., *Rapidly prototyped three-dimensional nanofluidic channel networks in glass substrates.* Anal Chem., 2005. **77**(16): p. 5083-5088.
358. Kim T.N., et al., *Femtosecond laser-drilled capillary integrated into a microfluidic device.* Appl Phys Lett, 2005. **86**(20): p. 1-3.
359. Wang, J., et al., *Embellishment of microfluidic devices via femtosecond laser micronanofabrication for chip functionalization.* Lab Chip, 2010. **10**(15): p. 1993-1996.

360. Kumi, G., et al., *High-speed multiphoton absorption polymerization: fabrication of microfluidic channels with arbitrary cross-sections and high aspect ratios.* Lab Chip, 2010. **10**(8): p. 1057-1060.
361. Wikberg, E., et al., *Grafting of silica with sulfobetaine polymers via aqueous reversible addition fragmentation chain transfer polymerization and its use as a stationary phase in HILIC.* Journal of separation science, 2009. **32**(12): p. 2008-2016.
362. Kunnavakkam, M.V., et al., *Low-cost, low-loss microlens arrays fabricated by soft-lithography replication process.* Applied physics letters, 2003. **82**(8): p. 1152-1154.
363. Moeller, H.-C., et al., *A microwell array system for stem cell culture.* Biomaterials, 2008. **29**(6): p. 752-763.
364. Rouleau, L., J. Rossi, and R.L. Leask, *Concentration and time effects of dextran exposure on endothelial cell viability, attachment, and inflammatory marker expression in vitro.* Annals of Biomedical Engineering, 2010. **38**(4): p. 1451-1462.
365. Lane, W.O., et al., *Parallel-plate flow chamber and continuous flow circuit to evaluate endothelial progenitor cells under laminar flow shear stress.* Journal of visualized experiments: JoVE, 2012(59).
366. Schlichting, H. and K. Gersten, *Boundary-layer theory*. 2000: Springer Science & Business Media.
367. Huo, Y., T. Wischgoll, and G.S. Kassab, *Flow patterns in three-dimensional porcine epicardial coronary arterial tree.* American Journal of Physiology-Heart and Circulatory Physiology, 2007. **293**(5): p. H2959-H2970.
368. Suo, J., J.N. Oshinski, and D. Giddens, *Blood flow patterns in the proximal human coronary arteries: relationship to atherosclerotic plaque occurrence.* MOLECULAR AND CELLULAR BIOMECHANICS, 2008. **5**(1): p. 9.
369. Archie Jr, J.P., et al., *Hemodynamic parameters and early intimal thickening in branching blood vessels.* Critical Reviews™ in Biomedical Engineering, 2001. **29**(1).
370. Virmani, R., et al., *Drug-eluting stents: caution and concerns for long-term outcome.* Coronary artery disease, 2004. **15**(6): p. 313-318.
371. Ojha, M., *Spatial and temporal variations of wall shear stress within an end-to-side arterial anastomosis model.* Journal of biomechanics, 1993. **26**(12): p. 1377-1388.
372. LaDisa, J.F., et al., *Axial stent strut angle influences wall shear stress after stent implantation: analysis using 3D computational fluid dynamics models of stent foreshortening.* Biomedical engineering online, 2005. **4**(1): p. 59.
373. Dolan, J.M., J. Kolega, and H. Meng, *High wall shear stress and spatial gradients in vascular pathology: a review.* Annals of Biomedical Engineering, 2013. **41**(7): p. 1411-1427.
374. Meng, H., et al., *Progressive aneurysm development following hemodynamic insult: laboratory investigation.* Journal of neurosurgery, 2011. **114**(4): p. 1095-1103.
375. Metaxa, E., et al., *Characterization of critical hemodynamics contributing to aneurysmal remodeling at the basilar terminus in a rabbit model.* Stroke, 2010. **41**(8): p. 1774-1782.
376. Wang, Z., et al., *Molecular alterations associated with aneurysmal remodeling are localized in the high hemodynamic stress region of a created carotid bifurcation.* Neurosurgery, 2009. **65**(1): p. 169.
377. Schirmer, C.M. and A.M. Malek, *Computational fluid dynamic characterization of carotid bifurcation stenosis in patient-based geometries.* Brain and behavior, 2012. **2**(1): p. 42-52.
378. Lovett, J.K. and P.M. Rothwell, *Site of carotid plaque ulceration in relation to direction of blood flow: an angiographic and pathological study.* Cerebrovascular diseases (Basel, Switzerland), 2002. **16**(4): p. 369-375.

379. Fujii, K., et al., *Intravascular ultrasound assessment of ulcerated ruptured plaques a comparison of culprit and nonculprit lesions of patients with acute coronary syndromes and lesions in patients without acute coronary syndromes.* Circulation, 2003. **108**(20): p. 2473-2478.
380. LaDisa, J.F., et al., *Circumferential vascular deformation after stent implantation alters wall shear stress evaluated with time-dependent 3D computational fluid dynamics models.* Journal of applied physiology, 2005. **98**(3): p. 947-957.
381. O'Keeffe, L.M., et al., *Vascular cell adhesion molecule-1 expression in endothelial cells exposed to physiological coronary wall shear stresses.* Journal of biomechanical engineering, 2009. **131**(8): p. 081003.
382. Van der Heiden, K., et al., *The effects of stenting on shear stress: relevance to endothelial injury and repair.* Cardiovascular research, 2013. **99**(2): p. 269-275.
383. Fledderus, J.O., et al., *KLF2 primes the antioxidant transcription factor Nrf2 for activation in endothelial cells.* Arteriosclerosis, thrombosis, and vascular biology, 2008. **28**(7): p. 1339-1346.
384. Dekker, R.J., et al., *Endothelial KLF2 links local arterial shear stress levels to the expression of vascular tone-regulating genes.* The American journal of pathology, 2005. **167**(2): p. 609-618.
385. SenBanerjee, S., et al., *KLF2 Is a novel transcriptional regulator of endothelial proinflammatory activation.* The Journal of experimental medicine, 2004. **199**(10): p. 1305-1315.
386. Zahedmanesh, H. and C. Lally, *Determination of the influence of stent strut thickness using the finite element method: implications for vascular injury and in-stent restenosis.* Medical & biological engineering & computing, 2009. **47**(4): p. 385-393.
387. Zahedmanesh, H. and C. Lally, *A multiscale mechanobiological modelling framework using agent-based models and finite element analysis: application to vascular tissue engineering.* Biomechanics and modeling in mechanobiology, 2012. **11**(3-4): p. 363-377.
388. Evans, D.J., et al., *The application of multiscale modelling to the process of development and prevention of stenosis in a stented coronary artery.* Philosophical Transactions of the Royal Society A: Mathematical, Physical and Engineering Sciences, 2008. **366**(1879): p. 3343-3360.
389. Boyle, C., et al., *Computational simulation methodologies for mechanobiological modelling: a cell-centred approach to neointima development in stents.* Philosophical Transactions of the Royal Society A: Mathematical, Physical and Engineering Sciences, 2010. **368**(1921): p. 2919-2935.
390. Boyle, C.J., A.B. Lennon, and P.J. Prendergast, *In silico prediction of the mechanobiological response of arterial tissue: application to angioplasty and stenting.* Journal of biomechanical engineering, 2011. **133**(8): p. 081001.
391. Helmlinger, G., et al., *Effects of pulsatile flow on cultured vascular endothelial cell morphology.* Journal of biomechanical engineering, 1991. **113**(2): p. 123-131.
392. Uzarski, J.S., E.W. Scott, and P.S. McFetridge, *Adaptation of endothelial cells to physiologically-modeled, variable shear stress.* PloS one, 2013. **8**(2): p. e57004.
393. Hsieh, H.J., N.Q. Li, and J.A. Frangos, *Pulsatile and steady flow induces c-fos expression in human endothelial cells.* Journal of cellular physiology, 1993. **154**(1): p. 143-151.
394. White, J., W. Amos, and M. Fordham, *An evaluation of confocal versus conventional imaging of biological structures by fluorescence light microscopy.* The Journal of cell biology, 1987. **105**(1): p. 41-48.

395. Eskin, S., et al., *Response of cultured endothelial cells to steady flow.* Microvascular research, 1984. **28**(1): p. 87-94.
396. Jones, T.R., et al., *CellProfiler Analyst: data exploration and analysis software for complex image-based screens.* BMC bioinformatics, 2008. **9**(1): p. 482.
397. Iftikhar, S., et al., *Segmentation of endothelial cell boundaries of rabbit aortic images using a machine learning approach.* Journal of Biomedical Imaging, 2011. **2011**: p. 4.
398. Gee, A.G., et al. *Universal visualization platform*. in *Electronic Imaging 2005*. 2005. International Society for Optics and Photonics.
399. Beucher, S. and F. Meyer, *The morphological approach to segmentation: the watershed transformation.* OPTICAL ENGINEERING-NEW YORK-MARCEL DEKKER INCORPORATED-, 1992. **34**: p. 433-433.
400. Grau, V., et al., *Improved watershed transform for medical image segmentation using prior information.* Medical Imaging, IEEE Transactions on, 2004. **23**(4): p. 447-458.
401. Carpenter, A.E., et al., *CellProfiler: image analysis software for identifying and quantifying cell phenotypes.* Genome biology, 2006. **7**(10): p. R100.
402. Bray, M.A., M.S. Vokes, and A.E. Carpenter, *Using CellProfiler for automatic identification and measurement of biological objects in images.* Current Protocols in Molecular Biology, 2014: p. 14.17. 1-14.17. 13.
403. Lamprecht, M.R., D.M. Sabatini, and A.E. Carpenter, *CellProfiler™: free, versatile software for automated biological image analysis.* Biotechniques, 2007. **42**(1): p. 71.
404. Jones, T.R., A. Carpenter, and P. Golland, *Voronoi-based segmentation of cells on image manifolds*, in *Computer Vision for Biomedical Image Applications*. 2005, Springer. p. 535-543.
405. Schwartz, E.A., et al., *Exposure of Human Vascular Endothelial Cells to Sustained Hydrostatic Pressure Stimulates Proliferation Involvement of the αV Integrins.* Circulation research, 1999. **84**(3): p. 315-322.
406. Lampugnani, M.G., et al., *Cell confluence regulates tyrosine phosphorylation of adherens junction components in endothelial cells.* Journal of Cell Science, 1997. **110**(17): p. 2065-2077.
407. Kataoka, N., et al., *The morphological responses of cultured bovine aortic endothelial cells to fluid-imposed shear stress under sparse and colony conditions.* JSME International Journal Series C, 1998. **41**(1): p. 76-82.
408. Yoshino, D., K. Sato, and M. Sato, *Endothelial cell response under hydrostatic pressure condition mimicking pressure therapy.* Cellular and Molecular Bioengineering: p. 1-8.
409. Kawata, Y., et al., *High pressure conditions promote the proliferation of rat cultured mesangial cells in vitro.* Biochimica et Biophysica Acta (BBA)-Molecular Cell Research, 1998. **1401**(2): p. 195-202.
410. Salwen, S., et al., *Three-dimensional changes of the cytoskeleton of vascular endothelial cells exposed to sustained hydrostatic pressure.* Medical and Biological Engineering and Computing, 1998. **36**(4): p. 520-527.
411. Maniotis, A.J., C.S. Chen, and D.E. Ingber, *Demonstration of mechanical connections between integrins, cytoskeletal filaments, and nucleoplasm that stabilize nuclear structure.* Proceedings of the National Academy of Sciences, 1997. **94**(3): p. 849-854.
412. Tremblay, D., et al., *Actin and microtubules play distinct roles in governing the anisotropic deformation of cell nuclei in response to substrate strain.* Cytoskeleton, 2013. **70**(12): p. 837-848.

413. Chatzizisis, Y.S., et al., *Role of endothelial shear stress in the natural history of coronary atherosclerosis and vascular remodeling: molecular, cellular, and vascular behavior.* Journal of the American College of Cardiology, 2007. **49**(25): p. 2379-2393.
414. Davies, P.F., et al., *The convergence of haemodynamics, genomics, and endothelial structure in studies of the focal origin of atherosclerosis.* Biorheology, 2002. **39**(3-4): p. 299-306.
415. Li, Y.-S.J., J.H. Haga, and S. Chien, *Molecular basis of the effects of shear stress on vascular endothelial cells.* Journal of biomechanics, 2005. **38**(10): p. 1949-1971.
416. Pienta, K.J. and D.S. Coffey, *Nuclear-Cytoskeletal interactions: Evidence for physical connections between the nucleus and cell periphery and their alteration by transformation.* Journal of cellular biochemistry, 1992. **49**(4): p. 357-365.
417. Dahl, K.N., A.J. Ribeiro, and J. Lammerding, *Nuclear shape, mechanics, and mechanotransduction.* Circulation research, 2008. **102**(11): p. 1307-1318.
418. Tkachenko, E., et al., *The nucleus of endothelial cell as a sensor of blood flow direction.* Biology open, 2013: p. BIO20134622.
419. Bissell, M.J., et al., *Tissue structure, nuclear organization, and gene expression in normal and malignant breast.* Cancer Research, 1999. **59**(7 Supplement): p. 1757s-1764s.
420. Paszek, M.J., et al., *Tensional homeostasis and the malignant phenotype.* Cancer cell, 2005. **8**(3): p. 241-254.
421. Franke, R.-P., et al., *Induction of human vascular endothelial stress fibres by fluid shear stress.* 1984.
422. Davies, P.F., et al., *Spatial relationships in early signaling events of flow-mediated endothelial mechanotransduction.* Annual Review of Physiology, 1997. **59**(1): p. 527-549.
423. Kadohama, T., et al., *Effects of different types of fluid shear stress on endothelial cell proliferation and survival.* Journal of cellular physiology, 2007. **212**(1): p. 244-251.
424. Arslan, N., S. Isik, and O. Uykan, *Steady and disturbed flow effects on human umbilical vein endothelial cells (HUVECs) in vascular system: an experimental study.* Acta Bioeng Biomech, 2010. **12**(4): p. 3-9.
425. Estrada, R., et al., *Microfluidic endothelial cell culture model to replicate disturbed flow conditions seen in atherosclerosis susceptible regions.* Biomicrofluidics, 2011. **5**(3): p. 032006.
426. Ando, J., H. Nomura, and A. Kamiya, *The effect of fluid shear stress on the migration and proliferation of cultured endothelial cells.* Microvascular research, 1987. **33**(1): p. 62-70.
427. Levesque, M., R. Nerem, and E. Sprague, *Vascular endottielial cell proliferation in culture and the influence of flow.* Biomaterials, 1990. **11**(9): p. 702-707.
428. Tardy, Y., et al., *Shear stress gradients remodel endothelial monolayers in vitro via a cell proliferation-migration-loss cycle.* Arteriosclerosis, thrombosis, and vascular biology, 1997. **17**(11): p. 3102-3106.
429. Flaherty, J.T., et al., *Endothelial nuclear patterns in the canine arterial tree with particular reference to hemodynamic events.* Circulation Research, 1972. **30**(1): p. 23-33.
430. Ostrowski, M.A., et al., *Microvascular endothelial cells migrate upstream and align against the shear stress field created by impinging flow.* Biophysical journal, 2014. **106**(2): p. 366-374.
431. Sprague, E.A., et al., *Impact of parallel micro-engineered stent grooves on endothelial cell migration, proliferation, and function: An in vivo correlation study*

of the healing response in the coronary swine model. Circulation: Cardiovascular Interventions, 2012. **5**(4): p. 499-507.
432. Kurowska-Nouyrigat, W. and J. Szumbarski, *Numerical Simulation of Restenosis in a Stented Coronary Artery.* World Academy of Science, Engineering and Technology, 2009. **58**: p. 42-45.
433. Young, J.J., *Neointimal formation following drug-eluting stents: physiology, timeline, and the influence of drug delivery systems.* Reviews in cardiovascular medicine, 2006. **8**: p. S3-10.
434. White, C.R. and J.A. Frangos, *The shear stress of it all: the cell membrane and mechanochemical transduction.* Philosophical Transactions of the Royal Society B: Biological Sciences, 2007. **362**(1484): p. 1459-1467.
435. Dewey, C., *Effects of fluid flow on living vascular cells.* Journal of biomechanical engineering, 1984. **106**(1): p. 31-35.
436. Levesque, M., et al., *The influence of shear stress on cultured vascular endothelial cells: The stress response of an anchorage-dependent mammalian cell.* Biotechnology progress, 1989. **5**(1): p. 1-8.
437. Albuquerque, M.L.C., et al., *Shear stress enhances human endothelial cell wound closure in vitro.* American Journal of Physiology-Heart and Circulatory Physiology, 2000. **279**(1): p. H293-H302.
438. Hsieh, H.-J., et al., *Shear-induced endothelial mechanotransduction: the interplay between reactive oxygen species (ROS) and nitric oxide (NO) and the pathophysiological implications.* J Biomed Sci, 2014. **21**(3).
439. Oeckinghaus, A. and S. Ghosh, *The NF-κB family of transcription factors and its regulation.* Cold Spring Harbor perspectives in biology, 2009. **1**(4): p. a000034.
440. Blaecke, A., et al., *Measurement of nuclear factor-kappa B translocation on lipopolysaccharide-activated human dendritic cells by confocal microscopy and flow cytometry.* Cytometry, 2002. **48**(2): p. 71-79.
441. Orr, A.W., et al., *The subendothelial extracellular matrix modulates NF-κB activation by flow a potential role in atherosclerosis.* The Journal of cell biology, 2005. **169**(1): p. 191-202.
442. Davis, M.E., et al., *Shear stress regulates endothelial nitric-oxide synthase promoter activity through nuclear factor κB binding.* Journal of Biological Chemistry, 2004. **279**(1): p. 163-168.
443. Nakadate, H., H. Minamitani, and S. Aomura. *Combination of shear stress and hydrostatic pressure decreases ICAM-1, VCAM-1 and E-selectin expressions induced by TNF-α in cultured endothelial cells*. in *5th European Conference of the International Federation for Medical and Biological Engineering*. 2012. Springer.
444. Morigi, M., et al., *Fluid shear stress modulates surface expression of adhesion molecules by endothelial cells.* Blood, 1995. **85**(7): p. 1696-1703.
445. Libby, P., P.M. Ridker, and A. Maseri, *Inflammation and atherosclerosis.* Circulation, 2002. **105**(9): p. 1135-1143.
446. Nagel, T., et al., *Vascular endothelial cells respond to spatial gradients in fluid shear stress by enhanced activation of transcription factors.* Arteriosclerosis, Thrombosis, and Vascular Biology, 1999. **19**(8): p. 1825-1834.
447. Mohan, S., et al., *I kappa B alpha-dependent regulation of low-shear flow-induced NF-kappa B activity: role of nitric oxide.* American Journal of Physiology-Cell Physiology, 2003. **284**(4): p. C1039-C1047.
448. Collins, T. and M.I. Cybulsky, *NF-κB: pivotal mediator or innocent bystander in atherogenesis?* Journal of Clinical Investigation, 2001. **107**(3): p. 255.

449. Mohan, S., N. Mohan, and E.A. Sprague, *Differential activation of NF-kappa B in human aortic endothelial cells conditioned to specific flow environments.* American Journal of Physiology-Cell Physiology, 1997. **273**(2): p. C572-C578.
450. Lan, Q., K.O. Mercurius, and P.F. Davies, *Stimulation of transcription factors NFκB and AP1 in endothelial cells subjected to shear stress.* Biochemical and biophysical research communications, 1994. **201**(2): p. 950-956.